Spring 3-20-2012

Circumstellar Disks Around Rapidly Rotating Be-Type Stars

Yamina Touhami
Georgia State University

CIRCUMSTELLAR DISKS AROUND RAPIDLY ROTATING Be-TYPE STARS

by

YAMINA N. TOUHAMI

Under the Direction of Douglas R. Gies

ABSTRACT

Be stars are rapidly rotating B-type stars that eject large amounts of material into a circumstellar disk. Evidence of the presence of a disk is found through hydrogen emission lines in their spectra, IR excess flux, and linear intrinsic polarization. In this dissertation, we report the first simultaneous interferometric and spectroscopic observations of circumstellar disks around 24 bright Be stars made using the techniques of long baseline interferometry and moderate resolution spectroscopy in the near infrared. The goal of the project is to characterize the fundamental geometrical and physical properties of the emitting regions that are responsible for the IR flux excesses detected in the K-band in our sample stars. This observational work has been conducted with both the Center for High Angular Resolution Astronomy (CHARA) Array at Mount Wilson Observatory, and the Mimir spectrograph at Lowell Observatory.

The visibility measurements were interpreted with different geometrical and physical disk models in order to determine the spatial extension of the disk, the inclination angle, the position angle, and the density profile of the disk. We find that the spatial extension of the circumstellar disk in the K-band is only about a few stellar radii, and that the density structure of the disk is consistent with a radially decreasing function with a density exponent that ranges between 2.5 and 3.5. The resulting disk densities are in a good agreement with those derived from the Infrared Astronomical Satellite (IRAS) measurements, and the resulting disk geometries are consistent with previous polarimetric measurements. We find that the K-band sizes of the emitting regions in the disk are smaller by a factor of two than the Hα sizes, and we show that this is due to the lower opacity of the continuum in the disk.

By combining recent measurements of the projected rotational velocities with the disk inclination angles derived from interferometry, we were able to estimate the actual equatorial linear rotational velocities of the Be stars in our sample. The obtained linear rotational velocities indicate that Be stars are rapid rotators with an equatorial velocity that is about 0.7 - 0.9 of their critical velocities.

INDEX WORDS: Stars, Circumstellar disk, Be stars, Infrared, Stellar interferometry, Spectroscopy

CIRCUMSTELLAR DISKS AROUND RAPIDLY ROTATING Be-TYPE STARS

by

YAMINA N. TOUHAMI

A Dissertation Submitted in Partial Fulfillment of Requirements for the Degree of

Doctor of Philosophy

in the College of Arts and Sciences

Georgia State University

2012

CIRCUMSTELLAR DISKS AROUND RAPIDLY ROTATING Be-TYPE STARS

by

YAMINA N. TOUHAMI

Committee Chair:	Douglas R. Gies
Committee:	Harold A. McAlister
	Russel J. White
	Vincent Coudé du Foresto
	Carol E. Jones
	D. Michael Crenshaw
	Unil Perera

Electronic Version Approved:

Office of Graduate Studies

College of Arts & Sciences

Georgia State University

May 2012

DEDICATION

To my parents

ACKNOWLEDGMENTS

for their tremendous love and support. I also want to express my gratitude to my extended family members and friends in France, Algeria, and here in the US.

TABLE OF CONTENTS

LIST OF FIGURES

LIST OF ABBREVIATIONS

2MASS	the Two Micron All-Sky Survey
AKARI	Japanese InfraRed Imaging Satellite
ALT	Altitude
AMBER	the near-infrared/red focal instrument of the VLTI
AZ	Azimuth
BeXRB	Be X-ray Binary
CHARA	Center for High Angular Resolution Astronomy
CCD	Charged Coupled Device
FOV	Field Of View
FWHM	full-width at half-maximum
FWSM	full-width of the second moment at half-maximum
HJD	Heliocentric Julian Date
HWHM	half-width at half-maximum
IDL	Interactive Data Language
IR	infrared
IRAF	Image Reduction and Analysis Facility
IRTF	Infrared Telescope Facility
ISI	Infrared Spatial Interferometer
JD	Julian Date
Keck	W.M. Keck Observatory
KPNO	Kitt Peak National Observatory
LTE	local thermodynamic equilibrium

MIDI	the Mid-Infrared instrument
MJD	Modified Julian Date
MIRC	Michigan Infrared Combiner
NASA	National Aeronautics and Space Administration
non-LTE	non local thermodynamic equilibrium
NPOI	Navy Prototype Optical Interferometer
NOAO	National Optical Astronomy Observatory
OPD	Optical Path Difference
OPLE	Optical Path Length Equalizer
PC	Parsec
RMS	Root Mean Square
RV	Radial Velocity
SED	Spectral Energy Distribution
SUSI	Sydney University Stellar Interferometer
VEGA	Visible spEctroGraph and polArimeter
VINCI	the VLT Interferometer Commissioning Instrument
VLTI	Very Large Telescope Interferometer
YSO	Young Stellar Object

Imagination is more important than knowledge.

—— Albert Einstein

− 1 −

Introduction

In this chapter, a brief introduction of the stellar properties of Be stars as well as the basic concepts of stellar interferometry is presented. A detailed description of Be stars can be found in the review article by Porter & Rivinius (2003), and more complete discussion of the theory of interferometry can be found in the excellent review papers by Quirrenbach (2001) and Monnier (2003). The interferometric observations in this work were made at the Center for High Angular Resolution Astronomy Array (CHARA), and in addition, a description of the most relevant aspects of this instrument is presented here.

1.1 Long Baseline Interferometry

1.1.1 Basic Concepts

The angular resolution of a single-dish telescope is diffraction limited to an angle $\frac{\lambda}{D}$, where λ is the effective wavelength and D is the aperture size of the telescope. The angular resolution is inversely proportional to the diameter of the telescope, which means that the larger the aperture size, the better the angular resolution. In reality, the angular resolution is highly affected by the atmospheric turbulence, and even with the adaptive optics correction, the limitation of the angular resolution imposed by the atmosphere is only partially corrected. Currently, the 10-meter Keck telescope using segmented mirrors with adaptive optics at visible wavelengths (0.55 μm) can reach an angular resolution of about 15 mas. In interferometry, where two or more telescopes are separated by a distance B, identified as the baseline of the interferometer, the angular resolution $\frac{\lambda}{B}$ can easily attain a fraction of a milliarcsecond with large baselines. Figure 1.1 illustrates the classical scheme of a
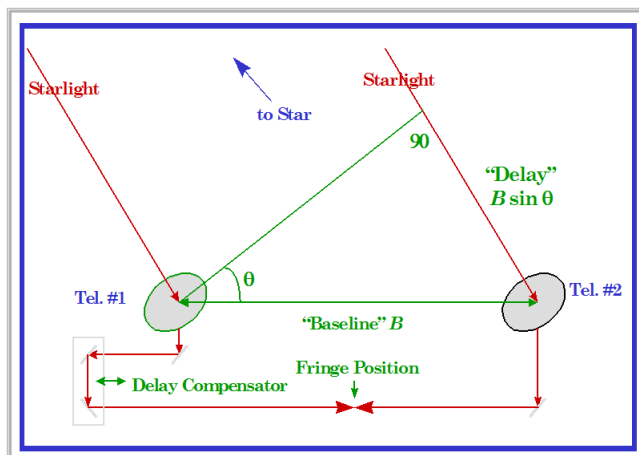
Figure 1.1: A scheme of a 2-Telescope Interferometer (courtesy H. McAlister).

two-telescope interferometer, where a quasi-monochromatic point source is observed by two separated apertures. The starlight reaches the second aperture of the interferometer with a delay that is proportional to the baseline. This delay, which is referred to as the optical path difference (OPD), is compensated for in the lab in order generate sinusoidal high contrast fringes on the detector. A maximum of signal intensity appears at positions where the OPD is an integer number of wavelengths, and the fringe separation corresponds to an angular resolution $\frac{\lambda}{B}$. If the angular size of the source is a significant fraction of the period of the fringes $\frac{\lambda}{B}$, then the observed source is resolved by the interferometer.

In practice, the starlight received on the detector is polychromatic, and thus each wavelength generates a set of fringes that is summed incoherently to form the resulting fringe pattern. The intensity of the resulting fringe pattern is called the interferometric visibility.

1.1.2 The Zernike-van Cittert Theorem

Another important concept in interferometry is the coherence, which measures the range in space and time over which the light beams may interfere. Temporal and spatial coherence

of a light-wave is about the interference at different instants and positions, respectively. An interferometer measures the tempo-spatial coherence of the electromagnetic field of the light source. The coherence length is given by:

$$l_c = \frac{\lambda^2}{\delta\lambda},$$

(1.1)

where $\delta\lambda$ is the wavelength bandwidth.

The Zernike-van Cittert theorem links the complex visibility γ measured by an interferometer to the intensity distribution of the observed source $S(\overrightarrow{\alpha})$, with an angular distance $\overrightarrow{\alpha}$, which is given by:

$$\gamma(\overrightarrow{u}) = \int\int S(\overrightarrow{\alpha})\exp{-2i\pi\overrightarrow{\alpha}.\overrightarrow{u}}d\overrightarrow{\alpha} = |\gamma|\exp(i\phi),$$

(1.2)

where $\overrightarrow{u}(u,v) = \frac{\overrightarrow{B}}{\lambda}$ is the spatial frequency in the Fourier plane at the wavelength of the observation.

The resulting intensity of interfering the two light beam intensities I_1 and I_2 is given by:

$$I = I_1 + I_2 + 2\sqrt{I_1 I_2}V_{inst}|\gamma|\cos(\phi_{obj} + \phi_{atm}),$$

(1.3)

where ϕ_{obj} is the phase of the object and ϕ_{atm} is the phase introduced by the atmosphere. V_{inst} is the interferometer instrumental response, and (u,v) are the components of the vector $\overrightarrow{u}$, which represent the baseline projection on the sky.

1.1.3 The Observed Visibility

Astronomical observations from the ground at visible and infrared wavelengths are highly degraded by atmospheric turbulence. The incoming wavefronts are phase-shifted, which corrupt the resulting images. The Fried parameter r_0 is the dimension over which the

incoming wavefront approximately conserves the same phase so that a point source appears to have an angular diameter given by λ/r_0. Nominal values for astronomical seeing under typical conditions are usually about $r_0 \sim 10$ cm at visible wavelengths and 50 cm at infrared wavelengths. In practice, the use of tip-tilt correction on single telescopes helps somewhat to minimize the instrumental loss of information. Therefore, the phase information collected by a two-telescope interferometer is totally lost and only the modulus of the fringe contrast is measured.

The fringe amplitude, or the contrast of the interferometric visibility $|\gamma|$ measured by the interferometer is called $Visibility$. For a point source, the ideal fringe contrast is 1 and decreases as the angular size of the source increases. Visibility measurements characterize angular scales of the source intensity distribution. Since only a symmetrical intensity distribution on the sky has a visibility function that is real, the symmetry information on the observed source is incomplete with a Classical two-telescope interferometer. In this case, we can only predict a normalized visibility versus baseline from a given brightness distribution model, and fit the interferometric data in order to determine the parameters that characterize the model. Figure 1.2 shows examples of different intensity distributions and their corresponding visibility curves. The top panels show the case of a binary system. The periodicity in the resulting visibility is a function of the binary separation and the magnitude difference between the two components. The middle set of panels show the case of a resolved source, and the bottom panels show the case of an unresolved central star with an extended emission such as a star plus a circumstellar disk.
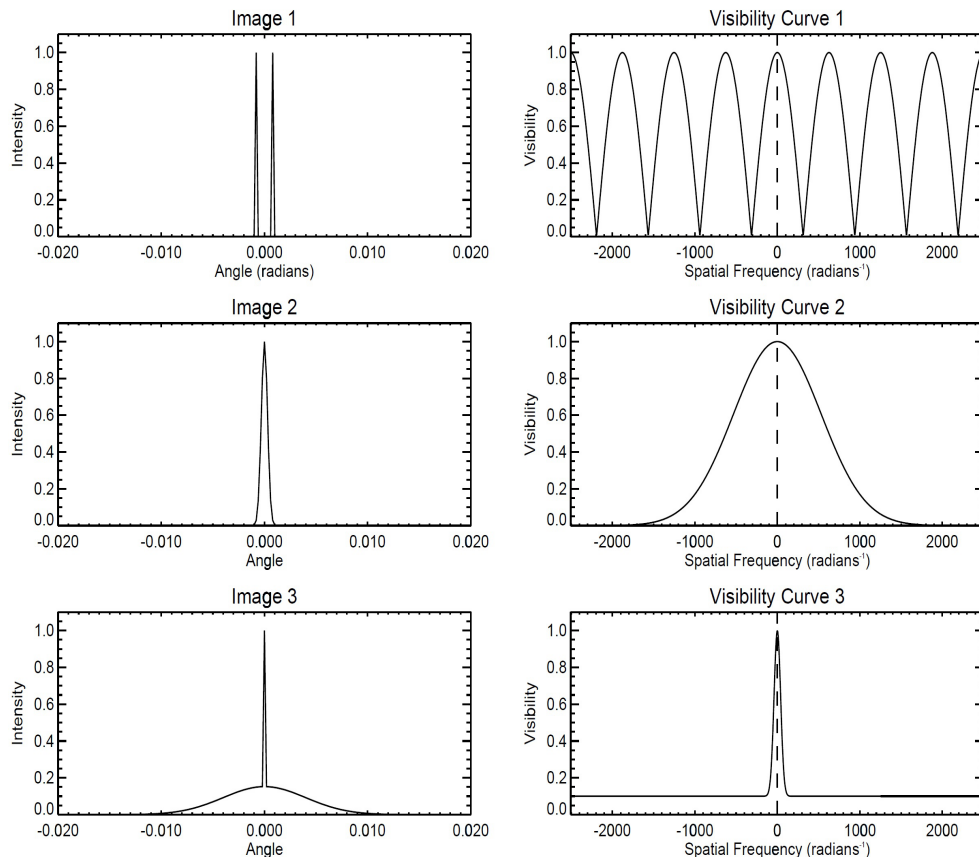
Figure 1.2: Simple models of intensity distributions and their corresponding visibility curves. The left panels show the assumed angular intensity, and the right panels show the Fourier amplitude of the image intensity distribution (courtesy J. Monnier).

1.1.4 The CHARA Array

The CHARA Array is an optical/near-infrared six-telescope interferometer array located at Mount Wilson Observatory, CA, and operated by Georgia State University. Figure 1.3 is a map of the CHARA Array along with the other operating facilities on Mount Wilson. For a more detailed description of the Array, see ten Brummelaar et al. (2005). The six telescopes of the Array are all 1 meter in aperture, and they compress the incoming starlight to a collimated beam of 12.5 cm. The position of each telescope and their orientation makes available 15 non-redundant baselines ranging from 34 to 331 meters.
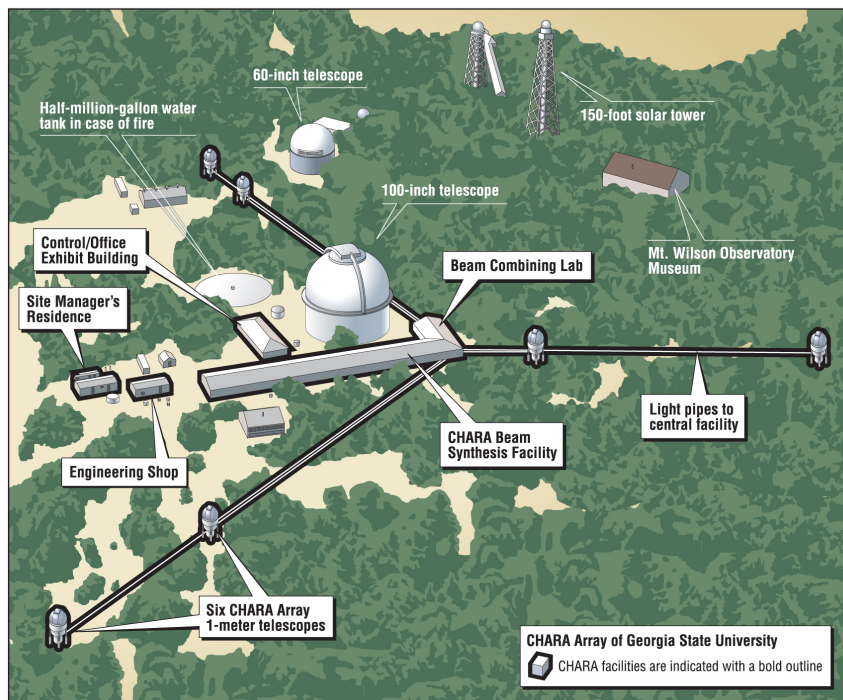
Figure 1.3: The CHARA Array and its surroundings. North is to the lower right.

There are six beam combination tables at CHARA. The two original beam combiners, CHARA Classic and FLUOR, combine the light in the near infrared from two telescopes only. The other beam combiners are: CLIMB, a three-telescope beam combiner operating in the H- and K-bands of the near infrared, PAVO, a three-telescope optical beam combiner, VEGA, a four-telescope beam combiner in the optical with high spectral dispersion capabilities, and MIRC, a six-telescope beam combiner with an associated fringe-tracker that operates in the H- and K-bands. The CHARA Classic and FLUOR beam combiners are the most relevant to the work presented in this dissertation.

There are currently a few interferometric arrays that are actively operating (e.g. CHARA, NOI, ISI, SUSI, VLTI), that are opening a new chapter in high resolution astronomy almost a century after A. A. Michelson measured the first stellar angular diameter of the supergiant

Betelgeuse and K. Schwarzschild first used interferometric measurements to study binary stars.

In this dissertation, the interferometric observations conducted with CHARA were mainly obtained with the CHARA Classic infrared beam combiner. This is a classical Michelson design of an interferometer, which is a pupil-plane beam combiner (see ten Brummelaar et al. 2005). Fringes are detected in a scanning mode created by dithering a mirror mounted to a piezoelectric device. The current resolution of the CHARA Array using the Classic beam combiner is about 0.6 mas in the K-band (2.13 μm) using the Array's largest baseline $S1 - E1$. The current limiting magnitudes for the Array are $K \leq 8.5$ for fringe detection, and $V \leq 11$ for tip/tilt locking.

1.2 Be stars

Be stars are B-type stars that eject large amounts of material into their circumstellar environments. Be stars have masses that range between 3 and 20 solar masses, effective temperatures that range from 10000 to 30000 K, radii that range between 2.5 and 10 solar radii, and short-scale lifetimes of 6 million to 600 million years. The circumstellar environments of Be stars are responsible for the observed emission lines, the polarization, and the high infrared excess flux detected in these stars. The Be phenomenon is still one of the most complicated problems in modern astrophysics, because it combines complex physical processes such as mass loss, stellar rotation, binarity, decretion disk formation and dissipation in one system. Figure 1.4 is an artistic representation of a typical Be star showing a central hot star with its extended circumstellar environment.
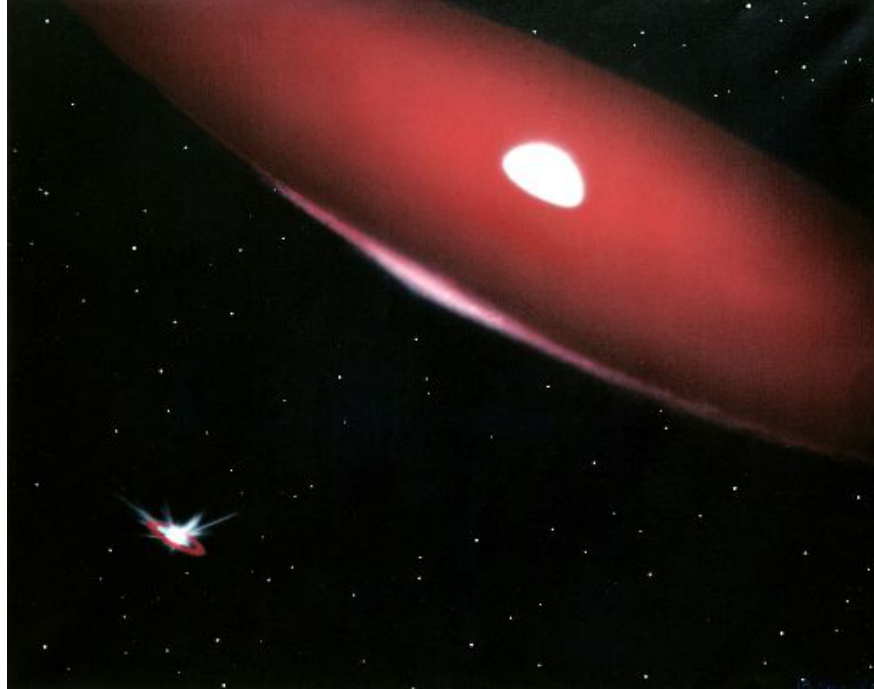
Figure 1.4: An artistic representation of a typical Be star (courtesy W. Pounds).

1.2.1 General Characteristics of Be Stars

A typical Be star is defined as a non-supergiant B star whose spectrum has, or had at some time, one or more Balmer lines in emission (Collins 1987). More generally, Be stars represent a category of stars that undergo large mass loss and that are surrounded by circumstellar regions driven by complex physical processes. For more details, see the review paper by Porter & Rivinius (2003). About 15% of all non-supergiant B-type stars exhibit or have exhibited emission lines in their spectra (Cote & van Kerkwijk 1993). The Hα emission line is the most common and strong hydrogen emission line observed in the spectra of Be stars. The Hα emission line equivalent width is correlated with the excess continuum emission of Be stars detected in the infrared (Touhami et al. 2010). This is explained by the fact that the excess continuum emission is due to the free-free and bound-free opacity processes in the disk, and it becomes larger in the infrared. The Hα emission line's red-to-violet peak

separation is found to be correlated with the stellar projected rotational velocity ($v \sin i$) derived from the photospheric lines, which suggests that the emission originates from a rotating disk-like envelope (Porter & Rivinius 2003). In fact, Be stars are characterized by high rotation rates, and the fact that they rotate very close to their critical rotational limit, where the centrifugal force balances gravity, hints that rotation in Be stars is connected to the process responsible for the disk formation. The reason for this intrinsic rapid rotation of Be stars is still unclear. Different scenarios suggest that Be stars may spin up by the redistribution of angular momentum at the end of core H burning (Ekström et al. 2008) or by accreting mass and angular momentum from a mass donor star in an interacting binary (Pols et al. 1991).

A simple model of Be stars represented by a central hot B spectral-type star surrounded by a circumstellar disk of a fixed radius and opening angle was adopted by Waters (1986). In this model, the gas density distribution in the disk decreases with the radial distance as it follows:

$$\rho(R) = \rho_0(R/R_s)^{-n} \tag{1.4}$$

where R_* is the stellar radius, ρ_0 is the density at the stellar surface, and n is the disk density exponent. The Infrared Astronomical Satellite (IRAS) observed many Be star systems, and based on these observations, the estimated values for the disk density exponent n range between 2.4 and 3.1, and the circumstellar disk extension in the infrared ranges from 6 to 8 stellar radii (Waters et al. 1987). These observations show that mass loss rates in Be stars are of order $10^{-8} M_\odot$ yr^{-1}, which is 50 - 100 times larger than that derived from the high velocity wind (Waters 1986). More sophisticated non-LTE radiative transfer models

are developed and currently available for data interpretation (Carciofi et al. 2007; Stee & Meilland 2006; Sigut et al. 2009), which we will discuss in more detail in Chapter 2.

Variability on different time scales is another important characteristic of Be stars that has been observed with many techniques. Flux variations on short time scales (days) are thought to be due to the non-radial pulsations of the central star, and the disk variations on long time scales (months to years) are thought to be due to more complicated physical processes responsible for the formation and the dissipation of the disk (Porter & Rivinius 2003).

1.2.2 Interferometry of Be stars

The first interferometric observations of Be stars were successfully conducted by Thom et al. (1986), who made use of the I2T interferometer to observe and resolve the circumstellar envelope of γ Cas. Spectrally resolved optical interferometric observations shortly followed using the GI2T interferometer (Mourard et al. 1989). The Mark III interferometer was then used by Quirrenbach et al. (1993) to measure the asymmetry of the Hα emitting regions around the Be stars γ Cas and ζ Tau, and this work opened a new era in the study of Be stars. The combination of the linear polarization with the interferometric observations of seven Be stars has shown that the emitting zones are flattened regions, which is the strongest observational evidence to date that the circumstellar envelopes of Be stars have a disk-like geometry (Quirrenbach et al. 1997).

Other observational efforts on the interferometry of near-IR continuum emission of Be stars were conducted using the Very Large Telescope Interferometer (VLTI). For instance, VLTI/MIDI observations of α Ara (HD 158427) showed a nearly unresolved circumstellar

disk in the N-band (Chesneau et al. 2005), and VLTI/VINCI observations of Achernar (α Eri) conducted in the H- and K-bands showed an elongated circumstellar envelope along the polar axis of the star, as well as rotational flattening of the stellar photosphere (Kervella & Domiciano de Souza 2006). Follow up VLTI/MIDI observations on Achernar reported in Kervella et al. (2009) show a signature of an extended emission in the thermal IR along the polar direction of the star, which is well reproduced by the SIMECA model (Stee 2003). Already detected at 2.2μm, this polar envelope could be an observational signature of a fast wind ejected by the hot polar caps of this rapid rotator. Meilland et al. (2008) used the VLTI/AMBER instrument operating in the H and K bands, and they resolved the disk and the binary companion of the Be star δ Cen. Meilland et al. (2009) reported the VLTI/MIDI N-band observations of the Be stars p Car, ζ Tau, κ CMa, α Col, δ Cen, β CMi, and α Ara. Gies et al. (2007) made the first observations of four Be stars (γ Cas, ϕ Per, ζ Tau, and κ Dra) using the CHARA Array, and they determined the geometrical and physical properties of their disks.

Tycner et al. (2004, 2005, 2006, 2008) followed on this analysis by using the NOI interferometer to resolve the circumstellar disks around the Be stars γ Cas, Alcyone, Pleione, ζ Tau, ϕ Per, β CMi, and χ Oph in Hα. The NOI observations show that the Hα emitting regions are largely extended, about a factor of two bigger than the envelopes' size in the near infrared. Jones et al. (2008) have computed theoretical models of circumstellar disks for the Classical Be stars κ Dra, β Psc, and υ Cyg. Models were constructed using a non-LTE radiative transfer code developed by Sigut & Jones (2007), which incorporates a number of improvements over previous treatments of the disk thermal structure, including a realistic chemical composition. These models were constrained by direct comparison with

long-baseline optical interferometric observations of the Be stars' emitting regions and by their contemporaneous Hα line profiles.

More recently, Meilland et al. (2011) reported VLTI/AMBER and CHARA/VEGA observations of δ Sco. The circumstellar disk size in Hα was found to be 4.8 ± 1.5 mas, the Brγ size was found to be 2.9 ± 0.5 mas, and the He I 2.06 μm size of 2.4 ± 0.3 mas. In addition, CHARA and VLTI near-infrared spectro-interferometry of β CMi and ζ Tau were reported in Kraus et al. (2012), who modeled the H- and K-band continuum and Brγ line to constrain the physical extent of the disk of these bright Be stars.

The need for high angular resolution in the infrared and for good (u, v) coverage in order to resolve and characterize the circumstellar environments of Be stars is the major motivation of this work. The CHARA Array with its maximum 331-meter baseline offers a unique resolving power of ~ 0.5 mas in the K-band, which represents a good compromise between the more challenging visible wavelengths and the thermal infrared. Long baseline interferometry of Be stars obtained on two baselines or more is currently the optimal way to resolve the innermost parts of the circumstellar disks, to determine the disk spatial extension, and to estimate the physical and geometrical properties of the disk.

1.3 Outline of the presentation

This dissertation describes a scientific study of circumstellar disks of Be stars at high resolution made possible by the CHARA Array. It consists of a simultaneous interferometric and spectrophotometric survey of the brightest Be stars in the northern hemisphere.

In Chapter 2, we give a detailed description of the different geometrical and physical models that we have used in this study for the data interpretation. In Chapter 3, we present

our spectrophotometric data covering a range of 0.4 to 4.2 μm, and taken both at NASA-IRTF using the SpeX spectrograph and at Lowell Observatory using the high-resolution Mimir spectrograph. In Chapter 4, we present our results of a multiwavelength modeling study of Be star emitting regions, and we compare our model predictions to a sample of 130 Be stars using photometry from 2MASS and the AKARI infrared camera all-sky survey. In Chapter 5, we present our multi-epoch observations and provide a full analysis of the well known Be star γ Cassiopeia. In Chapter 6, we present our survey data on 24 Be stars obtained with the CHARA Classic beam combiner and we derive fundamental properties of Be star disks using simple geometrical and physical models. In Chapter 7, we present our CHARA Classic and FLUOR observations of the yellow hypergiant ρ Cassiopeia. Our conclusions are summarized in Chapter 8, where we also point to promising areas of future research using the CHARA Array.

The work presented in this dissertation has resulted in two publications in refereed journals: Touhami et al. (2010), which describes the spectral energy distributions of our sample Be stars from the spectrophotometry data as described in Chapter 3, and Touhami et al. (2011), which presents our multiwavelength modeling of Be stars disks as described in Chapter 4. Two more publications presenting the results from our results on γ Cas and our survey of Be stars disks are currently close to completion.

The more sand that has escaped from the hourglass of our

life, the clearer we should see through it.

—— Jean Paul

<center>

– **2** –

Disk Models

</center>

<center>ABSTRACT</center>

The current paradigm of the circumstellar environments of Be stars comes from the recent models of an optically thick disk in the innermost regions, surrounded by an optically thin disk at large scales, with a density in the equatorial plane that declines as a power law of the radial distance from the central star. In this chapter, we explore different models using bound-free and free-free emission processes in the optically thick regions of the circumstellar disks close to the star to characterize the disk's geometrical and physical properties. Using radiative transfer theory, we demonstrate that these models are a good representation of the inner disk, and can thus be used for the interpretation of the interferometric data.

2.1 Introduction

Be stars and their circumstellar environments have been frequently studied with many techniques in the past few decades. Both observational and theoretical facts strongly suggest that the circumstellar material is constrained within a highly ionized, dense, equatorial disk (Quirrenbach et al. 1997; Carciofi et al. 2006). The spectral lines detected in Be stars are also consistent with an equatorial disk model in near Keplerian rotation, in which the density drops as a power law in radial distance from the central star. Waters (1986) modeled the disks of Be stars with a radial power law for the density, $\rho \propto R^{-n}$, and used the slope of the IR excess to probe the radial density structure of the disks. Waters (1986), assuming an isothermal disk with a temperature $T_d = 0.8\ T_{\text{eff}}$, gives estimates of the disk density exponent n that ranges between $\sim$ 2 - 3.5.

Recent advances in long baseline interferometry have made the study of the innermost regions of circumstellar environments of Be stars accessible at the milliarcsecond scales. Stee & Bittar (2001) and Stee (2003) developed a code (SIMECA) that generates intensity maps for a large set of disk parameters representative of early to late Be spectral types, along with several visible and near-IR emission line profiles. Using the SIMECA code, Stee (2003) showed a correlation between the mass loss rates and the continuum luminosity near Brγ as a function of the opening angle of the disk for a sample of 8 Be stars. He also presented a relationship between the mass of the circumstellar disk and the 2.16μm flux. Meilland et al. (2006) used the SIMECA code to investigate spectral energy distributions (SEDs), Brγ line profiles, and interferometric visibilities for two scenarios that potentially could explain the disk dissipation process in active hot Be stars, which accounts for the transition from the Be to the B spectroscopic phase. Kanaan et al. (2008) used the SIMECA code to investigate three possible geometries of the circumstellar environments: an equatorial disk, a polar wind, and a disk+wind geometry, and they were able to compare these synthetic models with spectroscopic and high angular resolution data from the VLTI/VINCI instrument.

The first attempts to quantify the complex radial and vertical temperature structures of Be disks were performed by Millar & Marlborough (1998). Carciofi et al. (2006) followed by developing a three-dimensional, non-LTE, Monte Carlo radiative transfer code to study the temperature and ionization structure of Be star disks. The optically thick inner parts of the disks were set to have temperatures that are similar to YSO disks, while the optically thin outer parts are like stellar winds. They find that, unlike the case of YSO disks, the disk flaring has little effect on the temperature structure of Be star disks. They also show that the disks are fully ionized, and that there is an ionization minimum in the vicinity

of the temperature minimum. The deficit of photoionization at this location makes it the most likely site for the low ionization state lines (e.g., Fe II) that produce the shell features observed in Be star spectra. A follow-up study by Carciofi & Bjorkman (2008) shows that viscous Keplerian disks can be highly nonisothermal. In this paper, the authors solve the full problem of the steady state, nonisothermal, viscous diffusion and vertical hydrostatic equilibrium.

Another important effort in modeling the disks of Be stars was conducted by Sigut & Jones (2007), who computed radiative equilibrium models for the gas in the circumstellar envelope surrounding the hot, classical Be star γ Cas. Their calculation was performed using a code that incorporates heating and cooling rates for H, He, CNO, Mg, Si, Ca, and Fe and their relevant ions. By comparing the predicted average disk temperature and the near-IR excess with observations, they report that the data can be accounted for by a disk that is in vertical hydrostatic equilibrium. They also discuss the changes in the disk's thermal structure that result from the additional heating and cooling processes available to a gas with a solar chemical composition over those available to a pure hydrogen plasma. Sigut et al. (2009) report that when the disk density is high enough, the circumstellar disk develops a cool equatorial region ($T < 10000$ K) close to the parent star. Based on these new hydrostatic disks, they predict an approximate relation between the global, density-averaged, disk temperature and the T_{eff} of the central star, covering the full range of central Be star spectral types.

Jones et al. (2008) were able to construct models of axisymmetric, circumstellar envelopes for Be star disks by successfully combining two numerical codes: a non-local thermodynamic equilibrium (non-LTE) radiative transfer code, which calculates the level populations and

disk temperature distribution self-consistently, and a hydrodynamical code. The output of one code is used as input to the other code, and hence evolving density and thermal structures may be examined. The temperatures, disk density and velocity distributions were used to investigate the outflowing viscous disc model for Be stars. Jones et al. (2008) find that these simulations place constraints on the power-law density decrease in the disk with increasing distance from the star, and that the power-law index for the line-forming region of the disks lies between 3 and 3.5 with a only small dispersion.

Here, we present different geometrical and physical models in order to analyze the CHARA interferometric data. In Section 2.2, we describe simple geometrical models, such as the Gaussian Elliptical model, while in Section 2.3, we describe the radiative transfer code and show how we extract the visibility information for the data interpretation. In Section § 2.3.4 and § 2.3.5, we present model results for the density structure of the disk, followed by a summary and our conclusions in Section § 2.4.

2.2 Geometrical Models

2.2.1 The Effective Baseline

The brightness distribution of the disk as seen by an interferometer at a baseline B_p is projected by the inclination of the disk and its position angle on the sky. For a flat disk inclined by an angle i and oriented at a position angle PA of the major axis (measured from north to east), we introduce the concept of the effective baseline B_{eff} (Tannirkulam et al. 2008), which is given by:

$$B_{\text{eff}} = B_p \sqrt{\cos(\phi_{\text{obs}} - PA)^2 + \cos^2 i (\sin(\phi_{\text{obs}} - PA)^2)}, \qquad (2.1)$$

where ϕ_{obs} is the baseline position angle at the time of the observations. This new quantity, the effective baseline, takes into consideration the decrease in the interferometric resolution due to the inclination of the disk in the sky, and thus for the purposes of analysis, it transforms the projected brightness distribution of the disk into a nearly circularly symmetric brightness distribution. The effective baseline may be considered as a good tool for constraining the disk geometry from the interferometric data. Note that if there is also a stellar flux contribution, than its projection and visibility will be a function of the projected baseline B_p only (if the star appears spherical in the sky). Consequently, models with both stellar and disk contributions should be presented for both the major and minor axis directions.

2.2.2 The Uniform Disk Model

A single star that has a uniform brightness distribution across its projected disk on the sky is modeled with a visibility function of the form:

$$V_{\mathrm{UD}} = \frac{2J_1(\pi B\theta_{\mathrm{UD}}/\lambda)}{(\pi B\theta_{\mathrm{UD}}/\lambda)}, \tag{2.2}$$

where J_1 is the first-order Bessel function, B is the projected baseline, θ_{UD} is the uniform disk (UD) diameter of the star, and λ is the effective wavelength of the interferometer. This simplified model is usually used to determine the angular sizes of single stars with high accuracy.

2.2.3 Gaussian Elliptical Model

We have used a two-component geometrical model to fit our CHARA Classic observations in order to measure the characteristic sizes of Be star circumstellar disks and their dependance on the different stellar properties of the sources. We first constrain the angular size and

geometry of the emitting region by fitting the visibility data using a simple geometrical model consisting of a point source representing the unresolved central star and a Gaussian elliptical component representing the circumstellar disk (Quirrenbach et al. 1997; Tycner et al. 2004). We remind the reader that because the Fourier transform is additive, the visibility functions of the system is the sum of the visibility function for the central star and for the disk. The total visibility of the system star+disk is thus given by (Tycner et al. 2004)

$$V_{\text{tot}} = c_p V_s + (1 - c_p) V_d, \tag{2.3}$$

where V_{tot}, V_s, and V_d are the total, stellar, and disk visibilities, respectively, and c_p is the ratio of the photospheric flux contribution to the total flux of the system. Because the central star is unresolved even at the longest baseline of the interferometer, we can assume that $V_s \simeq 1$. The disk model visibility is given by a Gaussian distribution

$$V_d = \exp\left[-\frac{(\pi \theta s)^2}{4 \ln 2}\right], \tag{2.4}$$

where θ is the full width at half-maximum (FHWM) of the Gaussian distribution and s is given by

$$s = \sqrt{r^2 (u \cos PA - v \sin PA)^2 + (u \sin PA + v \cos PA)^2}, \tag{2.5}$$

where r is the axial ratio and PA is the position angle of the disk major axis. This simple elliptical Gaussian model has four free parameters which are the photospheric contribution c_p, the axial ratio r, the position angle along the disk major axis PA, and the disk angular size θ.

2.3 The Thick Disk Model of Be Star Disks

2.3.1 Description of the Model

For a physical interpretation of the measured visibilities, we have employed a thick disk model that solves the radiative transfer problem considering an axisymmetric and isothermal equatorial disk of gas, and assuming free-free and bound-free opacities of the gas. This model was first introduced by Hummel & Vrancken (2000) to explore the emission line shapes, and was applied by Gies et al. (2007) and by Touhami et al. (2011). The model assumes that disk begins at the stellar surface and radiates as a black-body at an isothermal disk temperature of $T_d = 0.6 \, T_{\text{eff}}$ (Carciofi et al. 2006). This assumption is based on detailed physical models for Be disks, which have shown that the gas temperature is actually a function of both the radial distance and distance with respect to the equatorial plane. Carciofi et al. (2006) showed that the actual disk temperature is about 60% T_{eff} in the outer optically thin regions of the disk, so we adopted this value for the isothermal approximation of our model. The gas density in the disk is given by

$$\rho(R, Z) = \rho_0 R^{-n} \exp\left[-\frac{1}{2}\left(\frac{Z}{H(R)}\right)^2\right],\tag{2.6}$$

where R and Z are the radial and vertical cylindrical coordinates (in units of stellar radii), ρ_0 is the base density at the stellar equator, n is a radial density exponent, and $H(R)$ is the disk vertical scale height given by:

$$H(R) = \frac{c_s}{V_K} R^{\frac{3}{2}},\tag{2.7}$$

where c_s is the sound speed and V_K is the Keplerian velocity at the stellar equator. The four parameters that define a disk model are the base density ρ_0, the density exponent n, and the

orientation angles: the inclination i and the position angle of the major axis PA. The stellar contribution is represented by a blackbody surface brightness at the effective temperature of the star. In this model, we assume that the outer boundary of the disk occurs at a radius R_d, which is set equal to the Roche radius of the Be star if the star has a binary companion. This boundary parameter may potentially be important for the mid-IR emission spectrum, but it is not important for the K-band emission since that emission is generally confined to regions well within the assumed outer boundary.

2.3.2 Disk Emissivity

The disk optical depth in the near-IR is predominantly due to bound-free and free-free processes, which along a given ray increment ds is expressed as

$$d\tau = C(\lambda, T_d) \; \rho(R, Z)^2 \; ds, \tag{2.8}$$

where the coefficient $C(\lambda, T_d)$ is given by equation (5) in Dougherty et al. (1994). This coefficient includes terms for the Gaunt factors for bound-free and free-free emission that we evaluated for the K-band using Gaunt value tables in Waters & Lamers (1984). We have adopted two ionization models for the hot and cool circumstellar disks. For hot Be star disks ($T_{\text{eff}} > 15000$ K), we assumed ionized H, singly-ionized He, and doubly-ionized C, N, and O atoms, while for cooler Be star disks, we assumed ionized H, neutral He, and singly ionized C, N, and O. Note that we evaluated the optical depth coefficient only at the central wavelength of the K-band filter since the coefficient varies slowly with wavelength. Also note that we have accounted only for continuum emission in this band since the Brγ line emission contribution is small compared to the flux integrated over the K-band.
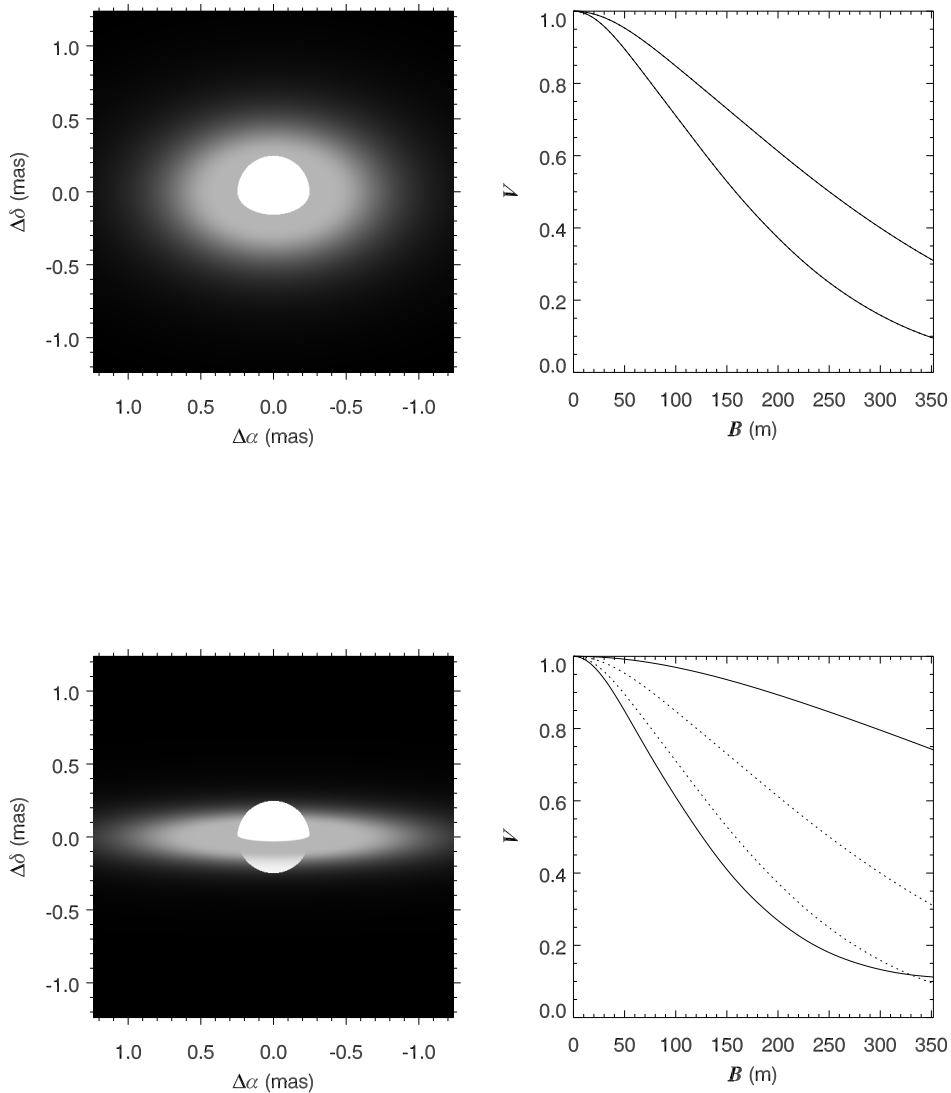
Figure 2.1: The top left panel is a depiction of the K-band image of a disk model for a typical Be star with a disk gas density of $\rho_0 = 7.2 \times 10^{-11}$ g cm^{-3}, a density exponent $n = 2.7$, and at $51°$ inclination as shown in Gies et al. (2007). The top right panel shows the corresponding interferometric visibility projected along the minor axis (upper curve) and along the major axis (lower curve). The bottom panels represent the K-band image and its corresponding visibility curves for a Be star with an disk inclination of $i = 80°$. The dotted lines in the visibility panel repeat the curves from the original model in the top panel.
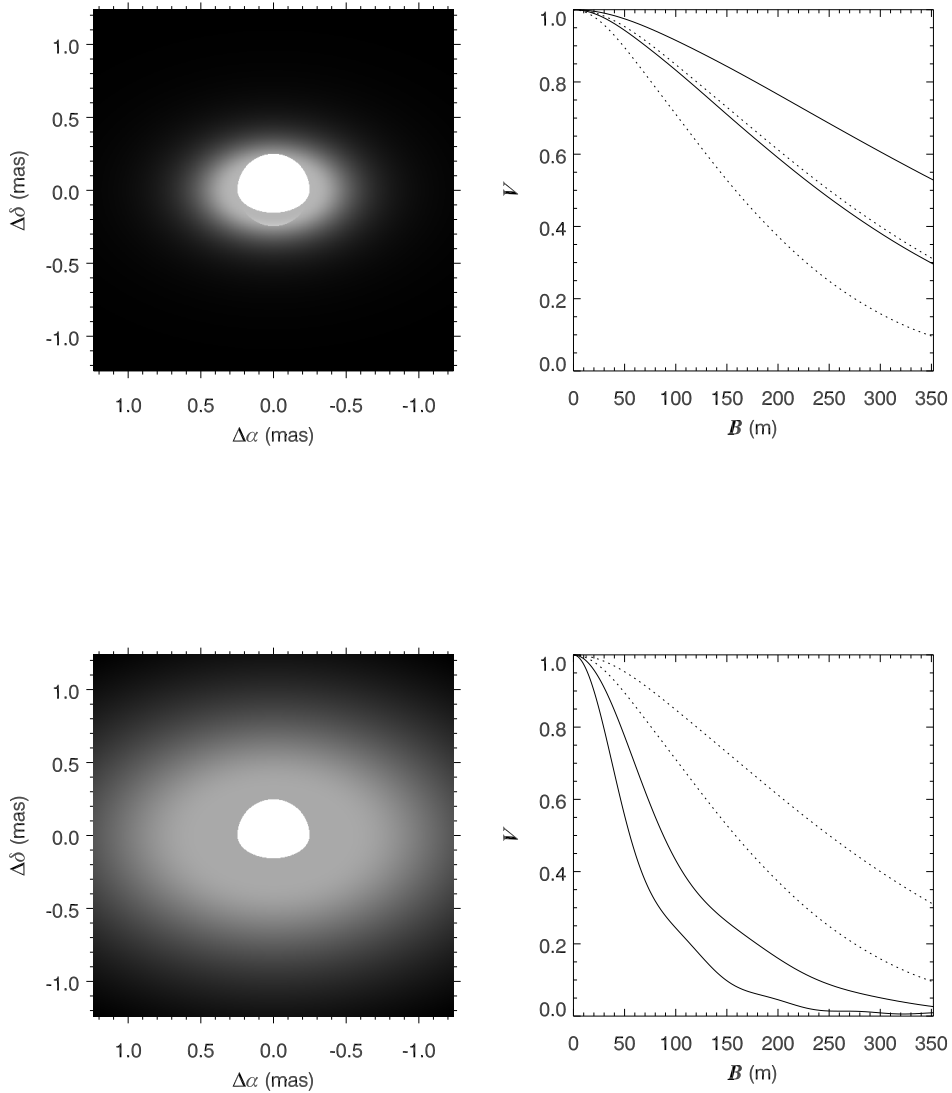
Figure 2.2: Top panel: A synthetic image and its corresponding visibility curve for the same model as in the top panel of Fig. 2.1 but with a smaller base density of $\rho_0 = 3.6 \times 10^{-11}$ g cm^{-3}. Bottom panel: A synthetic image and its corresponding visibility curve for the same model as in Fig. 2.1 but with a smaller radial density exponent of $n = 2.0$. The dotted lines repeat the visibility curves plotted in the top panel of Fig. 2.1.

In order to investigate the disk emission over a wide range of wavelengths in the near and mid-IR, we have extended the model to determine the Gaunt factors, compute the optical depths, and calculate the disk flux distribution at 1.66 (H-band), 2.13 (K-band), 4.8, 9, and 18 μm. More details about the multiwavelength disk characterization are given in Chapter 3.

2.3.3 Continuum Images and Interferometric Visibility

The surface brightness of the disk plus star over a projected rectilinear coordinate grid on the sky is determined by solving the equation of transfer along a ray through the center of each grid position,

$$I = S_d(1 - e^{-\tau}) + I_s e^{-\tau} \qquad (2.9)$$

where I is the derived specific intensity, S_d is the source function for the disk gas taken as the Planck function for the disk temperature T_d, I_s is the specific intensity for a uniform disk star taken as the Planck function for T_{eff}, and τ is the integrated optical depth along the ray. Note that we have neglected the effect of scattered light due to Thomson scattering by the disk of the photospheric flux (see eq. [6] in Bjorkman & Bjorkman 1994). For the typical electron densities of Be stars, this term will amount to only a few percent of the stellar specific intensity close to the star, and thus the scattered light flux is much less than the disk source function in the inner, optically thick portions.

The synthetic image of the Be star is constructed by integrating the optical depth along each ray and populating each pixel of the image by solving the transfer equation. The pixel scale on the sky is set by the adopted angular diameter of the star that we derived from the stars' spectral energy distributions. Also, the model includes a binary star option where

the emission from a secondary component is added to the model at an angular position that corresponds to a prediction made from known orbital elements at the time of observation, and the total visibility signature of the system is used to fit the interferometric observations of the Be star and its companion.

2.3.4 The Interferometric Visibility

The interferometric visibility is calculated by computing the Fourier transform of the disk model synthetic images following the techniques described by Aufdenberg et al. (2006). The Fourier transforms along the major and minor axes of the projected disk image are computed and are usually plotted against the data as a function of the effective baseline of the interferometer. We show example synthetic Be star images and their corresponding visibility curves adopted from Gies et al. (2007) in Figures 2.1 and 2.2. The top panel of Figure 2.1 shows the K-band image of a disk model for a typical Be star with a disk gas density of $\rho_0 = 7.2 \times 10^{-11}$ g cm^{-3}, a density exponent $n = 2.7$, and at 51° inclination. Note that the star itself is so small that its visibility curve is close to unity at all baselines. The bottom panel shows how the synthetic image and its visibility change by altering the disk inclination angle from an intermediate inclination angle to a higher inclination angle. In the latter case, the rays through the outer positions along the major axis traverse a longer optical depth because of the oblique projected disk on the sky, which makes the disk effectively larger along the major axis, while along the minor axis, the projected visibility is reduced and becomes unresolved in this direction. Therefore, the interferometric visibility is highly sensitive to the disk inclination angle. The changes resulting from a decrease in disk base density ρ_0 are illustrated the top panel of Figure 2.2. When the disk gas density

is lower, the optically thick parts of the disk appears smaller in both dimensions, which causes the visibility curves to decline more gradually with baseline. A decrease in the disk density exponent n results an increase in the disk brightness distribution as shown in the bottom panel of Figure 2.2. These examples show that the interferometric visibility is most sensitive to the disk size as given by the boundary between the optically thick and thin regions. Since the optical depth unity radius in the disk plane depends on $\rho_0^2 \, R^{-2n+3/2}$ (Gies et al. 2007), accurate determinations of both the density ρ_0 and the density exponent n will require visibility measurements over a broad range of baselines to remove the degeneracy between the effect of these two model parameters.

2.3.5 Inner Gaps

The expansion and dissipation of the material ejected with large equatorial outburst speeds occur when the mass transfer between the stellar photosphere and the circumstellar environment shuts down. The ejected material then moves to the outer parts of the disk, clearing out a gap in the innermost parts close to the Be star photosphere. This phenomenon could be taken into consideration in our thick disk model. For that, we allow the inner radius of the disk to be detached from the stellar photosphere in order to produce a ring-like brightness distribution around the central star. The density function $\rho(R, Z)$ is in this case given by:

$$\rho(R, Z) = 0, \text{ where } R < R_{\text{in}},$$

$$\rho(R, Z) = \rho_0 \, (R/R_s)^{-n} \, \exp\left[-\frac{1}{2}\left(\frac{Z}{H(R)}\right)^2\right], \text{ where } R \geq R_{\text{in}},$$

where R_{in} is the thick disk inner radius, R and Z are the radial and the vertical cylindrical coordinates respectively, R_s is the stellar radius, ρ_0 is the gas base density at the stellar photosphere if the inner radius reached to the star, and n is the radial density exponent.

Figure 2.3: A montage of synthetic K-band images of model circumstellar disks for a typical Be star with different inner radii assuming an inclination angle of $i = 75°$, a base density of $\rho_0 = 10^{-10}$ g cm^{-3}, and a density exponent of $n = 3$.

$H(R)$ is the disk vertical scale height defined by $H(R) = \frac{c_s}{V_K} R^{3/2}$, where c_s is the sound speed and V_K is the Keplerian velocity at the stellar equator.

This physical model follows the same computational steps as the thick disk model in order to simulate the disk flux distribution. The source function of the disk here too is assumed to be a Planck function characterized by an isothermal temperature profile. The model with an inner gap has five input parameters, which are the thick disk inner radius $R_{\rm in}$, the inclination i, and position angle of the disk's major axis PA, the gas base density ρ_0, and the radial density exponent n. The model computes the disk flux distribution by solving the transfer equation along a series of rays through the disk, and then generates synthetic infrared images of the Be star surrounded by a circumstellar disk. The model visibility is then computed similarly to the thick disk model, as being the Fourier transform of the intensity distribution of disk, and is compared to the interferometric data.
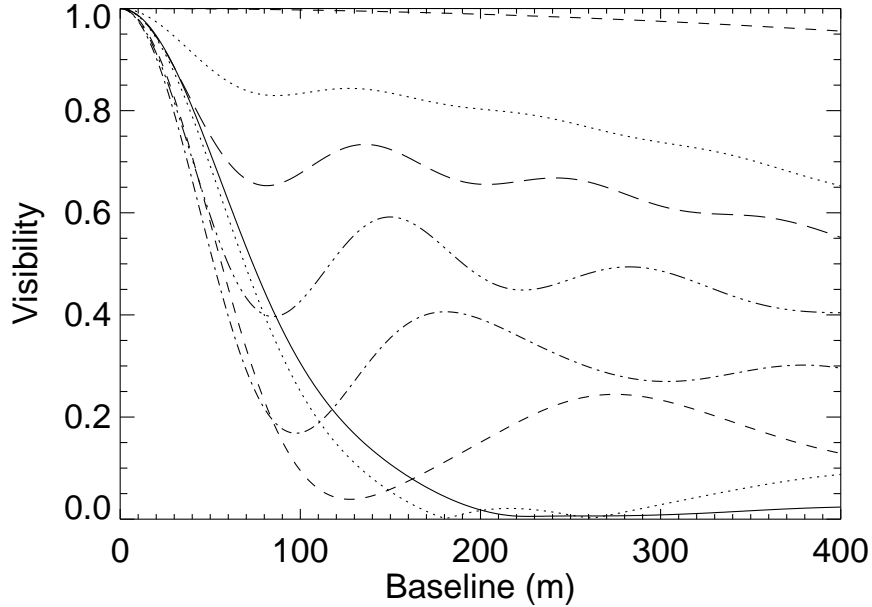
Figure 2.4: The thick disk model visibility projected along the major axis as a function of the baseline for different values of the disk inner radius. The solid line is the projected visibility for $R_{in} = 1R_s$, the dotted line is for $R_{in} = 2R_s$, the small-dashed line is for $R_{in} = 3R_s$, the dash-dotted line is for $R_{in} = 4R_s$, the dashed-triple-dotted line is for $R_{in} = 5R_s$, the long dashed line is for $R_{in} = 6R_s$, the upper dotted line is for $R_{in} = 8R_s$, and the last dashed line on the top of this plot is for $R_{in} = 15R_s$, which represents a totally dissipated thick disk leaving only the unresolved central star.

To illustrate the interferometric signature of this model, we plot in Figure 2.3 a set of intensity maps of a typical Be star disk with increasing values of the inner radius of the circumstellar disk. In this demonstration, we have adopted a disk inclination angle of $i = 75°$, a position angle of $PA = 100°$, and a typical gas base density in the disk of $\rho_0 = 10^{-10}$ g cm^{-3}. The central star is assumed to be 10 solar masses with an effective temperature of 30 kK. For this montage image, we have adopted a disk density exponent equal to $n = 3$. Figure 2.4 shows the disk model visibility projected along the major axis as a function of the baseline for different values of the disk inner radius. The solid line in Figure 2.3 is the projected visibility for $R_{in} = 1R_s$, the dotted line is for $R_{in} = 2R_s$, the

small-dashed line is for $R_{\text{in}} = 3R_s$, the dash-dotted line is for $R_{\text{in}} = 4R_s$, the dashed-triple-dotted line is for $R_{\text{in}} = 5R_s$, the long dashed line is for $R_{\text{in}} = 6R_s$, the upper dotted line is for $R_{\text{in}} = 8R_s$, and finally the dashed line on the top of this plot is for $R_{\text{in}} = 15R_s$, which represents a totally dissipated disk.

The starting configuration in Figure 2.3, where the disk inner radius is connected to the stellar equator, shows a fully resolved object with a low second lobe represented by the solid line in Figure 2.4. As the inner radius of the disk R_{in} increases, the flux ratio between the unresolved central star and the outer parts of the disk increases and the system star plus disk is resolved at even shorter baselines. The second lobe of the visibility curve becomes more important as the disk inner radius increases, and the gas density in the remaining parts of the disk sharply decreases bringing the visibility curve of the system to appear similar to that of a partially resolved structure, and reaches the shape of a nearly uniform disk for an inner disk radius of $R_{\text{in}} = 15R_s$. Similar models and trends of an expanding circumstellar ring developing around the Be star were also discussed by Meilland et al. (2006).

2.4 Conclusions

In this chapter, we have described geometrical and physical disk models that will be used to constrain the structure of the inner parts of circumstellar disks around Be stars. We have shown that the interferometric visibility is highly sensitive to the density profile of the disk and its geometry. Synthetic images and visibilities for the disk model have been computed, highlighting differences between various geometrical and physical models, and these will be adopted in the following chapters to interpret our near-IR interferometry observations.

Knowledge comes, but wisdom lingers.

—— Alfred Lord Tennyson

<center>– 3 –</center>

The Near-IR Spectral Energy Distributions of Be Stars

<center>ABSTRACT</center>

We present spectrophotometric data from 0.4 to 4.2 μm for bright, northern sky, Be stars and several other kinds of massive stars. Our goal is to use these data with ongoing, high angular resolution, interferometric observations to model the density structure and sky orientation of the gas surrounding these stars. We also present a montage of the Hα and near-infrared emission lines that form in Be star disks. We find that a simplified measurement of the IR excess flux appears to be correlated with the strength of emission lines from high level transitions of hydrogen. This suggests that the near-IR continuum and upper level line fluxes both form in the inner part of the disk, close to the star.

3.1 Introduction

The observed absolute flux from an astronomical source (after correction for telluric and interstellar extinction) is directly related to its emitted flux and angular size in the sky. As we enter the era of optical long-baseline interferometry, it will become easier to measure the angular dimensions of many objects and, consequently, to explore the relationship between the observed and emitted flux distributions. This effort is especially important to determine effective temperatures of stars, but it also plays a key role in the interpretation of circumstellar environments, in particular the disks surrounding Be stars and the winds and outflows of massive stars.

Be stars are rapidly rotating B-type stars that manage to eject gas into a circumstellar disk (observed in H emission lines, an infrared flux excess, and linear polarization; Porter

& Rivinius 2003). The IR flux excess from the disk results from bound-free and free-free emission from ionized gas, and this emission increases with wavelength, so that in the near and mid-IR the disk flux will dominate over the stellar flux. Models of the IR excess can relate the observations to the disk radial density function (Waters 1986; Dougherty et al. 1994; Porter 1999). Such models are also required to interpret recent near-IR interferometric observations of Be stars where the ratio of disk to stellar flux is a key parameter (Stee & Bittar 2001; Gies et al. 2007; Meilland et al. 2007; Carciofi et al. 2009). However, Be star disks are intrinsically variable on timescales of months to years (Hubert & Floquet 1998; Porter & Rivinius 2003; McSwain et al. 2008), so it is necessary to obtain contemporaneous spectrophotometry in order to model both the total flux and its angular distribution in the sky. There are many emission lines of H and He in the near-IR spectra of Be stars (Claret 2000; Steele & Clark 2001; Lenorzer et al. 2002b; Mennickent et al. 2009), and they offer additional diagnostics of the disk density, temperature, and geometry (Hony et al. 2000; Lenorzer et al. 2002a; Jones et al. 2009).

We have embarked on a number of programs of interferometry with the Georgia State University Center for High Angular Resolution Astronomy (CHARA) Array, a six-telescope, optical/IR interferometer with baselines up to 331 m (ten Brummelaar et al. 2005). Here we describe a program of complementary optical and near-IR spectrophotometry of our targets that we will use in detailed modeling of the source angular flux distribution. The observations and their calibration are described in §3.2, and we present figures of the target spectral energy distributions and emission line strengths in §3.3 and §3.4, respectively. In §3.5 we discuss the relationship between the disk continuum and line emission of Be stars, and we present a summary of the work in §3.6.

3.2 Observations and Reductions

We obtained optical spectrophotometry in 2006 and 2008 with NOAO Kitt Peak National Observatory Coudé Feed Telescope. These observations cover parts of the blue and red spectrum as outlined in Table 3.1 that lists (1) the UT dates and (2) heliocentric Julian dates of observation, (3) the wavelength range recorded, (4) the spectral resolving power (for a nominal projected slit equivalent to three pixels), (5) the number of spectra made, and (6) a summary of the telescope, spectrographic grating, and detector. The KPNO observations were made with a slit width of 4".3 - 9".0 to record most to all of the starlight, so the actual spectral resolution depends on the stellar point spread function and image motion during the exposure. Each observation was immediately preceded or followed by an identical observation of a flux calibrator star (discussed further below). All the observations were accompanied by dark, flat field, and ThAr comparison lamp (for wavelength calibration) frames, and the spectra were reduced and extracted by standard means in IRAF[1] to produce a spectrum of integrated counts per second as a function of heliocentric wavelength.

---

[1]IRAF is distributed by the National Optical Astronomical Observatory, which is operated by the Association of Universities for Research in Astronomy, Inc. (AURA), under cooperative agreement with the National Science Foundation.

Table 3.1: Journal of Spectroscopic Observations

UT Date (1)	Julian Date (HJD-2,450,000) (2)	Wavelength Range (μm) (3)	Resolving Power ($\lambda/\triangle\lambda$) (4)	Number of Spectra (5)	Telescope Spec., Grating/Detector
2006 Sep 15 − 16	3993.8 − 3995.1	1.92 − 4.21	1700	22	IRTF/3.0m/SpeX, Long XD1.9/Aladdin 3 InSb
2006 Oct 12	4020.8 − 4020.9	0.64 − 0.71	6500	12	KPNO/0.9m/Coudé, B (order 2)/T2KB
2006 Oct 20 − 21	4028.6 − 4029.8	0.42 − 0.46	8500	18	KPNO/0.9m/Coudé, A (order 2)/T2KB
2008 Oct 18 − 20	4757.6 − 4760.0	1.40 − 2.50	930	18	Lowell/1.8m/Mimir, JHK grism/Aladdin 3 InSb
2008 Oct 27 − 29	4766.6 − 4769.0	0.64 − 0.71	10300	17	KPNO/0.9m/Coudé, B (order 2)/F3KB
2008 Nov 30	4800.6 − 4801.0	0.43 − 0.46	13900	16	KPNO/0.9m/Coudé, A (order 2)/F3KB

We also obtained near-IR spectroscopy of most of the targets in 2006 with the NASA Infrared Telescope Facility and SpeX cross-dispersed spectrograph (Rayner et al. 2003) and in 2008 with the Mimir camera/spectrograph and Lowell Observatory Perkins Telescope (Clemens et al. 2007). Both sets of observations were made with a wide slit to accommodate most of the stellar flux (3".0 and 10".0 for SpeX and Mimir, respectively), although we also obtained a set of narrow slit (0".3), high-resolution spectra with SpeX. The SpeX data cover the photometric K and L bands while the Mimir spectra record the H and K bands. These spectra were made with multiple short exposures at dithered positions along the slit. Additional details are listed in Table 3.1. As with the blue and red spectra, we obtained flux calibrator spectra at close to the same time and air mass of the target spectra. The SpeX results were reduced with the Spextool package Cushing et al. (2004) and the Mimir spectra were extracted using software developed by D. Clemens[2].

All the stars observed are targets of continuing programs of interferometry with the CHARA Array. The targets are listed in Table 3.2, which gives (1) the Henry Draper catalog number, (2) common name, (3) spectral classification, (4) stellar effective temperature T_{eff}, (5) logarithm of the stellar gravity $\log g$, (6) interstellar reddening $E(B-V)$, and (7) the HD number of the flux calibrator star adopted. The classifications for the Be stars are from the compilation of Yudin (2001). In addition to the Be stars, the list includes three Orion supergiants (classifications from Walborn 1976), the luminous blue variable star P Cygni (classification from Lamers et al. 1983), the interacting binary υ Sgr (classification from Yudin 2001), and the yellow supergiant ρ Cas (classification from Bidelman 1957). The stellar parameters T_{eff} and $\log g$ for the Be stars are taken from the apparent values (the

---

[2]http://people.bu.edu/clemens/mimir/software.html

average over the visible hemisphere) derived by Frémat et al. (2005), and those for other stars are from the work of Searle et al. (2008) (HD 37128, HD 38771), Bouret et al. (2008) (HD 37742), Dudley & Jeffery (1993) and Leushin (2001) (HD 181615), Najarro et al. (1997) (HD 193237), Neiner et al. (2005) (HD 202904), and Gorlova et al. (2006) (HD 224014). The reddening estimates $E(B-V)$ are from Dougherty et al. (1994) for the Be stars, from Shull & van Steenberg (1985) for the O-type stars, and from Dudley & Jeffery (1993), Najarro et al. (1997), and Zsoldos & Percy (1991) for HD 181615, HD 193237, and HD 224014, respectively.

Table 3.2: Targets and Flux Calibrator Stars

Target HD No. (1)	Name (2)	Spectral Classification (3)	T_{eff} (kK) (4)	$\log g$ (cm s^{-2}) (5)	$E(B-V)$ (mag) (6)	Calibrator HD No. (7)
HD 004180	o Cas	B2 Ve	14.4	3.3	0.11	HD 001561
HD 005394	γ Cas	B0 IVe + sh	26.4	3.8	0.22	HD 011946
HD 010516	ϕ Per	B0.5 IVe + sh	25.6	3.9	0.21	HD 011946
HD 022192	ψ Per	B4.5 Ve + sh	15.8	3.5	0.11	HD 025152
HD 023630	η Tau	B7 IIIe	12.3	3.0	0.06	HD 023258
HD 023862	28 Tau	B8 Vpe + sh	12.1	3.9	0.09	HD 023258
HD 024534	X Per	O9.5 Vep	25.2	3.6	0.40	HD 019600
HD 025940	48 Per	B4 Ve	16.2	3.6	0.19	HD 029526
HD 037128	ϵ Ori	B0 Ia	27.5	3.1	0.05	HD 034203
HD 037202	ζ Tau	B1 IVe + sh	19.3	3.7	0.00	HD 034203
HD 037742	ζ Ori	O9.7 Ib	29.5	3.3	0.04	HD 034203
HD 038771	κ Ori	B0.5 Ia	26.0	3.0	0.04	HD 045380
HD 058715	β CMi	B8 Ve	11.8	3.8	0.01	HD 060357
HD 149757	ζ Oph	O9 Ve	26.4	3.8	0.33	HD 143459
HD 181615	υ Sgr	B2 Vpe	11.8	2.0	0.20	HD 182678
HD 191610	28 Cyg	B3 IVe	18.4	3.7	0.06	HD 192538
HD 193237	P Cyg	B1 Ia+	18.2	1.2	0.51	HD 192538
HD 200120	59 Cyg	B1.5 Ve + sh	21.8	3.8	0.21	HD 205314
HD 202904	υ Cyg	B2.5 Vne	19.1	3.9	0.19	HD 206774
HD 209409	o Aqr	B7 IVe + sh	12.9	3.7	0.05	HD 212061
HD 212076	31 Peg	B1.5 Vne	19.3	3.7	0.10	HD 212061
HD 212571	π Aqr	B1 Ve + sh	26.1	3.9	0.22	HD 212061
HD 217891	β Psc	B5 Ve	14.4	3.7	0.05	HD 212061
HD 224014	ρ Cas	F8 Ia var	6.0	0.7	0.42	HD 223386

All the near-IR spectra were transformed to an absolute flux scale (and excised of atmospheric telluric features) using the *xtellcor* software package described by Vacca et al. (2003). The method uses flux calibrator stars of spectral classification A0 V that are transformed to flux through reference to a model Vega spectrum calculated by R. Kurucz. In brief, the procedure involves convolving the model Vega spectrum with a kernel designed to match the net instrumental and rotational broadening of the calibrator spectrum, shifting the model to match the Doppler shifted calibrator spectrum, scaling and reddening the Vega model to match the calibrator's observed magnitudes, dividing the observed calibrator by the model spectrum to arrive at a system response spectrum (that includes telluric features), and finally dividing the target spectrum by the response spectrum to obtain a calibrated flux spectrum. The transformation is parameterized in the software by setting the Johnson B and V magnitudes for the calibrator star (essentially setting the flux zero-point and allowing for a slope adjustment due to interstellar extinction and/or small temperature differences between the calibrator and Vega). These B and V magnitudes were selected by making a non-linear, least-squares fit of the calibrator $BVJHK_S$ magnitudes to a version of the Vega model that was renormalized and reddened for interstellar extinction in the same way as done by the *xtellcor* software. A small revision of the final B and V magnitudes was made to bring the results into consistency with the absolute calibration of IR fluxes by Rieke et al. (2008).

The blue and red optical spectra were transformed to absolute flux following the same basic approach given by Vacca et al. (2003), but the broadening kernel for the calibrator was calculated rather than fit using the known instrumental broadening and published values of the calibrators' projected rotational velocities. In addition, we also applied a small flux correction dependent on the difference in air mass between the target and calibrator

observations that was calculated based upon the mean atmospheric extinction coefficients in BVR for KPNO derived by Landolt & Uomoto (2007).

3.3 Optical to Near-IR Spectral Energy Distributions

The spectral energy distributions (SEDs) derived for our 24 targets are illustrated in Figures 3.1 – 3.3 (in order of increasing HD number). Each panel shows the flux in a $(\log \lambda, \log \lambda F_\lambda)$ format, where λ is the wavelength (μm) and F_λ is the physical flux received at Earth (in units of W m^{-2} μm^{-1} = 0.1 erg cm^{-2} s^{-1} Å^{-1}). The first set of measurements from 2006 are depicted as black dotted lines, while those for 2008 are shown overplotted as gray dotted lines. We calculated the average flux over a range of $\pm 0.001\lambda$ for five wavelengths that correspond to line-free regions near the centers of the Johnson $BRHKL$ filters, and these mean fluxes appear in Table 3.3. The errors quoted in Table 3.3 are the quadratic sum of several components: (1) instrumental error (primarily from Poisson noise detection for these well-exposed spectra), (2) repeatability errors (due to fast atmospheric changes between the target and calibrator exposures), and (3) errors in setting the flux calibration of the calibrator (based upon the scatter in the $BVJHK_S$ fit of the calibrator magnitudes). In addition, we included a term for the blue and red spectra equal to the amount of the extinction correction applied to account for air mass mismatch. We had many cases of multiple observations of targets and calibrators that we used to estimate the repeatability error ($\approx 4\%$ for the blue and red spectra; wavelength dependent for the near-IR spectra, but generally just a few percent in wavelength regions with good atmospheric transmission).
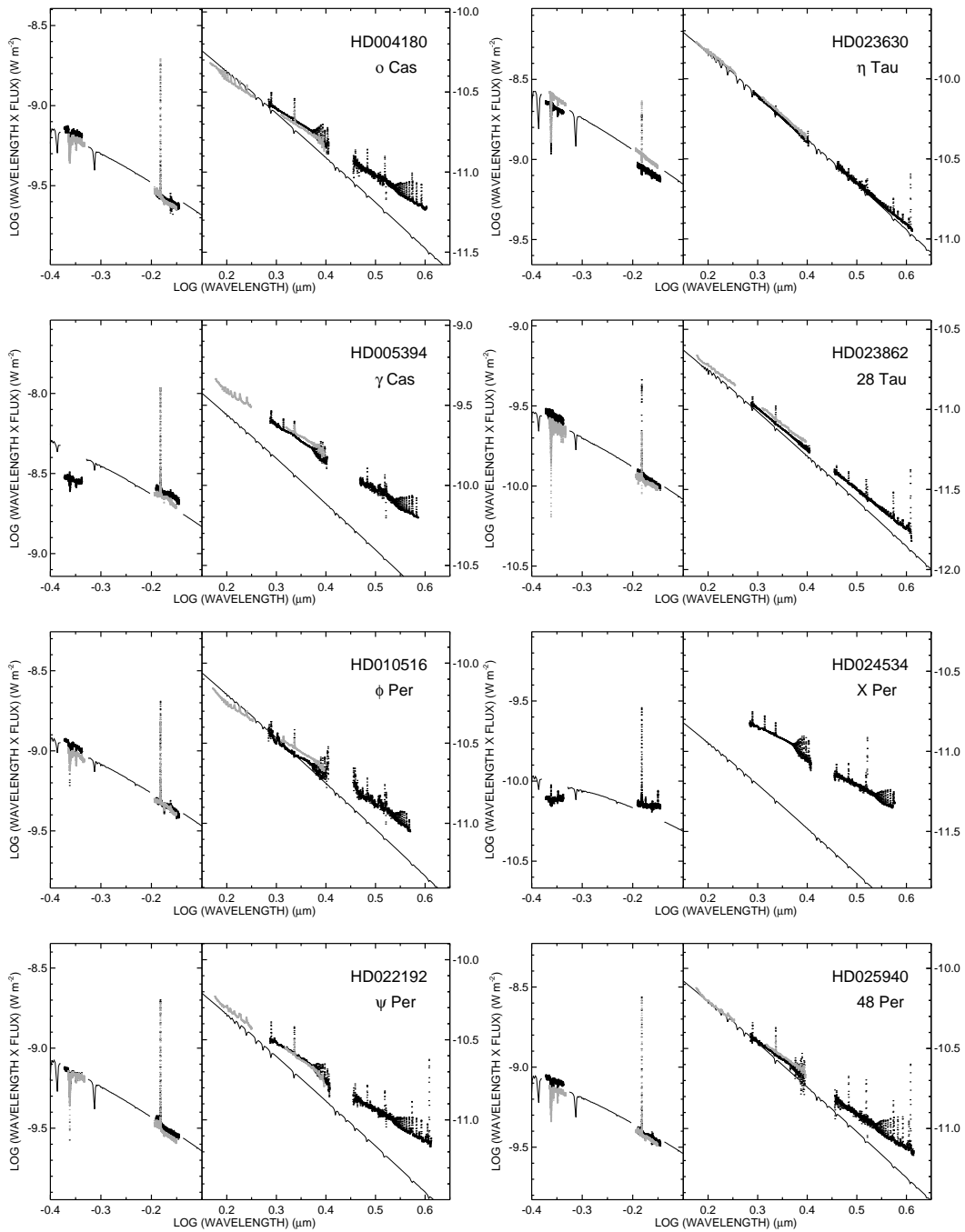
Figure 3.1: The spectral energy distributions of the targets observed in 2006 (*black*) and 2008 (*gray*). The solid lines show the predicted stellar SEDs for the parameters from Table 3.2.
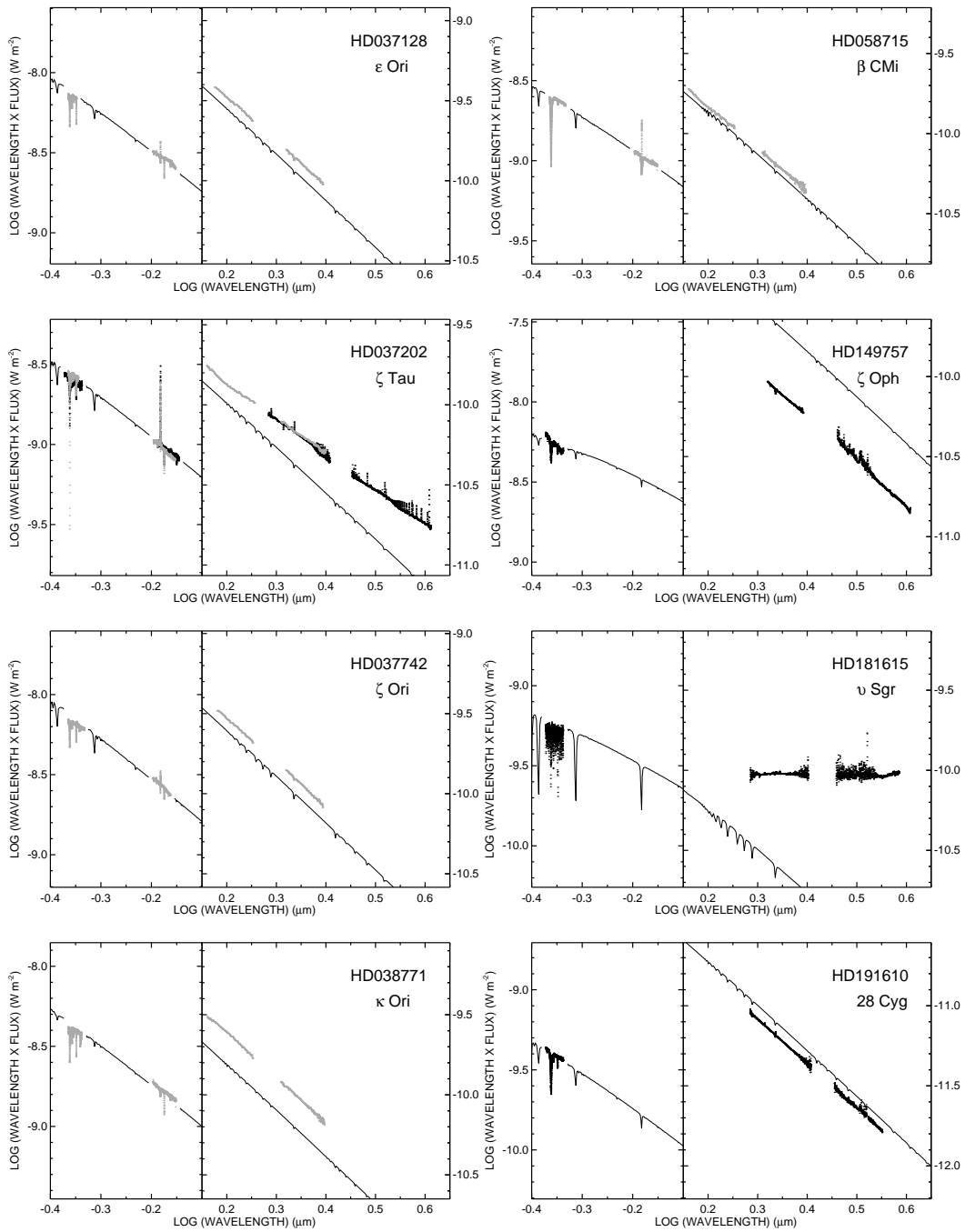
Figure 3.2: The spectral energy distributions in the same format as Fig. 3.1.
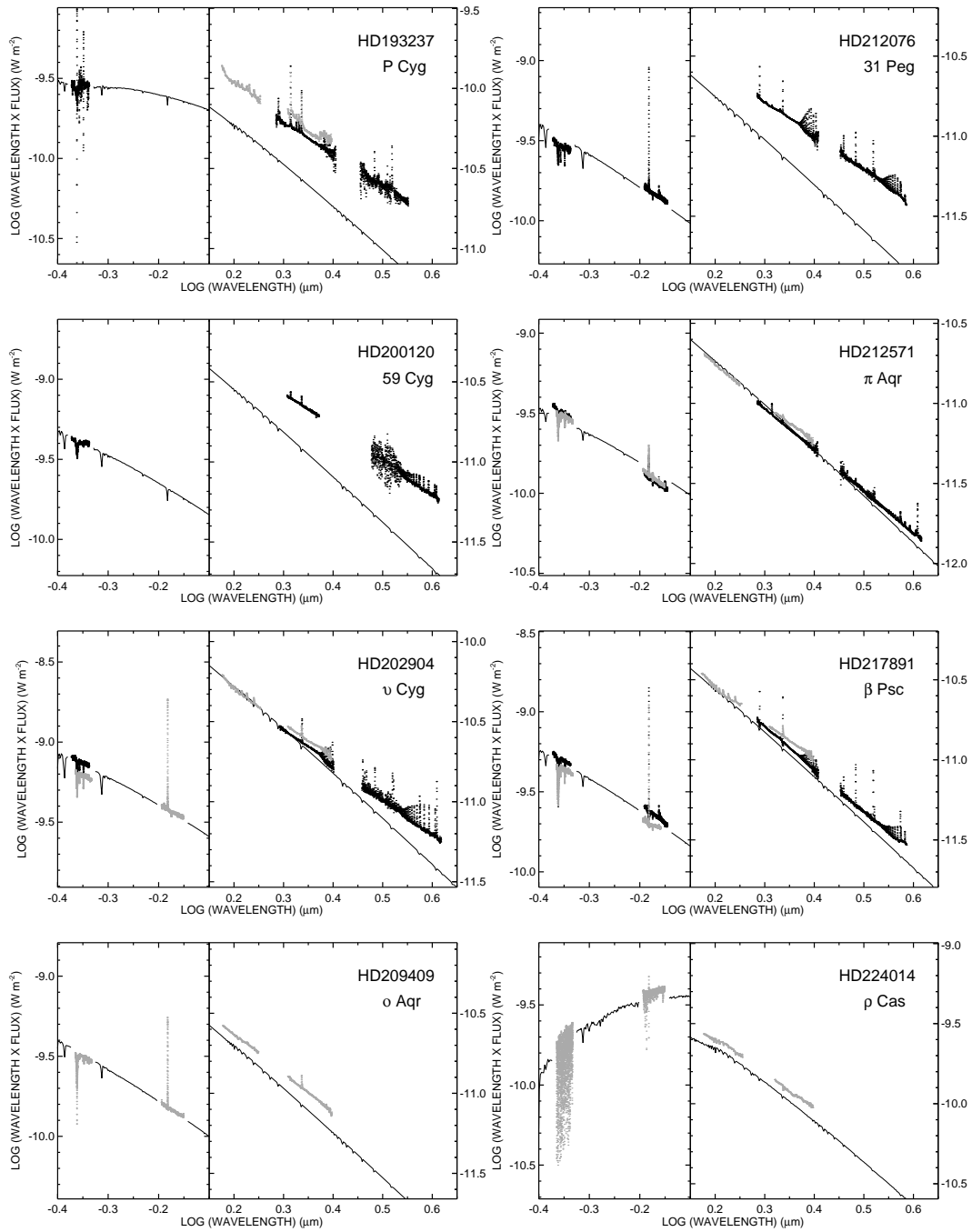
Figure 3.3: The spectral energy distributions in the same format as Fig. 3.1.

45

Table 3.3: Monochromatic Fluxes[a]

Star (1)	Year (2)	log $F_\lambda(0.440)$ (3)	log $F_\lambda(0.680)$ (4)	log $F_\lambda(1.654)$ (5)	log $F_\lambda(2.179)$ (6)	log $F_\lambda(3.410)$ (7)
HD004180	2006	−8.808 (26)	−9.435 (25)	. . .	−11.019 (11)	−11.611 (12)
HD004180	2008	−8.843 (27)	−9.445 (24)	−10.681 (13)	−11.039 (13)	. . .
HD005394	2006	−8.168 (26)	−8.460 (25)	. . .	−10.036 (11)	−10.616 (12)
HD005394	2008	. . .	−8.490 (24)	−9.681 (13)	−10.015 (13)	. . .
HD010516	2006	−8.595 (29)	−9.179 (25)	. . .	−10.917 (11)	−11.468 (12)
HD010516	2008	−8.646 (28)	−9.187 (24)	−10.512 (13)	−10.870 (13)	. . .
HD022192	2006	−8.794 (25)	−9.345 (23)	. . .	−10.935 (9)	−11.524 (11)
HD022192	2008	−8.799 (25)	−9.380 (23)	−10.569 (12)	−10.942 (12)	. . .
HD023630	2006	−8.313 (24)	−8.913 (23)	. . .	−10.553 (9)	−11.271 (10)
HD023630	2008	−8.249 (25)	−8.841 (22)	−10.089 (11)	−10.530 (11)	. . .
HD023862	2006	−9.207 (24)	−9.794 (23)	. . .	−11.434 (9)	−12.113 (10)
HD023862	2008	−9.261 (24)	−9.819 (22)	−10.986 (11)	−11.405 (12)	. . .
HD024534	2006	−9.756 (22)	−9.992 (21)	. . .	−11.246 (7)	−11.803 (9)
HD025940	2006	−8.720 (19)	−9.267 (21)	. . .	−10.884 (5)	−11.501 (7)
HD025940	2008	−8.778 (19)	−9.281 (19)	−10.474 (8)	−10.865 (8)	. . .
HD037128	2008	−7.788 (27)	−8.379 (22)	−9.742 (11)	−10.197 (11)	. . .
HD037202	2006	−8.235 (23)	−8.877 (23)	. . .	−10.513 (9)	−11.133 (10)
HD037202	2008	−8.202 (24)	−8.896 (22)	−10.135 (11)	−10.510 (11)	. . .
HD037742	2008	−7.813 (25)	−8.447 (22)	−9.796 (11)	−10.247 (11)	. . .
HD038771	2008	−8.032 (30)	−8.631 (19)	−9.882 (8)	−10.340 (8)	. . .
HD058715	2008	−8.251 (24)	−8.840 (22)	−10.096 (11)	−10.536 (11)	. . .
HD149757	2006	−7.893 (99)	. . .	. . .	−10.424 (7)	−11.150 (9)
HD181615	2006	−8.920 (20)	. . .	. . .	−10.355 (5)	−10.568 (8)
HD191610	2006	−9.046 (26)	. . .	. . .	−11.531 (11)	−12.264 (13)
HD193237	2006	−9.184 (26)	. . .	. . .	−10.624 (11)	−11.204 (12)
HD193237	2008	. . .	. . .	−10.220 (13)	−10.567 (13)	. . .
HD200120	2006	−9.034 (26)	. . .	. . .	−10.990 (10)	−11.566 (12)
HD202904	2006	−8.758 (21)	. . .	. . .	−10.974 (6)	−11.582 (9)
HD202904	2008	−8.838 (23)	−9.280 (21)	−10.562 (9)	−10.936 (9)	. . .
HD209409	2008	−9.135 (24)	−9.680 (23)	−10.895 (12)	−11.307 (12)	. . .
HD212076	2006	−9.172 (33)	−9.676 (35)	. . .	−11.201 (9)	−11.805 (10)
HD212571	2006	−9.127 (25)	−9.765 (26)	. . .	−11.473 (9)	−12.169 (10)
HD212571	2008	−9.145 (24)	−9.751 (22)	−11.026 (12)	−11.437 (12)	. . .
HD217891	2006	−8.935 (31)	−9.486 (41)	. . .	−11.230 (9)	−11.941 (10)
HD217891	2008	−8.991 (27)	−9.548 (22)	−10.819 (12)	−11.193 (12)	. . .
HD224014	2008	−9.559 (19)	−9.242 (20)	−9.843 (8)	−10.233 (8)	. . .

[a] $\log_{10}$ of the observed flux in units of W m^{-2} μm^{-1} at wavelengths specified in microns. Numbers in parentheses give the errors in units of the last digit quoted.

We find that there is overall good agreement between the flux levels of the targets between 2006 and 2008, and in most cases there is excellent agreement between the K-band fluxes from the SpeX and Mimir instruments. There are a few cases where variability may be present (η Tau, 28 Tau, 48 Per, P Cyg, υ Cyg, and β Psc), and, indeed, the decrease in B-band flux in 28 Tau = Pleione between 2006 and 2008 occurred during the development of a new shell phase in that star (Grundstrom 2007) when additional disk gas projected against the star may have caused its optical flux to decline. We also note that the Be star HD 24534 = X Per, the star with the largest IR flux excess in our sample (see below), was in an historically very bright and strong emission state in 2006 (Grundstrom et al. 2007).

Any estimate of a flux excess in the SED requires some method to determine the stellar contribution across the spectrum. We chose to use model spectra based upon the stellar and reddening parameters in Table 3.1 that we normalized to the observed fluxes in the blue and red parts of the spectrum (assuming that the disk contribution is small there). We selected solar abundance models with an adopted microturbulence parameter of 2 km s^{-1} that are derived from the grid of line-blanketed, local thermodynamical equilibrium (LTE) atmospheres calculated by R. Kurucz[3]. These models have limited applicability to our set of targets for a number of reasons. The Be stars, for example, are rapid rotators with non-spherical shape and with polar regions that are hotter than their equatorial zones, and in some cases their flux is attenuated by obscuration or increased by scattering from their surrounding disks. The supergiants in the sample are very luminous and low gravity

---

[3]http://kurucz.harvard.edu/grids.html

objects, for which a non-LTE and extended atmosphere treatment is necessary (that includes wind outflow). Finally, the interacting binary, υ Sgr has a He-enriched atmosphere (Dudley & Jeffery 1993). Nevertheless, the LTE flux calculations from Kurucz offer an important starting point to search for the deviations in the SED that are related to mass outflows and these other effects.

The flux models were calculated by a bilinear interpolation in the Kurucz grid using T_{eff} and $\log g$ from Table 3.1. The spectrum was then attenuated for interstellar extinction using the reddening from Table 3.1, a ratio of total-to-selective extinction of 3.1, and the extinction law from Fitzpatrick (1999). The resulting spectrum was normalized by (1) smoothing all the available blue and red spectra to the spectral resolution of the Kurucz flux spectrum, (2) interpolating these to the wavelengths of the model spectrum, (3) forming an average ratio of observed-to-model flux for each spectrum, and (4) determining a global normalization factor from the average of all the available spectra. This process makes the tacit assumptions that the year-to-year flux variations are small (compared to the flux calibration errors) and that the stellar component dominates the optical flux in the blue and red. While these assumptions are reasonable in most cases, we caution that the optical flux of the Be stars may be significantly altered by the presence of a disk. For example, the optical flux may brighten by ≈ 0.5 mag during emission outbursts when the disk is dense (Hubert & Floquet 1998; Porter & Rivinius 2003) or may decrease by a comparable amount in Be-shell stars with dense disks that block stellar flux in the direction of the observer (Underhill & Doazan 1982; Hubert & Floquet 1998). We plan to investigate the extent of the disk contribution to the optical spectrum in a subsequent analysis that will use simple disk density models to fit the interferometric and SED observations.

The model stellar flux distributions are indicated by thin solid lines in the SED plots of Figures 3.1 – 3.3. These appear as continuous in the near-IR range in the right hand panels, but they appear only in the gaps between the observed spectral regions in the optical region in the left hand panels to avoid confusion with the observations. We find that the expected IR flux excess is observed in the SED of most of the Be stars (from disks), O-supergiants and P Cyg (from winds), and the interacting binary v Sgr (from its circumbinary gas). We attach no special significance to the relative IR weakness observed in the SEDs of HD 149757 and HD 191610 that is probably due to somewhat larger errors in their optical flux calibration. We note that the relatively high, red-to-blue flux ratio observed in the Be star HD 24534 = X Per may indicate that a significant flux excess is present in the red, so our stellar flux normalization made in the optical range may be too high and, consequently, the already large IR excess may be underestimated in this case.

For the Be stars in our sample with good wavelength coverage, we calculated the flux excesses near the centers of the HKL bands by determining the ratio of the observed and model average fluxes. These flux excesses are given in terms of a magnitude difference in Table 3.4. Since these are determined from a normalization of the optical spectrum in the B and R bands, we symbolically write these with reference to the intermediate V band as $E^\star(V - H)$, $E^\star(V - K)$, and $E^\star(V - L)$, where the asterisk is used to differentiate the excess due to disk emission from interstellar reddening (which is accounted for in calculating the model photospheric spectra).

Table 3.4: Be Star Flux Excess[a]

Star (1)	Year (2)	$E^{\star}(V-H)$ (mag) (3)	$E^{\star}(V-K)$ (mag) (4)	$E^{\star}(V-L)$ (mag) (5)
HD004180	2006	...	0.15 (9)	0.51 (9)
HD004180	2008	−0.12 (9)	0.10 (9)	...
HD005394	2006	...	0.61 (31)	1.04 (31)
HD005394	2008	0.36 (31)	0.66 (31)	...
HD010516	2006	...	−0.01 (6)	0.49 (6)
HD010516	2008	−0.13 (6)	0.11 (6)	...
HD022192	2006	...	0.30 (4)	0.67 (5)
HD022192	2008	0.09 (5)	0.28 (5)	...
HD023630	2006	...	0.00 (12)	0.03 (12)
HD023630	2008	0.03 (12)	0.05 (12)	...
HD023862	2006	...	0.07 (9)	0.21 (9)
HD023862	2008	0.07 (9)	0.14 (9)	...
HD024534	2006	...	1.01 (29)	1.46 (29)
HD025940	2006	...	0.07 (7)	0.36 (7)
HD025940	2008	−0.01 (7)	0.12 (7)	...
HD037202	2006	...	0.51 (4)	0.84 (4)
HD037202	2008	0.30 (4)	0.52 (4)	...
HD058715	2008	0.08 (4)	0.10 (4)	...
HD191610	2006	...	−0.21 (11)	−0.18 (11)
HD200120	2006	...	0.68 (11)	1.09 (11)
HD202904	2006	...	0.05 (12)	0.37 (12)
HD202904	2008	−0.04 (12)	0.14 (12)	...
HD209409	2008	0.18 (7)	0.27 (7)	...
HD212076	2006	...	0.68 (16)	1.03 (16)
HD212571	2006	...	−0.05 (13)	0.09 (13)
HD212571	2008	−0.06 (13)	0.04 (13)	...
HD217891	2006	...	0.11 (10)	0.18 (10)
HD217891	2008	0.01 (10)	0.20 (11)	...

[a]Numbers in parentheses give the errors in units of the last digit quoted.

3.4 Emission Line Equivalent-Widths

The near-IR spectra of the Be stars contain many emission lines formed in the disk, and our data set offers a good opportunity to compare the well studied, optical Hα emission with these near-IR lines in data obtained contemporaneously. Figures 3.4 – 3.7 show a montage of the Hα (*left*) and near-IR emission lines (*right*) normalized to the local continuum flux (the combined stellar and disk flux). The H-band portions are from Mimir data in 2008 and the KL-band sections are from the 2006 SpeX data (high resolution versions). Tick marks under each spectrum show the locations of the H Brackett, Pfund, and Humphreys series of lines. The Hα profiles are smoothed to the resolution of SpeX ($R = 2500$). The Hα profiles are from 2006 (2008 for υ Cyg), and these include profiles of 28 Cyg and 59 Cyg from Grundstrom (2007) and of P Cyg from the University of Toledo Ritter Observatory (Richardson et al. 2011). P Cygni (HD 193237) is not a Be star, but we include it here as an example of emission formed in a wind where the gas density is lower than typical for Be disks (Hony et al. 2000). Our results can be compared directly (in the 2.4 – 4.1 μm range) to spectra from the *Infrared Space Observatory* presented by Lenorzer et al. (2002b) for HD 5394, 191610, 193237, and 212571.
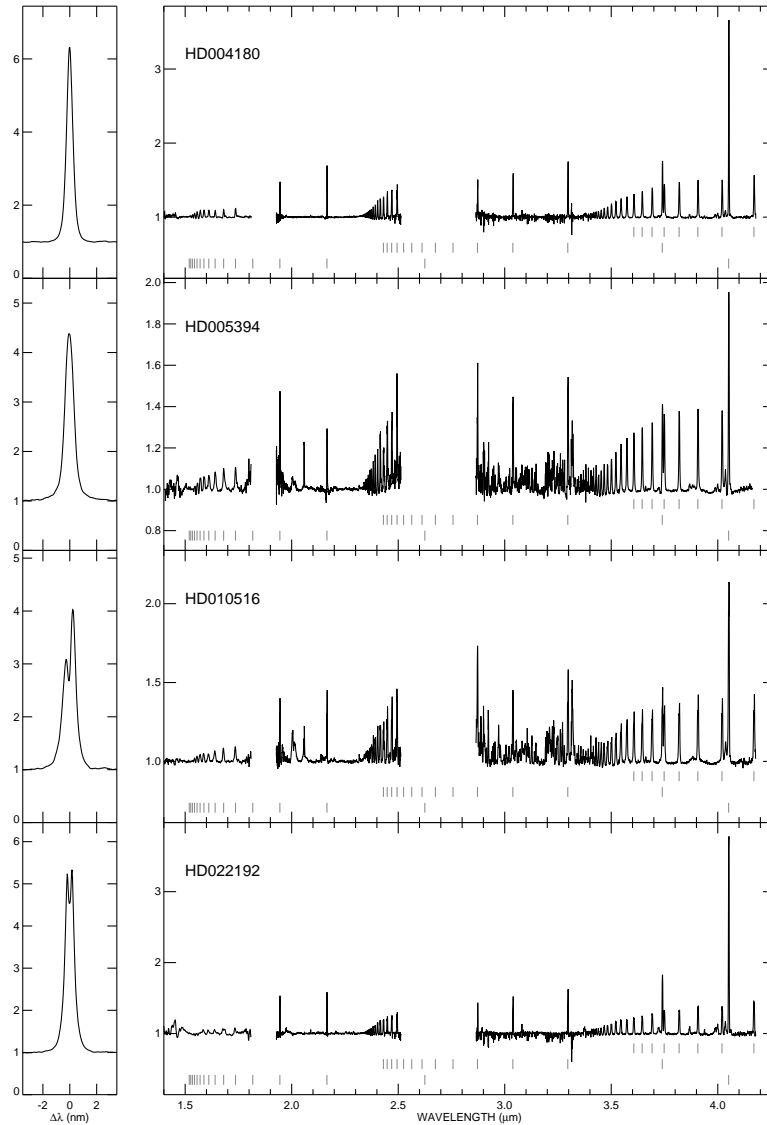
Figure 3.4: The emission line spectra at Hα (*left*) and in the near-IR (*right*). Gray tick marks below each spectrum mark the H Brackett, Pfund, and Humphreys series (*bottom to top*). The feature at 2.0 μm (HD 5394 and 10516) results from incomplete telluric removal.
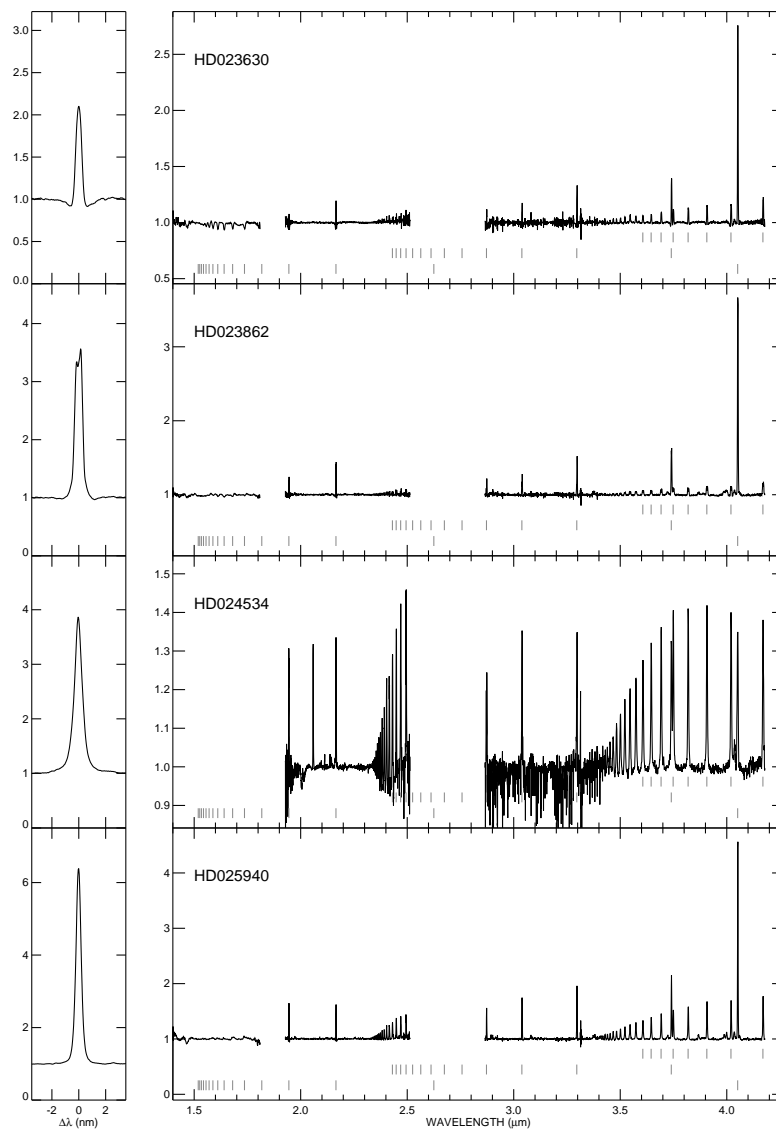
Figure 3.5: The emission line spectra in the same format as Fig. 3.4.
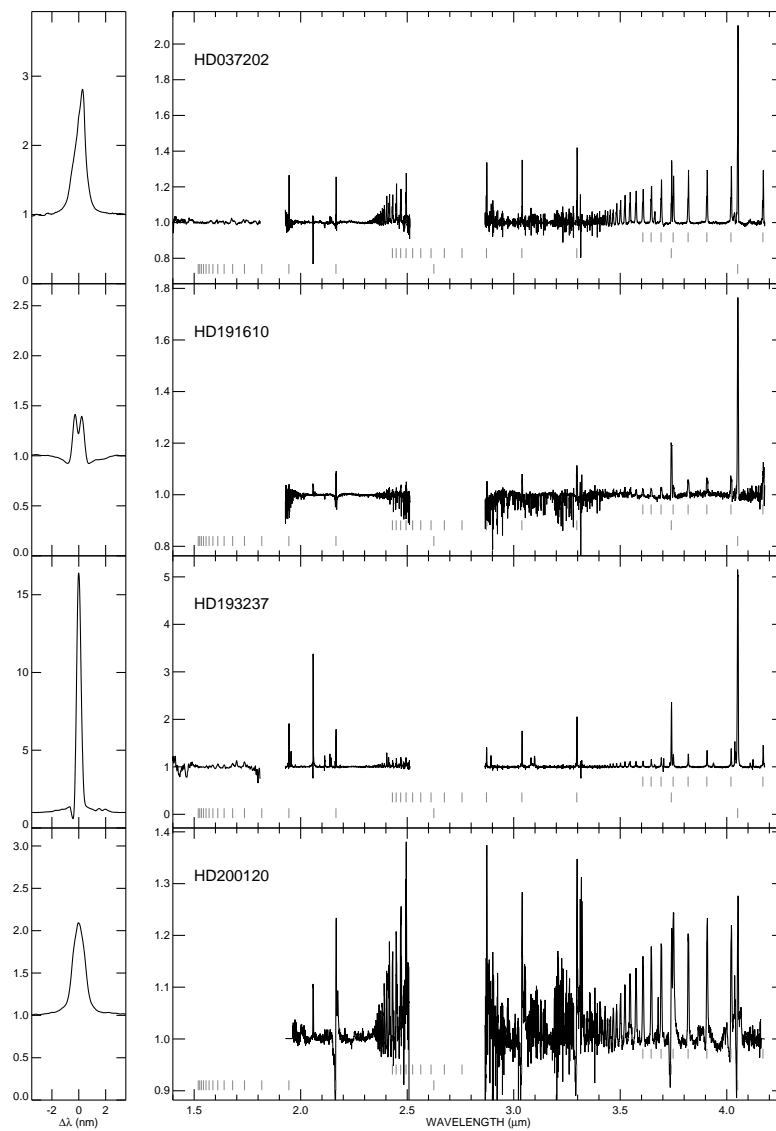
Figure 3.6: The emission line spectra in the same format as Fig. 3.4.
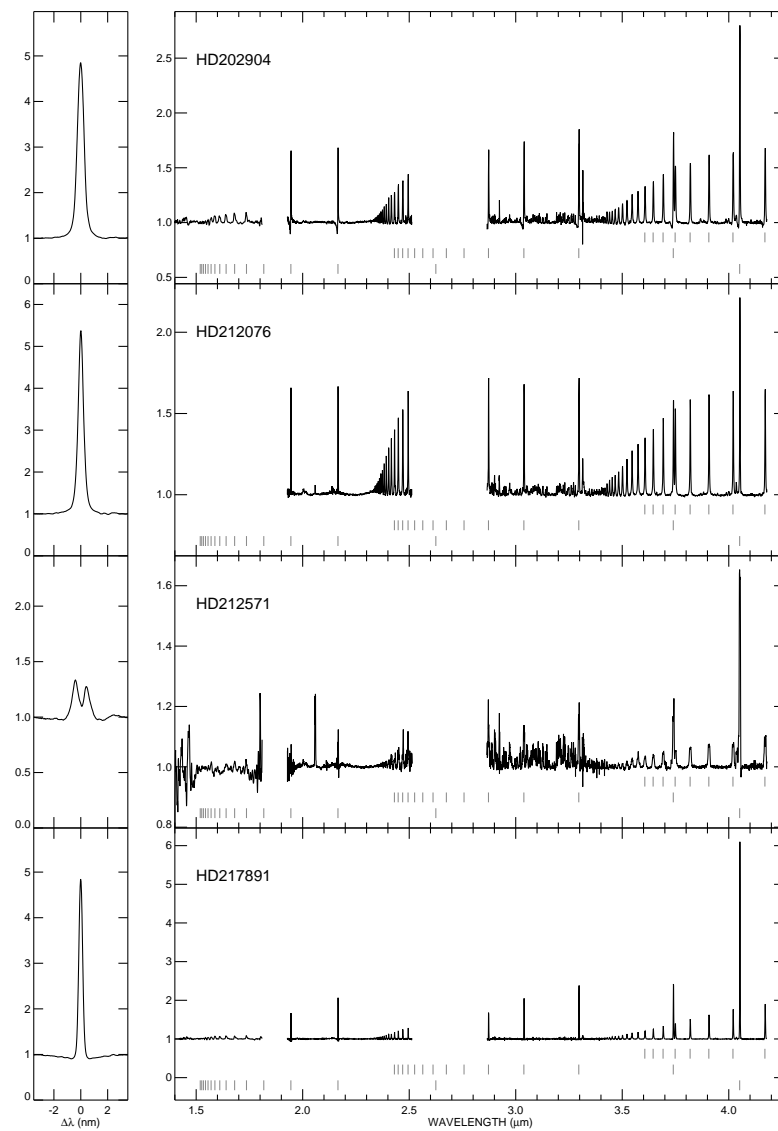
Figure 3.7: The emission line spectra in the same format as Fig. 3.4.

We measured the equivalent-width W_λ (relative to the local continuum) by direct integration for the most prominent H emission lines of Hα, Brα, Brγ, Pfγ, Pfδ, and Hu14 $\lambda 4.021$ μm, and these are listed in columns 2 − 7 of Table 3.5. We use the standard notation of expressing net emission as a negative equivalent-width. The profiles of Pfγ $\lambda 3.741$ μm are partially blended with those of Hu17 $\lambda 3.749$ μm in most of the spectra, and we set the upper boundary for the integration of Pfγ at the minimum position between the two features. The formal measurement errors are approximately 1% (3% for Pfδ), but these do not include any errors introduced in the telluric removal and flux calibration process (where uncertainties in the H line strengths of the calibrator spectrum may introduce errors in the final spectrum of the target). Furthermore, there were a number of cases where the measurement included both emission and absorption components. For example, the Brγ profile displayed broad photospheric absorption plus narrower disk emission for several of the Be stars, and it appeared like a wind feature with blue absorption plus red emission for P Cyg, 28 Cyg, 59 Cyg, and υ Cyg. In all these cases, the equivalent-width reported in Table 3.5 is the net integration of the absorption and emission components.

Table 3.5: Be Star Line Equivalent-Widths and Ratios

Star	$-W_\lambda(\text{H}\alpha)$ $(10^{-3}\ \mu\text{m})$	$-W_\lambda(\text{Br}\alpha)$ $(10^{-3}\ \mu\text{m})$	$-W_\lambda(\text{Br}\gamma)$ $(10^{-3}\ \mu\text{m})$	$-W_\lambda(\text{Pf}\gamma)$ $(10^{-3}\ \mu\text{m})$	$-W_\lambda(\text{Pf}\delta)$ $(10^{-3}\ \mu\text{m})$	$-W_\lambda(\text{Hu14})$ $(10^{-3}\ \mu\text{m})$	$\log(\text{Hu14}/\text{Pf}\gamma)$	$\log(\text{Hu14}/\text{Br}\alpha)$
(1)	(2)	(3)	(4)	(5)	(6)	(7)	(8)	(9)
HD004180	3.35	8.77	1.33	2.96	2.27	2.58	−0.14	−0.51
HD005394	3.12	4.35	0.55	1.94	2.15	2.10	−0.05	−0.28
HD010516	3.01	6.35	1.18	2.43	2.75	2.44	−0.12	−0.39
HD022192	3.77	11.34	1.23	3.45	1.80	2.05	−0.28	−0.71
HD023630	0.42	5.70	−0.02	1.20	0.76	0.49	−0.33	−0.93
HD023862	1.71	11.21	0.76	2.68	1.31	0.65	−0.64	−1.15
HD024534	2.41	2.05	0.95	1.87	1.20	2.35	−0.02	0.07
HD025940	2.81	10.83	0.98	3.73	3.04	2.89	−0.21	−0.56
HD037202	1.81	4.00	0.20	1.08	0.89	1.34	0.00	−0.45
HD191610	0.18	4.17	−0.03	1.09	0.36	0.39	−0.52	−0.93
HD193237[a]	6.66	22.85	1.89	5.05	3.47	1.36	−0.62	−1.20
HD200120	1.35	1.15	0.08	0.66	0.75	1.05	0.10	−0.06
HD202904	2.58	6.48	1.06	2.94	2.73	3.10	−0.10	−0.32
HD212076	2.43	3.72	1.35	2.28	2.56	2.60	−0.05	−0.14
HD212571	0.30	4.75	0.41	1.51	1.13	0.78	−0.41	−0.75
HD217891	1.11	12.12	1.07	3.84	3.57	2.46	−0.29	−0.67

[a]P Cygni is a Luminous Blue Variable and not a Be star, but it is included here for comparison.

3.5 Discussion

Since both the H emission lines and IR-excess originate in the circumstellar disks of Be stars, we might expect that the two observables are correlated. Past work indicates that the Hα emission strength is related to the IR excess. Kastner & Mazzali (1989) used published data to show that the Hα luminosity is correlated with the IR excess luminosity and the spectral type of the underlying star. van Kerkwijk et al. (1995) obtained near simultaneous Hα spectroscopy and near-IR photometry (to avoid ambiguities introduced by time variability of the sources), and they found that the equivalent-width of Hα was loosely correlated with a disk color excess $E^\star(J - L)$, but there was an intrinsic scatter in the relationship. These results were confirmed (although with somewhat less scatter) in a study of the relationship of the Hα equivalent-width and the disk color excess $E^\star(H - K)$ by Howells et al. (2001). Given the new spectra available from our study, we have also explored the relationship between the line and continuum emission.

We need to refer the line emission to the photospheric continuum (rather than the observed sum of the photospheric and disk flux), so we used the flux excess data from Table 3.4 to derive a line equivalent-width relative to the stellar continuum,

$$W_\lambda^\star = W_\lambda \ 10^{0.4 E^\star(V - \lambda)} \tag{3.1}$$

where W_λ is the observed equivalent-width (Table 3.5) and $E^\star(V - \lambda)$ is the wavelength-interpolated, flux excess from the disk (Table 3.4). We show the derived relationship between $W_\lambda^\star(\mathrm{H}\alpha)$ and $E^\star(V - L)$ in Figure 3.8. In this case since the photospheric flux was normalized in the optical, there is no net flux excess near Hα by definition, and hence $W_\lambda^\star = W_\lambda$. We see

that there is a correlation, but the scatter from a one-to-one relationship is significant (the Spearman's rank correlation coefficient is $\rho = 0.54$). We found a similar degree of scatter in plots of $W_\lambda^\star$ and $E^\star(V - L)$ for Brα, Brγ, Pfγ, and Pfδ, and the least scatter is seen in the diagram for Hu14 $\lambda 4.021$ μm (Fig. 9) where the Spearman's rank correlation is $\rho = 0.77$. The two most discrepant points in Figure 3.9 (found below the trend, near $E^\star(V - L) = 1.0$) correspond to the stars ζ Tau (HD 37202) and 59 Cyg (HD 200120). The spectra of both stars show interesting structure in the higher resolution SpeX spectra (asymmetric double peaks for ζ Tau and blue absorption for 59 Cyg), which suggests that a simple equivalent-width measurement may be insufficient to explore the relationship between the line and continuum emission strengths for these two stars.
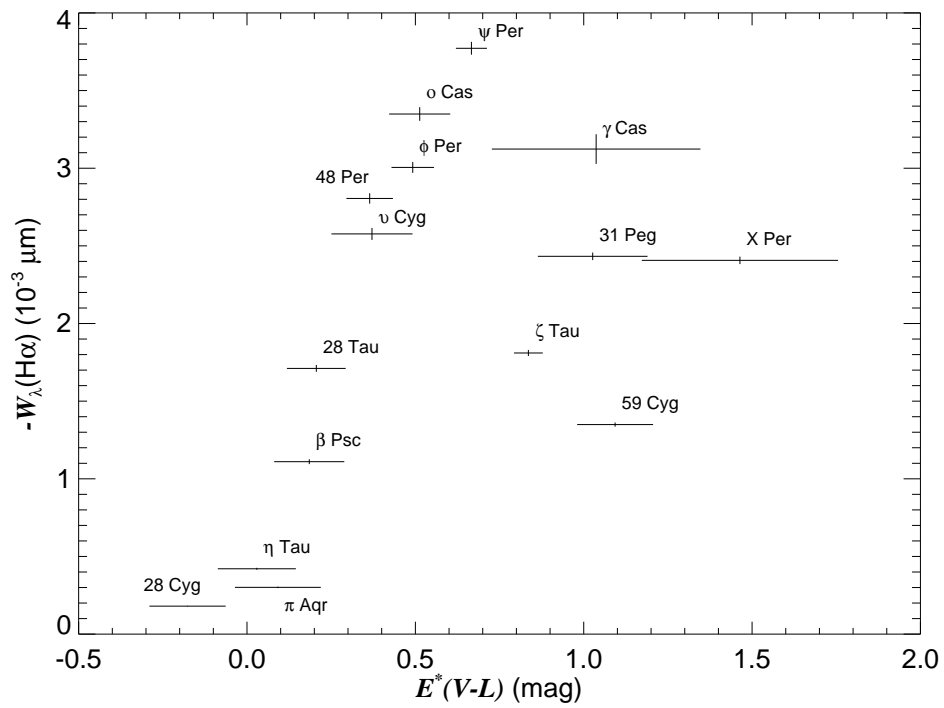
Figure 3.8: Equivalent-width of the Hα emission relative to the photospheric continuum plotted against infrared excess $E^{\star}(V - L)$.
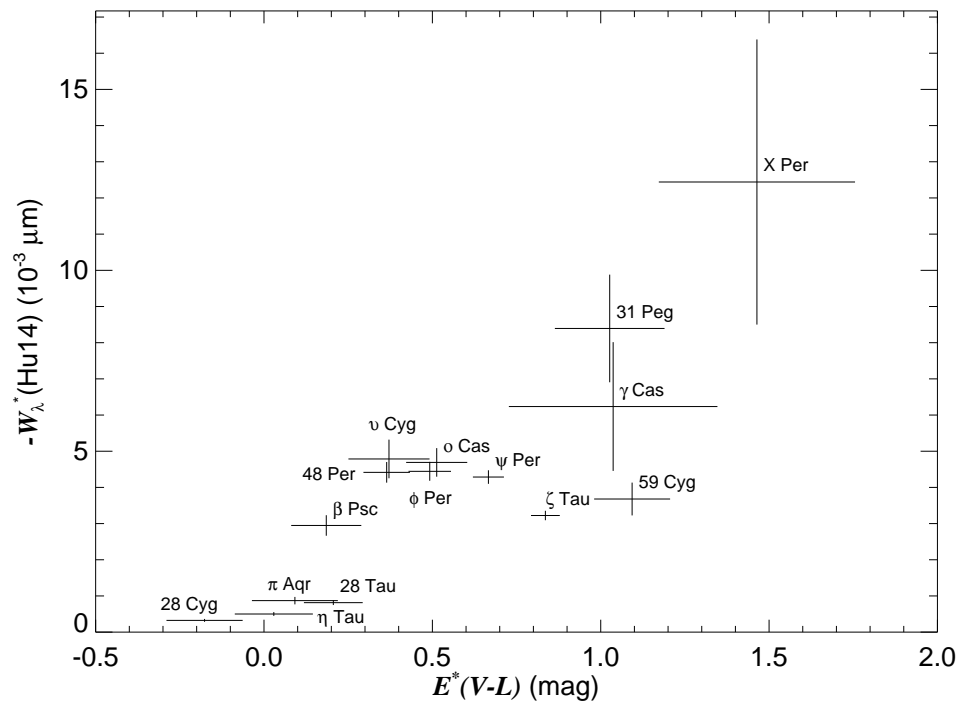
Figure 3.9: Equivalent-width of the Hu14 emission relative to the photospheric continuum plotted against infrared excess $E^{\star}(V - L)$.

We expect that features of high optical depth will be formed over a large range of disk radii (appearing uniformly bright over the optically thick regions for an isothermal disk) while low optical depth features will only appear bright in the denser regions of the inner disk. For example, Gies et al. (2007) found that the angularly resolved disks appear smaller in the lower opacity K-band continuum compared to that seen in the high opacity Hα line, which is consistent with the idea that the K-band excess forms mainly in the inner, denser part of the disk. Similarly, the emission lines of the upper Humphreys series (like Hu14) are particularly interesting since they probably form mainly in the densest region of the disk near the star (Hony et al. 2000; Jones et al. 2009). Since Be disks are time variable and outflowing, we might expect that diagnostics that probe like parts of the disk will be better correlated than those that form over different ranges of radii. This expectation agrees with our result that the excess $E^\star(V - L)$ is better correlated with $W_\lambda^\star(\text{Hu14})$ (both forming in the inner disk) than with $W_\lambda(\text{H}\alpha)$ (which forms out to larger disk radii).

In fact, there is a hint of a better defined relation between $W_\lambda(\text{H}\alpha)$ and $E^\star(V - L)$ in Figure 3.8 for $E^\star(V - L) < 0.7$ mag, and the scatter in the relation occurs only for stars with the largest IR excesses (densest, largest disks). Stars with relatively low density and small disks may have similar radial density functions, so that the ratio of flux from Hα to that in the near-IR continuum is approximately constant. However, the radial density law for Be stars with large, extensive disks may be much more complex, reflecting past episodes of differing mass loss rates and possibly developing non-axisymmetric structure. In such a situation, the conditions probed by Hα in the outer regions may be very different from those in the inner disk where the near-IR excess forms. It is interesting to note that all the strong excess stars in Figure 3.8 (with the exception of 31 Peg = HD 212076) are known

binaries with periods of order ~ 100 d. The outer boundaries of the disks in these systems are truncated by tidal forces (Okazaki & Negueruela 2001), which may explain the relative weakness of the Hα feature compared to the near-IR excess.

Lenorzer et al. (2002a) suggest that a diagram of the line flux ratios of $(\log(\text{Hu}14/\text{Pf}\gamma), \log(\text{Hu}14/\text{Br}\alpha))$ is a useful diagnostic tool to estimate the gas density in disks of Be stars (Jones et al. 2009; Mennickent et al. 2009). We measured these line fluxes by first transforming the continuum of the higher resolution SpeX spectra to that of the better flux calibrated lower resolution spectra and then subtracting a fit of local continuum. We measured the line fluxes by direct integration and then calculated these two line ratios (given in columns 8 and 9 of Table 3.5). The results are plotted in Figure 3.10, where each ratio is assigned a gray intensity proportional to the infrared excess $E^\star(V-L)$ (darkest at large $E^\star(V-L)$). We see a general trend that the Be stars in the upper right part of the diagram are those with the largest IR excess. As Lenorzer et al. (2002a) point out, in optically thick disks, the line flux ratio will be given by the product of the line source function ratio and the ratio of projected radiating surfaces. We expect that in very dense environments both these ratios will approach unity, so that the ratios for Be stars with dense disks will appear in the upper right part of the diagram near $(\log(\text{Hu}14/\text{Pf}\gamma), \log(\text{Hu}14/\text{Br}\alpha)) = (0,0)$, the same region where stars with large IR excesses are plotted. On the other hand, stars with low density, circumstellar environments (like the extended wind of the star P Cygni, indicated by a plus sign in Fig. 10) will have line ratios that tend to populate the lower, left part of the diagram (Jones et al. 2009). However, we suspect that the position in the diagram also is modified by the gas temperature in the disk (Jones et al. 2009), since the lowest point in

the diagram corresponds to the coolest Be star in our sample, 28 Tau (HD 23862; observed during a shell phase).
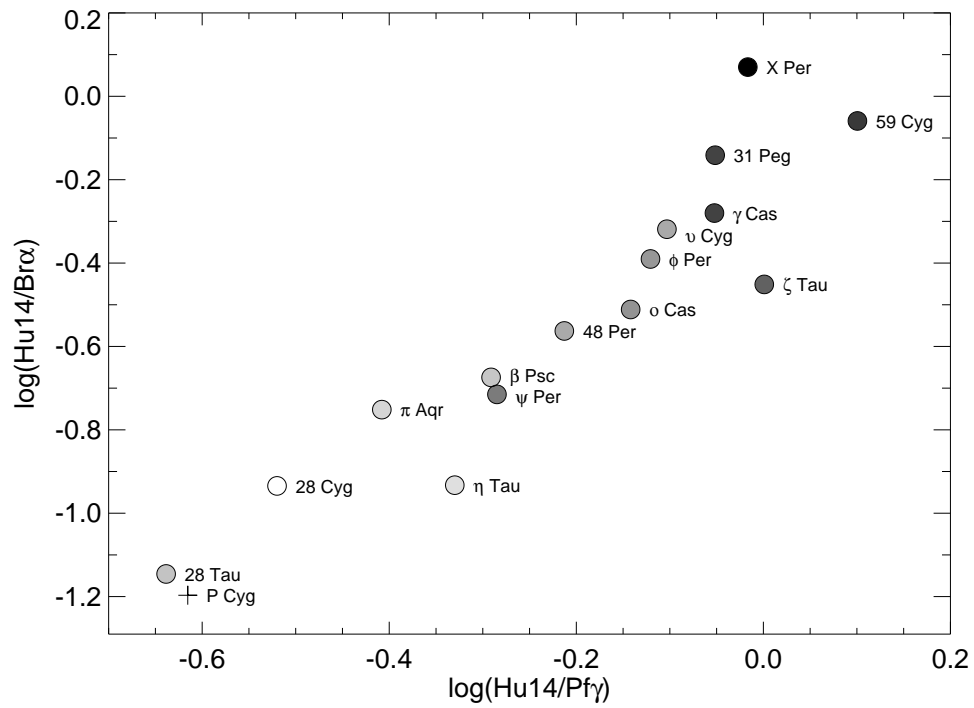
Figure 3.10: Line flux ratios from Table 3.5 plotted with a gray intensity proportional to the infrared excess $E^\star(V - L)$. The plus sign indicates the ratios found in the LBV star P Cyg.

Curiously, we might expect that in the densest disk regions near the star that both the continuum and the Hu14 source functions would be similar because they form in regions of similar temperature. If so, then in the optically thick parts, the lines would disappear since both lines and continuum would radiate with the same source function. Consequently, unless the optically thick region of line emission is significantly larger than the continuum emitting region, we would expect high excitation transition lines to vanish in the observed spectrum. The fact that the Hu lines remain as emission features in Be stars with dense disks led Hony et al. (2000) to argue that the lines must form in a region of elevated temperature compared to the site of continuum formation, perhaps in locations above the disk plane. Their suggestion appears to be verified in recent models of Be disks that show that the mid-plane region is cooler than off-plane regions in the inner part of the disk (Sigut & Jones 2007; Carciofi & Bjorkman 2008).

3.6 Conclusions

Our spectrophotometric observations of nearby Be stars show that all the stars with strong Hα emission also display an IR excess relative to the expected photospheric flux distribution. The size of the IR excess is correlated with the Hα equivalent-width but the relation shows the largest scatter among those stars with very dense circumstellar disks. On the other hand, the IR excess shows a better correlation with the equivalent-widths (corrected for disk continuum emission) of high excitation transitions like Hu14. Since only a trace number of H atoms populate these excited states, transitions like Hu14 have a low opacity except in the densest parts of the disk. We argue that these results can be understood in terms of the spatial range in radius over which any emission mechanism is optically thick. The

good correlation between the IR continuum emission and the high excitation line emission suggests that both quantities form in the inner, dense part of the disk, while the less marked correlation between the IR continuum and Hα emission results from changes in the density distribution in the inner as well as the outer parts of the disk (perhaps due to the temporal evolution of the disk and/or the tidal influence of a binary companion).

It is a common experience that a problem difficult at night

is resolved in the morning after the committee of sleep has

worked on it.

—— John Steinbeck

– 4 –

The Infrared Continuum Sizes of Be Star Disks

ABSTRACT

We present an analysis of the near-infrared continuum emission from the circumstellar gas disks of Be stars using a radiative transfer code for a parametrized version of the viscous decretion disk model. This isothermal gas model creates predicted images that we use to estimate the HWHM emission radius along the major axis of the projected disk and the spatially integrated flux excess at wavelengths of 1.7, 2.1, 4.8, 9, and 18 μm. We discuss in detail the effect of the disk base density, inclination angle, stellar effective temperature, and other physical parameters on the derived disk sizes and flux excesses. We calculate flux excess estimates relative to the stellar V-band flux for a sample of 130 Be stars using photometry from 2MASS and the AKARI infrared camera all-sky survey. The flux excess relations from our models make a good match of the observed flux excesses of Be stars. We also present our results on the projected size of the disk as a function of wavelength for the classical Be star ζ Tauri, and we show that the model predictions are consistent with interferometric observations in the H, K, and 12 μm bands.

4.1 Introduction

Be stars are rapidly rotating B-type stars that at times host a circumstellar gas disk (Porter & Rivinius 2003). They exhibit various observational attributes such as photospheric non-radial pulsations, hydrogen and iron emission lines that are formed in the disk, infrared, millimeter, and radio continuum excess emission from the disk, intrinsic linear polarization from electron scattering in the disk, and, in an increasing number of cases, the presence of a compact

companion (Struve 1931; Slettebak 1988; Porter & Rivinius 2003). The circumstellar ionized gas around Be stars gives rise to a large infrared excess emission that is seen in their spectral energy distribution. Observations conducted by Woolf et al. (1970) at 10 μm were the first to suggest that the IR flux excess detected in Be stars is due to the free-free and bound-free emission processes, and is not a result of a thermal dust emission. Another study by Gehrz et al. (1974) confirmed that the large IR emission detected from 33 Be stars originates in the free-free emission only and that thermal dust emission fails to reproduce the observations at 20 μm. The IR excess from ionized disk gas was subsequently investigated with space-based data from IRAS (Cote & Waters 1987; Waters et al. 1987; Dougherty et al. 1994), ISO (Waters et al. 2000), and MSX (Clarke et al. 2005), and with ground-based mid-IR (Rinehart et al. 1999) and near-IR data from the 2MASS survey (Zhang et al. 2005). The near- and mid-IR excess flux emission is known to increase with wavelength and to dominate over the stellar flux at long wavelengths. Observations probing the circumstellar disk structure at many wavelengths and across all Be spectral types are necessary to understand the complex physical processes involving disk formation.

Models of the disk continuum emission have become increasingly comprehensive in recent years. Some of the first models that assumed a simple geometry and gas density distribution (Waters 1986; Kastner & Mazzali 1989; Dougherty et al. 1994; Rinehart et al. 1999) were successful in fitting the flux excesses in many cases. A significant improvement came with the development of the viscous decretion disk model (Lee et al. 1991; Porter 1999; Okazaki & Negueruela 2001) in which the gas orbits with nearly-Keplerian velocity, but with a small radial outflow motion caused by turbulent viscosity. These models characterize the disk density with a radial power law, $\rho \propto R^{-3.5}$, and a vertical extension set by hydrostatic equi-

librium. The IR-excesses predicted are similar to those observed, but often require a density exponent with smaller absolute value and/or a non-isothermal temperature distribution in order to match observations (Porter 1999; Porter & Rivinius 2003). Recent models include radiation processes in the disk and determine fully consistent temperature and density distributions (Carciofi & Bjorkman 2006; Jones et al. 2008), and these are remarkably successful in explaining the continuum and line emission in some Be stars (Carciofi et al. 2006; Halonen et al. 2008).

The advent of optical long baseline interferometry has now led to the direct resolution of Be star disks in both emission lines (Quirrenbach et al. 1997; Stee & Bittar 2001; Tycner et al. 2006; Meilland et al. 2007; Carciofi et al. 2009) and in the IR-continuum (Gies et al. 2007; Meilland et al. 2007, 2009). These observations offer us the means to explore the geometry of Be disks and to measure the disk gas temperature. Since the IR-excess flux depends mainly on the projected size of the disk and the gas surface brightness (from the temperature dependent source function), a comparison of the angular size and flux excess provides a way to investigate the disk-to-star temperature ratio and (in principle) to study spatial temperature variations in the disk.

Our goal in this chapter is to explore the IR-excess flux predictions for a parameterized version of the isothermal, viscous disk model that we have developed to study CHARA Array K-band observations of Be disks (Gies et al. 2007). We calculate the near-IR flux excesses for various representative stellar and disk parameters and compare these with new IR measurements from the AKARI satellite (Ita et al. 2010). In §4.2, we describe the model in detail and discuss how the different physical parameters of the model influence the flux excess. In §4.3, we discuss the flux-flux diagrams and compare our results to the AKARI

all-sky survey observations of Be stars. Finally in §4.4, we consider the example of the Be

star ζ Tau, and we show that the predicted variation of circumstellar disk angular size with

wavelength is consistent with the available multi-wavelength observations.

4.2 Be Star Circumstellar Disk Models

Our original model (Gies et al. 2007) created images of Be stars and their disks for comparison

with K'-band interferometry from the GSU CHARA Array. In order to investigate the disk

emission over a range of wavelengths in the near and mid-IR, we have extended the model

to calculate the disk flux distribution at 1.66 (H-band), 2.13 (K-band), 4.8, 9, and 18 μm.

Our code is a realization of an isothermal viscous decretion disk model. In brief, the gas

density distribution is given by:

$$\rho(R, Z) = \rho_0 R^{-n} \exp\left[-\frac{1}{2}\left(\frac{Z}{H(R)}\right)^2\right], \tag{4.1}$$

where R and Z are the radial and the vertical cylindrical coordinates, respectively, in units

of stellar radii, ρ_0 is the gas base density, and n is the radial density exponent. $H(R)$ is the

disk vertical scale height defined by

$$H(R) = \frac{c_s}{V_K} R^{3/2} \tag{4.2}$$

where c_s is the sound speed (in turn dependent on the disk gas temperature) and V_K is the

Keplerian velocity at the stellar equator. Our multi-wavelength disk model has four physical

parameters: the base density ρ_0, the density exponent n, the disk-to-star temperature ratio

T_d/T_{eff}, and the outer boundary disk radius R_{out}, and two observational parameters: the

wavelength λ and the disk inclination angle i.

The code follows the method of Hummel & Vrancken (2000) and solves the equation of transfer along a grid of sight-lines around the star and disk. The result is a spatial image of the system (see examples in Gies et al. 2007). We assume source functions equal to the Planck functions for the temperatures of the star and disk. The disk optical depth in the near-IR is mainly due to free-free and bound-free processes, and it can be expressed using an incremental step ds along a projected rectilinear coordinate grid as follows

$$dr = C(\lambda, T_d)\rho(R, Z)^2 \, ds \qquad (4.3)$$

where the coefficient $C(\lambda, T_d)$ is given by equation (5) in Dougherty et al. (1994). This coefficient includes terms for the Gaunt factors for bound-free and free-free emission. We set these Gaunt factors by interpolating in wavelength in the tables from Waters & Lamers (1984). For simplicity, we estimate the ionization equilibrium and Gaunt factors throughout the disk for two idealized cases (adopted from Lamers & Waters 1984 and Waters & Lamers 1984): (1) a hot plasma with ionized H, singly ionized He, and doubly ionized C, N, O for disk temperatures above 15000 K, and (2) a warm plasma consisting of ionized H, neutral He, and singly ionized C, N, and O for lower temperatures. Note that we ignored the flux due to the electron scattering in the model, since this flux source is proportional to the stellar flux and hence is relatively small at longer wavelengths.

Here we focus on two results of the calculation, the flux excess and apparent disk size. We determine from the derived image the total monochromatic flux of the star and disk, F_{total}, and then we estimate the net disk contribution as $F_d = F_{\text{total}} - F_s$, i.e., the net flux relative to the unobscured star. We show this quantity in a magnitude form of flux excess as $E^\star(V^\star - m_\lambda) = 2.5 \log(1 + F_d/F_s)$. This notation is based upon the assumption that

the disk flux contribution is negligible in the optical V-band, so that we can write the flux excess as how many magnitudes brighter the system appears at longer wavelengths where the disk shines brightly. This latter assumption should be taken with caution. In fact, there is ample evidence from the V-band brightening of Be stars during their active phases that the disks do contribute to the V-band by as much as 50% in those cases with dense and large circumstellar disks. Consequently, by referring the fluxes to a V magnitude that is brighter than that for the star alone, the observed flux excesses may be lower than the calculated flux excesses in some cases. The star superscript is used here to differentiate this type of "reddening" or flux-excess from the kind normally associated with interstellar extinction. Waters (1986) expresses the monochromatic flux excess as $Z = F_{\text{total}}/F_s$, so in our notation $E^\star(V^\star - m_\lambda) = 2.5 \log Z$. We also use the calculated spatial image of the star plus disk to find the HWHM of the emission envelope along the projected major axis of the disk, and we define an effective, observational disk radius R_d/R_s as the ratio of the angular HWHM to the angular stellar radius.

We begin by showing our results on the flux excess and disk size for a default model, and then we show how changes in the physical and observational parameters affect the results. In the default model, we assume that the central star is an early-type star with effective temperature $T_{\text{eff}} = 30$ kK, radius $R_s/R_\odot = 10$, and mass $M_s/M_\odot = 15.5$. The infrared excesses derived from observations suggest that the power-law density exponent of the circumstellar disk falls in the range $n \approx 2.0$ to 3.5 (Cote & Waters 1987; Waters et al. 1987), so we assumed $n = 3$ here, a value consistent with our prior interferometric results (Gies et al. 2007). The other adopted parameters for the default model are a disk-to-star temperature ratio $T_d/T_{\text{eff}} = 2/3$, an outer boundary disk radius $R_{\text{out}}/R_s = 21.4$, and an

inclination angle $i = 45°$. These parameters are selected from an earlier model for the Be star γ Cas (Gies et al. 2007), and the outer boundary, for example, corresponds to the Roche radius of this binary system. Our results for the flux excess and disk radius are listed in Table 4.1 as a function of waveband and base density for this model and several others described below.

Table 4.1: IR Color Excesses for Different Viscous Disk Models

Parameter	ρ_0 (g cm^{-3})						
	1.0×10^{-12}	5.1×10^{-12}	1.0×10^{-11}	3.1×10^{-11}	8.1×10^{-11}	1.0×10^{-10}	2.0×10^{-10}
$n = 3$, $i = 45°$, $T_{\text{eff}} = 30$ kK, $R_{\text{out}} = 21.4R_s$, $T_d = 2/3\,T_{\text{eff}}$							
$E^*(V^* - H)$	0.02	0.03	0.06	0.29	0.91	1.08	1.65
$E^*(V^* - K)$	0.02	0.05	0.11	0.59	1.38	1.57	2.19
$E^*(V^* - 4.8\ \mu m)$	0.02	0.11	0.31	1.04	1.86	2.06	2.69
$E^*(V^* - 9\ \mu m)$	0.04	0.43	0.91	1.86	2.76	2.97	3.61
$E^*(V^* - 18\ \mu m)$	0.13	1.00	1.61	2.59	3.51	3.71	4.33
$R_d/R_s(H)$	1.23	1.24	1.25	1.41	2.10	2.28	2.97
$R_d/R_s(K)$	1.23	1.24	1.26	1.58	2.39	2.61	3.40
$R_d/R_s(4.8\ \mu m)$	1.24	1.27	1.39	2.17	3.15	3.44	4.56
$R_d/R_s(9\ \mu m)$	1.24	1.38	1.79	2.76	4.07	4.49	6.05
$R_d/R_s(18\ \mu m)$	1.26	1.95	2.55	3.92	5.95	6.57	8.82
$n = 3$, $i = 80°$, $T_{\text{eff}} = 30$ kK, $R_{\text{out}} = 21.4R_s$, $T_d = 2/3\,T_{\text{eff}}$							
$E^*(V^* - H)$	0.02	0.03	0.04	0.11	0.39	0.49	0.91
$E^*(V^* - K)$	0.02	0.03	0.04	0.25	0.72	0.87	1.41
$E^*(V^* - 4.8\ \mu m)$	0.02	0.05	0.13	0.48	1.11	1.28	1.88
$E^*(V^* - 9\ \mu m)$	0.03	0.19	0.43	1.11	1.95	2.15	2.78
$E^*(V^* - 18\ \mu m)$	0.07	0.49	0.89	1.78	2.68	2.88	3.48
$R_d/R_s(H)$	1.24	1.26	1.31	1.83	2.77	2.95	3.99
$R_d/R_s(K)$	1.24	1.27	1.39	2.14	3.13	3.49	4.56
$R_d/R_s(4.8\ \mu m)$	1.24	1.39	1.80	2.87	4.29	4.62	6.21
$R_d/R_s(9\ \mu m)$	1.26	1.77	2.43	3.64	5.61	6.11	8.17
$R_d/R_s(18\ \mu m)$	1.37	2.57	3.43	5.33	8.03	8.86	11.97
$n = 3$, $i = 45°$, $T_{\text{eff}} = 15$ kK, $R_{\text{out}} = 21.4R_s$, $T_d = 2/3\,T_{\text{eff}}$							
$E^*(V^* - H)$	0.02	0.04	0.08	0.43	1.11	1.28	1.86
$E^*(V^* - K)$	0.02	0.06	0.15	0.73	1.53	1.73	2.35
$E^*(V^* - 4.8\ \mu m)$	0.04	0.17	0.46	1.26	2.11	2.31	2.94
$E^*(V^* - 9\ \mu m)$	0.05	0.49	1.01	1.96	2.86	3.07	3.71
$E^*(V^* - 18\ \mu m)$	0.14	1.04	1.64	2.63	3.54	3.79	4.36
$R_d/R_s(H)$	1.23	1.24	1.27	1.64	2.46	2.68	3.51
$R_d/R_s(K)$	1.23	1.25	1.29	1.77	2.62	2.85	3.76
$R_d/R_s(4.8\ \mu m)$	1.24	1.30	1.55	2.44	3.59	3.94	5.23
$R_d/R_s(9\ \mu m)$	1.24	1.52	2.04	3.12	4.63	5.12	6.86
$R_d/R_s(18\ \mu m)$	1.27	1.99	2.62	4.03	6.07	6.71	9.03
$n = 3$, $i = 45°$, $T_{\text{eff}} = 30$ kK, $R_{\text{out}} = 21.4R_s$, $T_d = 2/3\,T_{\text{eff}}$							
$E^*(V^* - H)$	0.02	0.03	0.06	0.30	0.91	1.08	1.65
$E^*(V^* - K)$	0.02	0.04	0.09	0.45	1.16	1.34	1.94
$E^*(V^* - 4.8\ \mu m)$	0.03	0.11	0.31	1.04	1.86	2.06	2.69
$E^*(V^* - 9\ \mu m)$	0.04	0.31	0.72	1.61	2.48	2.68	3.33
$E^*(V^* - 18\ \mu m)$	0.09	0.79	1.35	2.32	3.22	3.42	4.05
$R_d/R_s(H)$	1.23	1.24	1.25	1.41	2.10	2.28	2.97
$R_d/R_s(K)$	1.23	1.24	1.26	1.55	2.34	2.54	3.31

Continued on Next Page...

Table 4.1 – Continued

Parameter	ρ_0 (g cm^{-3})						
	1.0×10^{-12}	5.1×10^{-12}	1.0×10^{-11}	3.1×10^{-11}	8.1×10^{-11}	1.0×10^{-10}	2.0×10^{-10}
$R_d/R_s(4.8\,\mu m)$	1.24	1.27	1.39	2.17	3.15	3.44	4.56
$R_d/R_s(9\,\mu m)$	1.24	1.39	1.79	2.76	4.07	4.49	6.06
$R_d/R_s(18\,\mu m)$	1.26	1.86	2.46	3.75	5.67	6.25	8.48
$n=3,\ i=45^\circ,\ T_{\mathrm{eff}}=30$ kK, $R_{\mathrm{out}}=14.6R_s$, $T_d=2/3\,T_{\mathrm{eff}}$							
$E^*(V^*-H)$	0.02	0.03	0.06	0.29	0.91	1.08	1.65
$E^*(V^*-K)$	0.02	0.05	0.12	0.60	1.38	1.57	2.18
$E^*(V^*-4.8\,\mu m)$	0.02	0.11	0.31	1.04	1.86	2.06	2.67
$E^*(V^*-9\,\mu m)$	0.05	0.43	0.92	1.86	2.75	2.96	3.57
$E^*(V^*-18\,\mu m)$	0.13	1.00	1.59	2.58	3.47	3.66	4.23
$R_d/R_s(H)$	1.23	1.24	1.25	1.42	2.10	2.29	2.97
$R_d/R_s(K)$	1.23	1.24	1.27	1.58	2.39	2.60	3.40
$R_d/R_s(4.8\,\mu m)$	1.24	1.27	1.39	2.17	3.15	3.44	4.56
$R_d/R_s(9\,\mu m)$	1.24	1.38	1.79	2.76	4.07	4.48	6.05
$R_d/R_s(18\,\mu m)$	1.26	1.95	2.55	3.92	5.95	6.56	8.82
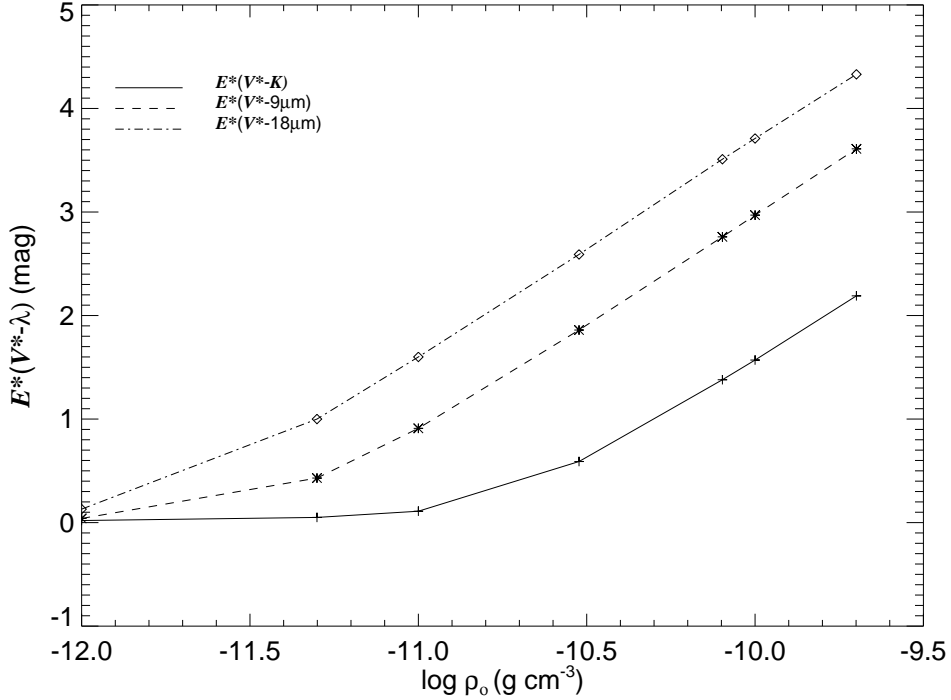
Figure 4.1: Plots of the variation in the flux excess as function of disk base density for the default model parameters ($n = 3$, $i = 45°$, $T_{\text{eff}} = 30$ kK, $R_{\text{out}} = 21.4R_s$, $T_d = 2/3T_{\text{eff}}$). The excess emission increases with increasing disk base density ρ_0 and wavelength.

We show in Figure 4.1 how the flux excesses $E^\star(V^\star - K)$, $E^\star(V^\star - 9\mu\text{m})$, and $E^\star(V^\star - 18\mu\text{m})$ vary as a function of the disk base density ρ_0. The disk flux excess is highly dependent on density ρ_0 and wavelength λ. The flux excesses at low densities are insignificant because the disk is optically thin in the continuum and the stellar photospheric flux dominates. As the density increases, the flux excess resulting from the disk emission becomes more important and dominates at longer wavelengths. In fact, the excess emission at 18 μm is higher than at 9 μm and at 2.13 μm because the optically thick-thin boundary of the disk becomes bigger and the excess flux larger at longer wavelengths.

The relationship between the 18 μm flux excess and apparent disk emission radius for the default model is shown as a solid line in Figure 4.2 (for $T_d/T_{\text{eff}} = 2/3$). We also show
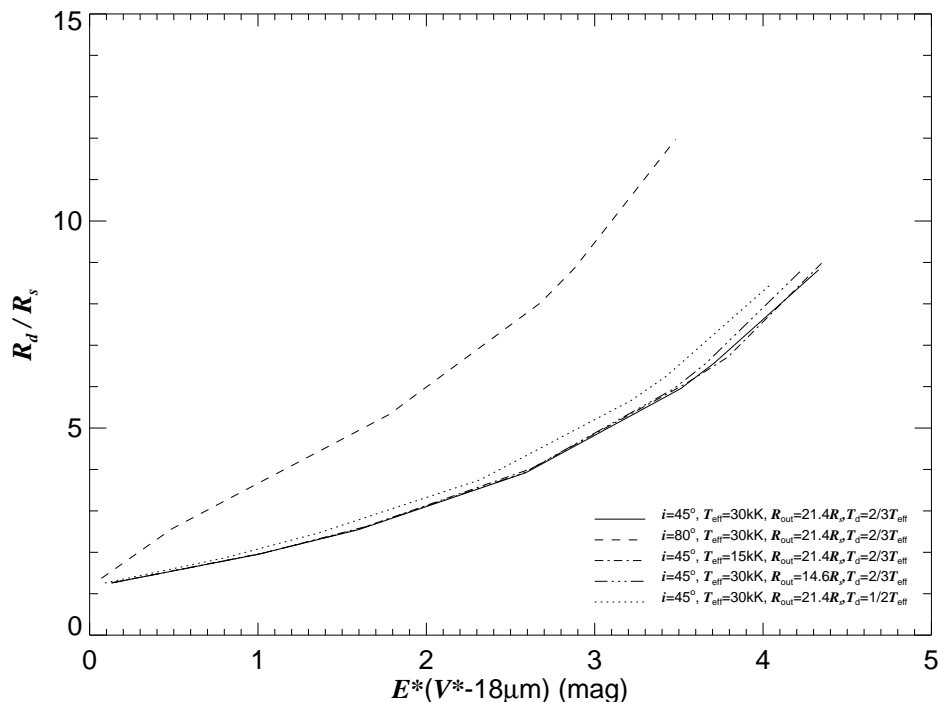
Figure 4.2: Plots of the ratio of disk HWHM radius to stellar radius as a function of the flux excess at 18 μm. The solid line illustrates the relationship for the default model while the other line styles show the results found by changing one of the model parameters (indicated in the legend).

a number of other models where different parameters are varied in turn. The case with a higher inclination angle $i = 80°$ is plotted with a dashed line. As the inclination increases, the projected disk surface area decreases and hence the disk flux excess also declines. However, at higher inclination, a ray through the outer part of the disk encounters significant density over a longer path, and the increased optical depth causes the effective radius to appear larger. Consequently, as the inclination increases, points on the default model curve are shifted to lower flux excess and higher effective radius.

Changes in the other parameters have less influence on the size – flux excess relation shown in Figure 4.2. For example, for the case of a cooler Be star with an effective tem-

perature of $T_{\rm eff} = 15$ kK (shown by the dashed-dotted line), the resulting flux excess and disk radius are almost identical to that for the default case ($T_{\rm eff} = 30$ kK; solid line) at all values of the disk base density. This is due to the temperature dependence of the optical depth coefficient, $C(\lambda, T_d) \propto T_d^{-1/2}$. The radius of the optically thick-thin boundary will vary with this optical depth term, and the source function is proportional to temperature in the Rayleigh-Jeans part of the spectrum. Thus, the disk emission flux will vary as the product of projected area and source function, or $\sim R_d^2 \, S \sim (T_d^{-1/2})^2 \, T_d$, which is approximately constant, all other parameters being equal.

If we adopt a smaller value of the outer radius of the disk ($R_{\rm out}/R_s = 14.6$; shown by the dash-triple dotted line), we see that there is no difference between this case and the default case ($R_{\rm out}/R_s = 21.6$) at low densities. It is only at very high density that the truncation of the outer disk leads to a slight decline in the flux excess.

Finally, the dotted line shows the influence of our choice of disk temperature. In the default model, we adopt an isothermal disk with a temperature of $T_d = 2/3 \, T_{\rm eff}$ following the example of Hummel & Vrancken (2000). We compare in Figure 4.2 the flux excess for two disk temperatures, $1/2 \, T_{\rm eff}$ and $2/3 \, T_{\rm eff}$. The source function varies approximately linearly with disk temperature T_d, so a drop of 25% in disk temperature will create a comparable decrease in emission flux (for a given disk radius). This decrease of ≈ 0.3 mag in $E^\star(V^\star - 18\mu{\rm m})$ is seen in Figure 4.2 at the high density end where the disk flux dominates. This suggests that coordinated interferometric and IR excess observations are potentially an important means to study the disk temperature properties, especially for Be stars with dense and large disks.

Our results show many similarities to the flux excesses derived by Dougherty et al. (1994) from a much simpler model. They confined the emitting gas to a wedge-like disk with

a density law dependent only on the distance to the star, and they solved the radiative transfer problem for just $i = 0$ and $i = 90°$. Dougherty et al. (1994) also investigated the dependence of the near-IR flux excess on the model parameters, but they present relative flux excesses between adjacent near-IR bands ($CE(J - K)$ and $CE(K - L)$; see their Fig. 7) rather than referencing the excess to the stellar V-band flux as we do here. Nevertheless, the agreement is reasonable, and, for example, their expression for the disk optically thick-thin boundary as a power law function of wavelength and base density (their eq. 7) is similar to our results for R_d/R_s in Table 4.1. Furthermore, Dougherty et al. (1994) also presented instructive results for a range in the density power law exponent, with values greater and less than the $n = 3$ value assumed here (they used the symbol β for the density exponent). Their work showed that a smaller n yields a more spatially extended disk and consequently larger flux excesses.

Recent models for Be star disks present detailed calculations of the gas temperature as a function of disk position. Carciofi & Bjorkman (2006) solve for the temperature distribution in the disk through a Monte-Carlo treatment of radiative transfer, and they find that gas temperature reaches $T_d \approx 0.6$ T_{eff} in optically thin parts of the disk in one representative model. Sigut et al. (2009) present results for a grid of models that maintain hydrostatic equilibrium with the spatial variations in temperature, and they find that the density averaged temperature is $T_d \approx 0.6 T_{\text{eff}}$, however, this average temperature declines with increasing disk density (perhaps by $20 - 30\%$; see their Fig. 8). Their models indicate that the temperatures tend to be cooler in the denser regions closer to the star and in the mid-plane. The IR flux excesses calculated from such models are similar to those derived from isothermal models. For example, Carciofi & Bjorkman (2006) show that the predicted flux excesses for different

inclination angles are almost the same for the isothermal and non-isothermal model they study (see the upper panel of their Fig. 10). However, since the disk gas temperatures decline with increasing density, we suspect that a plot like Figure 4.2 of flux excess and radius for such fully consistent, non-isothermal models would look similar to our $T_d = (2/3)T_{\text{eff}}$ curve at small excess (low density), but would tend towards the $T_d = (1/2)T_{\text{eff}}$ curve at large excess (high density).

4.3 AKARI IR Fluxes of Be Stars

With the recent release of the AKARI/IRC mid-infrared all-sky survey (Ishihara et al. 2010), we now have the opportunity to compare the observed and model flux excesses at 9 and 18 μm. We took as our sample 130 Be stars from the work of Dougherty et al. (1994) that have reliable estimates of interstellar reddening $E(B-V)$. We then collected V, K_s, $m(9\,\mu\text{m})$, and $m(18\,\mu\text{m})$ magnitudes from Ita et al. (2010) for each target. The V magnitudes were taken from the SIMBAD database, K_s magnitudes from 2MASS (Cutri et al. 2003; Skrutskie et al. 2006), and $m(9\mu\text{m})$ and $m(18\mu\text{m})$ magnitudes from AKARI. These last two are based on the Vega magnitude scale, where a model spectrum by R. L. Kurucz defines the flux zero point as a function of wavelength (Tanabé et al. 2008). The photometry we use here was collected at different times, and since Be stars are inherently variable (Porter & Rivinius 2003), some scatter must be expected in the results because the flux excesses will change with disk density variations. We also collected stellar effective temperatures for each target from the work of Frémat et al. (2005) in order to estimate the intrinsic stellar fluxes.

Our goal is to determine a flux excess by comparing the observed and intrinsic stellar fluxes of the targets. Using the same magnitude notation given in the previous section, we

determine the near-IR flux excesses by:

$$E^\star(V^\star - m_\lambda) = V - m_\lambda - E(B - V) \times (3.10 - R_\lambda) - (V - m_\lambda)(\text{Kurucz})$$

where the ratio of interstellar extinction to reddening is $R_\lambda = A_\lambda/E(B - V)$ (Fitzpatrick 1999) and $(V - m_\lambda)$(Kurucz) is the intrinsic stellar flux derived from monochromatic sampling of flux ratios of model spectra with the Vega spectrum from R. L. Kurucz. These model spectra are also from Kurucz atmospheres for solar metallicity, gravity $\log g = 4.0$, and a microturbulent velocity of 2 km s^{-1} (parameters appropriate for main sequence B-stars). The intrinsic fluxes are listed in Table 4.2 as a function of effective temperature T_{eff}, and we found that they made a reliable match to the AKARI fluxes of B-stars with known T_{eff} from interferometry and bolometric luminosity (Code et al. 1976). The derived flux excesses for the Be stars are listed in Table 4.3. The typical errors in the AKARI magnitudes are ± 0.05 mag, but they can be larger for the 2MASS K_s magnitudes since many of the Be stars are bright and their magnitudes were determined from the the wings of the point spread function. We caution that the intrinsic fluxes from Table 4.2 may not be appropriate in some cases because rotational gravity darkening will make stars with large inclination appear redder (although the flux difference may be negated if opaque disk gas blocks the cooler equatorial zones from view). We have ignored these complications because they are difficult to estimate accurately and because these fluxes are not too sensitive to temperature for hot stars.

Table 4.2: Adopted Main Sequence Colors

T_{eff} (kK)	$V - K$ (mag)	$V - 9\ \mu\mathrm{m}$ (mag)	$V - 18\ \mu\mathrm{m}$ (mag)
10	-0.06	-0.07	-0.07
12	-0.23	-0.29	-0.29
14	-0.34	-0.43	-0.44
16	-0.43	-0.54	-0.55
18	-0.51	-0.64	-0.65
20	-0.58	-0.74	-0.75
22	-0.64	-0.82	-0.83
24	-0.70	-0.90	-0.91
26	-0.74	-0.96	-0.98
28	-0.79	-1.02	-1.03
30	-0.83	-1.07	-1.08

Table 4.3: Be Star Color Excesses

Star (HD)	$E^\star(V^\star - K)$ (mag)	$E^\star(V^\star - 9\ \mu\text{m})$ (mag)	$E^\star(V^\star - 18\ \mu\text{m})$ (mag)
144	0.05	0.12	$\cdots$
4180	0.13	1.54	2.44
5394	0.54	1.83	2.51
6811	-0.34	-0.02	0.41
10144	0.03	0.29	0.43
10516	0.46	1.68	2.68
18552	0.11	0.74	1.62
20336	0.03	1.47	2.16
22192	0.33	1.75	2.62
23016	0.03	0.06	$\cdots$
23302	-0.07	0.72	3.24
23480	-0.06	0.29	1.72
23552	-0.07	0.53	1.54
23630	0.29	0.28	0.97
23862	0.10	0.45	1.25
25940	0.08	1.16	1.99
28497	0.30	1.87	2.51
29866	0.03	0.72	1.49
30076	0.57	1.63	2.60
32343	0.39	1.21	2.43
32990	-0.05	0.07	$\cdots$
32991	0.46	1.56	2.65
35439	-0.23	1.54	2.12
36576	0.70	1.88	2.95
37202	0.72	1.71	2.56
37490	-0.15	0.96	1.68
37795	0.10	0.51	1.30
41335	0.52	1.90	$\cdots$
44458	-0.19	1.49	2.21
45542	0.00	0.32	0.89
45910	1.02	1.79	2.15
46860	0.06	0.13	$\cdots$
50013	0.23	1.49	2.21
50123	0.90	1.60	2.08
50820	1.01	0.80	1.33
54309	0.39	1.00	1.90
56014	-0.04	0.88	1.40
56139	0.01	1.28	2.36
57150	0.40	1.67	2.52
57219	-0.06	0.12	$\cdots$
58155	-0.04	0.00	$\cdots$
58343	-0.25	$\cdots$	2.19
58715	-0.03	0.47	1.17
60606	0.52	1.41	2.57
60855	0.75	$\cdots$	3.09
63462	0.28	$\cdots$	1.94
65875	0.39	1.73	2.64
66194	0.64	1.52	2.69
68980	0.48	1.62	2.45
71510	0.01	0.09	$\cdots$
72067	-0.02	1.08	2.03
75311	-0.09	0.19	1.05
77320	0.39	1.16	1.41
79621	0.03	0.02	$\cdots$
83953	0.50	$\cdots$	2.37
86612	0.10	1.57	2.58
88661	0.54	1.78	2.69
91120	0.06	0.46	1.21
91465	0.32	1.51	2.23
105435	0.29	1.64	2.49
107348	0.03	0.55	$\cdots$

Continued on Next Page. . .

Table 4.3 – Continued

Star (HD)	$E^\star(V^\star - K)$ (mag)	$E^\star(V^\star - 9\ \mu\mathrm{m})$ (mag)	$E^\star(V^\star - 18\ \mu\mathrm{m})$ (mag)
109387	0.29	1.42	2.30
110432	0.26	1.82	2.50
113120	−0.44	1.33	2.09
120324	0.07	1.69	2.24
120991	0.29	0.07	1.03
121847	−0.03	0.00	$\cdots$
124367	0.42	1.56	2.50
127972	0.10	1.13	1.87
137387	0.07	0.45	$\cdots$
138749	−0.01	0.07	0.20
142184	0.09	0.54	1.18
142926	0.11	0.48	1.05
148184	0.49	1.93	2.71
153261	0.83	2.09	2.92
156325	0.00	0.12	$\cdots$
157042	0.20	1.34	2.02
158427	0.64	$\cdots$	2.48
158643	0.39	$\cdots$	4.40
164284	−0.13	0.05	0.59
164447	−0.07	0.12	$\cdots$
167128	0.03	0.62	1.34
168797	−0.02	0.24	$\cdots$
170235	−0.13	0.07	$\cdots$
171780	0.29	0.12	$\cdots$
173370	0.04	0.26	0.28
173948	0.12	−0.03	0.23
174237	0.21	0.75	$\cdots$
175869	0.03	0.06	$\cdots$
178175	0.29	$\cdots$	2.40
183362	0.55	1.77	$\cdots$
185037	0.04	0.61	$\cdots$
187567	0.56	1.78	2.63
187811	0.33	0.35	1.38
189687	0.04	0.33	1.46
191610	0.25	0.14	0.78
192044	0.12	0.81	1.37
193911	0.00	0.51	1.23
194244	0.04	0.24	$\cdots$
194335	0.19	1.34	2.41
195554	0.03	0.17	$\cdots$
196712	−0.04	0.53	$\cdots$
197419	0.28	0.88	$\cdots$
198183	−0.09	−0.08	0.28
199218	0.08	0.84	$\cdots$
200120	0.45	1.69	2.13
200310	−0.03	0.26	1.79
202904	0.04	1.62	2.50
203025	−0.32	−0.12	$\cdots$
203467	0.58	1.91	3.47
205551	−0.14	0.06	$\cdots$
205637	0.14	0.69	1.37
208057	−0.06	0.03	$\cdots$
208682	−0.28	−0.14	$\cdots$
209014	0.04	0.62	1.32
209409	0.22	1.10	1.94
209522	−0.01	−0.06	$\cdots$
210129	−0.09	1.24	1.99
212076	0.41	1.74	2.48
212571	−0.41	0.51	0.91
214168	0.25	0.62	$\cdots$
214748	−0.02	0.14	0.99
216057	−0.07	0.01	$\cdots$
216200	0.25	0.63	$\cdots$

Continued on Next Page. . .

Table 4.3 – Continued

Star (HD)	$E^\star(V^\star - K)$ (mag)	$E^\star(V^\star - 9\ \mu\mathrm{m})$ (mag)	$E^\star(V^\star - 18\ \mu\mathrm{m})$ (mag)
217050	0.28	1.65	2.58
217543	−0.07	0.33	$\cdots$
217675	−0.12	0.04	0.44
217891	−0.05	0.93	1.58
224544	0.00	−0.07	$\cdots$
224559	0.10	1.52	2.15

We plot the results in two flux-flux diagrams in Figures 4.3 and 4.4. These show the flux excesses at 9 and 18 μm, respectively, as a function of the K_s-band excess. Also shown in these figures are plots of our model near-IR excesses (§4.2) for the default model and cases with differing stellar temperature and disk inclination. All these models make similar predictions about flux-flux excesses, and they appear to match the observations well, especially if allowance is made for the slight negative shift in observed fluxes caused by our neglect of disk flux in the V-band. There are three objects plotted in Figures 4.3 and 4.4 with $E^\star(V^\star - K) \approx 1.0$ that fall well below the predicted trends. All three are binary stars in which the companion is a K-giant (HD 45910 = AX Mon, Elias et al. 1997; HD 50123 = HZ CMa, Sterken et al. 1994; HD 50820, Ginestet & Carquillat 2002), and we suspect that their relatively large brightness in K_s is due to the flux from the cool giant companion. Otherwise, the overall agreement suggests that the viscous decretion disk model provides a satisfactory description of the near-IR flux excesses.

Inspection of Figures 4.3 and 4.4 shows that at the high density limit, the flux-flux excess diagrams assume a linear form. This part of the relation occurs when the disk flux dominates over the stellar flux and the fluxes become those of the disk. Thus, we expect that all Be stars will appear with approximately the same near-IR flux for those cases with sufficiently dense disks. As an example, we show in Figure 4.5 a near-IR flux-magnitude diagram for all those sample stars with Hipparcos parallax data yielding absolute magnitude errors less than 0.5 mag (van Leeuwen 2007). This plot shows the interstellar extinction corrected, absolute K_s magnitude versus an interstellar reddening corrected, flux index $K_s - m(9 \ \mu\mathrm{m})$ (shown as plus signs). Each of these is connected by a dotted line to a flux and magnitude coordinate corresponding to one with the derived flux excess removed (nominally for the star itself;
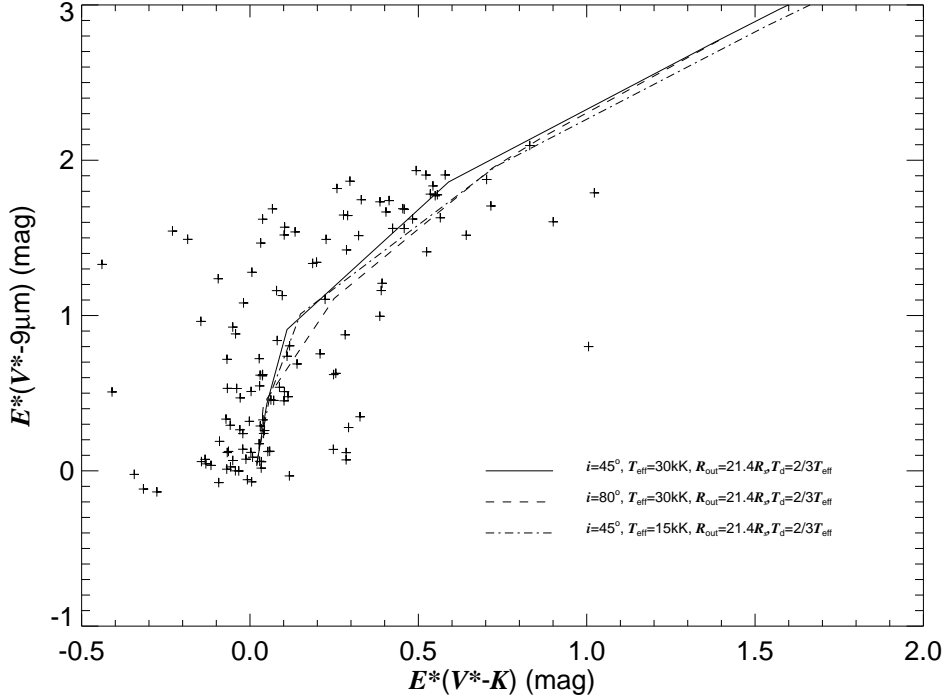
Figure 4.3: A color excess – color excess diagram showing the 9 μm flux excess as a function of the K_s-band excess. The solid line shows our results using the default model input parameters, the dashed line represent a model with a high-inclination disk ($i = 80°$), and the dashed-dotted line shows the case of a cooler Be star ($T_{\mathrm{eff}} = 15$ kK). The plus signs indicate the observed excesses of Be stars derived from 2MASS and AKARI/IRC photometry.

shown as diamonds). Also plotted is the zero-age main-sequence (left dashed line) from the

work of Lejeune & Schaerer (2001) that was formed from the theoretical (T_{eff}, V) track and

the fluxes in Table 4.2 for $T_{\mathrm{eff}} = 10 - 30$ kK. From Figure 4.3, the asymptotic form of the

excess relation is

$$E^\star(V^\star - 9\ \mu\mathrm{m}) \approx E^\star(V^\star - K_s) + 1.35$$

and we also plot the main-sequence translated in flux by this expression and brighter in K_s

by 1 magnitude (see Fig. 1) to represent the approximate positions of the dense disk case

(right dashed line). We see that the Be stars appear over a range in flux between the no
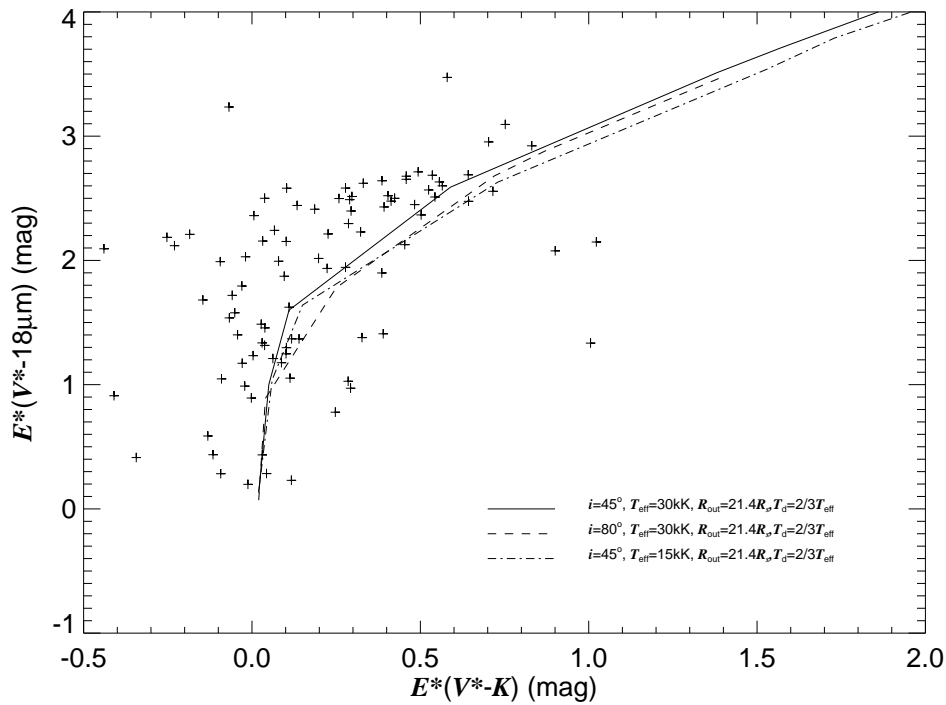
Figure 4.4: A color excess – color excess diagram showing the 18 μm flux excess as a function of the K_s-band excess (in the same format as Fig. 3).

disk and strong disk cases, with many of the Be stars having fluxes close to the strong disk limit. This diagram is similar in appearance to that for the Be stars discovered in the LMC by Bonanos et al. (2010), who present a plot in the $(J - [3.6\mu\mathrm{m}], J)$ plane.
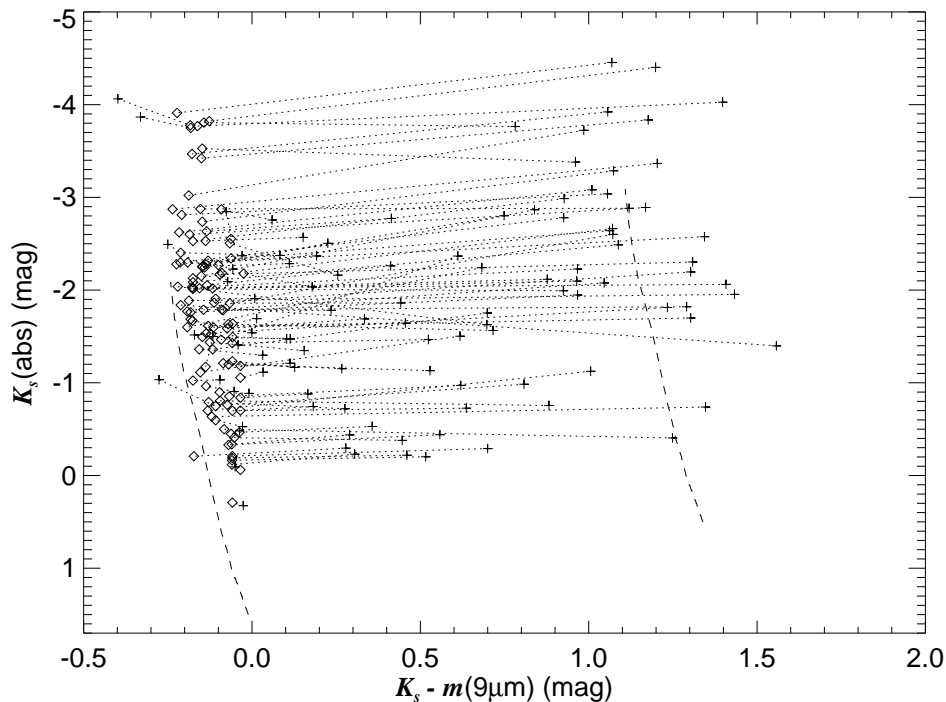
Figure 4.5: A color – magnitude diagram showing the absolute K_s magnitude corrected for interstellar extinction as a function of the interstellar reddening corrected, color index $K_s - m(9~\mu m)$ for our Be star sample (shown as plus signs). Each target point is connected by a dotted line to a diamond representing the color and magnitude of the B star alone. The left dashed line represents the zero-age main-sequence for stars with $T_{\text{eff}} = 10 - 30$ kK, and this also is shown translated in color and magnitude for a dense disk as the dashed line on the right hand side.

4.4 Angular Size of the Disk of ζ Tau

Meilland et al. (2009) measured some of the first Be disk diameters at 8 and 12 μm using the VLTI and MIDI instrument. Their results suggested that the disk sizes do not increase with wavelength as predicted by simple models. For example, they found that the angular size of the disk of the Be star α Ara was approximately constant between 2 and 12 μm, and they speculated that the disks may be truncated by the tidal effects of a binary companion. Our models and those of Dougherty et al. (1994) suggest that the flux excesses and effective radii could reach finite limits in those cases with high disk density and a small outer boundary.

Here we demonstrate that at least for one case, ζ Tau, the angular size variation with wavelength is consistent with model predictions. The Be star ζ Tau (HD 37202, HR 1910, HIP 26451) is a frequently observed target with a strong IR-excess (Touhami et al. 2010). The Hα emission line in its spectrum shows cyclic V/R variations on a timescale of few years, which are explained by the presence of a one-armed oscillation in its circumstellar disk (Okazaki et al. 2002; Carciofi et al. 2009). The star is the primary in a spectroscopic binary with an orbital period of $P = 133$ d (Ruždjak et al. 2009). The system is composed of a $11M_\odot$ primary Be type star and a $1.3M_\odot$ secondary star (Floquet et al. 1989). Several interferometric studies of the Hα emission line (Quirrenbach et al. 1997; Tycner et al. 2004) and the IR-continuum (Gies et al. 2007; Carciofi et al. 2009; Meilland et al. 2009) have resolved the circumstellar disk around the primary Be star. A recent CHARA Array investigation by Schaefer et al. (2010) shows that the disk of ζ Tau is viewed almost edge-on and that the disk may be precessing with the V/R cycle.

We used our model to estimate R_d/R_s for ζ Tau over the wavelength range of 1.7 – 18 μm. We adopted the stellar parameters from (Gies et al. 2007): mass $M_s = 11.2M_\odot$, radius $R_s = 5.5R_\odot$, effective temperature $T_{\rm eff} = 19$ kK, and parallax $\pi = 7.82$ mas. The disk parameters assumed are $\rho_0 = 1.4 \times 10^{-10}$ g cm^{-3}, $n = 2.9$, $i = 87°$, and $T_d/T_{\rm eff} = 2/3$ (based on fits of recent K' observations with the CHARA Array). The outer disk boundary was set at the binary Roche radius, $R_{\rm out} = R_{\rm Roche} = 146R_\odot$. We then determined the disk effective radius over the wavelength grid, and our results for R_d/R_s are plotted in Figure 4.6.

In order to test our model predictions, we collected recent interferometric measurements of the angular size of ζ Tau. We start with the two CHARA Array results. The weighted average of the H-band, Gaussian elliptical disk size along the major axis $\theta_{\rm maj}$ from Schaefer
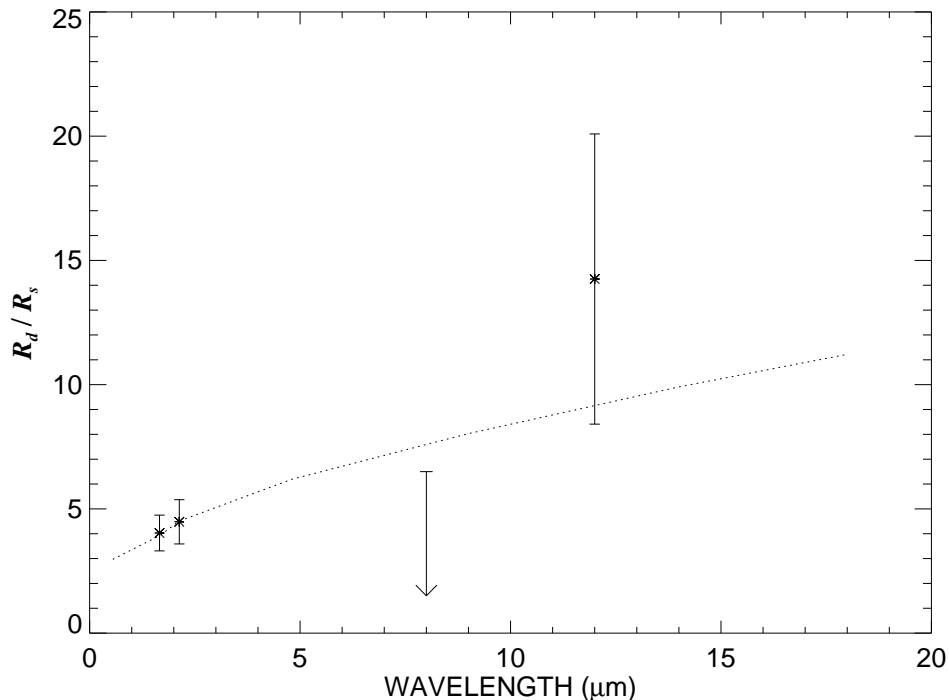
Figure 4.6: The disk-to-stellar radius ratio as a function of wavelength for our model of the Be star ζ Tau (dotted line). Also shown are the measured sizes from interferometry (or upper limit on the size for the 8 μm observation) based on an adopted stellar angular diameter of 0.40 mas.

et al. (2010) is 1.61±0.05 mas, and the corresponding K'-band value of θ_{maj} is 1.79±0.07 mas (Gies et al. 2007). The target was also observed at longer wavelengths with VLTI/MIDI by Meilland et al. (2009). They found an upper limit of θ_{maj} less than 2.6 mas at 8 μm, but they resolved the disk at 12 μm and found $\theta_{\mathrm{maj}} = 5.7 \pm 2.2$ mas. These estimates are over-plotted for comparison on the theoretical dotted-line shown in Figure 4.6 by assuming a stellar, limb darkened, angular diameter of $\theta_{LD} = 0.40 \pm 0.04$ mas. We find that the size of the emitting region does increase with increasing wavelength in a manner mostly consistent with the observations. The 8 μm upper limit falls slightly below the model curve in Figure 4.6, but we suspect that this difference is marginal given the fact that the VLTI/MIDI observations

were not made at an optimal position angle for the disk's orientation in the sky. Thus, we suggest that the viscous decretion disk predictions about disk size as a function of wavelength pass the test for the case of ζ Tau. However, it is certainly possible that disk truncation effects will be more important in binary Be stars with smaller semimajor axes.

He who devotes sixteen hours a day to hard study may

become at sixty as wise as he thought himself at twenty.

—— Mary Wilson Little

<div align="center">

– 5 –

The Circumstellar Environment of γ Cassiopeia

</div>

<div align="center">

ABSTRACT

</div>

We present new interferometric observations of the circumstellar disk of the Be star γ Cassiopeia obtained with the CHARA Array long baseline interferometer. These observations were accompanied with contemporaneous spectroscopic measurements made with the Mimir spectrograph at Lowell Observatory. Our measurements show a totally resolved circumstellar disk around γ Cas at a projected baseline of 330 meters. Using a radiative-transfer model that accounts for the density structure of the disk of γ Cas, we find that the best-fit disk inclination of γ Cas is $48°\pm4°$, and that the position angle of the disk major axis is $34°\pm5°$. We also find that the disk base density of γ Cas disk is equal to $\rho_0 = (7.2\pm0.3)\times\ 10^{-11}$ g cm^{-3}, and that the density exponent is equal to $n = 2.7 \pm 0.2$. Using these K-band best-fitting parameters, we are able to predict the size of the circumstellar disk of γ Cas at several other wavelengths in the infrared.

5.1 Introduction

The brightest Be star of the northern hemisphere, Gamma Cassiopeia (γ Cas, 27 Cas, HD5394, HR264, HIP4427, B0.5 V, ADS 782A), is a non supergiant, B-spectral type star that is rapidly rotating and ejecting large quantities of gas to its circumstellar environment. This young massive star shows broad emission lines, especially hydrogen and helium emission lines, an infrared and millimeter-wavelength excess flux, and a large intrinsic linear polarization, which are strong indications of the presence of a circumstellar disk around the star. γ Cas has been regularly monitored due to its short- and long-term spectroscopic and

photometric variations. Several long periods of weak and strong Balmer, He I and Fe II emissions have been observed, and the system has passed through several stages of a regular B star without any emission detected from the circumstellar disk (Underhill & Doazan 1982; Rivinius et al. 2006).

The long-term observations of γ Cas between 1866 and 1932 showed that γ Cas was in a long calm Be phase with moderate to strong emission detected in its spectrum. This steady-disk phase was followed by several spectacular episodes of variations that lasted from 1932 to 1942, and that ended with the total dissipation of the circumstellar disk. By 1942, γ Cas had lost almost all its emission leaving only a very weak Hα component and fell back into a quasi-normal B phase. Observations showed that from 1948 to 1981, γ Cas slowly started rebuilding another disk to regain its Be status, with irregularly increasing emission and small fluctuations (Howarth 1979). A clear correlation was found to exist between the emission phases and the luminosity of the star (Baldwin 1939; Underhill & Doazan 1982).

The variations that γ Cas exhibits and its relatively rapid transition through Be to B to Be phases show that the density structure of the disk is highly variable. The long monitoring of γ Cas shows that for nearly a century, the dominant phase of the star was the relatively quiet Be phase, during which the spectral lines showed only small variations compared to the spectacular variation episodes. The case of γ Cas, like that of many other Be stars observed over a long time span shows that the description of the Be phenomenon requires long-term monitoring from the beginning of the formation of the disk, to its complete dissipation, up to its regeneration, which is on time scales of the order of the Be - B - Be cycle.

The discovery of a companion to γ Cas by Harmanec et al. (2000) through regular radial velocity variations of the hydrogen and helium lines has introduced more questions about

γ Cas. Harmanec et al. (2000) found that the binary has a period of 203.59 days and an orbital eccentricity of 0.26. The presence of a companion was confirmed by Miroshnichenko et al. (2002), Nemravová et al. (2012), and Smith et al. (2012). The nature of the secondary is still unknown, but as observed in Be/X-ray binary systems, the companion is suspected to be a white dwarf or neutron star (Okazaki et al. 2002; Nemravová et al. 2012; Smith et al. 2012).

The high spatial-resolution study of the properties of γ Cas has recently become possible with long baseline interferometry. In fact, the first interferometric observations were conducted by Thom et al. (1986), and they were able to resolve the Hα emitting regions of γ Cas with the French I2T interferometer. Hα interferometric observations of seven Be stars including γ Cas were presented by Quirrenbach et al. (1997), and they showed consistent disk orientations with those from polarimetry measurements. Gies et al. (2007) presented the first long baseline interferometric observations of four bright Be stars including γ Cas obtained with the CHARA Array in the K-band, and a similar analysis conducted in the optical wavelengths using the NPOI interferometer was presented by Tycner et al. (2005) and Tycner et al. (2006).

In this chapter, we report interferometric observations of γ Cas obtained with the CHARA Array contemporaneously with spectrophotometric observations made with Mimir spectrograph at Lowell Observatory. A summary of the interferometric observations and the data analysis process is described in §5.2. In §5.3 and §5.4, we describe our approach of modeling the structure of the circumstellar disk and in characterizing its properties using geometrical and physical models, respectively, and compare our results with previously published data. In §5.5, we summarize our results and draw our conclusions.

5.2 Observations and data analysis

5.2.1 Classic Observations

Interferometric observations of γ Cas were taken during several nights in 2008 and in 2009 using the CHARA Classic beam combiner operating in the K-band of the infrared (1.94 - 2.36 μm) (ten Brummelaar et al. 2005). γ Cas was observed with both short and long baselines of CHARA ($\sim$ 54 - 310 meters) to probe both the large- and small-scale structures of the emitting regions of γ Cas. A typical observation consists of 200 scans in 1-5 minutes, depending on the stability of the fringes according to each night's seeing conditions. Each observation is usually followed by an identical sequence obtained on an unresolved calibrator star (usually HD 6210) in order to correct for the atmospheric and instrumental fluctuations.

We list in Table 5.1 the stellar properties of the calibrator stars used in this study. Column 1 gives the HD number of each calibrator. Columns 2 and 3 list their effective temperatures (T_{eff}), and gravities ($\log g$), respectively, and columns 4 and 5 list the spectral classification and the reddening $E(B - V)$ of the star, respectively. We compute the limb-darkened angular diameter θ_{LD} by direct comparison of the observed and model flux distributions of each calibrator (with a model based on their T_{eff} and $\log g$), and based on the limb-darkening coefficients given by Claret (2000), we transformed the limb-darkened diameter to an equivalent uniform disk angular diameter θ_{UD} assuming a baseline of 300 m. The diameter results for each calibrator are presented in columns 6 and 7 of Table 5.1.

The interferometric raw visibilities are estimated using ReduceIR (ten Brummelaar et al. 2005), which performs an integration of the fringe power spectrum and then averages the results over the total number of scans. The raw visibilities are then calibrated using a

transfer function of the instrument, which is measured using calibrator stars of known angular diameters. We present a detailed summary of the Classic observations in Table 5.2. In order to increase our data coverage, we made use of previous CHARA observations of γ Cas obtained in 2003 and 2005. These measurements, previously published by Gies et al. (2007), are presented in the first 56 lines of Table 5.2 and are included here for convenience of the reader. The first column of Table 5.2 gives the heliocentric Julian date of the observations, column 2 gives the telescope pair used for each observation, columns 3 and 4 show the u and v coordinates in cycles arcsec^{-1} for an effective wavelength of 2.133 μm, column 5 is the projected baseline in meters, column 6 gives the effective baseline prorated to an elliptical angular size at the position angle of each observation (see §5.4.2 below), column 7 gives the calibrated visibility measurements and column 8 gives the visibility errors. The uncertainties on the calibrated visibility are mainly due to the internal uncertainty from calculating the raw visibilities when fitting the fringe power spectrum (typically $\leq$ 5%), plus the uncertainty introduced by the calculation of the calibrators' angular diameters generated from their assumed stellar parameters.

Table 5.1: Calibrator Star Angular Diameters

Calibrator Name	T_{eff} (K)	$\log g$ (cm s^{-2})	Spectral Classification	$E(B-V)$ (mag)	θ_{LD} (mas)	θ_{UD} (mas)	Ref.
HD 5234	4380	2.63	K2 III	0.08 ± 0.06	1.97 ± 0.02	1.92 ± 0.02	1
HD 6210	6065	3.85	F6 V	0.01 ± 0.02	0.52 ± 0.02	0.52 ± 0.01	2
HD 9022	5000	2.0	K2-3 III	0.28 ± 0.06	1.08 ± 0.01	1.05 ± 0.01	3

References - 1. Soubiran et al. (2008); 2. Lambert & Reddy (2004); 3. from the spectral classification calibration of Gray (2005).

Table 5.2: Classic Calibrated Visibilities

Date (HJD-2,400,000)	Telescope Pair	u (cycles arcsec^{-1})	v (cycles arcsec^{-1})	Baseline (m)	Effective Baseline^a (m)	V	δV
52919.721	W1/S2	−142.884	543.823	247.371	206.269	0.445	0.016
52919.731	W1/S2	−170.359	535.178	247.089	202.565	0.448	0.016
52919.742	W1/S2	−198.990	524.275	246.706	198.654	0.490	0.017
52919.751	W1/S2	−223.714	513.167	246.285	195.250	0.516	0.017
52919.759	W1/S2	−243.759	502.902	245.868	192.483	0.608	0.019
52922.794	W1/S2	−340.384	433.001	242.308	179.351	0.496	0.016
52922.804	W1/S2	−359.146	413.995	241.118	176.901	0.522	0.016
52922.812	W1/S2	−372.997	398.271	240.060	175.125	0.595	0.015
52922.819	W1/S2	−384.172	384.308	239.063	173.714	0.593	0.017
52922.825	W1/S2	−393.513	371.581	238.108	172.551	0.592	0.024
52922.834	W1/S2	−407.069	350.990	236.466	170.886	0.624	0.018
52926.747	W1/S2	−259.229	494.138	245.491	190.349	0.458	0.019
52926.754	W1/S2	−277.221	482.935	244.981	187.875	0.381	0.014
52926.763	W1/S2	−297.965	468.523	244.276	185.040	0.424	0.018
52926.770	W1/S2	−312.348	457.474	243.700	183.093	0.509	0.016
52926.777	W1/S2	−326.448	445.691	243.049	181.200	0.533	0.018
52928.731	W1/S2	−233.941	508.078	246.082	193.838	0.281	0.026
52928.740	W1/S2	−256.338	495.835	245.566	190.748	0.266	0.023
52928.746	W1/S2	−269.851	487.662	245.200	188.887	0.313	0.016
52928.753	W1/S2	−287.813	475.789	244.638	186.424	0.287	0.010
52928.761	W1/S2	−305.131	463.134	243.999	184.068	0.298	0.011
52928.770	W1/S2	−323.150	448.538	243.210	181.641	0.303	0.009
53655.813	W1/W2	241.055	−45.314	107.908	85.221	0.826	0.019
53655.826	W1/W2	243.720	−27.729	107.915	87.240	0.790	0.018
53655.842	W1/W2	244.700	−6.905	107.697	89.546	0.791	0.021
53655.854	W1/W2	243.778	10.015	107.339	91.310	0.816	0.019
53655.866	W1/W2	241.416	26.317	106.838	92.882	0.807	0.019
53655.879	W1/W2	237.635	42.368	106.195	94.282	0.756	0.019
53655.891	W1/W2	232.126	58.985	105.367	95.545	0.781	0.017
53655.904	W1/W2	225.422	74.478	104.445	96.522	0.777	0.017
53655.916	W1/W2	217.360	89.474	103.411	97.253	0.779	0.018
53655.929	W1/W2	207.172	105.010	102.186	97.748	0.782	0.019
53655.942	W1/W2	195.986	119.232	100.925	97.922	0.735	0.018
53655.961	W1/W2	177.421	138.423	99.001	97.636	0.741	0.021
53656.652	W1/W2	95.120	−205.227	99.515	78.326	0.839	0.024
53656.664	W1/W2	112.564	−198.090	100.236	76.966	0.809	0.023
53656.678	W1/W2	130.492	−189.132	101.090	75.860	0.830	0.029
53656.691	W1/W2	147.009	−179.204	101.973	75.176	0.792	0.027
53656.707	W1/W2	166.462	−165.020	103.121	74.897	0.829	0.032
53656.720	W1/W2	180.971	−152.242	104.043	75.156	0.833	0.024
53656.734	W1/W2	193.930	−138.745	104.905	75.814	0.859	0.021

Continued on Next Page…

Table 5.2 – Continued

Date (HJD-2,400,000)	Telescope Pair	u (cycles arcsec^{-1})	v (cycles arcsec^{-1})	Baseline (m)	Effective Baseline^a (m)	V	δV
53656.747	W1/W2	205.570	−124.362	105.701	76.839	0.839	0.021
53656.762	W1/W2	217.551	−106.299	106.524	78.461	0.878	0.022
53656.775	W1/W2	226.169	−90.066	107.101	80.135	0.840	0.020
53656.788	W1/W2	232.797	−74.352	107.514	81.875	0.884	0.025
53658.701	W1/W2	166.215	−165.220	103.105	74.896	0.875	0.021
53658.714	W1/W2	179.783	−153.373	103.965	75.117	0.830	0.020
53658.727	W1/W2	193.238	−139.525	104.858	75.767	0.851	0.018
53658.741	W1/W2	205.127	−124.958	105.670	76.791	0.878	0.019
53658.814	W1/W2	243.075	−33.188	107.931	86.618	0.779	0.021
53658.827	W1/W2	244.559	−16.005	107.822	88.553	0.742	0.021
53658.840	W1/W2	244.424	1.709	107.535	90.458	0.740	0.023
53658.855	W1/W2	242.301	21.287	107.009	92.412	0.704	0.024
53658.876	W1/W2	235.609	49.085	105.880	94.817	0.684	0.022
53658.891	W1/W2	227.816	69.350	104.767	96.222	0.740	0.022
53658.906	W1/W2	218.942	86.758	103.609	97.138	0.754	0.025
54754.703	S1/W1	139.084	−607.765	274.306	231.158	0.303	0.019
54754.711	S1/W1	165.175	−600.436	273.983	227.589	0.324	0.021
54754.722	S1/W1	194.453	−590.507	273.525	223.502	0.350	0.022
54754.730	S1/W1	219.570	−580.451	273.038	219.937	0.360	0.022
54754.746	S1/W1	259.566	−561.204	272.040	214.171	0.394	0.022
54754.754	S1/W1	280.443	−549.397	271.385	211.130	0.408	0.023
54758.765	S1/E1	−354.366	−576.322	297.658	296.711	0.135	0.013
54758.773	S1/E1	−335.716	−592.279	299.530	297.903	0.145	0.011
54758.781	S1/E1	−314.532	−608.507	301.370	298.796	0.124	0.011
54758.789	S1/E1	−294.521	−622.229	302.876	299.257	0.132	0.010
54758.804	S1/E1	−255.926	−644.924	305.268	299.276	0.147	0.011
54758.968	S1/E1	235.831	−655.016	306.292	248.023	0.186	0.015
54758.976	S1/E1	256.817	−644.451	305.219	244.459	0.181	0.011
54760.816	S1/E1	−210.001	−666.447	307.424	298.080	0.163	0.010
54760.828	S1/E1	−177.144	−678.694	308.604	296.556	0.151	0.008
54760.840	S1/E1	−137.760	−690.286	309.689	294.109	0.161	0.010
54766.656	E1/E2	127.804	−7.489	56.326	48.422	0.969	0.058
54766.668	E1/E2	130.796	1.022	57.547	49.382	0.882	0.062
54766.672	E1/E2	131.950	5.101	58.097	50.392	0.840	0.062
54766.680	E1/E2	132.995	9.479	58.661	53.292	0.877	0.061
54766.699	E1/E2	134.968	22.648	60.211	54.232	0.848	0.050
54766.703	E1/E2	135.250	27.140	60.691	55.091	0.850	0.054
55116.718	S1/E1	−459.951	−432.035	277.633	276.146	0.219	0.036
55116.726	S1/E1	−453.050	−446.835	279.962	278.908	0.103	0.032
55153.031	E1/W1	−372.570	592.870	308.070	233.694	0.393	0.027
55153.039	E1/W1	−393.023	580.994	308.609	232.103	0.364	0.027
55154.023	E1/W1	−354.456	602.648	307.604	235.204	0.314	0.018

^{a} We have used a disk axial ratio $r = 0.722$ and a disk position angle $PA = 38.2$ degrees to compute the effective baseline.

5.2.2 FLUOR Observations

We also observed γ Cas in 2006 with the Fiber Linked Unit for Optical Recombination (FLUOR) beam combiner at CHARA (Coudé du Foresto et al. 2003; Mérand et al. 2006) in the K-band with an effective wavelength of $\lambda = 2.2$ μm, using intermediate and long baselines. We reduced the data useing the FLUOR Data Reduction Software as described in Coudé du Foresto et al. (1998) to extract the raw visibility squared of the fringes. For more details about the FLUOR data analysis, see Coudé du Foresto et al. (2003), Kervella et al. (2004), and Mérand et al. (2006). The FLUOR calibrated visibilities are then determined by performing a linear interpolation in time between the γ Cas and the calibrator's raw visibilities. We used the stars HD 5234 and HD 9022 as calibrator stars for the FLUOR observations (see Table 5.1). A detailed summary of FLUOR observations is presented in Table 5.3. The resulting (u, v) plane of the total observations using both Classic and FLUOR is presented in Figure 5.1. The FLUOR data reduction pipeline produces the squared visibilities and their corresponding errors from the observations. For comparison with CHARA Classic data, we estimate the visibility measurements as being the square root of the squared visibilities $V = \sqrt{V^2}$, and the errors as $\delta V = \frac{\delta V^2}{2V}$.

Table 5.3: FLUOR Calibrated Visibilities

Date (HJD-2,400,000)	Telescope Pair	u (cycles arcsec^{-1})	v (cycles arcsec^{-1})	Baseline (m)	Effective Baseline^a (m)	V^2	δV^2
54053.782	W1/W2	240.276	31.863	106.633	93.384	0.763	0.040
54054.784	W1/W2	238.606	38.787	106.351	93.984	0.660	0.010
54054.808	W1/W2	227.942	69.067	104.784	96.205	0.630	0.010
54054.841	W1/W2	204.632	108.470	101.892	97.816	0.624	0.010
54054.863	W1/W2	184.079	132.055	99.668	97.806	0.654	0.009
54055.647	W1/W2	−198.694	133.160	105.229	76.178	0.725	0.012
54055.902	W1/W2	135.992	168.869	95.388	95.385	0.635	0.009
54055.925	W1/W2	104.788	184.303	93.272	92.774	0.644	0.013
54056.883	W1/W2	155.851	155.976	97.005	96.681	0.654	0.022
54056.917	W1/W2	111.970	181.209	93.713	93.426	0.631	0.018
54056.939	W1/W2	80.7990	192.891	92.005	90.424	0.656	0.015
54057.636	S2/E2	303.657	452.588	239.776	239.447	0.072	0.005
54057.682	S2/E2	223.654	519.493	248.828	244.855	0.055	0.004
54057.751	S2/E2	72.606	575.947	255.389	238.608	0.056	0.004
54057.828	S2/E2	−494.662	154.989	228.055	173.931	0.255	0.014

^{a} We have used a disk axial ratio $r = 0.722$ and a disk position angle $PA = 38.2$ degrees to compute the effective baseline.
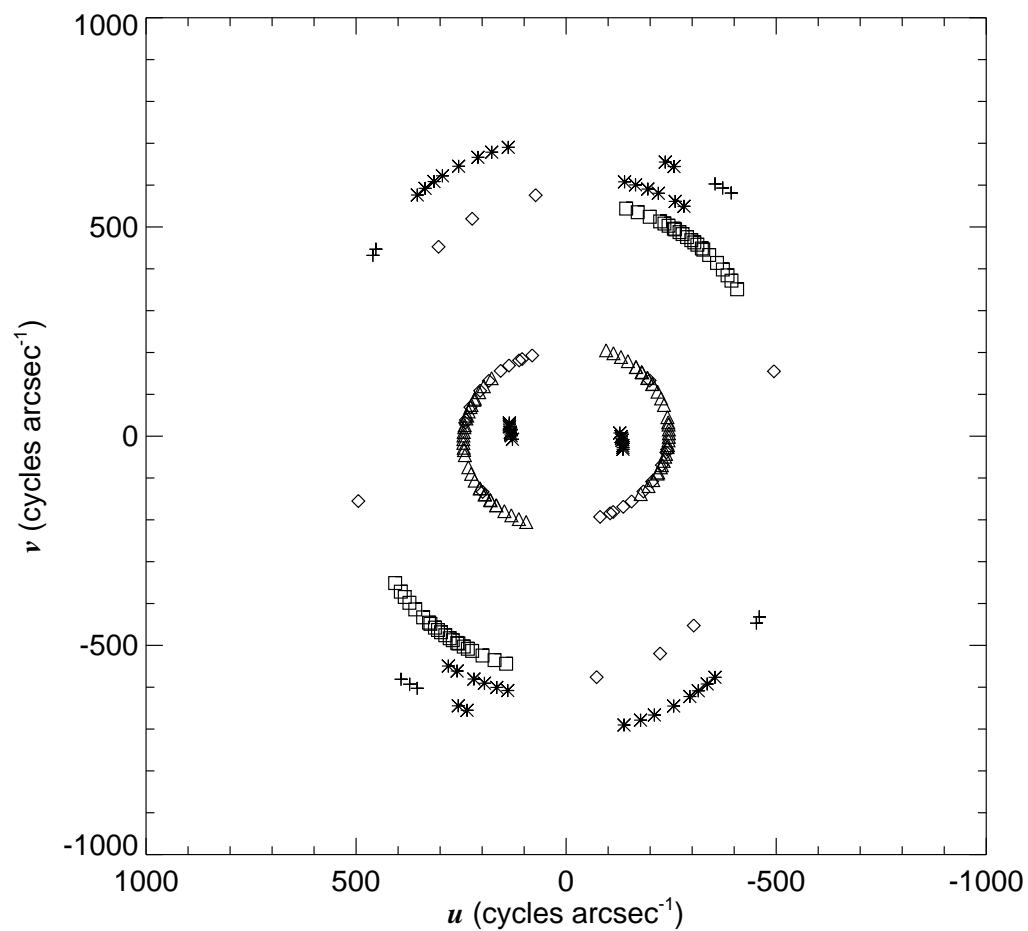
Figure 5.1: (u, v) plane coverage of our interferometric observations. Plus signs are the 2009 Classic data, the stars represent the 2008 Classic data, diamonds are the 2006 FLUOR data, and triangles and squares are the 2005 and the 2003 Classic data taken from Gies et al. (2007). The scales are in units of $\frac{B}{\lambda}$ expressed as cycles arcsec^{-1}.

5.3 Gaussian Elliptical Model Fits

5.3.1 Method

In order to interpret the our interferometric data, we presented different disk models in detail in Chapter 2. Here we summarize the ones relevant to this study. We remind the reader about the concept of effective baseline (§2.2.1) which accounts for the projection effects of the disk on the sky due to its inclination as

$$B_{\text{eff}} = B_{\text{p}} \sqrt{\cos^2 \theta + \cos^2 i \ \sin^2 \theta} \tag{5.1}$$

where $\theta = \phi_{\text{obs}} - PA$ is the angle between the disk's major axis and the observed vector $\vec{u}(u, v)$, and i is the disk inclination angle. The observed visibilities are modeled with a two-component model consisting of a point source representing the unresolved central star and an elliptical Gaussian component representing the circumstellar disk,

$$V_{\text{tot}} = c_p V_s + (1 - c_p) V_d, \tag{5.2}$$

where V_{tot}, V_s, and V_d are the total, stellar, and disk visibility, respectively, and c_p is the ratio of the photospheric flux contribution to the total flux of the system. Because the central star is unresolved even at the longest baseline of the interferometer, its visibility will always be close to unity, $V_s \simeq 1$, so the fitting procedure is in fact not very sensitive to the assumed diameter of the central star. The circumstellar disk model visibility V_d is represented by a Gaussian distribution

$$V_d = \exp \left[-\frac{(\pi \theta s)^2}{4 \ln 2} \right], \tag{5.3}$$

where θ is the full width at half-maximum (FWHM) of the Gaussian distribution and s is given by:

$$s = \sqrt{r^2(u\cos(PA) - v\sin(PA))^2 + (u\sin(PA) + v\cos(PA))^2}, \qquad (5.4)$$

where r is the axial ratio and PA is the position angle of the disk major axis. The model has four free parameters which are the photospheric contribution c_p, the axial ratio r, the position angle of the major axis PA, and the disk angular size θ. Table 5.4 lists the stellar and orbital parameters we have adopted for γ Cas (from Gies et al. 2007).

Table 5.4: Adopted Stellar and Orbital Parameters

Parameter	Value	Uncertainty
Spectral Classification	B0.5 Ve	. . .
π (mas)	5.32	0.56
R_1 $(R_\odot)$	10.0	2.0
M_1 $(M_\odot)$	15.5	3.1
$T_{1\ \mathrm{eff}}$ (K)	28840	1000
$V \sin i$ (km s^{-1})	295	24
R_2 $(R_\odot)^a$	1.0	. . .
M_2 $(M_\odot)^a$	1.0	. . .
$T_{2\ \mathrm{eff}}$ (K)^a	30000	. . .
P (d)	203.59	. . .
T_S (HJD–2,400,000) . .	50654.3	. . .
$a_1 \sin i$ $(R_\odot)$	15.279	. . .
R_d $(R_\odot)$	214.2	. . .

References - [a]Example Parameters for an assumed hot subdwarf companion(Gies et al. 1998).

5.3.2 The Angular Size of the γ Cas Disk

We used the Gaussian elliptical disk model to fit the interferometric data and to determine the angular size of the disk of γ Cas. In order to increase our visibility coverage and better constrain the model fit, we have combined the entire Classic and FLUOR data sets with 2003 and 2005 measurements taken from Gies et al. (2007).

The Gaussian elliptical disk model has four independent parameters, and the fitting procedure consisted of solving for the model parameters using the IDL non-linear least squares curve fitting routine MPFIT (Markwardt 2009), which provides a robust way to perform least-squares curves and multiple-parameter surface fitting. Model parameters can be fixed or free depending on how well the distribution of the $(u,\ v)$ coverage of each star is constrained. Also, simple boundary constraints can be imposed on parameters that are well defined from previous studies, especially for the cases of Be systems where the fitting fails because of a lack of data.

We assumed that the visibility of the stellar photosphere is well represented with a uniform disk model, and we adopted an angular diameter of $\theta_s = 0.446$ mas for the central star, which we derived from fitting the spectral energy distribution of the star (see §6.4). We were able to find a good fit by applying the Gaussian elliptical disk model to the interferometric data of γ Cas. The best-fit Gaussian elliptical disk model obtained from the data has a disk axial ratio $r = 0.722 \pm 0.038$, a position angle $PA = 38° \pm 5°$, a photospheric contribution fraction $c_p = 0.082 \pm 0.036$, and an angular size of the disk's major axis $\theta_{\mathrm{maj}} = 1.236 \pm 0.063$ mas, with a reduced χ^2_ν that equals 15.63. Figure 5.2 shows the visibility curve of the best-fit
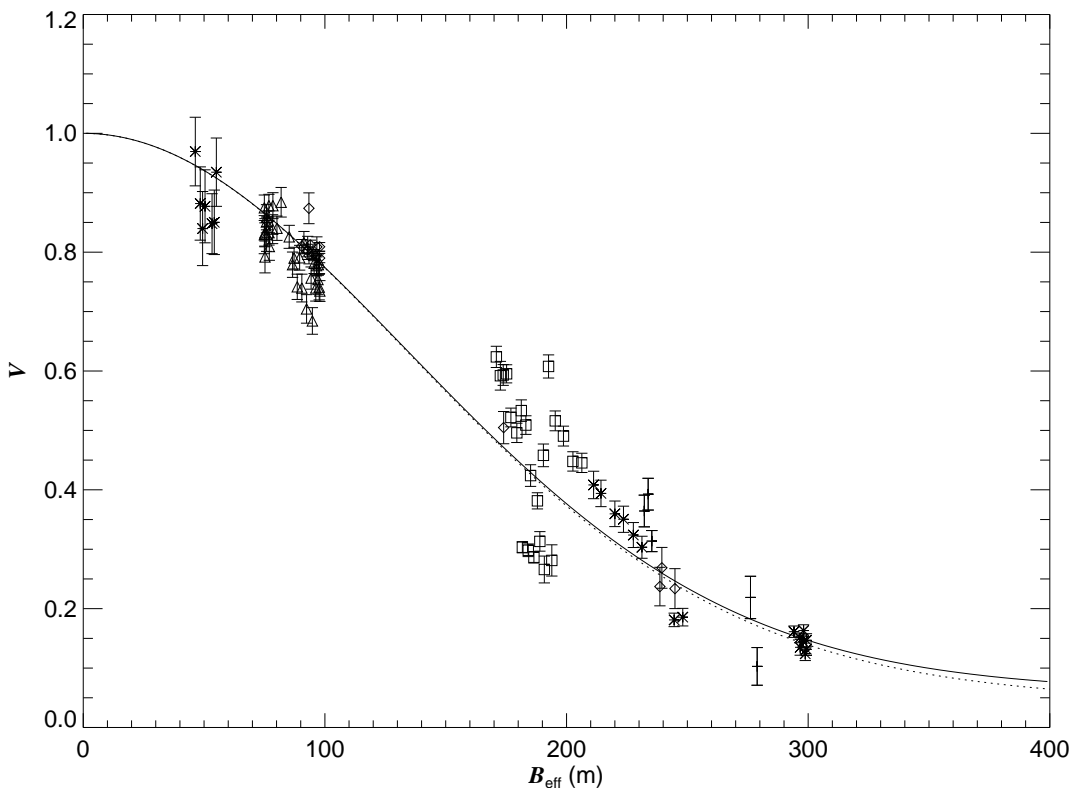
Figure 5.2: The visibility curve of γ Cas. The solid line represents the Gaussian elliptical model projected along the major axis while the dotted line represent the Gaussian elliptical model projected along the minor axis. Plus signs are the 2009 Classic data, the stars represent the 2008 Classic data, diamonds are the 2006 FLUOR data, and triangles and squares are the 2005 and the 2003 Classic data taken from Gies et al. (2007).

Gaussian model along with the interferometric data plotted with different symbols per year of observations.

Although the Gaussian elliptical model successfully constrains the disk axial ratio and the position angle of the disk major axis, we found that a family of solutions of the stellar photospheric contribution and the disk sizes (c_p, θ_{maj}) may exist and fit the interferometric data of γ Cas reasonably well. So, in order to investigate the uniqueness of our best-fit model, we tabulated solutions of the Gaussian elliptical disk model for a wide range of values of the photospheric distribution c_p, and we show our results in Figure 5.3. The

upper left panel in Figure 5.3 shows how the reduced χ^2_ν changes according to the different values of the photospheric contribution c_p for the entire data set (solid line), for the 2003 and 2005 data (dotted line), and for the 2006, 2008, and 2009 data (dashed line). These calculations show that the best fit for the three curves occurs at lower values of c_p, which is consistent with our best-fit solution presented above. The upper right panel of Figure 5.3 shows the relationship between the disk axial ratio r and the photospheric contribution c_p, while the bottom left panel shows the relationship between the disk position angle PA and the photospheric contribution c_p, and the bottom right panel of Figure 5.3 shows the relationship between the angular size of the disk major axis θ_{maj} and the photospheric contribution c_p. These plots show that although a degeneracy seems to exist between the parameter solutions of the Gaussian elliptical models, one best-fit solution is usually discerned depending on the (u, v) plane distribution of the observations. Independent constraints on the value of c_p may be necessary in cases where the distribution of the observations in the (u, v) plane is poorly determined. In fact, an accurate estimate of the IR flux excess at the time of the observations helps constrain c_p with confidence since these two quantities are related by $E^\star(V - K) = -2.5 \log c_p$.
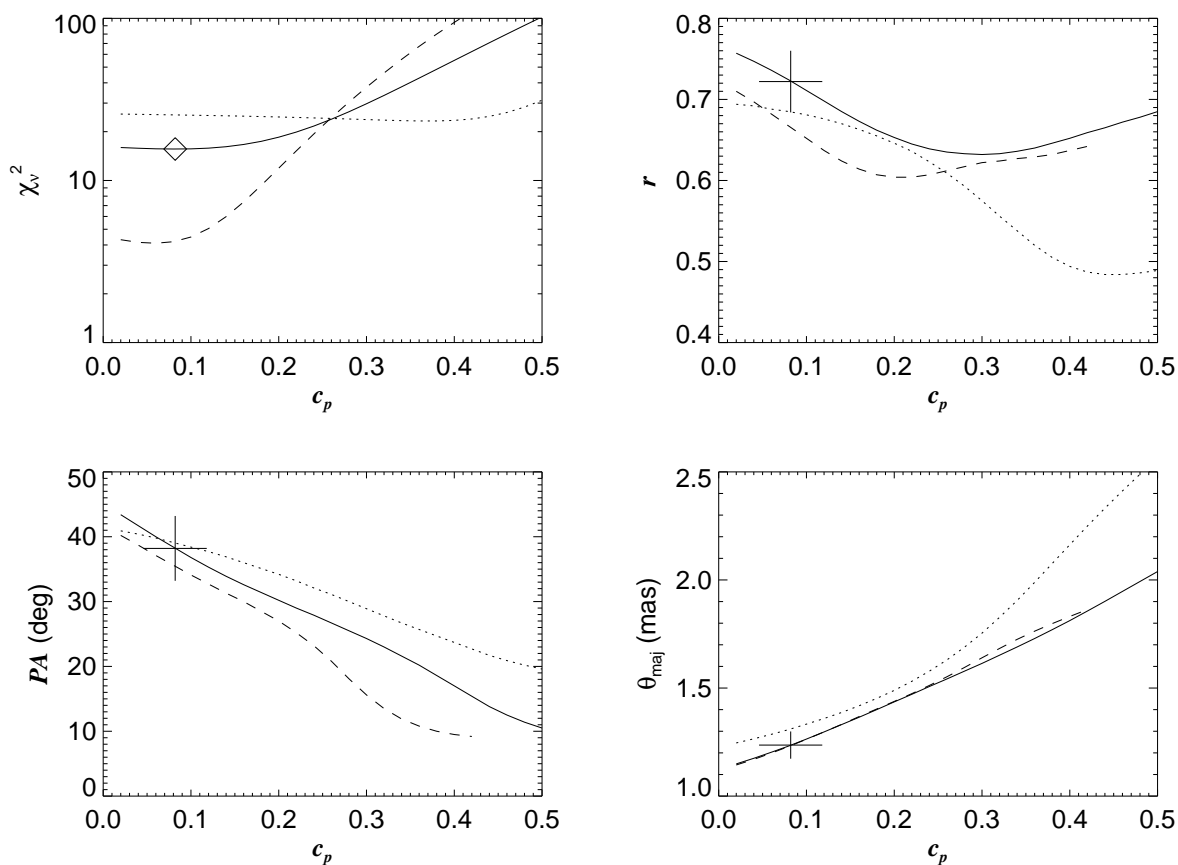
Figure 5.3: Family of solutions of the Gaussian elliptical disk model of γ Cas. Solid lines represent the solution for the entire set of data, dotted lines represent solution for the 2003 and 2005 data, and the dashed lines represent solutions for the 2006, 2008, and 2009 data. The diamond in the upper left panel shows the location of the χ^2_ν minimum for the full sample, while the plus sign shows the parameter value and error range for the best fit in the other three panels.

The valley of solutions of the Gaussian elliptical model also explains the different results listed by Gies et al. (2007) in analyzing γ Cas's 2003 and 2005 CHARA-Classic data. Gies et al. (2007) found that the best-fit value of photospheric contribution of γ Cas was $c_p \approx 0.4$ and their best-fit angular diameter of the major axis of the disk was $\theta_{\mathrm{maj}} = 1.95$ mas. We find that this solution is one of the many possible solutions shown in Figure 5.3, which barely shows an absolute minimum in the values of the χ^2_ν (see dotted line in the upper left panel of Figure 5.3). Gies et al. (2007) were not able to discern the best-fit solution because of the limited (u, v) coverage of their interferometric data, and because of the lack of visibility measurements at long baselines (300 m and above). We will show later in this chapter (§5.4) that the radiative-transfer thick disk model gives a more realistic description of the interferometric data for the disk of γ Cas.

5.3.3 Time Variability of the Disk of γ Cas

Because our interferometric data cover a long time span, we aimed to investigate the time variation of the circumstellar disk of γ Cas during the period between 2003 - 2009. We fitted each data set per year of observation separately by fixing the values of the disk axial ratio to $r = 0.722$, and the disk position angle to $PA = 38°$, and for each year we determined the best-fitting photospheric contribution c_p and angular disk size θ_{maj}. Table 5.5 lists these parameters along with the corresponding χ^2_ν, and Figure 5.4 shows plots of these best-fit models per year of observation. From the upper left panel to the lower right panels of Figure 5.4, we show the best-fit Gaussian disk model for the 2003, 2005, 2006, 2008, and 2009 data, respectively.

Table 5.5: Gaussian Fits of the Visibility Measurements

by Year

Obs. year	r	PA (deg)	c_p	θ_{maj} (mas)	χ^2_ν	$c_p(\mathrm{corr})$	R_d/R_s
All .	0.722 ± 0.038	$38.2° \pm 05.0°$	0.082 ± 0.036	1.236 ± 0.063	15.63	0.190 ± 0.032	2.946 ± 0.134
2003	0.7222	38.2°	0.262 ± 0.473	1.497 ± 0.961	67.38	0.322 ± 0.435	3.502 ± 2.018
2005	0.7222	38.2°	0.010 ± 0.000	1.277 ± 0.020	2.48	0.119 ± 0.006	3.032 ± 0.073
2006	0.7222	38.2°	0.028 ± 0.083	1.167 ± 0.058	1.97	0.155 ± 0.072	2.802 ± 0.120
2008	0.7222	38.2°	0.061 ± 0.034	1.201 ± 0.064	4.89	0.177 ± 0.030	2.872 ± 0.133
2009	0.7222	38.2°	0.010 ± 0.033	1.058 ± 0.073	18.21	0.165 ± 0.020	2.575 ± 0.150

We find that there was no significant change in the angular size of the disk of γ Cas between 2003 and 2009, although the errors in the 2003 data are quite large (see Fig. 5.5). The fact that the angular sizes of the major axis derived from the 2005, 2006, 2008, and 2009 data are all consistent with each other within 2 - 3 standard deviations suggests that the optically thick region of the inner disk of γ Cas has remained in a steady state between at least the period from 2005 to 2009. Furthermore, V-band photometric observations from the same time span show only low-amplitude variability, which indirectly supports our results, because the V-band excess may also form in the inner part of the disk. Figure 5.6 shows the V-band magnitudes (middle panel) and Hα equivalent width (bottom panel) of γ Cas taken between 1998 and 2010 (Smith et al. 2012). These measurements confirm the fact that the V magnitude displayed only a small variation during the time frame of our interferometric observations.

Interestingly, the Hα emission seems to have grown by about 20% as displayed by the lower panel of Figure 5.6 while the V-magnitude of the Be system remained stable during the period between 2003 and 2009 ($\triangle V < 0.02$ mag). We suspect that such differences can arise because of differences in the disk opacity between the V-band continuum and the Hα emission line. In fact, Hα is much more optically thick than the V-band or the K-band continuum (see e.g., Carciofi & Bjorkman 2008), and therefore, the optically thin-thick boundary, which occurs at an optical depth τ equal to unity, lies progressively farther from the star for the V-band, the K-band, and Hα. Consequently, changes in density in the outer disk may cause variations in Hα strength that are independent of the inner disk state sampled by the continuum flux of the disk.
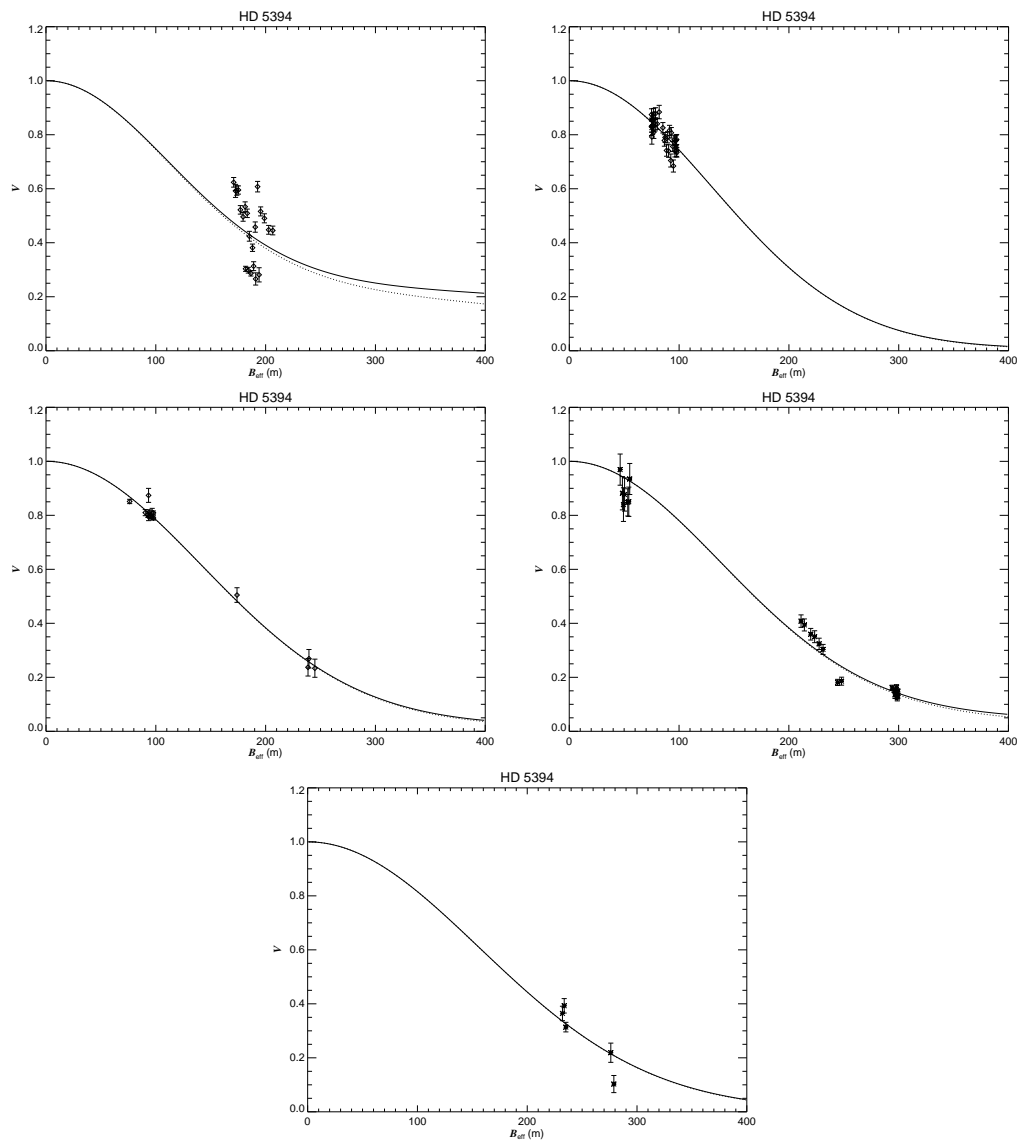
Figure 5.4: The visibility curve of γ Cas for each year of observation. From the upper left to the lower right, the panels show the Gaussian best-fit model for the 2003, 2005, 2006, 2008, and 2009 data, respectively. The solid line represents the Gaussian model along the major axis. The star signs represent the interferometric data.
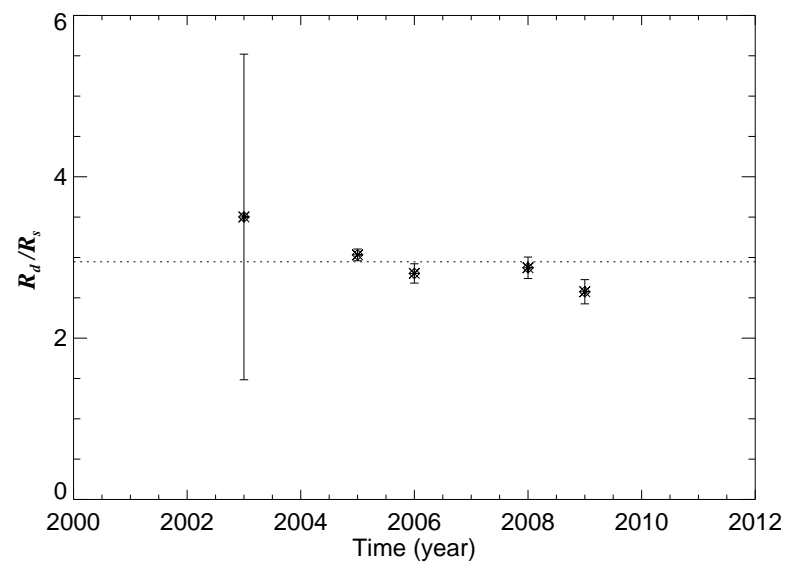
Figure 5.5: The circumstellar disk size of γ Cas from K-band interferometric observations taken between 2003 and 2009. The dotted line represents the best-fit disk size derived from fitting the entire set of data.
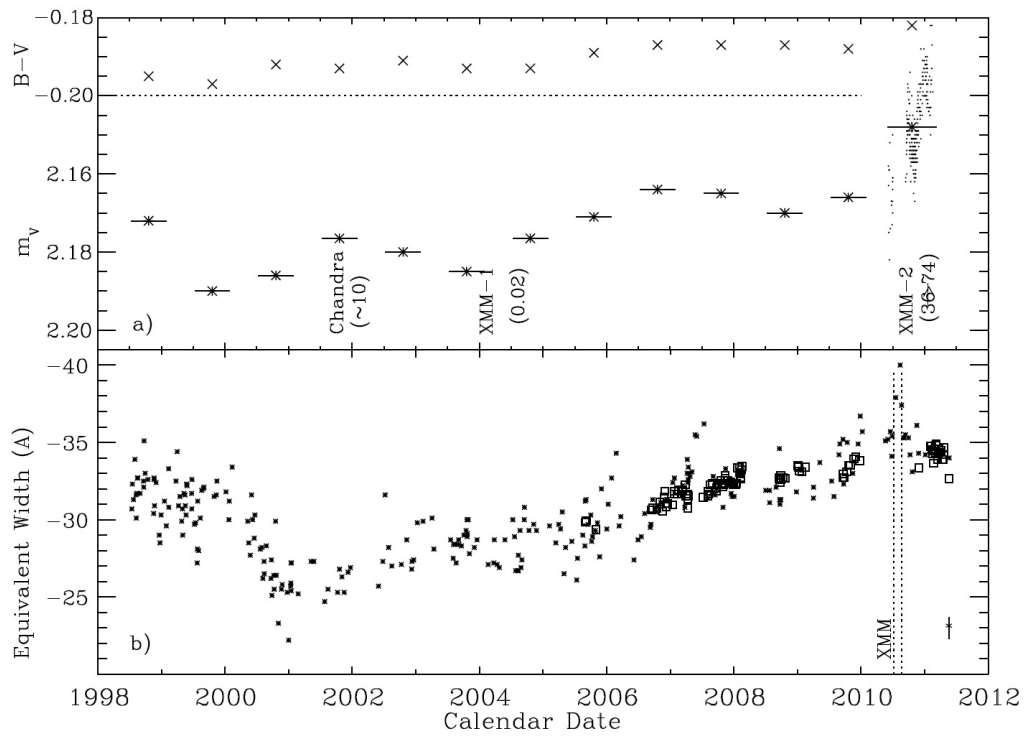
Figure 5.6: Upper panel: V magnitudes and $(B - V)$ color of γ Cas over the 1998-2010 seasons. Error bars on these magnitudes are much smaller than the symbols, as each point represents a few hundred individual observations. Bottom Panel: The Hα emission equivalent widths in Angstroms. Reproduced with permission from Smith et al. (2012).

5.3.4 Comparison with Previous Studies

Optical interferometric observations of γ Cas were obtained with the Mk III optical interferometer using the continuum and the Hα line filters by Quirrenbach et al. (1997), and with the Navy Optical Interferometer (NOI) in Hα by Tycner et al. (2005) and Tycner et al. (2006). The Hα interferometric data presented in Quirrenbach et al. (1997) were fitted with a simple Gaussian elliptical model assuming a stellar angular diameter of 0.56 mas. The authors find an angular diameter of γ Cas disk major axis of $\theta = 3.47 \pm 0.02$ mas, a disk position angle of $PA = 19° \pm 2°$, an axial ratio of $r = 0.70 \pm 0.02$, and a photospheric contribution of $c_p = 0.23$. Hα interferometric observations of γ Cas conducted by Tycner et al. (2006) show that a Gaussian intensity distribution is more consistent with the observations than any other geometrical structures of the circumstellar disk. Tycner et al. (2006) report an Hα disk angular diameter along the major axis of 3.59 ± 0.04 mas, a position angle of the disk major axis of $PA = 31° \pm 1°$, an axial ratio of $r = 0.58 \pm 0.03$, and a photospheric contribution of $c_p = 0.51 \pm 0.01$, and this assuming the same value of 0.56 mas for the angular diameter of the central star as in Quirrenbach et al. (1997).

Smith et al. (2012) conducted a multiwavelength campaign study of γ Cas in 2010 including X-ray observations using XMM-Newton, H-band continuum observations using CHARA-MIRC, and R-band continuum observations using CHARA-VEGA. Smith et al. (2012) resolved a flattened circumstellar disk, and used Gaussian elliptical models to fit the MIRC data. They find that the γ Cas disk size along the major axis is 0.82 mas in the H-band data, and 0.76 mas in the R-band. The authors report inclination angle values of the disk that range between 41° and 44°. We have listed in Table 5.6 the best fitting parameters of

the Gaussian elliptical disk model of γ Cas derived from these studies for comparison with our results.

Table 5.6: Gaussian Elliptical Fits of the Interferometric Visibilities

Study	Flux Source	r	PA (deg)	c_p	θ_{maj} (mas)
Quirrenbach et al. (1997)	Hα	0.70±0.02	19±2	0.23	3.47±0.02
Tycner et al. (2006)	Hα	0.56±0.03	31±2	0.51±0.02	3.64±0.05
Gies et al. (2007)	K-band	0.59±0.04	25±4	0.39±0.02	1.95±0.07
Smith et al. (2012)........	H-band	0.75±0.01	17±4	0.35±0.01	0.82±0.02
Smith et al. (2012)........	R-band	0.74±0.05	19±5	0.55±0.02	0.76±0.04
This study	K-band	0.72±0.04	38±5	0.082 ± 0.036	1.24±0.06

Comparing the Hα results from Quirrenbach et al. (1997) and Tycner et al. (2006) with our K-band interferometric observations, we find that the geometry of the circumstellar disk of γ Cas derived from our analysis is similar with their results. However, our best-fit value for the position angle of the disk major axis, $PA = 38°$, is close to the estimate derived from NOI observations (Tycner et al. 2006), but differs by about 2σ from the lower value of major axis position angle of $PA = 19°$ reported in Quirrenbach et al. (1997), and $PA = 17°$ given by Smith et al. (2012). The major difference between the Hα and the K-band results is the value of the angular diameter of the disk of γ Cas. The CHARA-MIRC data analysis presented by Smith et al. (2012) seems to suggest the presence of a diffuse flux source. The authors claim that the data is much better fitted with a disk model that accounts for a diffuse light component. It is possible that the flux of the companion (§5.4.5.1) might alter the visibility in a way that is also consistent with a diffuse source. However, our K-band results do not show the systematic visibility decline relative to the model at short baselines that Smith et al. found in their H-band interferometric data.

The Hα disk angular diameter is found to be about twice the disk angular diameter measured in the K-band. This characteristic of the circumstellar disk is not exclusive to γ Cas, but it is also seen in many Be stars that we have surveyed with the CHARA Array interferometer. A possible explanation of this disk size characteristic is the difference in opacity between free-free and bound-free process and Hα. We further explore this hypothesis with additional results from our K-band survey presented in §6.5.2.

5.4 Thick Disk Models of γ Cas

5.4.1 Thick Disk Models

For a physical interpretation of our interferometric data, we have adopted the thick disk

model from Hummel & Vrancken (2000) that assumes a flattened axisymmetric geometry

for the circumstellar disk around the central star. We use a power law distribution to describe

the gas density radial variation, and an exponential profile to describe the decrease of the

gas density along the vertical axis in the disk. The expansion and dissipation of the disk

gas should also be taken into consideration. We therefore allow the inner radius of the

circumstellar disk of γ Cas to be detached from the stellar photosphere in order to produce

a ring-like density structure around the central star. The total gas density distribution

function $\rho(R, Z)$ is thus given by

$$\rho(R, Z) = 0, \text{ where } R < R_{\text{in}},$$

$$\rho(R, Z) = \rho_0 (R/R_s)^{-n} \exp\left[-\frac{1}{2}(\frac{Z}{H(R)})^2\right], \text{ where } R \geq R_{\text{in}},$$

where R_{in} is the thick disk inner radius, and R and Z are the radial and the vertical cylindrical

coordinates, respectively. R_s is the stellar radius, ρ_0 is the gas base density at the stellar

photosphere if the disk extended to the stellar equator, and n is the disk radial density

exponent. $H(R)$ is the disk vertical scale height defined by $H(R) = \frac{c_s}{V_K} R^{3/2}$, where c_s is the

sound speed and V_K is the Keplerian velocity at the equator of γ Cas.

This physical model generates a grid of radial and azimuthal intensities by solving the

radiative transfer equation of the emission produced by the bound-free and free-free ab-

sorption processes as explained by Gies et al. (2007) and Touhami et al. (2011). Based on

non-LTE simulations of the disk (Carciofi et al. 2006), the source function of the disk is

assumed to be a Planck function characterized by an isothermal temperature profile that equals $T_d = 0.6 \, T_{\text{eff}}$. The model has five geometrical input parameters, which are the stellar radius R_s, the thick disk inner and outer radius R_{in}, R_d, the inclination i, and position angle of the disk's major axis (PA). There are two additional physical parameters that describe the density profile, which are the gas base density ρ_0 and the density radial exponent n. The model computes the disk flux distribution by solving the transfer equation along a series of rays through the disk and then generates synthetic infrared images of the Be star surrounded by a circumstellar disk. The model visibility is then computed as being the Fourier transform of the intensity distribution of image, and the results are compared to the observational data.

5.4.2 The Density Profile of γ Cas

In order to determine the disk gas density distribution of γ Cas disk, we used the radiative-transfer disk model described above. We fitted the (2008 - 2009) CHARA-Classic data with a full thick disk model and were able to produce a reasonably good fit to the observations. The thick disk model has four free parameters (i, PA, ρ_0, n), and the fits were performed by solving for one parameter at a time, and by fixing the other three. The errors on the best-fit parameters are estimated by performing a grid search of all possible values of one parameter at a time, and by fixing the rest of the model input parameters. For each parameter grid, we computed the corresponding χ_ν^2 and interpolated the obtained estimates of χ_ν^2(s) in order to determine the minimum χ_ν^2 and the error on each model parameter.

Using the thick disk model, we were able to find a best-fit solution to our CHARA-Classic data. The best-fit thick disk disk model gives an inclination angle the disk of $54° \pm 4°$, and

a disk position angle $33° \pm 5°$, a disk base density $\rho_0 = 7.90 \pm 0.60 \times 10^{-11}$ g cm^{-3}, and a density exponent $n = 2.7 \pm 0.1$, along with a reduced $\chi^2_\nu = 6.3$. This disk model produces an IR flux excess equal to $E^\star(V - K)_{\mathrm{model}} = 1.65 \pm 0.13$ mag. These results are close to results reported in Gies et al. (2007) using CHARA-Classic data obtained in 2003 and 2005. Gies et al. (2007) report a disk base density of $\rho_0 = 7.2 \pm 0.2 \times 10^{-11}$ g cm^{-3} and a density exponent of $n = 2.7 \pm 0.3$. These fitting parameters produce an IR flux excess of $E^\star(V - K)_{\mathrm{model}} = 1.60 \pm 0.14$ mag.

Because we suspect that the disk of γ Cas has remained in a stable state during the period between 2003 and 2009, we have combined the entire set of our interferometric data, including FLUOR data, and produced a thick disk model fit. The best fitting parameters of this disk model are a disk inclination of $i = 48° \pm 4°$, a disk position angle along the major axis of $PA = 34° \pm 5°$, a disk base density of $\rho_0 = 7.21 \pm 0.33 \times 10^{-11}$ g cm^{-3}, and a disk density exponent of $n = 2.71 \pm 0.18$, with a $\chi^2_\nu = 20$. These best-fit parameters produce a circumstellar disk of γ Cas that generates an IR flux excess of $E^\star(V - K)_{\mathrm{model}} = 1.63 \pm 0.12$ mag. The uncertainties in the base density were calculated by varying the density exponent within the minimum and maximum errors, while the uncertainties in the density exponent were calculated from the residual scatter around the best fit solution. We find that both the thick disk model and the Gaussian elliptical disk model find similar estimates of the disk geometry and the disk size as shown in Figure 5.7, but that the thick disk model provides additional constraints on the density structure of the disk that could not be derived from a simple geometrical model.

We have derived the IR flux excess of γ Cas from fitting its SED according to the spectrophotometric measurements taken at the time of the interferometric observations (see
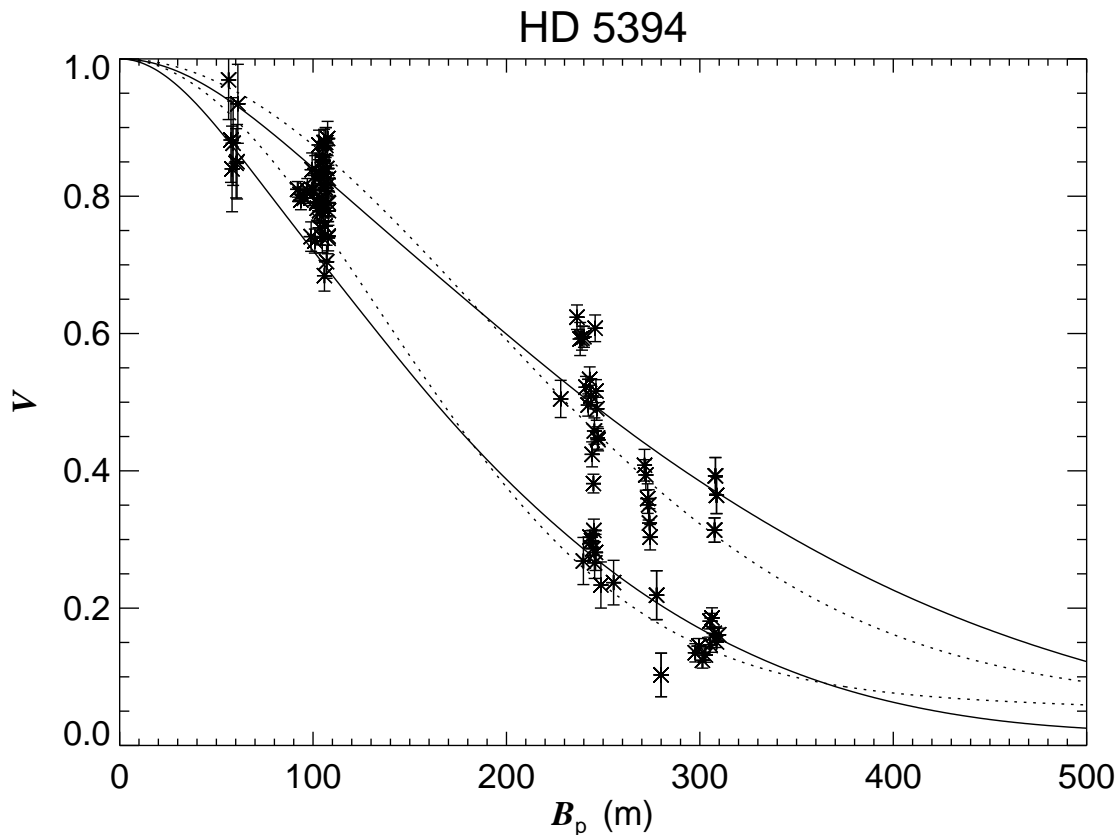
Figure 5.7: γ Cas visibility versus projected baseline. The solid lines represent the thick disk model visibility projected over the minor (upper solid line) and major (bottom solid line) axes, respectively. The dotted lines represent the Gaussian elliptical disk model visibility projected over the minor (upper dotted line) and major axes (bottom dotted line), respectively.

§3.3). We found that the actual IR flux excess of γ Cas is $E^\star(V-K)_{obs} = 0.66 \pm 0.31$ mag. This IR flux excess estimate was obtained by normalizing the stellar photospheric flux to the optical fluxes, assuming that compared to the stellar flux, the circumstellar disk flux was negligible in the optical. However, there are two lines of evidence that weaken this assumption and show that the circumstellar disk flux contribution could actually be important in the optical.

The first evidence is the diskless state of γ Cas, which shows that the central star has a V magnitude of 2.8 mag when the disk is absent (Howarth 1979; Underhill & Doazan

1982). On the other hand, we determined the IR flux excess from our spectrophotometric observations by normalization using an SED fit set to the optical flux during the current brighter state of the star, at a V magnitude of 2.17 mag. Thus, resetting the IR flux excess by adding 0.63 mag to the original estimate of γ Cas IR flux excess (see §3.3) brings the best-fit IR flux excess to a revised value of $E^\star(V - K) = 1.29$ mag.

Secondly, Smith et al. (2012) estimated the disk contribution to the total flux of the γ Cas system in the R-band as 45 ± 2 %. This result was determined by fitting a Gaussian disk model to R-band interferometric data obtained with the CHARA-VEGA beam combiner (Smith et al. 2012). This value should be at least similar to the V-band disk flux excess, which suggests that an offset of $2.5 \log \frac{1}{f_s} = 0.65$ mag should be applied to correct for the disk flux contribution in the optical. Therefore, this offset should be added to our estimate of γ Cas's IR flux excess of $E^\star(V - K) = 0.66$ mag, which brings the IR flux excess of the system to a true value of $E^\star(V - K) = 1.31$ mag

Thirdly, we derived another estimate of the IR flux excess of γ Cas independently by fitting its spectral energy distribution normalized to the UV-magnitude of the central star, and we found that $E^\star(UV - K) = 1.44 \pm 0.23$ mag (see §6.4). We suspect that this is a a better estimate of the IR flux excess since the disk contribution in the UV is negligible. We have thus averaged these three estimates to find an acceptable value of the observed IR flux excess of γ Cas, $E^\star(V - K) = 1.35 \pm 0.29$ mag. This value is about 0.3 mag less than, but within the errors, of the IR flux excess of $E^\star(V - K)_{\mathrm{model}} = 1.63 \pm 0.12$ mag predicted by the thick disk model.
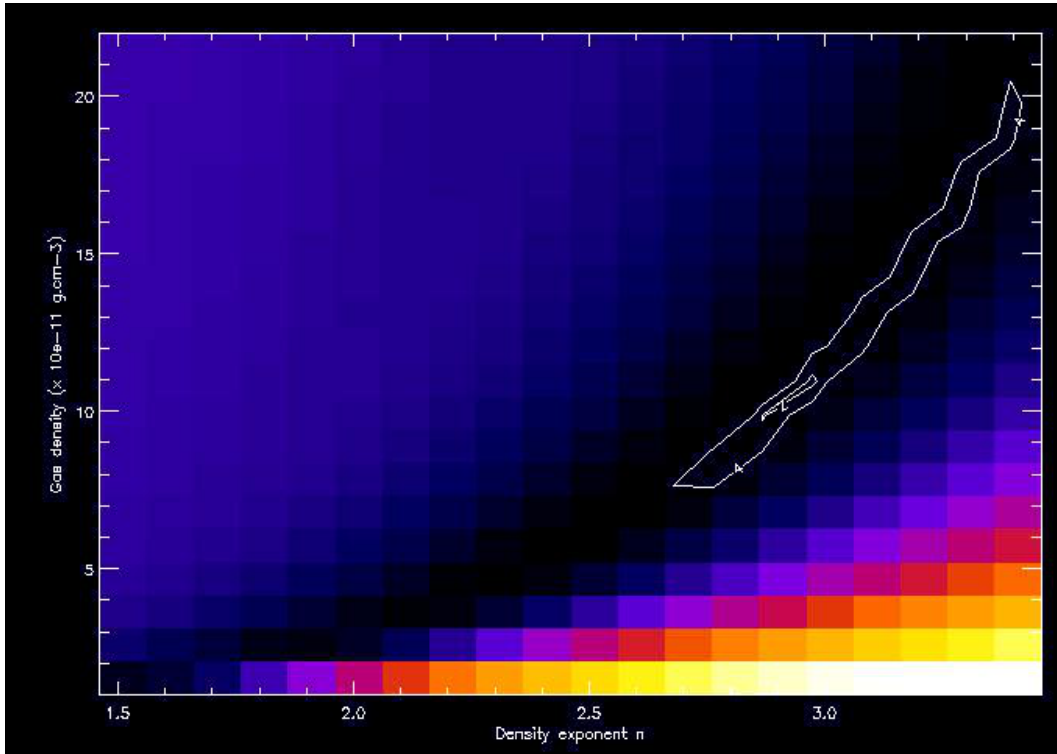
Figure 5.8: Reduced χ_ν^2 surface for the disk base density ρ_0 and the disk density exponent n using the thick disk model to fit the visibilities of γ Cas.

5.4.3 The Degeneracy of the Thick Disk Model

Here we aim to determine how well the thick disk model constrains the physical and geometrical properties of the circumstellar disk of γ Cas. We started by investigating the gas density profile of the disk determined by the model. In order to probe for degeneracies in the model best-fitting parameters, we ran a series of 2500 disk models over large ranges of disk base density ρ_0 and density exponent n while keeping the values of the geometrical properties of the disk fixed to their best-fit values. For each model, we generated synthetic K-band images, computed their theoretical visibilities, compared them to the FLUOR data set only, and calculated the corresponding reduced χ_ν^2.
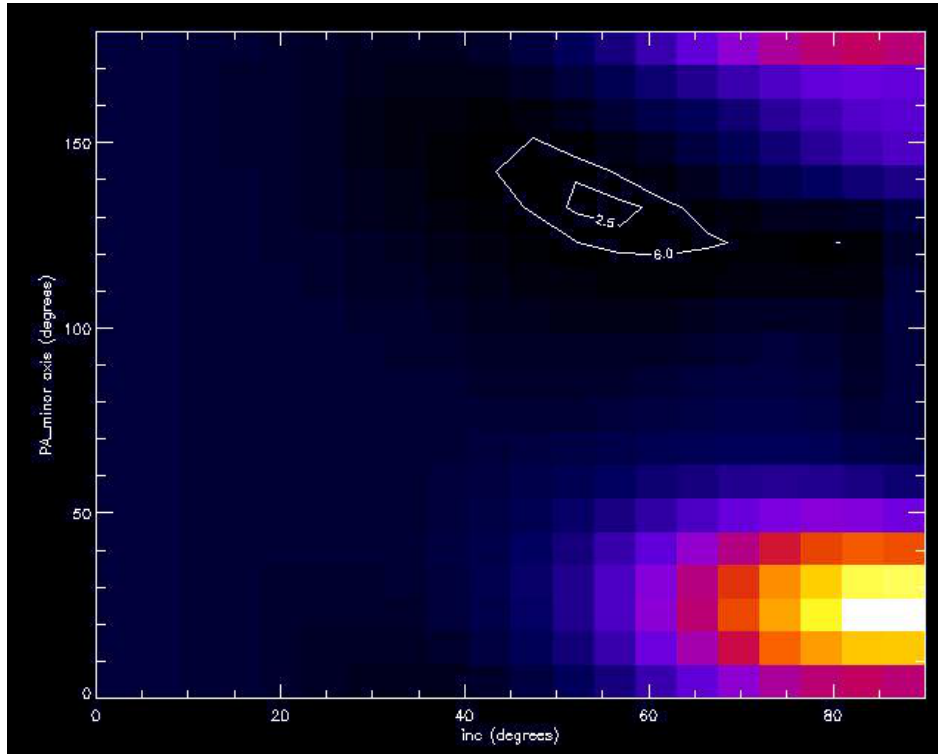
Figure 5.9: Reduced χ^2_ν surface for the disk inclination angle i and the disk position angle along the minor axis using the thick disk model to fit the visibilities of γ Cas.

Because typical values for the disk density exponent n usually fall in the range of 1 to 4 based on IR continuum fits (Waters 1986; Jones et al. 2008), we set the disk density exponent n to vary only within this range, and allowed the disk base density to vary between 5×10^{-12} g cm^{-3} and 3×10^{-10} g cm^{-3}. We show the resulting χ^2_ν surface for the family of (n, ρ_0) in Figure 5.8. We then set the disk base density and the density exponent to the fixed values of $\rho_0 = 7.8 \times 10^{-11}$ g cm^{-3} and $n = 2.7$, which correspond approximately to the best-fit of the density profile for FLUOR data, and allowed the inclination and the position angle of the disk model to vary over a range of $0°$ to $90°$, and $0°$ to $180°$, respectively. We show the resulting χ^2_ν surface for the family of (i, PA) in Figure 5.9.
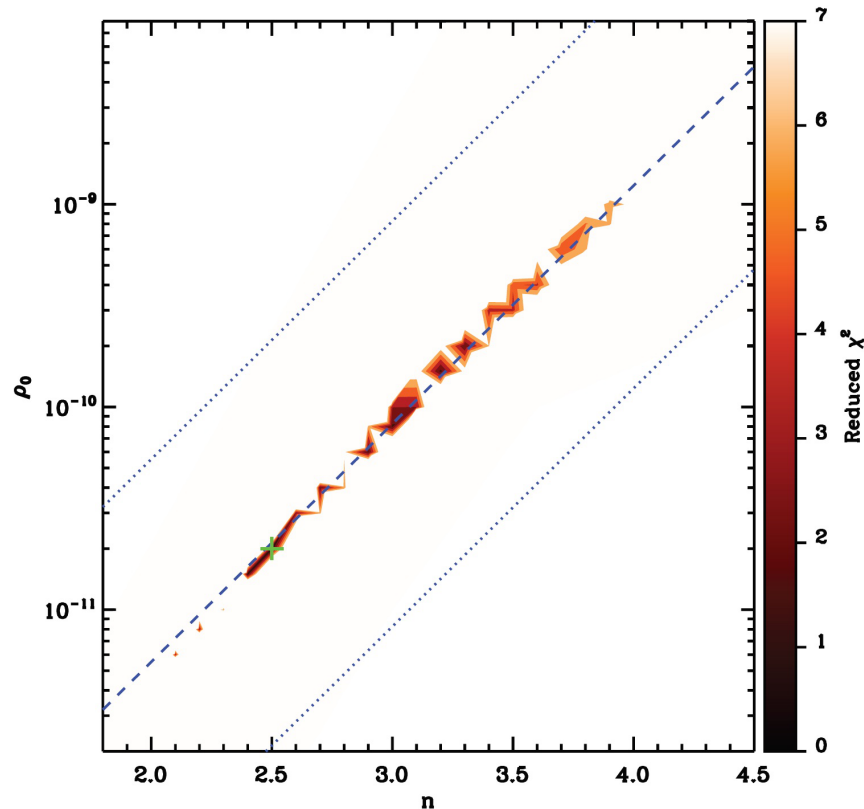
Figure 5.10: Contour plot showing the reduced χ^2_ν values as a function of the disk density profile (ρ_0, n) for fits of Hα interferometry from Tycner et al. (2008). Only regions of reduced $\chi^2_\nu < 7$ are shown in this plot.

We found that while the geometry of the disk (i.e., inclination and position angle) are well constrained with the thick disk model, the χ^2_ν surface in Figure 5.8 shows the existence of a valley of (n, ρ_0) that produces model visibilities that match reasonably well the interferometric observations. This implies that a degeneracy in the values of the pairs of (n, ρ_0) exists for the thick disk model, and that additional constraints are necessary in order to determine the disk density profile. Note that because we fitted the FLUOR data set only, the best solutions we found are slightly different than the best-fit geometry and density profile of γ Cas presented in §5.4.3.

Jones et al. (2008) computed Hα models of circumstellar disks around typical Be stars using the non-LTE radiative transfer code described in Sigut & Jones (2007), and they found similar trends between density parameters. Their model includes realistic chemical compositions and was constrained by direct comparison with Hα interferometric data and by contemporaneous Hα line profiles. They present an image of the χ_ν^2 surface as a function of the base density and density exponent, and they find a degeneracy similar to that shown in Figure 5.8 (see their Fig. 2). Tycner et al. (2008) also conducted a parameter study of the disk density profile using Hα interferometric data collected with the NPOI interferometer, and they show that a wide range of parameter values (ρ_0, n) (reproduced in Fig. 5.10) produce disk models that fit their observational data acceptably well.

Therefore, the solution we suggested for the density profile of γ Cas is one possible solution, which corresponds to the minimum χ_ν^2, although, in order to completely discern the absolute best solution and solve the degeneracy, additional observational constraints based on other diagnostics, such as multiwavelength observations of the sizes of the disk along with the IR flux excess of the system star plus disk at the time of the observations at each wavelength, are thus absolutely necessary for a full description of the density profile of the disk.

5.4.4 The Inner Radius of γ Cas

In the thick disk model, we considered the inner boundary of the disk of γ Cas attached to the stellar photosphere. In this section, we discuss this assumption and consider the case of circumstellar disk that is detached from the photosphere of the central star. In this scenario, a gap could be created by reducing the mass loss at the stellar equator allowing the ejected

material to clear out. In order to investigate this possibility, we used a physical model of a circumstellar disk with an inner boundary that is detached from the stellar photosphere, and that is allowed to vary as an independent model-parameter (see §5.4.1).

We set the disk geometrical properties (i.e. the inclination and position angle of the major axis) and the disk density profile equal to the best-fitting results obtained from the thick disk model, and we ran a series of physical models on the entire set of data, allowing the value of the inner radius of the disk to vary between one to four stellar radii. We found that the best-fit detached disk model yields an inner radius of $R_{\rm in} = 1.28 \pm 0.26 \ R_s$, with a $\chi^2_\nu = 21$. The resulting model IR flux excess in this case is $E^\star(V - K)_{\rm model} = 1.33 \pm 0.07$ mag, which is similar to the averaged observed value described in §5.4.2. Interestingly, this value of the inner radius of the gap is in good agreement with a ring model of H-band interferometric data presented by Smith et al. (2012), which predicts a gap at an inner radius of about $R_{\rm in}$ $= 1.36 \ R_s$, but the large errors on the estimate of the disk inner radius makes our model fitting inconclusive.

We then allowed all five parameters of the detached disk model (i, PA, ρ_0, n, $R_{\rm in}$) to vary within a limited grid of values, and we were able to determine the best-fit values along with the uncertainties of these parameters by fitting the model to the entire set of interferometric data. The results we obtained are similar to the values predicted by the full disk model. Only the IR flux excess resulting from the two models differs, but both estimates are still well within the errors. Thus, the significance of the additional parameter in the detached model fit to the interferometric data is inconclusive. We show the visibility curves derived from the full disk model and the detached disk model along with the data in Figure 5.11. The solid line in Figure 5.11 represents the detached disk model while the dashed line represents the
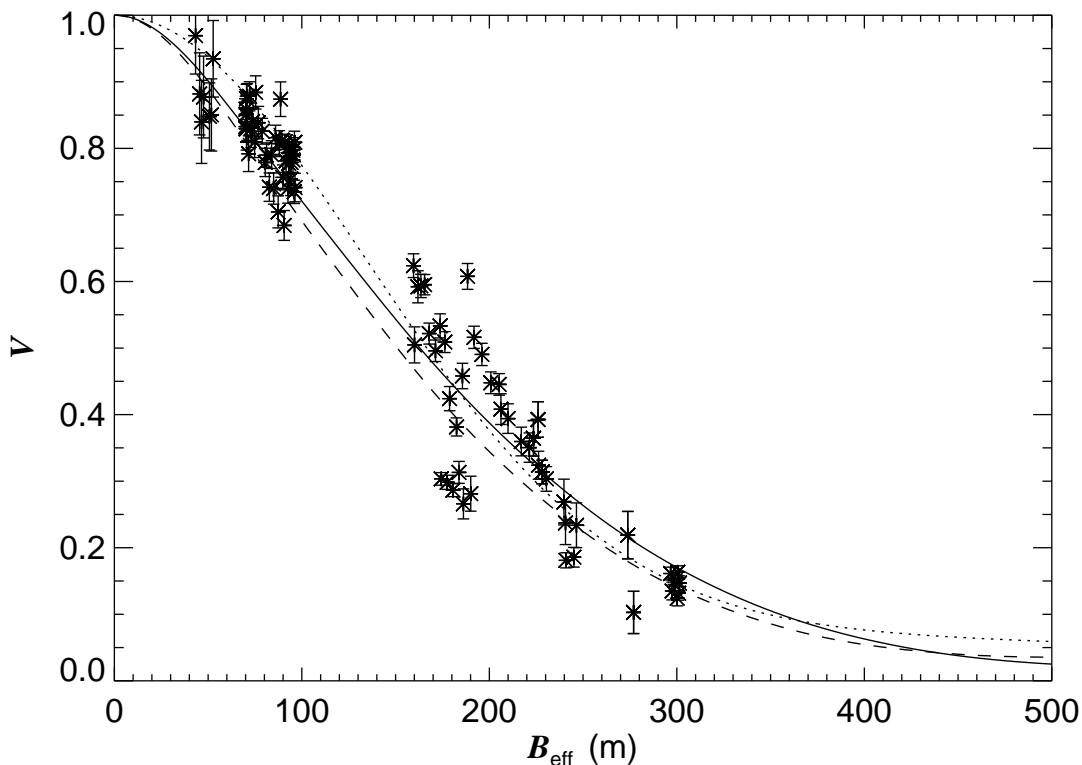
Figure 5.11: The best-fit thick disk model of γ Cas. The star signs are the interferometric data. The solid line is the thick disk model with an inner gap. The dashed line is the full thick disk model. the dotted line is the visibility curve of the best-fit Gaussian elliptical model. All the fits shown correspond to the predictions for the projected disk major axis.

full disk model. For the convenience of the reader, we also re-plotted the best-fit Gaussian elliptical model of γ Cas, with a dotted line in Figure 5.11. Note that because the best-fit disk inclination and disk position angle obtained using the Gaussian elliptical model and the thick disk model are slightly different, the Gaussian elliptical visibility curve plotted as a function of the effective baseline is different in Figure 5.11 than it appears in Figure 5.2.

We conclude that our current set of data is unable to confirm whether or not a gap is present within the inner parts of the disk of γ Cas since the errors on the model inner radius and the model IR flux excess are too high. The 0.3 mag difference between the observed

and the model IR excess might indicate the presence of a gap, but this difference is well within the errors of the fit of the spectral energy distribution. Interferometric observations at baselines of over 500 m are needed to clearly distinguish between the full and the gap models. Unfortunately, the current setup of the CHARA Array interferometer does not offer baselines this large. Note that the Gaussian model, the thick disk model, and the disk model with an inner gap all give consistent estimates of the geometrical properties of the circumstellar disk of γ Cas, and they are also consistent with previous studies of γ Cas by Quirrenbach et al. (1997), Tycner et al. (2006), and Gies et al. (2007). We have summarized our fitting results from these geometrical and physical models in Table 5.7.

Table 5.7: Comparison of Model Fits of γ Cas

Parameter	Elliptical Gaussian Model	Full Thick Disk Model	Detached Thick Disk Model
i (deg)	44 ± 3	48 ± 4	56 ± 5
PA (deg)	38 ± 5	34 ± 5	31 ± 8
$\rho_{0\,\mathrm{fit}}$ (10^{-11}g cm^{-3})	...	7.21 ± 0.33	7.10 ± 0.30
n_{fit}	...	2.71 ± 0.18	2.70 ± 0.10
R_{in}/R_s	...	...	1.28 ± 0.26
$E(V - K)_{\mathrm{fit}}$ (mag) .	1.80 ± 0.30	1.63 ± 0.12	1.33 ± 0.07
R_d/R_s	2.946 ± 0.134	2.665 ± 0.177	2.658 ± 0.186
χ^2_ν	16	20	21

5.4.5 Discussion

5.4.5.1 Binary Contribution

The presence of multiple faint companions of the Be star in γ Cas has been confirmed through several observational studies. One companion at least is suspected to be either a white dwarf (Murakami et al. 1986) or a neutron star (Frontera et al. 1987). Harmanec et al. (2000) measured radial velocities using Hα line series covering nearly 2500 days from 1993 to 2000. Harmanec et al. (2000) discovered periodic radial velocity variations with a period of 203 d, a semi-amplitude of 4.68 km s^{-1}, and an eccentricity of about 0.26, which they attributed to the presence of a low-mass companion. These results were confirmed by Miroshnichenko et al. (2002), who also measured the RVs of the Hα emission wings in a series of 130 electronic echelle spectra between 1993 and 2002.

Roberts et al. (2007) found that a second companion of γ Cas is at a distance of 2070 mas, orbits with a period of 1800 years. We estimated the K-band magnitude difference between γ Cas and this companion to be close to ≈ 6.5 mag. Because this companion is well outside the field of view of CHARA and the magnitude difference between the secondary and the Be star is so large, the flux of this companion has no influence on our measurements. We thus conclude that our K-band interferometric data fully characterize the circumstellar disk around the central star and should not be significantly affected by the companions of γ Cas.

5.4.5.2 The Physical Origins of the Inner Gap

As we have shown in §5.4.4, one fit of the interferometric data was made with a detached thick disk model with an inner radius of $R_{\rm in} \approx 1.3 R_s$, and this fit produced a good match to the observations, although the errors associated with $R_{\rm in}$ are large. If the gap model is

correct, then physically it could be interpreted as a result of the presence of a low-emitting region in the innermost parts of the disk close to the stellar photosphere. Two scenarios could explain this flux reduction. In the first scenario, an inner cavity is present in the inner regions of the disk that could be attributed to some magnetic activity that originates in the stellar photosphere (Smith et al. 2012). In this scenario, magnetic loops control the mass transfer process from the stellar photosphere to the disk, leaving the area close to the equator empty of material. Magnetic processes may help to explain the X-ray characteristics of γ Cas (Smith et al. 2012).

In the second scenario, a cool and dense equatorial region could be formed and tied to the surface of the star (Sigut et al. 2009). Simulations supporting this scenario have shown that when the density is large enough, which is the case of the innermost regions of γ Cas, the disk develops cool equatorial regions close to the stellar photosphere (Sigut et al. 2009; Carciofi et al. 2007), and this region would thus contribute a smaller proportion of the total emissivity of the disk, making it appear detached from the central star. Both scenarios are possible explanations and more high spatial resolution observations are needed in order to investigate the innermost parts of the thick disk of γ Cas.

5.4.5.3 Multiwavelength Modeling of γ Cas Disk

Using the same approach presented in §4.4, we have used the best-fit physical and geometrical parameter values of γ Cas disk obtained in the K-band to simulate the properties of the disk brightness distribution in order to predict its size at 1.7, 2.1, 4.8, 9, and 18 μm. We then compared the model predictions with recent H- and K-band interferometric measurements of the disk size of γ Cas, in addition to an estimate of the disk size at 12 μm from Waters

et al. (1987). We used the Gaussian elliptical model best-fit of 1.236 ± 0.063 for the angular diameter of the γ Cas disk in the K-band, and adopted a value of 1.12 mas for the disk size in the H-band derived from 2010 - 2011 CHARA-MIRC observations (G. Schaefer, private communication).

Smith et al. (2012) reported a multiwavelength campaign study of γ Cas in 2010 including X-ray observations using XMM-Newton, H-band continuum observations using CHARA-MIRC, and R-band continuum observations using CHARA-VEGA. The authors resolved a flattened circumstellar disk, and used Gaussian elliptical models to fit the their data. They reported a disk size along the major axis of γ Cas of 0.82 mas in the H-band data, and 0.76 mas in the R-band. The H-band angular size of the disk is much smaller than the multiwavelength model prediction, and smaller than results from the Gaussian elliptical disk model conducted by Schaefer et al. (priv. communication). We suspect that this difference is due to an additional component that Smith et al. (2012) used to fit their data, and which they attributed to a diffuse flux source, a source that if present, it would have caused a sharp decrease in the K-band visibilities at short baselines, which was not the case. Thus, we adopted the value of 1.12 mas as the H-band angular size of the disk of γ Cas with 10% errors because of this discrepancy, and a angular size of $\theta_s = 0.446$ mas for the central star that we derived from fitting the spectral energy distribution of γ Cas.

These estimates of γ Cas disk sizes are compared with the model in Figure 5.12. The model is shown with a dotted-line, while the disk-to-star size ratios at different wavelengths are plotted against the model. Figure 5.12 clearly shows that the size of the emitting region of γ Cas, similarly to ζ Tau, does increase with increasing wavelength, and that the few disk size measurements available are consistent with the model. We conclude that our
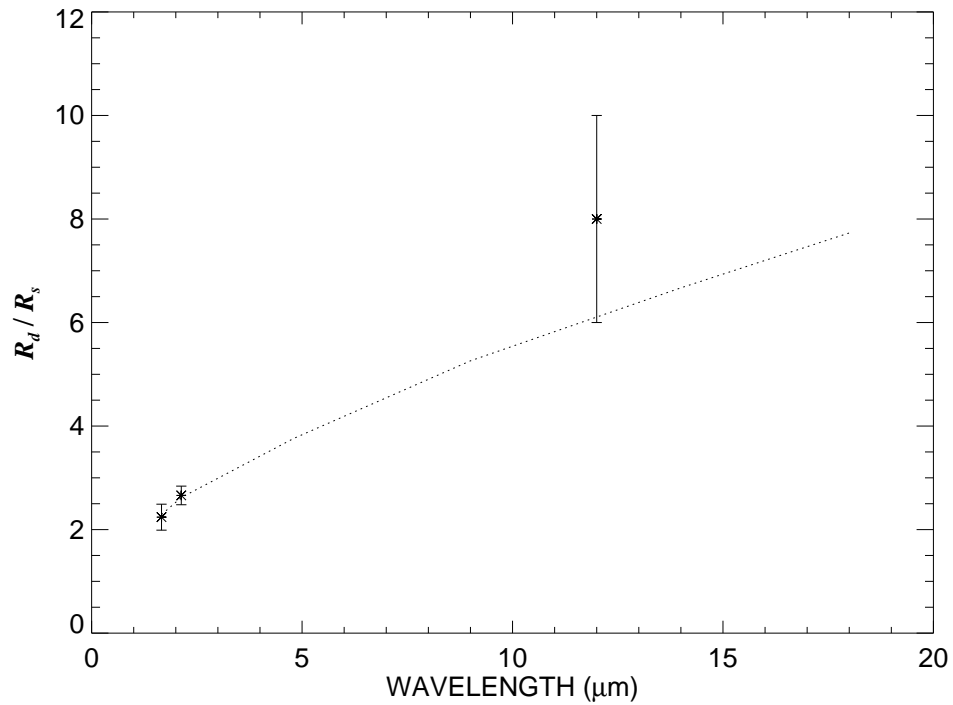
Figure 5.12: The disk-to-stellar radius ratio as a function of wavelength for our best-fit model of γ Cas (dotted line). The H- and K-band data plotted are the measured angular sizes from CHARA, and the 12 μm measure is taken from Waters (1986).

multiwavelength model predictions of the disk size as a function of wavelength represent well the overall free-free and bound-free emission in the disk of γ Cas.

5.5 Conclusions

We presented in this chapter long-baseline interferometric observations of γ Cas and we used these to constrain the physical and geometrical properties of the inner parts of its disk. We successfully resolved the circumstellar disk of γ Cas, and we found a K-band disk angular diameter using a Gaussian elliptical model of 1.236 ± 0.063 mas. Our multi-epoch observations from 2003 to 2009 show no evidence of variations in disk size larger than the errors, which suggests that the circumstellar disk has remained relatively stable during the time frame of our observations.

Using a radiative transfer model of γ Cas, we found that the best-fit disk base density is equal to $\rho_0 = 7.21 \pm 0.33 \times 10^{-11}$ g cm^{-3} and that the model best-fit density exponent is $n = 2.71 \pm 0.18$. These values of the gas density profile produce a disk model with an IR excess that is close to the observed one at the time of our observations.

In addition, we used a simple multiwavelength approach to predict γ Cas's disk sizes at several infrared wavelengths, and we found that the model predictions agree with the H- and K-band disk sizes derived from interferometric data.

Do not go where the path may lead, go instead where there

is no path and leave a trail.

—— Ralph Waldo Emerson

– 6 –

A K-band Interferometric Survey of Be Stars

ABSTRACT

We report results of a survey with the CHARA Array of circumstellar disks around 24 bright, northern, Be stars. Observations were made in the K-band with baselines that range between 30 and 331 m. The interferometric data were corrected for the flux contribution of a stellar companion in cases where the Be star is in a known binary or multiple system. For Be systems with good (u, v) coverage, we used a four-parameter Gaussian elliptical disk model to fit the data and determine the axial ratio, the disk position angle, the photospheric flux contribution, and the angular diameter of the disk's major axis. For Be systems with poor (u, v) coverage, constraining the axial ratio, the inclination, and the disk position angle was necessary to solve the model degeneracy between the wide range of possible solutions. In these cases, we adopted values of the axial ratio and the disk position angle from the literature, and estimated the photospheric contribution from fitting the spectral energy distribution of the Be stars. We find that in the cases where we used a four-parameter Gaussian elliptical fit, our results are generally in good agreement with previous studies of Be stars. We examine the relationship between the disk sizes in Hα and in the K-band, and using some Hα equivalent width measurements, we show that these two quantities are correlated. By combining the projected rotational velocity with disk inclinations derived from interferometry, we provide estimates of the equatorial rotational velocities and we show that most Be stars rotate very close to their critical velocities.

6.1 Introduction

Classical Be stars are hot, non-supergiant, B-type stars that are surrounded by circumstellar gas that is responsible many observational characteristics, such as the hydrogen Balmer emission lines detected in their spectra, the IR flux excess detected at multiple wavelengths, and their short- and long-term variability. The circumstellar environments of Be stars have been studied extensively in the past few decades using spectroscopy, polarimetry, and interferometry (Quirrenbach et al. 1997; Porter & Rivinius 2003; Gies et al. 2007; Rivinius 2007). Both the observational and theoretical results of these studies suggest that most of the circumstellar material is contained in a equatorial, dense, disk-like envelope (Quirrenbach et al. 1997). The circumstellar material ejected from Be stars dissipates and re-appears on different time scales that range from days to several years (Hanuschik 1996; Rivinius et al. 2003).

Basic quantities such as the geometry or the density structure of these disks were poorly constrained from the observations, and it is only recently, mainly due to long baseline interferometry, that observations have constrained the physical and geometrical properties of Be disks with high accuracy. During this last decade, optical and infrared interferometry has become an important tool in monitoring and characterizing Be stars and their circumstellar environments, and has resulted in a large scientific contribution to our understanding of these systems. The first interferometric observations of Be stars were successfully conducted by Thom et al. (1986) who made use of the I2T interferometer to observe and resolve the circumstellar envelope of γ Cas. The Mark III interferometer was then used by Quirrenbach et al. (1997) to observe seven Be stars, and their survey showed that the emitting regions around Be stars are flattened regions, which is the strongest observational evidence to date

that the circumstellar envelopes of Be stars have a disk-like geometry. Quirrenbach et al. (1997) combined their optical interferometry and spectropolarimetry data, derived the position angle of the disk from both techniques, and found good agreement. Meilland et al. (2009) used VLTI/MIDI operating in the N-band to observe the Be stars p Car, ζ Tau, κ CMa, α Col, δ Cen, β CMi, and α Ara, and determined their angular sizes. Gies et al. (2007) made the first long baseline interferometric observations of four Be stars (γ Cas, ϕ Per, ζ Tau, and κ Dra) using the CHARA Array, and they were able to resolve the disks and to determine their geometrical and physical properties. Tycner et al. (2004, 2005, 2006, 2008) used the NOI interferometer to observe the Hα emission from the disks of γ Cas, Alcyone, Pleione, ζ Tau, ϕ Per, β CMi, and χ Oph. The NOI observations showed that the Hα emitting regions are more extended than is observed in the near infrared and that a direct correlation exists between the disk size and the net Hα luminosity.

In this chapter, we present the results of a large interferometric survey that we have conducted in the K-band using the CHARA Array that covers a sample of 24 bright, northern, Be stars. We give in §6.2 a detailed description of our sample stars, and we present the complete observational sets and the data reduction process. In §6.3, we show a simplistic method that we used to correct the interferometric measurements for the flux of a companion, and in §6.4 we discuss the stellar angular diameters and the IR flux excesses determined from the flux distribution in the ultraviolet. We show fits of corrected data made using simple geometrical models in §6.5. In §6.6 we compare the K-band results with those obtained in Hα. §6.7 summarizes our results and draws our conclusions.

6.2 Observations and Data Reduction

6.2.1 Description of the Sample

We selected 24 bright Be stars as targets for this project. The main selection criterion was that the stars are bright, so that they are nearby and well within the limiting magnitude of the CHARA Classic tip-tilt servo system ($V < 11$) and the near-IR fringe detector ($K < 8.5$). The selected Be stars had to have declinations north of about $-15°$ to be accessible with the interferometer telescopes at good air-mass values. Furthermore, in order to have as an homogeneous sample as possible, we have primarily selected our sources to have recently shown some hydrogen emission and a near-IR flux excess in their spectral energy distribution. We relied particularly on studies that were conducted by Tycner et al. (2006), Grundstrom (2007), Gies et al. (2007), and Touhami et al. (2010).

Table 6.1: Adopted Stellar Parameters

HD Number	Star Name	Spec. Type[b]	R_s^a ($R_\odot$)	M_s ($M_\odot$)	log L_s^a ($L_\odot$)	T_{eff}^b (K)	π^c (mas)	$v\sin i^d$ (km s^{-1})
HD 004180	o Cas	B2 Ve	5.0	6.2[1]	4.86	15584	3.27	195
HD 005394	γ Cas	B0 IVe	10.0	15.5[2]	5.13	28840	5.32	432
HD 010516	ϕ Per	B0.5 IVe	7.0	10.0[1]	4.71	29031	4.32	440
HD 022192	ψ Per	B4.5 Ve	6.0	6.2[3]	3.52	17690	4.69	275
HD 023630	Alcyone	B5 IIIe	8.2	6.0[5]	3.21	12885	8.87	140
HD 023862	Pleione	B8 Vpe	3.2	3.0[5]	2.46	13436	8.54	286
HD 025940	48 Per	B4 Ve	6.5	7.5[3]	3.42	17593	7.14	197
HD 037202	ζ Tau	B1 IVe	5.5	10.1[3]	3.54	19000	7.82	310
HD 058715	β CMi	B8 Ve	2.5	3.4[4]	2.41	12769	20.17	230
HD 109387	κ Dra	B6 IIIpe	6.4	4.8[5]	3.19	15383	6.14	209
HD 138749	θ CrB	B6Vnne	4.2	4.6[4]	2.83	14440	10.50	327
HD 142926	4 Her	B9 pe	3.2	5.0[5]	2.52	13866	6.49	338
HD 142983	48 Lib	B3 IVe	6.6	12.8[6]	3.57	17645	6.33	407
HD 148184	χ Oph	B1.5 Vpe	7.0	10.0[1]	2.69	21330	6.89	151
HD 164284	66 Oph	B2 IV	5.4	8.8[3]	3.72	22822	4.52	280
HD 166014	o Her	B9.5 III	3.1	3.5[4]	2.13	20500	9.39	142
HD 198183	λ Cyg	B5 Ve	5.0	5.4[4]	2.67	14233	3.71	125
HD 200120	59 Cyg	B1.5 Ve	6.9	15.7[3]	4.20	24808	2.90	379
HD 202904	υ Cyg	B2.5 Vne	5.7	9.5[3]	3.70	20460	3.90	167
HD 203467	6 Cep	B2.5 Ve	4.5	11.7[3]	3.17	18249	3.02	153
HD 209409	o Aqr	B7 IVe	4.3	3.8[4]	2.87	14562	8.39	282
HD 212076	31 Peg	B1.5 Vne	5.5	11.9[3]	3.56	19236	3.36	98
HD 217675	o And	B6 IIIpe	5.2	7.0[3]	3.27	16741	4.71	274
HD 217891	β Psc	B5 Ve	3.5	4.3[4]	2.56	14376	8.60	95

References - [a] Waters et al. (1987); [b] Frémat et al. (2005); [c] van Leeuwen (2007); [d] Grundstrom (2007).

References for mass estimates: [1] Hohle et al. (2010); [2] Gies et al. (2007); [3] Tetzlaff et al. (2011); [4] Zorec & Royer (2012); [5] Mass derived from spectral type; [6] Hernández et al. (2005).

Table 6.2: Photometry of The Targets

HD Number	Star Name	B^a (mag)	V^a (mag)	R^b (mag)	J^c (mag)	H^c (mag)	K^c (mag)
HD 004180	o Cas	4.432	4.477	4.500	4.653	4.612	4.404
HD 005394	γ Cas	2.290	2.470	2.200	2.039	1.993	1.756
HD 010516	ϕ Per	4.000	4.090	4.070	4.049	3.955	3.709
HD 022192	ψ Per	4.255	4.310	4.330	4.316	4.153	4.107
HD 023630	Alcyone	2.806	2.873	2.870	2.735	2.735	2.636
HD 023862	Pleione	4.967	5.048	5.090	5.087	5.067	4.937
HD 025940	48 Per	3.967	4.003	4.020	3.978	3.899	3.796
HD 037202	ζ Tau	2.840	3.030	3.040	3.001	3.047	2.808
HD 058715	β CMi	2.814	2.886	2.880	3.061	3.109	3.101
HD 109387	κ Dra	3.766	3.881	3.920	3.823	3.908	3.820
HD 138749	θ CrB	4.036	4.153	4.230	4.429	4.472	4.430
HD 142926	4 Her	5.654^b	5.737^b	5.790	5.821	5.887	5.850
HD 142983	48 Lib	4.867	4.943	4.990	5.097^b	4.828^b	4.591^b
HD 148184	χ Oph	4.700	4.420	4.150	3.404	3.149	2.885
HD 164284	66 Oph	4.684	4.784	4.800	4.987	5.079	5.030
HD 166014	o Her	3.804^b	3.825^b	3.850	3.968	3.960	3.954
HD 198183	λ Cyg	4.453	4.563	4.820	4.663	4.779	4.794
HD 200120	59 Cyg	4.690	4.740	4.790	4.657	4.457	4.345
HD 202904	υ Cyg	4.320	4.430	4.430	4.701	4.540	4.478
HD 203467	6 Cep	5.139	5.185	5.200	4.828	4.774	4.589
HD 209409	o Aqr	4.630	4.700	4.820	4.865	4.809	4.661
HD 212076	31 Peg	4.720	4.810	4.860	4.818	4.803	4.685
HD 217675	o And	3.538^b	3.619^b	3.670	3.827	3.841	3.886
HD 217891	β Psc	4.376	4.486	4.530	4.764	4.808	4.750

References - ^{a} Soubiran et al. (2010); ^{b} Zacharias et al. (2004); ^{c} Zhang et al. (2005).

The sources along with their adopted stellar parameters are presented in Table 6.1. Columns 1 and 2 list the stars names, columns 3 - 5 list their corresponding stellar radii, masses, and luminosities, respectively. Column 6 lists the effective temperature of the central star, column 7 lists the adopted parallax of the systems, and finally column 8 lists the projected equatorial rotational velocities of the target stars. Most of our sample stars are highly variable in brightness, and we have collected in Table 6.2 $BVRJHK$ photometry from the literature that is contemporaneous with our interferometric observations.

6.2.2 Properties of the Calibrator Stars

Measuring the instrumental transfer function of an interferometer is necessary to estimate accurate visibility measurements. This is performed by observing selected calibrator stars with known angular sizes before and after each target observation. The calibrators are selected based on their spectral types, distances, and their known diameters. The calibrator stars are usually close to the targets, unresolved at the interferometer's largest baseline, and have no known companions. For the purpose of this Be star survey, we have selected calibrator stars based on these criteria, and we collected photometric data on each one in order to reconstruct the spectral energy distribution and determine an accurate angular diameter. The collected $BVRJHK$ photometry is transformed into calibrated flux measurements using the procedures described in Gray (1998) and Cohen et al. (2003). The effective temperature T_{eff} and the surface gravity $\log g$ are used to produce a model flux distribution based on the Kurucz stellar atmosphere models. We then estimated the limb darkened angular diameters of the calibrator stars by comparing their observed and model flux distributions. We also

collected measurements of $E(B-V)$ and applied a reddening correction for each calibrator while fitting the spectral energy distributions.

Although, most of the calibrator stars selected for this survey program are close by and the interstellar reddening could be considered negligible, there were a few cases where applying this correction was relevant. We compute the limb-darkened angular diameter θ_{LD} by direct comparison of the observed and model flux distributions of each calibrator (with model based on their $T_{\rm eff}$ and $\log g$), and based on the limb-darkening coefficients given by Claret (2000), we transformed the limb-darkened diameter to an equivalent uniform disk angular diameter θ_{UD} assuming a baseline of 300 m.

Table 6.3: Photometry of the Calibrator Stars

Calibrator Name	Object Name	U^a (mag)	B^b (mag)	V^b (mag)	R^c (mag)	I^c (mag)	J^b (mag)	H^b (mag)	K^b (mag)
HD 004222	HD 004180	...	5.43	5.41	5.40	5.41	5.25	5.29	5.26
HD 006210	HD 005394	6.47	6.35	5.84	5.49	5.23	4.75	4.79	4.44
HD 011151	HD 010516	...	6.35	5.96	5.69	5.49	5.12	4.96	4.89
HD 020675	HD 022192	6.32	6.34	5.94	5.67	5.47	5.27	4.92	4.87
HD 024167	HD 023630	6.55	6.41	6.22	6.11	6.02	5.77	5.70	5.65
HD 024357	HD 023862	6.31	6.27	5.96	5.76	5.61	5.25	5.16	5.09
HD 025948	HD 025940	...	6.64	6.25	5.98	5.79	5.35	5.25	5.16
HD 037147	HD 037202	5.84	5.74	5.53	5.41	5.30	5.06	5.01	4.93
HD 057006	HD 058715	6.47	6.40	5.92	5.60	5.36	4.96	4.77	4.66
HD 111456	HD 109387	6.27	6.31	5.85	5.41	5.13	5.17	4.74	4.55
HD 142640	HD 142983	6.80	6.76	6.33	6.04	5.83	5.39	5.19	5.11
HD 144585	HD 148184	7.14	6.95	6.33	6.91	5.61	5.18	4.97	4.80
HD 159139	HD 166014	5.64	5.64	5.64	5.65	5.67	5.62	5.66	5.64
HD 161941	HD 164284	6.34	6.36	6.22	6.17	6.12	5.64	5.66	5.60
HD 166233	HD 164284	6.38	6.35	6.03	5.80	5.35	5.26	4.81	4.76
HD 168914	HD 166014	5.47	5.32	5.12	5.00	4.90	4.49	4.48	4.47
HD 192455	HD 203467	6.21	6.18	5.71	5.39	5.16	5.01	4.67	4.46
HD 196629	HD 198183	6.81	6.82	6.50	6.29	6.13	5.77	5.66	5.60
HD 203454	HD 202904	6.93	6.89	6.40	6.06	5.81	5.23	4.90	4.87
HD 211575	HD 209409	6.79	6.78	6.38	6.12	5.92	5.59	5.35	5.32
HD 213617	HD 212076	6.79	6.76	6.43	6.23	6.08	5.73	5.64	5.58
HD 217877	HD 217891	7.30	7.24	6.69	6.33	6.06	5.65	5.38	5.29
HD 217926	HD 217891	6.82	6.79	6.43	6.19	6.01	5.62	5.41	5.35
HD 218470	HD 217675	6.04	6.07	5.68	5.44	5.25	4.82	4.64	4.64

References - [a] Karataş & Schuster (2006); [b] Ammons et al. (2006); [c] Monet et al. (2003).

Table 6.4: Calibrator star angular diameters

Calibrator Name	Object Name	$T_{\rm eff}^a$ (K)	$\log g^a$ (cm s^{-3})	Spectral Type	$E(B-V)$ (mag)	$E(B-V)$ Ref.	$\theta_{\rm LD}$ (mas)	$\theta_{\rm UD}$ (mas)
HD 004222	HD 004180	8970	4.20	A2 V	0.007	c	0.303 ± 0.017	0.301 ± 0.021
HD 006210	HD 005394	6065	3.86	F6 V	0.009	b	0.516 ± 0.025	0.506 ± 0.035
HD 011151	HD 010516	6405	4.01	F5 V	0.003	b	0.424 ± 0.011	0.416 ± 0.029
HD 020675	HD 022192	6571	4.28	F6 V	0.018	a	0.418 ± 0.018	0.417 ± 0.028
HD 024167	HD 023630	8200	4.01	A5 V	0.012	d	0.246 ± 0.015	0.243 ± 0.017
HD 024357	HD 023862	6890	4.50	F4 V	0.006	d	0.374 ± 0.014	0.368 ± 0.026
HD 025948	HD 025940	6440	4.07	F5 V	0.008	b	0.374 ± 0.014	0.367 ± 0.025
HD 037147	HD 037202	7200	4.13	F0 V	0.002	d	0.403 ± 0.021	0.397 ± 0.028
HD 057006	HD 058715	6000	4.16	F8 V	0.001	b	0.501 ± 0.031	0.491 ± 0.034
HD 111456	HD 109387	6313	4.70	F6 V	0.000	b	0.477 ± 0.028	0.467 ± 0.033
HD 142640	HD 142983	6481	4.09	F6 V	0.005	b	0.363 ± 0.013	0.356 ± 0.025
HD 144585	HD 148184	5831	4.03	G5 V	0.005	b	0.438 ± 0.012	0.429 ± 0.030
HD 159139	HD 166014	9550	4.17	A1 V	0.005	a	0.248 ± 0.013	0.246 ± 0.017
HD 161941	HD 164284	10512	3.67	G5 V	0.180	a	0.194 ± 0.037	0.194 ± 0.014
HD 166233	HD 164284	6661	3.57	F2 V	0.003	b	0.405 ± 0.026	0.398 ± 0.027
HD 168914	HD 166014	7585	3.60	A7 V	0.000	a	0.456 ± 0.023	0.450 ± 0.031
HD 192455	HD 203467	6251	4.05	F5 V	0.001	d	0.504 ± 0.026	0.494 ± 0.035
HD 196629	HD 198183	6996	4.25	F0 V	0.004	d	0.285 ± 0.010	0.280 ± 0.020
HD 203454	HD 202904	6146	4.50	F8 V	0.009	d	0.406 ± 0.025	0.398 ± 0.028
HD 211575	HD 209409	6300	4.00	F3 V	0.013	d	0.367 ± 0.024	0.360 ± 0.025
HD 213617	HD 212076	7259	4.40	F1 V	0.014	e	0.278 ± 0.010	0.274 ± 0.019
HD 217877	HD 217891	5953	4.29	F8 V	0.003	b	0.365 ± 0.149	0.358 ± 0.025
HD 217926	HD 217891	6528	3.63	F2 V	0.005	b	0.335 ± 0.013	0.329 ± 0.023
HD 218470	HD 217675	6407	4.07	F5 V	0.009	d	0.491 ± 0.028	0.482 ± 0.033

References - [a] Soubiran et al. (2010); [b] Ammons et al. (2006); [c] Renson & Manfroid (2009); [d] Philip & Egret (1980); [e] Gerbaldi et al. (2007).

We list the photometry of the calibrator stars used in this study in Table 6.3. Columns 1 and 2 of Table 6.3 list the calibrator star and the target star, respectively, columns 3 to 10 give $UBVRIJHK$ magnitudes of the stars that we used to construct their spectral energy distributions. Table 6.4 lists the physical properties of these calibrators. Columns 1 and 2 of Table 6.4 list the calibrator star and the target star, respectively, columns 3 and 4 list the effective temperature T_{eff} and the surface gravity $\log g$ for each calibrator, column 5 gives the spectral type, and columns 6 and 7 list the adopted interstellar reddening $E(B-V)$ and the source reference, respectively. Column 8 lists our best-fit limb-darkened angular diameter θ_{LD} derived from fitting the spectral energy distribution, and column 9 lists the uniform disk angular diameter θ_{UD} for each calibrator star. Plots of the resulting SEDs are shown in Figures 6.1 and 6.2.
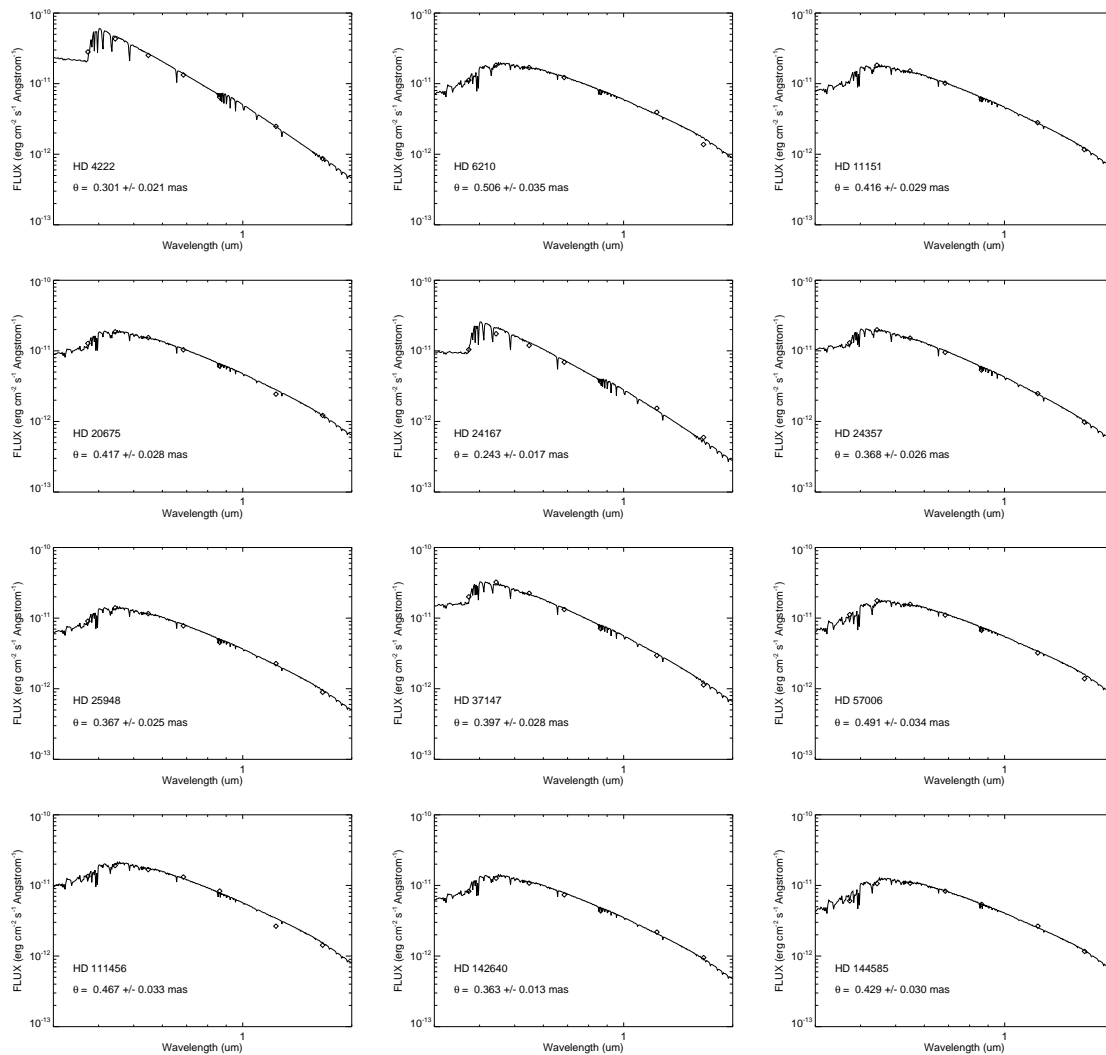
Figure 6.1: SED fits of the calibrator stars and estimates of their uniform disk angular diameters. Diamonds show the observed fluxes from the magnitudes listed in Table 6.3, and the solid line shows the adopted model flux spectrum.
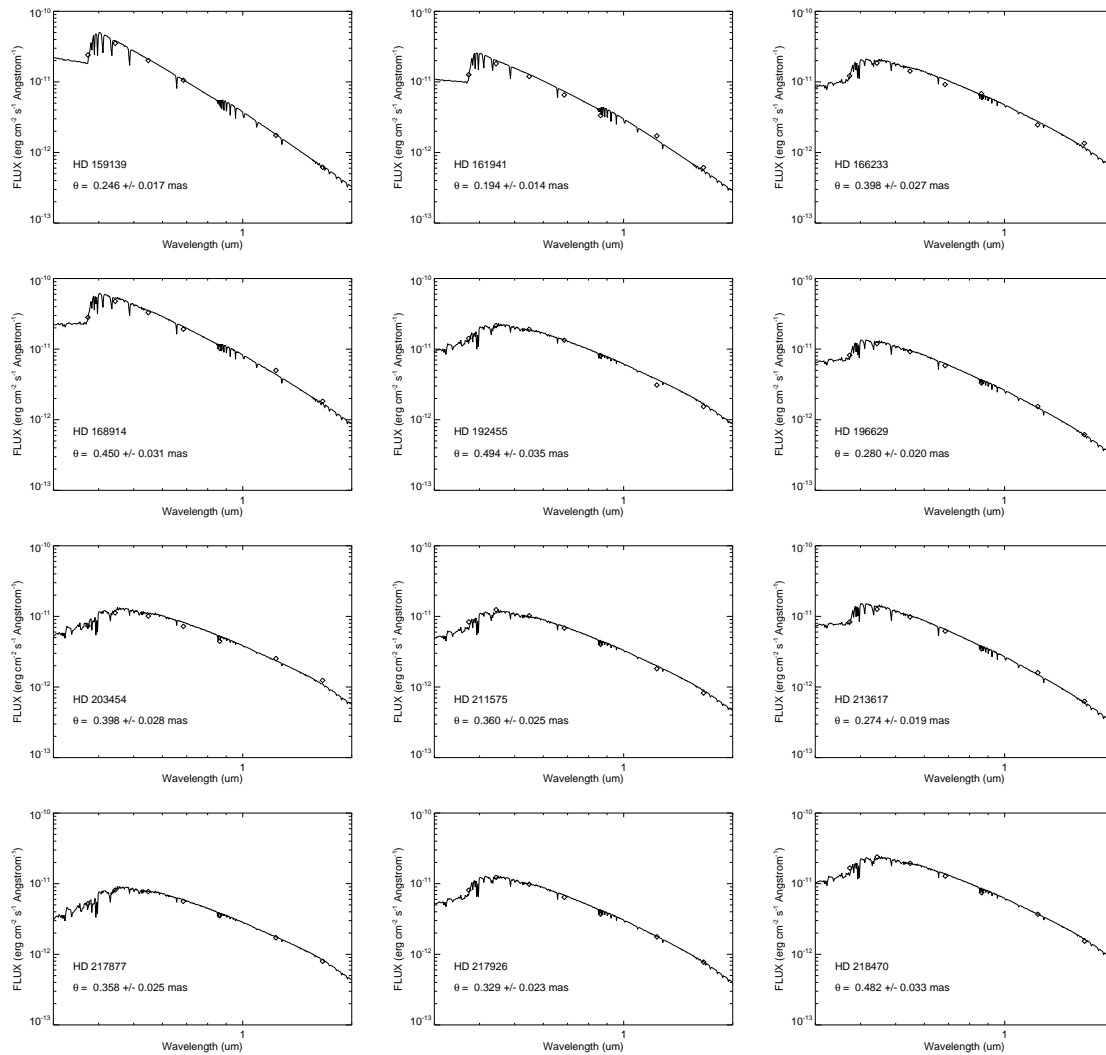
Figure 6.2: SED fits of the calibrator stars and estimates of their uniform disk angular diameters, in the same format a Fig. 6.1.

6.2.3 CHARA Classic Observations and Data Calibration

The observations were carried out with the CHARA Array between 2007 October and 2010 November using the CHARA Classic beam combiner operating in the K-band at a wavelength of 2.1329 μm (ten Brummelaar et al. 2005). In order to map the circumstellar disks around our target Be stars, a minimum of two interferometer orthogonal baselines were used for most cases: the South-West baseline of length 278 m oriented at 39° west of north (S1/W1) and the South-East baseline of length $\sim$ 330 m oriented at 22° east of north (S1/E1). Each target star and its calibrator were observed throughout the night in series of 200 scans recorded with a near-IR detector on a single pixel at a frequency of 500 - 750 Hz, depending on the seeing conditions of each particular night of observation. The interferometric raw visibility is usually estimated by performing an integration of the fringe power spectrum. Many algorithms are available to perform such a procedure. For our program, we made use of the CHARA Data Reduction Software (ReduceIR; ten Brummelaar et al. 2005) to extract the raw visibility for the target stars and their corresponding calibrators. The raw visibilities are then calibrated with the transfer function of the instrument measured by using the calibrator stars of known angular diameter, as described above.

The calibrated visibility measurements are shown in Table 6.5. Column 1 lists target HD number, column 2 lists the heliocentric Julian date, column 3 gives the telescope pair used in each observation, columns 4 and 5 list the u and v coordinates in units of cycles arcsec^{-1}, respectively, columns 6 and 7 list the projected and effective baselines in meters, columns 8 and 9 list the calibrated visibilities and their corresponding errors, respectively, and lastly, columns 10 and 11 list the visibility measurements corrected for the flux of stellar companions

for those cases with known orbits and K-band magnitude differences, which we will discuss in detail in the next section.

The internal error from fitting individual fringes is generally small ($< 3\%$). The error bars and the scatter in the data depend mostly on the system magnitude and on the seeing conditions at the time of the observations, which usually varies with a Fried parameter that ranges between $r_0 \simeq 2.5 - 14$ cm. The error bars for the brightest targets typically range between 2% and 5%, while the error bars on the fainter ones mainly depend on the SNR and on the particular conditions of observations, and their errors range up to about 8%. Our interferometric campaign was successful, and we obtained a good set of observations at different hour angles for each one of our targets with the exceptions of HD 58715 and HD 148184 where the position angle coverage is limited. Figures 6.3 to 6.5 show the distribution of the observations in the (u, v) plane for our Be star targets.

Table 6.5: Calibrated Visibilities

Star	Date (HJD−2400000)	Telescope Pair	u (cycles arcsec^{-1})	v (cycles arcsec^{-1})	Baseline (m)	Effective baseline (m)	V	δV	V_{corr}	δV_{corr}
HD 004180	54756.622	S1/W1	−75.187	−627.643	278.114	162.970	0.705	0.042	0.689	0.046
HD 004180	54756.629	S1/W1	−44.906	−630.398	278.055	164.379	0.693	0.042	0.838	0.045
HD 004180	54756.637	S1/W1	−15.062	−631.747	278.024	166.438	0.821	0.047	0.826	0.051
HD 004180	54756.649	S1/W1	19.818	−631.622	278.027	169.637	0.736	0.044	0.865	0.048
HD 004180	54756.661	S1/W1	52.167	−629.866	278.067	173.303	0.767	0.048	0.793	0.053
HD 004180	54757.610	S1/W1	−91.896	−625.513	278.157	162.450	0.812	0.045	0.863	0.049
HD 004180	54757.626	S1/W1	−53.847	−629.731	278.070	163.890	0.569	0.032	0.670	0.035
HD 004180	54757.633	S1/W1	−21.944	−631.555	278.029	165.906	0.724	0.041	0.762	0.045
HD 004180	54757.645	S1/W1	11.396	−631.820	278.023	168.790	0.609	0.032	0.680	0.035
HD 004180	54757.657	S1/W1	44.336	−630.437	278.054	172.357	0.790	0.035	0.863	0.038
HD 004180	54757.665	S1/W1	77.830	−627.335	278.120	176.648	0.668	0.029	0.717	0.031
HD 004180	54759.958	S1/E1	230.947	−702.578	325.380	229.379	0.609	0.024	0.670	0.026
HD 004180	54759.965	S1/E1	251.849	−693.810	324.740	232.929	0.577	0.022	0.627	0.024
HD 004180	54759.973	S1/E1	273.565	−683.594	323.945	236.659	0.596	0.024	0.651	0.026
HD 004180	54759.985	S1/E1	297.619	−670.821	322.880	240.810	0.552	0.024	0.597	0.027
HD 004180	54759.993	S1/E1	324.424	−654.529	321.402	245.410	0.498	0.035	0.547	0.038
HD 004180	54767.629	E1/E2	122.971	0.450	54.103	53.424	0.948	0.035	1.002	0.038
HD 004180	54767.637	E1/E2	124.960	3.844	55.004	54.111	0.861	0.030	0.899	0.033
HD 004180	54767.641	E1/E2	126.845	7.417	55.902	54.758	0.837	0.030	0.865	0.033
HD 004180	54767.649	E1/E2	128.894	11.841	56.948	55.457	0.876	0.028	0.903	0.030
HD 004180	54767.657	E1/E2	130.759	16.587	57.990	56.086	0.934	0.032	0.961	0.035
HD 004180	54767.665	E1/E2	131.999	20.340	58.760	56.500	0.910	0.035	0.933	0.038
HD 004180	54767.668	E1/E2	133.025	24.046	59.475	56.838	0.875	0.035	0.893	0.039
HD 004180	54767.692	E1/E2	135.194	38.016	61.787	57.521	0.946	0.045	0.974	0.049
HD 004180	54767.700	E1/E2	135.336	42.509	62.411	57.550	0.990	0.055	1.025	0.060
HD 004180	54767.708	E1/E2	135.106	48.520	63.159	57.450	0.924	0.050	0.960	0.055
HD 004180	55130.751	W1/W2	−234.308	64.271	106.895	106.693	0.935	0.055	0.936	0.060
HD 004180	55130.766	W1/W2	−240.004	47.195	107.615	107.615	0.952	0.051	0.988	0.055
HD 004180	55130.778	W1/W2	−243.174	31.895	107.904	107.769	0.871	0.046	0.952	0.050
HD 004180	55130.794	W1/W2	−244.593	16.546	107.858	107.308	0.872	0.043	1.007	0.047
HD 004180	55130.805	W1/W2	−244.315	1.671	107.492	106.283	0.772	0.042	0.930	0.046
HD 005394	54754.703	S1/W1	139.084	−607.765	274.306	231.158	0.303	0.019	⋯	⋯
HD 005394	54754.711	S1/W1	165.175	−600.436	273.983	227.589	0.324	0.021	⋯	⋯
HD 005394	54754.722	S1/W1	194.453	−590.507	273.525	223.502	0.350	0.022	⋯	⋯
HD 005394	54754.730	S1/W1	219.570	−580.451	273.038	219.937	0.360	0.022	⋯	⋯
HD 005394	54754.746	S1/W1	259.566	−561.204	272.040	214.171	0.394	0.022	⋯	⋯
HD 005394	54754.754	S1/W1	280.443	−549.397	271.385	211.130	0.408	0.023	⋯	⋯
HD 005394	54758.765	S1/E1	−354.366	−576.322	297.658	296.711	0.135	0.013	⋯	⋯
HD 005394	54758.773	S1/E1	−335.716	−592.279	299.530	297.903	0.145	0.011	⋯	⋯
HD 005394	54758.781	S1/E1	−314.532	−608.507	301.370	298.796	0.124	0.011	⋯	⋯

Continued on Next Page…

Table 6.5 – Continued

Star	Date (HJD−2400000)	Telescope Pair	u (cycles arcsec⁻¹)	v (cycles arcsec⁻¹)	Baseline (m)	Effective baseline (m)	V	δV	V_corr	δV_corr
HD 005394	54758.789	S1/E1	−294.521	−622.229	302.876	299.257	0.132	0.010	...	...
HD 005394	54758.804	S1/E1	−255.926	−644.924	305.268	299.276	0.147	0.011	...	...
HD 005394	54758.968	S1/E1	235.831	−655.016	306.292	248.023	0.186	0.015	...	...
HD 005394	54758.976	S1/E1	256.817	−644.451	305.219	244.459	0.181	0.011	...	...
HD 005394	54760.816	S1/E1	−210.001	−666.447	307.424	298.080	0.163	0.010	...	...
HD 005394	54760.828	S1/E1	−177.144	−678.694	308.604	296.556	0.151	0.008	...	...
HD 005394	54760.840	S1/E1	−137.760	−690.286	309.689	294.109	0.161	0.010	...	...
HD 005394	54766.656	E1/E2	127.804	−7.489	56.326	48.422	0.969	0.058	...	...
HD 005394	54766.668	E1/E2	130.796	1.022	57.547	49.382	0.882	0.062	...	...
HD 005394	54766.672	E1/E2	131.950	5.101	58.097	50.392	0.840	0.062	...	...
HD 005394	54766.680	E1/E2	132.995	9.479	58.661	53.292	0.877	0.061	...	...
HD 005394	54766.699	E1/E2	134.968	22.648	60.211	54.232	0.848	0.050	...	...
HD 005394	54766.703	E1/E2	135.250	27.140	60.691	55.091	0.850	0.054	...	...
HD 005394	55116.718	S1/E1	−459.951	−432.035	277.633	276.146	0.219	0.036	...	...
HD 005394	55116.726	S1/E1	−453.050	−446.835	279.962	278.908	0.103	0.032	...	...
HD 005394	55153.031	E1/W1	−372.570	592.870	308.070	233.694	0.393	0.027	...	...
HD 005394	55153.039	E1/W1	−393.023	580.994	308.609	232.103	0.364	0.027	...	...
HD 005394	55154.023	E1/W1	−354.456	602.648	307.604	235.204	0.314	0.018	...	...
HD 010516	54759.000	S1/E1	222.132	−699.878	323.058	288.495	0.753	0.038	0.787	0.040
HD 010516	54759.008	S1/E1	244.525	−690.563	322.307	292.424	0.718	0.036	0.728	0.038
HD 010516	54759.012	S1/E1	262.220	−682.355	321.615	295.266	0.778	0.039	0.778	0.041
HD 010516	54759.020	S1/E1	282.941	−671.709	320.675	298.271	0.759	0.033	0.749	0.035
HD 010516	54759.032	S1/E1	302.160	−660.737	319.655	300.718	0.773	0.041	0.763	0.043
HD 010516	54759.040	S1/E1	327.099	−644.721	318.072	303.338	0.774	0.039	0.772	0.042
HD 010516	54759.907	S1/E1	−48.629	−738.941	325.810	218.245	0.661	0.023	0.645	0.025
HD 010516	54759.915	S1/E1	−27.475	−740.209	325.889	225.058	0.682	0.025	0.678	0.026
HD 010516	54759.918	S1/E1	−6.288	−740.771	325.924	231.666	0.698	0.026	0.715	0.027
HD 010516	54759.926	S1/E1	13.171	−740.665	325.917	237.546	0.674	0.027	0.711	0.029
HD 010516	54759.930	S1/E1	31.856	−740.004	325.876	248.579	0.659	0.030	1.000	0.100
HD 010516	54759.938	S1/E1	51.441	−738.719	325.796	253.709	0.618	0.030	0.692	0.032
HD 010516	54759.946	S1/E1	70.139	−736.921	325.683	214.956	0.623	0.032	0.710	0.034
HD 010516	54760.899	S1/E1	−58.610	−738.096	325.757	222.431	0.748	0.038	0.745	0.040
HD 010516	54760.907	S1/E1	−35.711	−739.799	325.864	229.572	0.819	0.042	0.841	0.044
HD 010516	54760.915	S1/E1	−13.076	−740.667	325.917	236.415	0.743	0.043	0.788	0.045
HD 010516	54760.922	S1/E1	9.379	−740.733	325.921	243.200	0.740	0.047	0.811	0.049
HD 010516	54760.930	S1/E1	32.475	−739.973	325.874	248.976	0.733	0.044	0.823	0.047
HD 010516	54760.938	S1/E1	52.866	−738.602	325.789	256.563	0.767	0.046	0.867	0.049
HD 010516	54760.946	S1/E1	80.824	−735.640	325.602	260.335	0.708	0.042	0.801	0.045
HD 010516	54760.950	S1/E1	95.289	−733.607	325.472	263.227	0.698	0.040	0.781	0.043
HD 010516	54769.723	E1/E2	135.096	34.364	61.330	31.328	0.912	0.032	1.021	0.034
HD 010516	54769.755	E1/E2	134.101	54.703	63.720	24.895	0.874	0.037	0.981	0.039
HD 010516	54769.762	E1/E2	133.191	59.162	64.120	23.294	0.915	0.043	1.024	0.045

Table 6.5 – Continued

Star	Date (HJD−2400000)	Telescope Pair	u (cycles arcsec^{-1})	v (cycles arcsec^{-1})	Baseline (m)	Effective baseline (m)	V	δV	V_{corr}	δV_{corr}
HD 010516	54769.766	E1/E2	132.223	62.922	64.424	21.893	0.882	0.052	0.988	0.055
HD 010516	54769.774	E1/E2	131.148	66.438	64.682	20.541	0.888	0.050	0.994	0.053
HD 010516	54769.782	E1/E2	129.555	70.870	64.970	18.783	0.900	0.049	1.005	0.052
HD 010516	55116.910	S1/E1	−107.331	−731.650	325.344	198.200	0.809	0.052	0.907	0.055
HD 010516	55116.922	S1/E1	−70.218	−736.912	325.683	211.070	0.774	0.041	0.869	0.043
HD 010516	55128.868	E1/E2	101.151	110.159	65.798	7.388	0.992	0.035	1.041	0.037
HD 010516	55128.883	E1/E2	90.130	118.704	65.574	11.468	0.995	0.036	1.044	0.038
HD 010516	55128.895	E1/E2	84.477	122.399	65.432	13.929	0.977	0.041	1.025	0.043
HD 010516	55131.856	E1/E2	102.124	109.303	65.813	7.150	0.954	0.034	1.010	0.036
HD 010516	55131.864	E1/E2	97.846	112.933	65.741	8.407	0.934	0.038	0.988	0.040
HD 010516	55131.872	E1/E2	94.108	115.844	65.665	9.815	0.997	0.028	1.053	0.030
HD 010516	55131.876	E1/E2	89.598	119.070	65.561	11.696	0.930	0.032	0.980	0.034
HD 010516	55152.739	E1/W1	688.207	157.539	310.617	164.924	0.610	0.014	0.649	0.015
HD 010516	55152.743	E1/W1	685.155	179.254	311.589	157.372	0.611	0.015	0.663	0.016
HD 010516	55152.751	E1/W1	681.154	199.973	312.330	149.851	0.610	0.019	0.674	0.020
HD 010516	55152.758	E1/W1	676.420	219.393	312.862	142.520	0.635	0.024	0.710	0.025
HD 010516	55152.762	E1/W1	670.547	239.335	313.245	134.708	0.643	0.023	0.722	0.024
HD 010516	55153.754	E1/W1	677.482	215.359	312.765	144.065	0.564	0.019	0.633	0.021
HD 010516	55153.762	E1/W1	668.702	244.959	313.323	132.452	0.588	0.022	0.664	0.023
HD 010516	55153.766	E1/W1	661.393	265.109	313.495	124.181	0.639	0.022	0.714	0.023
HD 010516	55153.774	E1/W1	653.107	284.940	313.500	115.751	0.660	0.026	0.724	0.028
HD 010516	55153.782	E1/W1	643.799	304.566	313.344	107.126	0.644	0.024	0.687	0.025
HD 022192	54754.914	S1/W1	396.051	−484.932	275.466	274.850	0.570	0.020	...	...
HD 022192	54754.941	S1/W1	440.224	−432.862	271.628	271.425	0.594	0.019	...	...
HD 022192	54754.973	S1/W1	475.710	−367.638	264.512	261.392	0.612	0.019	...	...
HD 022192	54754.980	S1/W1	483.126	−346.949	261.689	257.091	0.640	0.017	...	...
HD 022192	54754.988	S1/W1	487.960	−329.929	259.152	253.183	0.664	0.017	...	...
HD 022192	54754.996	S1/W1	491.828	−312.155	256.290	248.755	0.616	0.016	...	...
HD 022192	54755.004	S1/W1	494.654	−293.205	252.989	243.655	0.652	0.015	...	...
HD 022192	54755.012	S1/W1	496.121	−275.144	249.595	238.433	0.695	0.018	...	...
HD 022192	54755.019	S1/W1	496.414	−257.767	246.093	233.080	0.687	0.017	...	...
HD 022192	54755.027	S1/W1	495.522	−239.275	242.098	227.029	0.654	0.014	...	...
HD 022192	54761.008	S1/E1	31.538	−744.865	328.007	254.144	0.626	0.031	...	...
HD 022192	54761.016	S1/E1	60.588	−742.831	327.904	261.564	0.645	0.033	...	...
HD 022192	54761.028	S1/E1	90.950	−739.309	327.721	268.924	0.612	0.031	...	...
HD 022192	54761.035	S1/E1	115.975	−735.302	327.505	274.676	0.620	0.033	...	...
HD 022192	54761.043	S1/E1	136.228	−731.306	327.283	279.113	0.642	0.035	...	...
HD 022192	54761.051	S1/E1	165.376	−724.320	326.875	285.138	0.527	0.030	...	...
HD 022192	54761.059	S1/E1	192.011	−716.593	326.397	290.248	0.550	0.032	...	...
HD 022192	54767.844	E1/E2	133.292	60.179	64.343	25.844	0.951	0.035	...	...
HD 022192	54767.852	E1/E2	132.335	63.837	64.643	24.805	0.992	0.050	...	...
HD 022192	54767.856	E1/E2	131.287	67.204	64.889	23.841	0.958	0.051	...	...

Continued on Next Page...

Table 6.5 – Continued

Star	Date (HJD −2400000)	Telescope Pair	u (cycles arcsec^{-1})	v (cycles arcsec^{-1})	Baseline (m)	Effective baseline (m)	V	δV	V_{corr}	δV_{corr}
HD 022192	54767.864	E1/E2	129.725	71.458	65.160	22.626	0.915	0.055	...	...
HD 022192	54767.891	E1/E2	120.558	88.550	65.811	18.207	0.933	0.058	...	...
HD 022192	54767.899	E1/E2	118.209	91.831	65.857	17.569	0.989	0.059	...	...
HD 022192	55131.930	E1/E2	105.236	106.142	65.760	16.662	0.994	0.031	...	...
HD 022192	55131.934	E1/E2	101.202	109.690	65.662	17.098	0.954	0.035	...	...
HD 022192	55131.950	E1/E2	93.269	115.809	65.421	18.612	0.990	0.037	...	...
HD 023630	54756.825	S1/W1	167.341	−549.381	252.672	252.672	0.964	0.069	...	...
HD 023630	54756.868	S1/W1	282.276	−525.282	262.360	262.360	0.921	0.058	...	...
HD 023630	54757.778	S1/W1	35.734	−560.721	247.197	247.197	0.982	0.043	...	...
HD 023630	54757.798	S1/W1	95.433	−557.466	248.832	248.832	0.960	0.046	...	...
HD 023630	54757.825	S1/W1	176.327	−548.027	253.285	253.285	0.864	0.046	...	...
HD 023630	54792.767	E1/E2	135.180	61.139	65.274	65.274	0.898	0.033	...	...
HD 023630	54792.779	E1/E2	134.040	66.114	65.756	65.756	0.938	0.042	...	...
HD 023630	54792.795	E1/E2	131.545	71.475	65.867	65.867	0.880	0.064	...	...
HD 023630	54792.822	E1/E2	124.778	79.887	65.185	65.185	0.857	0.035	...	...
HD 023630	54792.838	E1/E2	118.104	85.475	64.142	64.142	0.814	0.034	...	...
HD 023630	54793.806	E1/E2	128.331	76.037	65.628	65.628	0.995	0.043	...	...
HD 023630	54793.818	E1/E2	124.264	80.381	65.113	65.113	0.867	0.047	...	...
HD 023630	54793.834	E1/E2	119.532	84.406	64.379	64.379	0.931	0.046	...	...
HD 023630	54793.846	E1/E2	114.828	87.738	63.580	63.580	0.918	0.052	...	...
HD 023630	54793.853	E1/E2	110.004	90.682	62.722	62.722	0.907	0.049	...	...
HD 023630	54793.873	E1/E2	98.911	96.211	60.708	60.708	0.833	0.053	...	...
HD 023630	54793.885	E1/E2	92.072	98.996	59.480	59.480	0.915	0.062	...	...
HD 023630	55153.806	E1/W1	690.865	158.091	311.812	311.812	0.896	0.061	...	...
HD 023630	55153.814	E1/W1	690.464	169.092	312.756	312.756	0.936	0.066	...	...
HD 023862	54757.860	S1/W1	271.038	−528.484	261.309	261.988	0.752	0.035	...	...
HD 023862	54757.876	S1/W1	310.060	−516.946	265.211	262.910	0.759	0.027	0.873	0.031
HD 023862	54757.888	S1/W1	341.209	−505.860	268.456	262.534	0.790	0.024	0.902	0.028
HD 023862	54757.919	S1/W1	400.768	−478.212	274.511	260.014	0.872	0.034	0.994	0.039
HD 023862	54757.942	S1/W1	436.869	−454.827	277.464	248.860	0.818	0.035	0.930	0.040
HD 023862	54757.985	S1/W1	484.700	−402.299	277.134	248.847	0.836	0.043	0.954	0.049
HD 023862	54792.830	E1/E2	122.541	81.960	64.861	31.198	0.944	0.044	1.079	0.050
HD 023862	54793.826	E1/E2	123.236	81.343	64.966	31.107	0.939	0.046	1.074	0.052
HD 023862	54793.849	E1/E2	113.734	88.465	63.394	32.322	0.974	0.056	1.104	0.064
HD 025940	54756.711	S1/W1	−218.655	−593.974	278.471	241.216	0.761	0.042	...	...
HD 025940	54756.726	S1/W1	−182.276	−605.864	278.360	241.079	0.751	0.044	...	...
HD 025940	54756.746	S1/W1	−120.276	−620.573	278.110	241.444	0.779	0.045	...	...

Continued on Next Page. . .

Table 6.5 – Continued

Star	Date (HJD−2400000)	Telescope Pair	u (cycles arcsec^{-1})	v (cycles arcsec^{-1})	Baseline (m)	Effective baseline (m)	V	δV	V_{corr}	δV_{corr}
HD 025940	54756.754	S1/W1	−89.8550	−625.449	278.000	241.913	0.811	0.049	…	…
HD 025940	54756.765	S1/W1	−55.292	−629.230	277.905	242.681	0.845	0.050	…	…
HD 025940	54756.777	S1/W1	−23.801	−631.092	277.855	243.593	0.876	0.051	…	…
HD 025940	54756.789	S1/W1	8.924	−631.455	277.845	244.748	0.792	0.046	…	…
HD 025940	54756.797	S1/W1	9.953	−630.324	277.876	246.029	0.748	0.040	…	…
HD 025940	54757.703	S1/W1	−231.784	−589.029	278.493	241.323	0.841	0.050	…	…
HD 025940	54757.715	S1/W1	−201.126	−600.025	278.425	241.119	0.783	0.048	…	…
HD 025940	54757.734	S1/W1	−142.573	−616.044	278.200	241.223	0.715	0.042	…	…
HD 025940	54757.703	S1/W1	−231.784	−589.029	278.493	241.323	0.843	0.049	…	…
HD 025940	54757.715	S1/W1	−201.126	−600.025	278.425	241.119	0.800	0.049	…	…
HD 025940	54757.734	S1/W1	−142.573	−616.044	278.200	241.223	0.730	0.042	…	…
HD 025940	54757.746	S1/W1	−108.068	−622.708	278.064	241.609	0.648	0.034	…	…
HD 025940	54760.969	S1/E1	−157.314	−727.311	327.390	284.001	0.785	0.044	…	…
HD 025940	54760.977	S1/E1	−130.427	−733.384	327.725	284.706	0.792	0.043	…	…
HD 025940	54760.984	S1/E1	−101.866	−738.510	327.993	285.508	0.807	0.043	…	…
HD 025940	54794.775	E1/E2	135.242	46.831	62.968	60.035	0.944	0.044	…	…
HD 025940	54794.779	E1/E2	134.880	51.319	63.493	60.291	0.911	0.048	…	…
HD 025940	54794.786	E1/E2	134.312	55.403	63.922	60.470	0.949	0.055	…	…
HD 025940	54794.794	E1/E2	133.376	60.087	64.361	60.614	0.892	0.052	…	…
HD 025940	54794.802	E1/E2	132.198	64.546	64.725	60.691	0.907	0.055	…	…
HD 025940	54794.806	E1/E2	130.896	68.544	65.008	60.711	0.913	0.054	…	…
HD 025940	54794.814	E1/E2	129.250	72.798	65.264	60.684	0.892	0.054	…	…
HD 025940	54794.821	E1/E2	127.503	76.677	65.459	60.616	0.863	0.054	…	…
HD 025940	54794.829	E1/E2	125.009	81.470	65.648	60.474	0.947	0.062	…	…
HD 025940	55152.954	E1/W1	474.998	488.627	299.815	267.938	0.808	0.025	…	…
HD 025940	55153.954	E1/W1	468.329	493.237	299.244	267.042	0.746	0.017	…	…
HD 037202	54756.956	S1/W1	315.314	−504.611	261.789	242.145	0.400	0.024	…	…
HD 037202	54756.964	S1/W1	340.858	−496.489	264.961	249.143	0.354	0.024	…	…
HD 037202	54756.995	S1/W1	400.023	−472.348	272.327	264.031	0.402	0.023	…	…
HD 037202	54757.007	S1/W1	420.278	−461.613	274.658	268.510	0.371	0.021	…	…
HD 037202	54757.015	S1/W1	434.880	−452.671	276.174	271.435	0.358	0.022	…	…
HD 037202	54757.022	S1/W1	446.674	−444.449	277.230	273.545	0.380	0.021	…	…
HD 037202	54757.030	S1/W1	457.800	−435.568	278.014	275.251	0.390	0.022	…	…
HD 037202	54757.042	S1/W1	467.205	−426.849	278.424	276.385	0.354	0.019	…	…
HD 037202	54758.011	S1/W1	433.810	−453.368	276.069	271.232	0.461	0.040	…	…
HD 037202	54758.019	S1/W1	446.273	−444.747	277.198	273.478	0.477	0.045	…	…
HD 037202	54758.026	S1/W1	455.748	−437.307	277.889	274.962	0.435	0.040	…	…
HD 037202	54758.038	S1/W1	466.863	−427.191	278.415	276.351	0.465	0.045	…	…
HD 037202	54758.042	S1/W1	473.745	−419.831	278.498	276.932	0.483	0.043	…	…
HD 037202	54758.054	S1/W1	481.449	−409.981	278.215	277.172	0.430	0.039	…	…
HD 037202	54758.062	S1/W1	486.635	−401.723	277.629	276.920	0.407	0.040	…	…
HD 037202	54758.065	S1/W1	490.242	−394.520	276.857	276.373	0.430	0.040	…	…

Continued on Next Page…

Table 6.5 – Continued

Star	Date (HJD−2400000)	Telescope Pair	u (cycles arcsec^{-1})	v (cycles arcsec^{-1})	Baseline (m)	Effective baseline (m)	V	δV	V_{corr}	δV_{corr}
HD 037202	54759.831	S1/E1	−492.805	−525.895	317.086	63.133	0.879	0.053	⋯	⋯
HD 037202	54759.839	S1/E1	−492.697	−534.146	319.712	62.032	0.775	0.047	⋯	⋯
HD 037202	54759.847	S1/E1	−491.534	−542.350	322.031	60.727	0.735	0.047	⋯	⋯
HD 037202	54759.855	S1/E1	−490.830	−545.410	322.822	60.193	0.864	0.050	⋯	⋯
HD 037202	54759.862	S1/E1	−488.463	−552.947	324.604	58.782	0.857	0.041	⋯	⋯
HD 037202	54759.890	S1/E1	−485.327	−560.197	326.096	57.325	0.822	0.030	⋯	⋯
HD 037202	54760.866	S1/E1	−459.301	−593.680	330.240	50.643	0.910	0.034	⋯	⋯
HD 037202	54760.870	S1/E1	−481.087	−567.847	327.439	55.721	0.759	0.052	⋯	⋯
HD 037202	54760.874	S1/E1	−477.619	−573.084	328.221	54.610	0.846	0.061	⋯	⋯
HD 037202	54760.878	S1/E1	−469.439	−583.359	329.438	52.497	0.869	0.063	⋯	⋯
HD 037202	54794.060	E1/E2	18.406	108.120	48.253	21.920	0.928	0.058	⋯	⋯
HD 037202	54794.068	E1/E2	12.478	108.366	47.992	23.965	0.882	0.063	⋯	⋯
HD 037202	54794.853	E1/E2	133.543	67.679	65.868	31.835	0.915	0.028	⋯	⋯
HD 037202	54794.861	E1/E2	132.529	69.650	65.870	31.021	0.874	0.029	⋯	⋯
HD 037202	54794.869	E1/E2	131.329	71.550	65.799	30.160	0.956	0.031	⋯	⋯
HD 037202	54794.923	E1/E2	111.541	87.405	62.346	19.810	0.929	0.043	⋯	⋯
HD 037202	54794.931	E1/E2	108.236	89.064	61.669	18.368	0.891	0.043	⋯	⋯
HD 037202	54794.939	E1/E2	104.510	90.774	60.903	16.808	0.934	0.042	⋯	⋯
HD 058715	54793.003	E1/E2	111.322	74.499	58.933	46.343	0.932	0.057	⋯	⋯
HD 058715	54793.015	E1/E2	105.857	75.560	57.220	44.910	0.903	0.052	⋯	⋯
HD 058715	54793.046	E1/E2	82.961	76.871	49.760	38.982	0.993	0.044	⋯	⋯
HD 058715	54793.054	E1/E2	77.393	77.381	48.150	37.775	0.882	0.044	⋯	⋯
HD 058715	54794.007	E1/E2	107.874	75.186	57.851	45.434	0.928	0.048	⋯	⋯
HD 058715	54794.011	E1/E2	106.582	75.428	57.447	45.098	0.936	0.049	⋯	⋯
HD 058715	54794.039	E1/E2	90.678	77.888	52.592	41.179	0.989	0.063	⋯	⋯
HD 058715	54795.031	E1/E2	93.593	77.497	53.461	41.863	0.968	0.062	⋯	⋯
HD 058715	54795.043	E1/E2	87.086	78.339	51.536	40.361	0.944	0.060	⋯	⋯
HD 058715	54795.050	E1/E2	82.285	78.894	50.154	39.312	0.904	0.053	⋯	⋯
HD 058715	54795.058	E1/E2	75.292	79.617	48.211	37.883	0.883	0.050	⋯	⋯
HD 058715	54795.066	E1/E2	69.955	80.106	46.791	36.881	0.901	0.047	⋯	⋯
HD 058715	55152.980	E1/W1	686.529	183.952	312.702	258.769	0.607	0.039	⋯	⋯
HD 058715	55152.983	E1/W1	682.963	187.829	311.635	257.515	0.635	0.042	⋯	⋯
HD 058715	55152.991	E1/W1	676.859	192.760	309.634	255.360	0.715	0.026	⋯	⋯
HD 058715	55152.999	E1/W1	670.171	197.000	307.326	252.998	0.735	0.026	⋯	⋯
HD 058715	55153.976	E1/W1	687.046	183.269	312.844	258.950	0.587	0.026	⋯	⋯
HD 058715	55153.984	E1/W1	683.049	187.747	311.662	257.545	0.668	0.026	⋯	⋯
HD 058715	55153.987	E1/W1	677.491	192.309	309.847	255.583	0.678	0.028	⋯	⋯
HD 058715	55153.995	E1/W1	671.522	196.209	307.798	253.474	0.718	0.030	⋯	⋯
HD 058715	55154.003	E1/W1	663.061	200.777	304.803	250.490	0.717	0.027	⋯	⋯
HD 109387	55009.693	S1/E2	96.843	−523.464	234.213	234.213	0.925	0.058	⋯	⋯

Continued on Next Page...

Table 6.5 – Continued

Star	Date (HJD−2400000)	Telescope Pair	u (cycles arcsec^{-1})	v (cycles arcsec^{-1})	Baseline (m)	Effective baseline (m)	V	δV	V_{corr}	δV_{corr}
HD 109387	55009.709	S1/E2	135.285	−512.037	233.008	233.008	0.946	0.053	...	...
HD 109387	55009.717	S1/E2	152.810	−505.398	232.298	232.298	0.875	0.051	...	...
HD 109387	55009.740	S1/E2	202.086	−481.294	229.660	229.660	0.798	0.050	...	...
HD 109387	55044.685	S1/E1	288.533	−571.023	281.480	281.480	0.744	0.046	...	...
HD 109387	55340.800	S2/W1	454.859	−39.202	200.854	200.854	0.872	0.055	...	...
HD 109387	55340.831	S2/W1	432.543	37.965	191.026	191.026	0.915	0.060	...	...
HD 109387	55340.843	S2/W1	417.555	71.308	186.360	186.360	0.907	0.045	...	...
HD 138749	54976.937	E1/E2	44.376	121.248	56.805	52.440	0.937	0.036	1.052	0.041
HD 138749	54976.957	E1/E2	30.815	123.292	55.913	53.560	0.932	0.043	1.061	0.049
HD 138749	55340.890	S2/W1	460.737	−296.485	241.040	146.197	0.945	0.048	1.038	0.052
HD 138749	55368.678	S1/E1	−399.306	−634.859	329.970	272.403	0.864	0.044	0.904	0.046
HD 138749	55368.694	S1/E1	−373.597	−651.798	330.534	280.073	0.825	0.041	0.937	0.046
HD 138749	55368.706	S1/E1	−344.618	−667.870	330.650	287.443	0.899	0.052	0.956	0.056
HD 138749	55381.760	S1/E1	−102.050	−735.429	326.662	321.006	0.864	0.056	0.938	0.060
HD 138749	55381.787	S1/E1	−18.564	−740.805	326.029	325.092	0.932	0.056	1.000	0.060
HD 138749	55382.740	S1/E1	−147.357	−729.256	327.330	317.432	0.866	0.045	0.915	0.047
HD 138749	55382.763	S1/E1	−86.244	−737.030	326.478	322.023	0.828	0.040	0.830	0.041
HD 142926	54666.774	S1/E1	30.879	−750.619	330.524	107.198	0.897	0.096	...	...
HD 142926	54666.782	S1/E1	53.255	−749.322	330.506	112.612	0.857	0.106	...	...
HD 142926	54666.833	S1/E1	209.170	−719.762	329.770	159.389	0.837	0.140	...	...
HD 142926	55009.865	S1/E2	160.860	−607.210	276.365	128.805	0.933	0.053	...	...
HD 142926	55009.884	S1/E2	200.328	−592.994	275.381	141.721	0.963	0.056	...	...
HD 142926	55009.888	S1/E2	214.384	−586.912	274.907	146.379	0.896	0.051	...	...
HD 142926	55009.896	S1/E2	227.778	−580.553	274.378	150.831	0.899	0.050	...	...
HD 142926	55009.920	S1/E2	267.352	−557.979	272.215	163.967	0.860	0.071	...	...
HD 142926	55367.771	S1/E1	−226.953	−713.827	329.549	102.526	0.913	0.051	...	...
HD 142926	55367.783	S1/E1	−195.798	−723.839	329.908	96.554	0.958	0.056	...	...
HD 142926	55367.791	S1/E1	−166.932	−731.570	330.137	92.492	0.964	0.059	...	...
HD 142926	55367.799	S1/E1	−141.225	−737.295	330.280	90.200	0.855	0.048	...	...
HD 142926	55367.818	S1/E1	−89.774	−745.697	330.448	89.627	0.979	0.054	...	...
HD 142926	55367.826	S1/E1	−62.982	−748.541	330.494	91.432	0.967	0.060	...	...
HD 142926	55367.846	S1/E1	−7.623	−751.234	330.533	99.191	0.979	0.069	...	...
HD 142926	55368.838	S1/E1	−22.053	−750.940	330.529	96.697	0.943	0.032	...	...
HD 142926	55368.846	S1/E1	12.878	−751.160	330.532	103.228	0.944	0.031	...	...
HD 142926	55368.857	S1/E1	46.772	−749.770	330.512	110.993	0.898	0.030	...	...
HD 142926	55368.865	S1/E1	69.455	−747.947	330.485	116.817	0.889	0.029	...	...
HD 142926	55368.873	S1/E1	92.188	−745.391	330.443	123.064	0.921	0.030	...	...
HD 142926	55381.829	S1/E1	65.757	−748.294	330.490	115.838	0.902	0.132	...	...
HD 142926	55382.779	S1/E1	−74.464	−747.447	330.477	90.489	0.948	0.045	...	...
HD 142926	55382.790	S1/E1	−42.888	−750.010	330.516	93.662	0.982	0.046	...	...

Continued on Next Page. . .

Table 6.5 – Continued

Star	Date (HJD−2400000)	Telescope Pair	u (cycles arcsec⁻¹)	v (cycles arcsec⁻¹)	Baseline (m)	Effective baseline (m)	V	δV	V_corr	δV_corr
HD 142926	55382.802	S1/E1	−15.243	−751.115	330.531	97.836	0.924	0.049	...	...
HD 142926	55382.806	S1/E1	7.932	−751.231	330.532	102.205	0.962	0.049	...	...
HD 142926	55382.814	S1/E1	30.267	−750.645	330.525	107.057	0.884	0.045	...	...
HD 142983	55011.700	S1/W2	112.136	−295.380	139.006	70.132	0.988	0.074	...	...
HD 142983	55011.708	S1/W2	123.875	−296.626	141.428	69.030	0.938	0.069	...	...
HD 142983	55011.716	S1/W2	135.067	−297.955	143.929	68.210	0.930	0.072	...	...
HD 142983	55013.692	S1/W2	107.516	−294.930	138.111	70.632	0.950	0.051	...	...
HD 142983	55013.700	S1/W2	118.650	−296.054	140.324	69.490	0.967	0.050	...	...
HD 142983	55046.674	S1/W1	463.050	−336.457	251.826	116.205	0.875	0.029	...	...
HD 142983	55046.682	S1/W1	471.151	−342.022	256.149	118.248	0.916	0.035	...	...
HD 142983	55046.689	S1/W1	478.538	−348.018	260.328	120.081	0.888	0.042	...	...
HD 142983	55046.701	S1/W1	488.031	−358.161	266.333	122.365	0.882	0.046	...	...
HD 142983	55046.713	S1/W1	492.957	−366.121	270.157	123.481	0.850	0.043	...	...
HD 142983	55046.721	S1/W1	495.510	−373.100	272.895	124.000	0.850	0.044	...	...
HD 142983	55046.729	S1/W1	496.428	−379.637	274.956	124.116	0.775	0.046	...	...
HD 148184	54627.787	S2/W2	126.666	−224.698	113.484	110.056	0.823	0.040	...	...
HD 148184	54627.799	S2/W2	139.956	−227.260	117.426	113.641	0.893	0.047	...	...
HD 148184	54627.807	S2/W2	152.452	−230.007	121.405	117.284	0.811	0.046	...	...
HD 148184	54628.787	S2/W2	128.750	−225.077	114.082	110.598	0.872	0.063	...	...
HD 148184	54628.799	S2/W2	145.465	−228.429	119.148	115.215	0.811	0.055	...	...
HD 148184	54628.810	S2/W2	160.231	−231.902	124.014	119.682	0.914	0.057	...	...
HD 148184	54628.822	S2/W2	174.203	−235.711	128.952	124.243	0.867	0.055	...	...
HD 148184	54628.834	S2/W2	187.099	−239.768	133.806	128.749	0.919	0.057	...	...
HD 148184	55013.786	S1/W1	221.156	−292.421	161.305	155.327	0.696	0.044	...	...
HD 148184	55013.806	S1/W1	241.808	−300.476	169.689	163.154	0.753	0.046	...	...
HD 164284	54627.825	S2/W2	89.106	−328.711	149.840	137.424	0.716	0.040	0.826	0.046
HD 164284	54627.833	S2/W2	102.037	−328.316	151.262	137.230	0.709	0.044	0.807	0.050
HD 164284	54627.845	S2/W2	114.585	−327.870	152.806	137.136	0.740	0.040	0.842	0.046
HD 164284	54627.853	S2/W2	126.037	−327.406	154.351	137.129	0.826	0.044	0.949	0.050
HD 164284	54627.861	S2/W2	137.571	−326.880	156.033	137.199	0.840	0.044	0.955	0.050
HD 164284	54627.868	S2/W2	149.041	−326.291	157.823	137.341	0.844	0.042	0.968	0.048
HD 164284	54627.876	S2/W2	159.587	−325.685	159.567	137.534	0.858	0.046	0.978	0.052
HD 164284	54627.888	S2/W2	171.767	−324.899	161.691	137.827	0.872	0.048	0.997	0.055
HD 164284	54627.896	S2/W2	181.990	−324.157	163.556	138.128	0.852	0.044	0.975	0.050
HD 164284	54627.907	S2/W2	194.160	−323.155	165.865	138.544	0.920	0.049	1.051	0.056
HD 164284	54627.915	S2/W2	203.831	−322.248	167.759	138.912	0.806	0.044	0.925	0.050
HD 164284	54627.923	S2/W2	212.586	−321.319	169.508	139.267	0.792	0.042	0.900	0.048

Continued on Next Page...

Table 6.5 – Continued

Star	Date (HJD−2400000)	Telescope Pair	u (cycles arcsec⁻¹)	v (cycles arcsec⁻¹)	Baseline (m)	Effective baseline (m)	V	δV	V_{corr}	δV_{corr}
HD 164284	54627.935	S2/W2	220.166	−320.410	171.041	139.582	0.891	0.054	1.022	0.062
HD 166014	54973.941	E1/E2	117.932	88.141	64.776	63.092	0.865	0.026	0.943	0.029
HD 166014	54973.956	E1/E2	108.693	94.991	63.510	60.733	0.868	0.030	0.947	0.032
HD 166014	54973.968	E1/E2	104.262	97.711	62.867	59.522	0.899	0.025	0.980	0.027
HD 166014	54973.976	E1/E2	99.882	100.132	62.225	58.290	0.894	0.022	0.974	0.024
HD 166014	54973.987	E1/E2	92.572	103.694	61.156	56.174	0.892	0.029	0.973	0.031
HD 166014	54973.995	E1/E2	88.031	105.652	60.504	54.832	0.901	0.026	0.982	0.029
HD 166014	54974.003	E1/E2	82.702	107.736	59.755	53.238	0.911	0.030	0.993	0.033
HD 166014	55010.703	S1/E2	−352.074	−516.042	274.847	238.510	0.681	0.045	0.742	0.049
HD 166014	55010.711	S1/E2	−345.619	−522.711	275.699	237.513	0.699	0.044	0.762	0.048
HD 166014	55010.718	S1/E2	−338.381	−529.463	276.454	236.262	0.780	0.051	0.850	0.056
HD 166014	55365.777	S1/W1	233.844	−555.002	264.970	115.293	0.887	0.027	0.967	0.029
HD 166014	55365.800	S1/W1	292.489	−537.299	269.148	120.120	0.796	0.031	0.867	0.034
HD 166014	55366.781	S1/W1	247.708	−551.302	265.911	115.971	0.793	0.041	0.864	0.044
HD 166014	55366.789	S1/W1	269.495	−544.901	267.454	117.620	0.836	0.049	0.911	0.053
HD 166014	55366.797	S1/W1	293.036	−537.107	269.189	120.189	0.941	0.061	1.026	0.066
HD 166014	55366.804	S1/W1	314.703	−529.032	270.823	123.257	0.940	0.056	1.025	0.061
HD 166014	55366.816	S1/W1	337.270	−519.570	272.530	127.139	0.902	0.058	0.983	0.064
HD 166014	55368.742	S1/E1	−462.476	−579.387	326.159	292.999	0.853	0.041	0.930	0.045
HD 166014	55368.754	S1/E1	−452.749	−591.114	327.587	291.717	0.764	0.032	0.832	0.035
HD 166014	55368.761	S1/E1	−441.205	−603.092	328.762	289.841	0.731	0.029	0.797	0.031
HD 166014	55368.773	S1/E1	−421.018	−620.687	329.975	285.966	0.772	0.033	0.841	0.036
HD 166014	55368.781	S1/E1	−408.099	−630.362	330.383	283.215	0.700	0.033	0.763	0.036
HD 166014	55368.793	S1/E1	−389.298	−642.828	330.641	278.950	0.832	0.046	0.907	0.050
HD 166014	55368.797	S1/E1	−377.650	−649.772	330.653	276.188	0.903	0.049	0.984	0.053
HD 166014	55368.804	S1/E1	−364.233	−657.154	330.564	272.917	0.758	0.038	0.827	0.042
HD 166014	55368.820	S1/E1	−334.985	−671.341	330.094	265.532	0.863	0.042	0.940	0.046
HD 166014	55381.695	S1/E1	−475.834	−559.216	323.048	293.996	0.771	0.049	0.841	0.053
HD 166014	55381.703	S1/E1	−468.553	−570.969	324.962	293.596	0.781	0.052	0.852	0.057
HD 166014	55381.711	S1/E1	−459.579	−583.074	326.638	292.653	0.771	0.056	0.840	0.061
HD 166014	55381.718	S1/E1	−450.679	−593.395	327.833	291.405	0.752	0.051	0.819	0.056
HD 166014	55381.726	S1/E1	−441.645	−602.666	328.725	289.918	0.725	0.048	0.790	0.053
HD 166014	55382.687	S1/E1	−479.906	−551.443	321.625	293.991	0.704	0.044	0.768	0.048
HD 166014	55382.691	S1/E1	−475.065	−560.569	323.283	293.975	0.793	0.048	0.864	0.052
HD 166014	55382.699	S1/E1	−469.400	−569.709	324.771	293.663	0.879	0.050	0.958	0.055
HD 166014	55382.707	S1/E1	−462.058	−579.931	326.231	292.951	0.808	0.051	0.880	0.056
HD 166014	55382.711	S1/E1	−454.688	−588.915	327.340	291.998	0.824	0.049	0.898	0.054
HD 166014	55383.711	S1/W1	184.316	−566.091	261.928	115.219	0.818	0.042	0.892	0.045
HD 166014	55383.718	S1/W1	204.183	−562.025	263.083	114.813	0.887	0.046	0.967	0.050
HD 166014	55405.655	W1/S1	−202.470	562.417	262.976	114.824	0.846	0.050	0.922	0.054
HD 166014	55405.667	W1/S1	−233.675	555.070	264.956	115.286	0.966	0.051	1.053	0.055
HD 166014	55405.694	W1/S1	−304.280	533.059	270.032	121.696	0.850	0.046	0.927	0.050

Continued on Next Page. . .

Table 6.5 – Continued

Star	Date (HJD−2400000)	Telescope Pair	u (cycles arcsec^{-1})	v (cycles arcsec^{-1})	Baseline (m)	Effective baseline (m)	V	δV	V_{corr}	δV_{corr}
HD 166014	55405.702	W1/S1	−324.862	524.943	271.591	124.917	0.954	0.049	1.040	0.053
HD 166014	55405.710	W1/S1	−343.167	516.929	272.970	128.262	0.876	0.047	0.955	0.051
HD 166014	55405.718	W1/S1	−361.824	507.871	274.339	132.118	0.826	0.046	0.900	0.050
HD 166014	55405.655	W1/S1	−202.470	562.417	262.976	114.824	0.846	0.050	0.922	0.054
HD 166014	55405.667	W1/S1	−233.675	555.070	264.956	115.286	0.966	0.051	1.053	0.055
HD 166014	55405.694	W1/S1	−304.280	533.059	270.032	121.696	0.850	0.046	0.927	0.050
HD 166014	55405.702	W1/S1	−324.862	524.943	271.591	124.917	0.954	0.049	1.040	0.053
HD 166014	55405.710	W1/S1	−343.167	516.929	272.970	128.262	0.876	0.047	0.955	0.051
HD 166014	55405.718	W1/S1	−361.824	507.871	274.339	132.118	0.826	0.046	0.900	0.050
HD 198183	55010.885	S1/E2	−248.823	−579.262	277.372	276.761	0.635	0.072	1.083	0.124
HD 198183	55010.897	S1/E2	−223.674	−590.906	277.979	276.831	0.668	0.073	1.091	0.121
HD 198183	55365.845	S1/W1	110.766	−603.531	269.966	251.306	0.664	0.027	1.029	0.041
HD 198183	55365.857	S1/W1	151.449	−596.899	270.935	249.108	0.704	0.026	1.069	0.040
HD 198183	55365.865	S1/W1	172.252	−592.632	271.526	248.034	0.632	0.026	1.047	0.042
HD 198183	55365.873	S1/W1	191.251	−588.185	272.116	247.082	0.514	0.020	0.832	0.031
HD 198183	55365.877	S1/W1	212.566	−582.540	272.826	246.042	0.572	0.022	0.983	0.034
HD 198183	55365.912	S1/W1	297.314	−552.170	275.912	242.113	0.732	0.025	1.030	0.043
HD 198183	55367.967	S1/E1	−237.700	−712.916	330.632	328.516	0.521	0.025	0.835	0.040
HD 198183	55367.978	S1/E1	−207.543	−722.002	330.518	327.446	0.641	0.025	1.048	0.041
HD 198183	55367.990	S1/E1	−176.748	−729.759	330.350	326.147	0.597	0.025	0.982	0.042
HD 198183	55368.002	S1/E1	−147.037	−735.907	330.172	324.735	0.610	0.028	1.045	0.047
HD 198183	55381.956	S1/E1	−162.820	−732.799	330.267	325.503	0.587	0.046	0.991	0.078
HD 198183	55381.983	S1/E1	−87.6450	−744.582	329.851	321.557	0.543	0.040	0.881	0.066
HD 198183	55381.995	S1/E1	−49.5940	−747.766	329.712	319.335	0.598	0.042	1.023	0.070
HD 198183	55382.842	S1/E1	−429.136	−600.319	324.662	324.178	0.590	0.034	1.004	0.059
HD 198183	55382.846	S1/E1	−418.669	−610.820	325.806	325.498	0.526	0.034	1.000	0.100
HD 198183	55382.854	S1/E1	−406.037	−622.303	326.916	326.762	0.611	0.035	1.000	0.100
HD 198183	55382.862	S1/E1	−393.004	−633.039	327.821	327.768	0.631	0.033	0.998	0.051
HD 198183	55382.874	S1/E1	−365.927	−652.508	329.141	329.133	0.600	0.032	1.000	0.100
HD 198183	55383.753	S1/W1	−23.4060	−610.649	268.860	259.400	0.599	0.021	0.987	0.033
HD 198183	55383.760	S1/W1	6.489	−610.952	268.812	257.503	0.542	0.019	0.816	0.028
HD 198183	55383.772	S1/W1	37.555	−610.131	268.943	255.581	0.674	0.020	1.024	0.031
HD 198183	55383.780	S1/W1	64.623	−608.465	269.208	253.956	0.621	0.023	0.886	0.035
HD 200120	55009.970	S1/E2	−88.246	−616.197	273.870	86.097	0.933	0.042	1.015	0.045
HD 200120	55009.982	S1/E2	−57.199	−620.607	274.201	85.011	0.864	0.044	0.941	0.048
HD 200120	55009.993	S1/E2	−29.247	−622.938	274.372	85.704	0.880	0.050	0.959	0.054
HD 200120	55043.741	S1/E1	−471.532	−489.003	298.873	201.254	0.766	0.040	0.832	0.043
HD 200120	55043.748	S1/E1	−464.247	−505.268	301.887	198.479	0.771	0.045	0.837	0.049
HD 200120	55043.756	S1/E1	−455.980	−521.176	304.670	195.354	0.773	0.047	0.842	0.051
HD 200120	55043.764	S1/E1	−447.224	−535.966	307.115	192.074	0.805	0.048	0.871	0.052

Continued on Next Page. . .

Table 6.5 – Continued

Star	Date (HJD−2400000)	Telescope Pair	u (cycles arcsec^{-1})	v (cycles arcsec^{-1})	Baseline (m)	Effective baseline (m)	V	δV	V_{corr}	δV_{corr}
HD 200120	55043.772	S1/E1	−437.289	−550.880	309.445	188.387	0.682	0.043	0.740	0.046
HD 200120	55043.780	S1/E1	−426.982	−564.750	311.492	184.603	0.751	0.041	0.816	0.045
HD 200120	55069.831	E1/E2	100.630	110.012	65.596	43.030	0.989	0.043	1.076	1.076
HD 200120	55069.843	E1/E2	94.069	115.029	65.377	40.448	0.993	0.051	1.081	1.081
HD 200120	55069.851	E1/E2	88.505	118.781	65.171	38.310	0.997	0.056	1.085	1.085
HD 200120	55069.858	E1/E2	82.816	122.213	64.952	36.175	0.953	0.053	1.038	0.057
HD 200120	55366.923	S1/W1	317.374	−546.760	278.143	174.911	0.968	0.038	1.050	0.042
HD 200120	55366.934	S1/W1	342.486	−530.269	277.729	183.497	0.938	0.036	1.020	0.039
HD 200120	55382.892	S1/E1	−347.147	−641.213	320.801	156.839	0.745	0.038	0.810	0.041
HD 200120	55382.900	S1/E1	−324.485	−656.784	322.303	149.544	0.731	0.035	0.795	0.038
HD 200120	55382.912	S1/E1	−302.793	−669.990	323.476	142.857	0.714	0.035	0.775	0.038
HD 200120	55382.919	S1/E1	−277.582	−683.543	324.585	135.499	0.764	0.037	0.831	0.040
HD 200120	55382.931	S1/E1	−245.074	−698.552	325.702	126.769	0.842	0.041	0.917	0.045
HD 202904	54688.926	S1/E1	−18.049	−747.138	328.809	127.427	0.872	0.045	...	...
HD 202904	54688.933	S1/E1	8.602	−747.284	328.799	135.631	0.766	0.039	...	...
HD 202904	54688.945	S1/E1	43.737	−746.215	328.870	146.820	0.768	0.042	...	...
HD 202904	54688.957	S1/E1	78.904	−743.691	329.033	158.310	0.759	0.046	...	...
HD 202904	54688.969	S1/E1	109.304	−740.306	329.238	168.389	0.807	0.049	...	...
HD 202904	54688.976	S1/E1	138.676	−735.936	329.483	178.197	0.644	0.040	...	...
HD 202904	54688.988	S1/E1	176.052	−728.726	329.836	190.705	0.607	0.038	...	...
HD 202904	54689.000	S1/E1	203.983	−722.046	330.107	200.028	0.674	0.042	...	...
HD 202904	54689.012	S1/E1	236.219	−712.834	330.392	210.711	0.726	0.048	...	...
HD 202904	55044.761	S1/E1	−462.100	−563.445	320.602	136.641	0.779	0.040	...	...
HD 202904	55044.769	S1/E1	−453.250	−576.138	322.517	132.771	0.818	0.049	...	...
HD 202904	55382.959	S1/E1	−212.399	−719.802	330.186	86.195	0.909	0.038	...	...
HD 202904	55382.967	S1/E1	−187.013	−726.241	329.943	88.507	0.821	0.034	...	...
HD 202904	55382.979	S1/E1	−154.719	−733.074	329.631	93.215	0.917	0.044	...	...
HD 202904	55382.987	S1/E1	−128.678	−737.548	329.396	98.226	0.861	0.039	...	...
HD 203467	55044.891	S1/E1	−185.852	−654.232	299.227	255.314	0.879	0.048	...	...
HD 203467	55044.903	S1/E1	−155.004	−664.531	300.217	253.607	0.839	0.048	...	...
HD 203467	55044.919	S1/E1	−109.489	−676.022	301.301	251.097	0.885	0.055	...	...
HD 203467	55044.926	S1/E1	−85.855	−680.349	301.703	249.823	0.827	0.050	...	...
HD 203467	55044.934	S1/E1	−63.105	−683.499	301.993	248.628	0.832	0.042	...	...
HD 203467	55044.942	S1/E1	−41.188	−685.611	302.187	247.512	0.855	0.043	...	...
HD 203467	55044.954	S1/E1	4.236	−687.155	302.329	245.339	0.857	0.045	...	...
HD 203467	55043.887	S1/E1	−210.332	−644.501	298.275	256.648	0.887	0.068	...	...
HD 203467	55043.895	S1/E1	−189.240	−652.971	299.105	255.501	0.832	0.067	...	...
HD 203467	55043.903	S1/E1	−165.099	−661.393	299.918	254.167	0.711	0.052	...	...
HD 203467	55043.911	S1/E1	−143.541	−667.829	300.531	252.971	0.784	0.057	...	...
HD 203467	55043.919	S1/E1	−120.150	−673.710	301.084	251.680	0.829	0.058	...	...

Continued on Next Page…

Table 6.5 – Continued

Star	Date (HJD−2400000)	Telescope Pair	u (cycles arcsec^{-1})	v (cycles arcsec^{-1})	Baseline (m)	Effective baseline (m)	V	δV	V_{corr}	δV_{corr}
HD 203467	55043.926	S1/E1	−95.132	−678.781	301.557	250.319	0.736	0.053	...	...
HD 203467	55043.934	S1/E1	−74.639	−682.025	301.858	249.229	0.746	0.050	...	...
HD 203467	55043.938	S1/E1	−52.206	−684.661	302.100	248.068	0.831	0.055	...	...
HD 203467	55043.946	S1/E1	−29.587	−686.367	302.257	246.938	0.693	0.045	...	...
HD 203467	55043.973	S1/E1	47.696	−685.077	302.138	243.468	0.731	0.042	...	...
HD 203467	55043.981	S1/E1	74.719	−682.014	301.857	242.422	0.767	0.047	...	...
HD 203467	55043.989	S1/E1	97.478	−678.358	301.518	241.614	0.905	0.054	...	...
HD 203467	55043.997	S1/E1	120.190	−673.701	301.084	240.878	0.864	0.060	...	...
HD 203467	55340.920	S2/W1	93.560	−548.997	245.010	196.078	0.855	0.042	...	...
HD 203467	55340.932	S2/W1	132.342	−540.130	244.655	195.480	0.895	0.044	...	...
HD 203467	55340.952	S2/W1	180.064	−524.571	243.999	195.365	0.934	0.046	...	...
HD 203467	55340.963	S2/W1	215.169	−509.503	243.321	195.725	0.903	0.045	...	...
HD 203467	55340.975	S2/W1	243.015	−495.085	242.633	196.279	0.889	0.049	...	...
HD 209409	54687.767	S1/E1	−428.715	−604.476	326.044	126.315	0.811	0.048	...	...
HD 209409	54688.779	S1/E1	−451.948	−559.568	316.460	136.914	0.759	0.043	...	...
HD 209409	54688.795	S1/E1	−433.490	−558.143	310.926	130.173	0.763	0.041	...	...
HD 209409	54688.806	S1/E1	−413.988	−556.905	305.301	123.146	0.734	0.036	...	...
HD 209409	54688.818	S1/E1	−392.844	−555.770	299.436	115.670	0.816	0.041	...	...
HD 209409	54688.838	S1/E1	−352.592	−554.012	288.922	101.995	0.826	0.049	...	...
HD 209409	55011.921	S1/W2	55.456	−363.928	161.963	80.066	0.936	0.062	...	...
HD 209409	55011.929	S1/W2	68.713	−364.034	162.990	84.897	0.943	0.067	...	...
HD 209409	55011.937	S1/W2	81.916	−364.163	164.222	89.801	0.855	0.057	...	...
HD 209409	55011.949	S1/W2	107.182	−364.481	167.148	99.393	0.854	0.057	...	...
HD 209409	55011.956	S1/W2	119.283	−364.667	168.805	104.067	0.958	0.057	...	...
HD 209409	55011.964	S1/W2	130.852	−364.868	170.540	108.576	0.794	0.050	...	...
HD 209409	55012.914	S1/W2	49.312	−363.887	161.560	77.863	0.840	0.040	...	...
HD 209409	55013.890	S1/W2	7.902	−363.736	160.068	63.799	0.870	0.044	...	...
HD 209409	55013.925	S1/W2	70.078	−364.046	163.107	85.400	0.804	0.036	...	...
HD 209409	55013.929	S1/W2	80.944	−364.153	164.124	89.437	0.925	0.034	...	...
HD 209409	55013.937	S1/W2	92.515	−364.285	165.360	93.794	0.954	0.043	...	...
HD 209409	55413.904	S1/E2	−107.555	−489.067	220.303	58.038	0.869	0.030	...	...
HD 209409	55413.916	S1/E2	−84.546	−488.843	218.256	61.262	0.869	0.030	...	...
HD 209409	55413.923	S1/E2	−65.526	−488.701	216.925	64.905	0.963	0.033	...	...
HD 209409	55413.931	S1/E2	−41.632	−488.575	215.724	70.513	0.963	0.036	...	...
HD 209409	55413.955	S1/E2	9.457	−488.494	214.950	85.310	0.936	0.043	...	...
HD 209409	55414.838	S1/E2	−242.611	−491.727	241.230	69.816	0.945	0.031	...	...
HD 209409	55414.853	S1/E2	−217.468	−491.022	236.260	64.101	0.955	0.029	...	...
HD 209409	55414.861	S1/E2	−199.716	−490.591	233.031	60.842	0.950	0.028	...	...
HD 209409	55414.869	S1/E2	−178.886	−490.148	229.549	58.007	0.940	0.028	...	...
HD 209409	55414.880	S1/E2	−157.221	−489.753	226.293	56.358	0.931	0.026	...	...

Table 6.5 – Continued

Star	Date (HJD−2400000)	Telescope Pair	u (cycles arcsec^{-1})	v (cycles arcsec^{-1})	Baseline (m)	Effective baseline (m)	V	δV	V_{corr}	δV_{corr}
HD 212076	55045.880	S1/W1	359.202	−456.312	255.499	255.368	0.967	0.043	...	...
HD 212076	55045.891	S1/W1	382.341	−450.810	260.068	259.829	0.935	0.039	...	...
HD 212076	55367.880	S1/E1	−490.121	−565.572	329.265	315.754	0.780	0.048	...	...
HD 212076	55367.892	S1/E1	−484.724	−573.431	330.348	316.900	0.873	0.050	...	...
HD 212076	55367.904	S1/E1	−477.105	−580.702	330.659	317.324	0.845	0.047	...	...
HD 212076	55367.916	S1/E1	−466.939	−587.908	330.315	317.148	0.921	0.048	...	...
HD 212076	55367.927	S1/E1	−454.366	−594.928	329.352	316.409	0.902	0.052	...	...
HD 212076	55367.939	S1/E1	−436.168	−603.074	327.452	314.849	0.991	0.056	...	...
HD 212076	55368.900	S1/E1	−479.483	−578.680	330.639	317.267	0.874	0.046	...	...
HD 212076	55368.920	S1/E1	−461.805	−590.962	329.972	316.896	0.900	0.048	...	...
HD 212076	55368.931	S1/E1	−443.510	−600.003	328.268	315.526	0.911	0.049	...	...
HD 217675	55044.819	S1/E1	−475.953	−505.723	305.541	290.158	0.743	0.043	0.950	0.055
HD 217675	55044.826	S1/E1	−468.254	−523.082	308.877	295.647	0.721	0.039	0.925	0.050
HD 217675	55043.811	S1/E1	−483.744	−483.104	300.788	282.589	0.852	0.043	1.000	0.100
HD 217675	55043.826	S1/E1	−472.681	−513.528	307.073	292.661	0.817	0.042	1.045	0.054
HD 217675	55043.850	S1/E1	−445.976	−560.784	315.234	306.536	0.854	0.046	1.094	0.059
HD 217675	55043.858	S1/E1	−434.472	−576.193	317.495	310.540	0.892	0.049	1.000	0.100
HD 217675	55043.865	S1/E1	−421.916	−591.043	319.495	314.126	0.866	0.056	1.112	0.071
HD 217675	55043.873	S1/E1	−408.693	−604.988	321.215	317.227	0.805	0.056	1.033	0.072
HD 217675	55045.811	S1/W1	96.826	−618.224	275.311	228.533	0.728	0.045	0.943	0.058
HD 217675	55045.815	S1/W1	112.630	−615.927	275.479	224.681	0.702	0.046	0.888	0.059
HD 217675	55045.826	S1/W1	151.470	−608.704	275.974	214.586	0.669	0.039	0.864	0.050
HD 217675	55045.850	S1/W1	212.086	−592.603	276.918	196.908	0.724	0.036	0.935	0.047
HD 217675	55045.858	S1/W1	238.145	−583.671	277.346	188.508	0.657	0.034	0.867	0.043
HD 217675	55046.803	S1/W1	84.6040	−619.753	275.198	231.414	0.761	0.034	0.973	0.044
HD 217675	55046.815	S1/W1	118.710	−614.946	275.549	223.161	0.780	0.038	0.984	0.049
HD 217675	55046.827	S1/W1	151.743	−608.645	275.978	214.512	0.882	0.040	1.000	0.100
HD 217675	55046.834	S1/W1	182.281	−601.295	276.436	205.909	0.825	0.039	1.052	0.050
HD 217675	55046.858	S1/W1	241.580	−582.395	277.402	187.361	0.804	0.039	1.058	0.050
HD 217675	55046.866	S1/W1	269.911	−570.920	277.840	177.526	0.644	0.033	0.839	0.042
HD 217675	55366.956	S1/W1	183.999	−600.828	276.460	205.404	0.716	0.029	0.920	0.038
HD 217675	55366.964	S1/W1	209.194	−593.508	276.867	197.806	0.749	0.031	0.956	0.040
HD 217675	55366.980	S1/W1	242.014	−582.223	277.405	187.212	0.770	0.032	0.979	0.041
HD 217675	55383.926	S1/W1	223.567	−588.828	277.107	193.271	0.825	0.039	1.069	0.050
HD 217675	55383.934	S1/W1	248.237	−579.852	277.509	185.111	0.824	0.037	1.059	0.047
HD 217675	55383.950	S1/W1	288.692	−562.311	278.096	170.607	0.904	0.050	1.000	0.100
HD 217675	55383.965	S1/W1	329.888	−540.167	278.468	154.134	0.907	0.052	1.000	0.100
HD 217675	55383.973	S1/W1	348.011	−528.757	278.499	146.223	0.811	0.050	1.043	0.064
HD 217675	55383.985	S1/W1	367.622	−515.015	278.391	137.107	0.700	0.044	0.892	0.056
HD 217675	55383.993	S1/W1	384.824	−501.550	278.132	128.551	0.786	0.048	1.008	0.062

Table 6.5 – Continued

Star	Date (HJD−2400000)	Telescope Pair	u (cycles arcsec^{-1})	v (cycles arcsec^{-1})	Baseline (m)	Effective baseline (m)	V	δV	V_{corr}	δV_{corr}
HD 217891	54687.821	S1/E1	−456.640	−578.466	324.245	322.770	0.741	0.049	…	…
HD 217891	54689.911	S1/E1	−265.340	−593.779	286.138	285.201	0.816	0.055	…	…
HD 217891	54689.923	S1/E1	−237.812	−594.869	281.859	280.178	0.741	0.051	…	…
HD 217891	54689.935	S1/E1	−208.736	−595.854	277.774	275.059	0.734	0.043	…	…
HD 217891	54689.993	S1/E1	−27.3410	−598.893	263.765	248.600	0.902	0.058	…	…
HD 217891	54690.009	S1/E1	14.6570	−598.929	263.586	244.092	0.891	0.057	…	…
HD 217891	54690.907	S1/W1	406.283	−410.876	254.223	184.300	0.882	0.038	…	…
HD 217891	54690.919	S1/W1	429.165	−408.495	260.676	187.690	0.948	0.039	…	…
HD 217891	54691.927	S1/W1	441.134	−407.041	264.081	189.529	0.822	0.079	…	…
HD 217891	54691.943	S1/W1	460.388	−404.244	269.554	192.545	0.883	0.087	…	…
HD 217891	55011.982	S1/W2	90.2910	−393.355	177.562	154.737	0.783	0.044	…	…
HD 217891	55011.986	S1/W2	102.915	−393.067	178.764	154.193	0.814	0.050	…	…
HD 217891	55012.955	S1/W2	44.4740	−394.064	174.474	157.605	0.932	0.038	…	…
HD 217891	55012.963	S1/W2	60.8400	−393.869	175.343	156.422	0.972	0.037	…	…
HD 217891	55012.979	S1/W2	88.4290	−393.394	177.398	154.826	0.952	0.036	…	…
HD 217891	55012.986	S1/W2	102.024	−393.089	178.675	154.228	0.908	0.037	…	…
HD 217891	55012.994	S1/W2	115.925	−392.726	180.155	153.746	0.919	0.034	…	…
HD 217891	55013.959	S1/W2	61.197	−393.864	175.365	156.398	0.898	0.044	…	…
HD 217891	55013.971	S1/W2	83.840	−393.486	177.005	155.057	0.971	0.041	…	…
HD 217891	55013.979	S1/W2	95.628	−393.238	178.053	154.494	0.941	0.046	…	…
HD 217891	55013.986	S1/W2	106.524	−392.977	179.135	154.058	0.864	0.038	…	…
HD 217891	55013.994	S1/W2	119.643	−392.619	180.580	153.640	0.894	0.042	…	…
HD 217891	55013.998	S1/W2	132.252	−392.228	182.112	153.349	0.821	0.038	…	…
HD 217891	55045.942	S1/W1	416.604	−409.857	257.121	185.806	0.909	0.036	…	…
HD 217891	55045.950	S1/W1	433.474	−407.991	261.901	188.348	0.935	0.036	…	…
HD 217891	55045.958	S1/W1	446.526	−406.324	265.617	190.369	0.877	0.034	…	…
HD 217891	55045.969	S1/W1	457.573	−404.699	268.757	192.102	0.919	0.035	…	…
HD 217891	55045.981	S1/W1	472.818	−401.951	273.033	194.488	0.744	0.033	…	…
HD 217891	55045.993	S1/W1	480.466	−400.193	275.110	195.646	0.889	0.047	…	…
HD 217891	55046.012	S1/W1	492.688	−395.930	278.084	197.241	0.860	0.044	…	…
HD 217891	55046.020	S1/W1	495.282	−394.131	278.481	197.390	0.808	0.042	…	…
HD 217891	55414.997	S1/E2	22.898	−527.803	232.421	214.139	0.851	0.043	…	…
HD 217891	55415.005	S1/E2	44.433	−527.677	232.969	212.205	0.947	0.051	…	…
HD 217891	55415.013	S1/E2	62.762	−527.505	233.709	210.730	0.880	0.052	…	…
HD 217891	55152.608	E1/W1	690.717	173.262	313.305	270.167	0.819	0.033	…	…
HD 217891	55152.616	E1/W1	690.649	175.406	313.507	270.612	0.783	0.036	…	…
HD 217891	55152.623	E1/W1	689.367	177.274	313.164	270.591	0.722	0.045	…	…
HD 217891	55153.592	E1/W1	687.498	169.694	311.552	268.309	0.815	0.036	…	…
HD 217891	55153.600	E1/W1	689.590	171.435	312.629	269.391	0.791	0.047	…	…
HD 217891	55153.592	E1/W1	687.498	169.694	311.552	268.309	0.815	0.036	…	…
HD 217891	55153.600	E1/W1	689.590	171.435	312.629	269.391	0.791	0.047	…	…
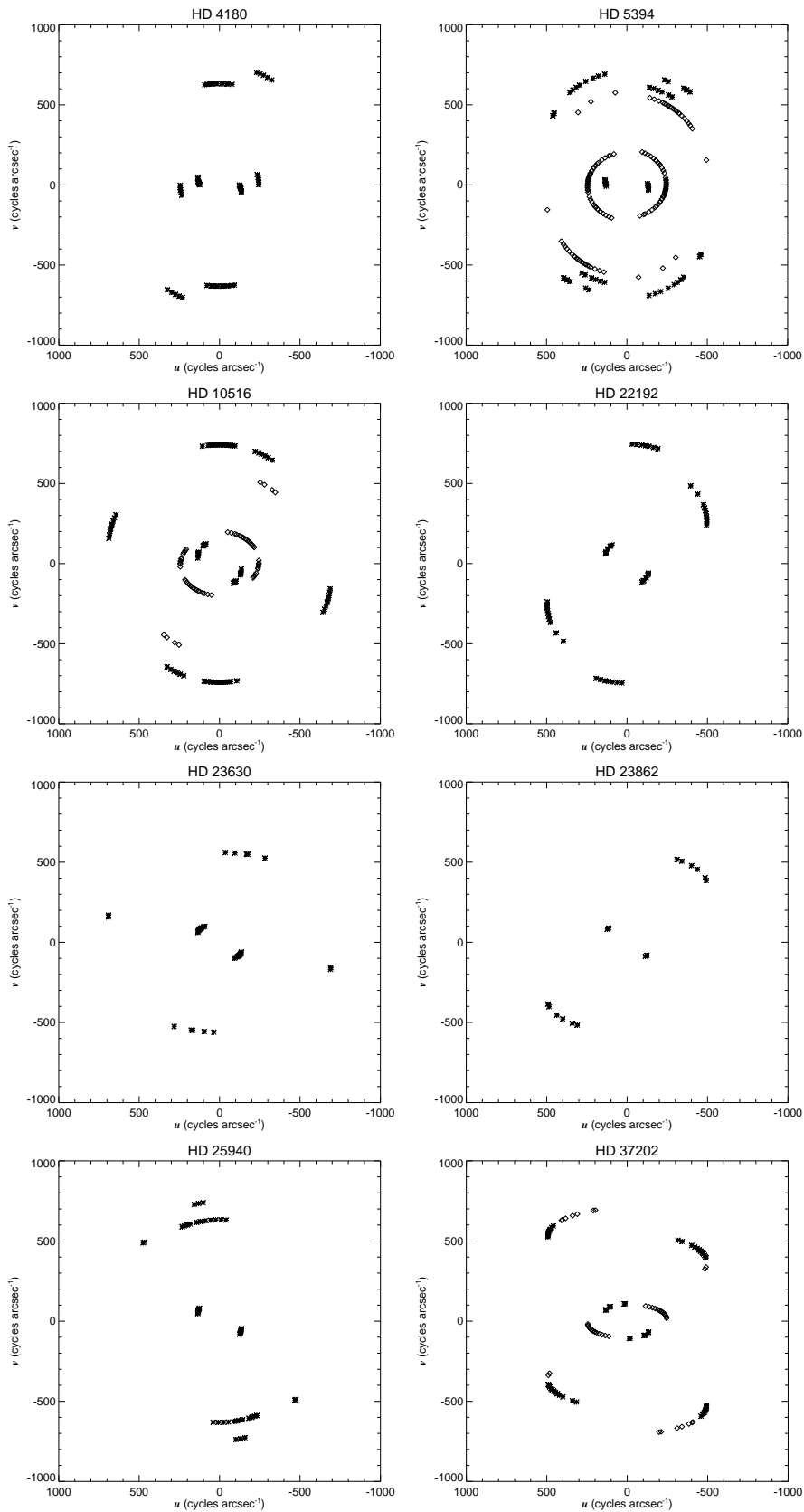
Figure 6.3: Sampling of the frequency (u, v) plane by the K-band observations for our sample stars. New observations are indicated by star symbols while archived measurements from Gies et al. (2007) are shown by diamonds.
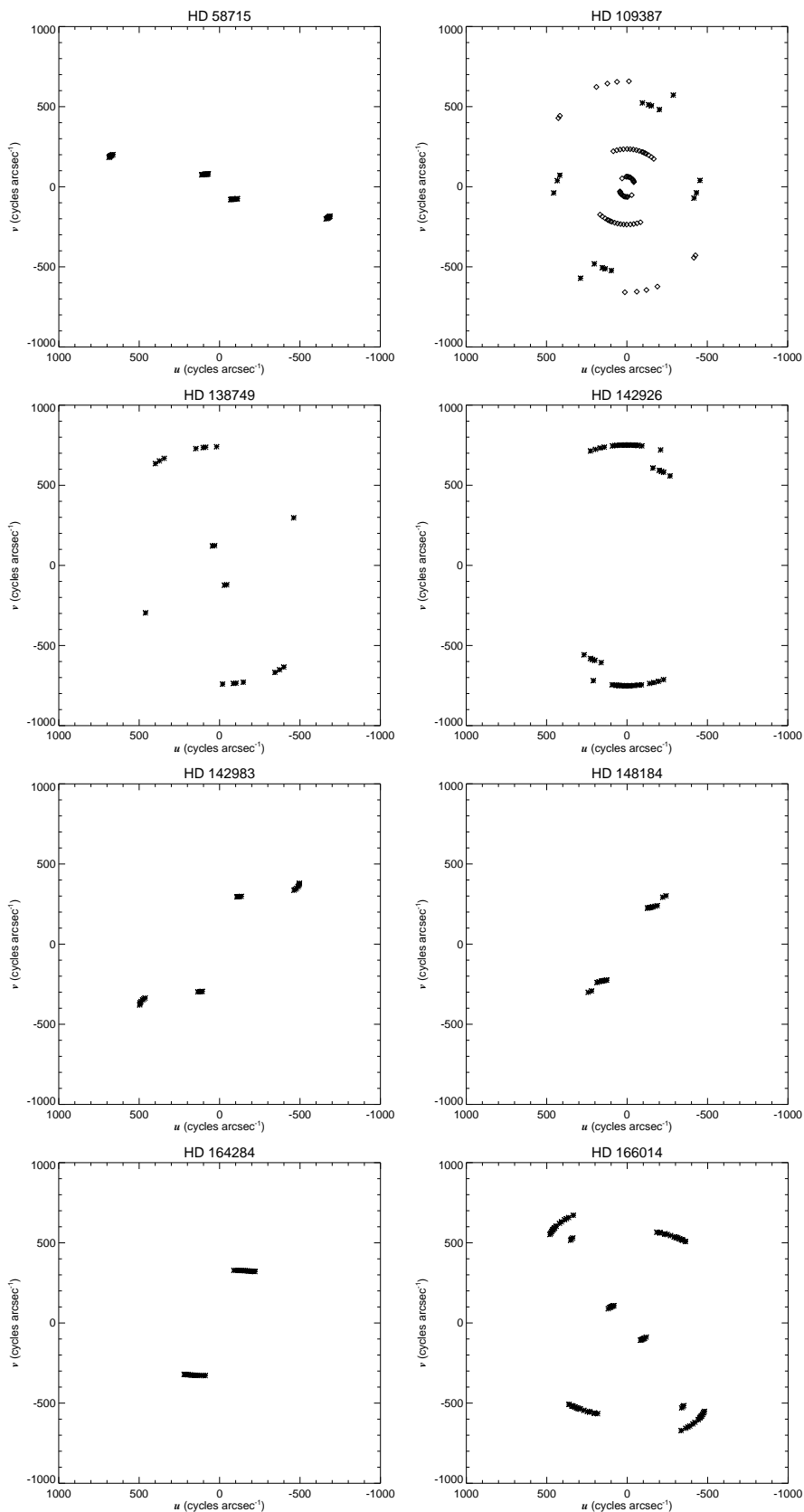
Figure 6.4: Sampling of the frequency (u, v) plane by the K-band observations for our sample stars, in the same format as Fig. 6.3.
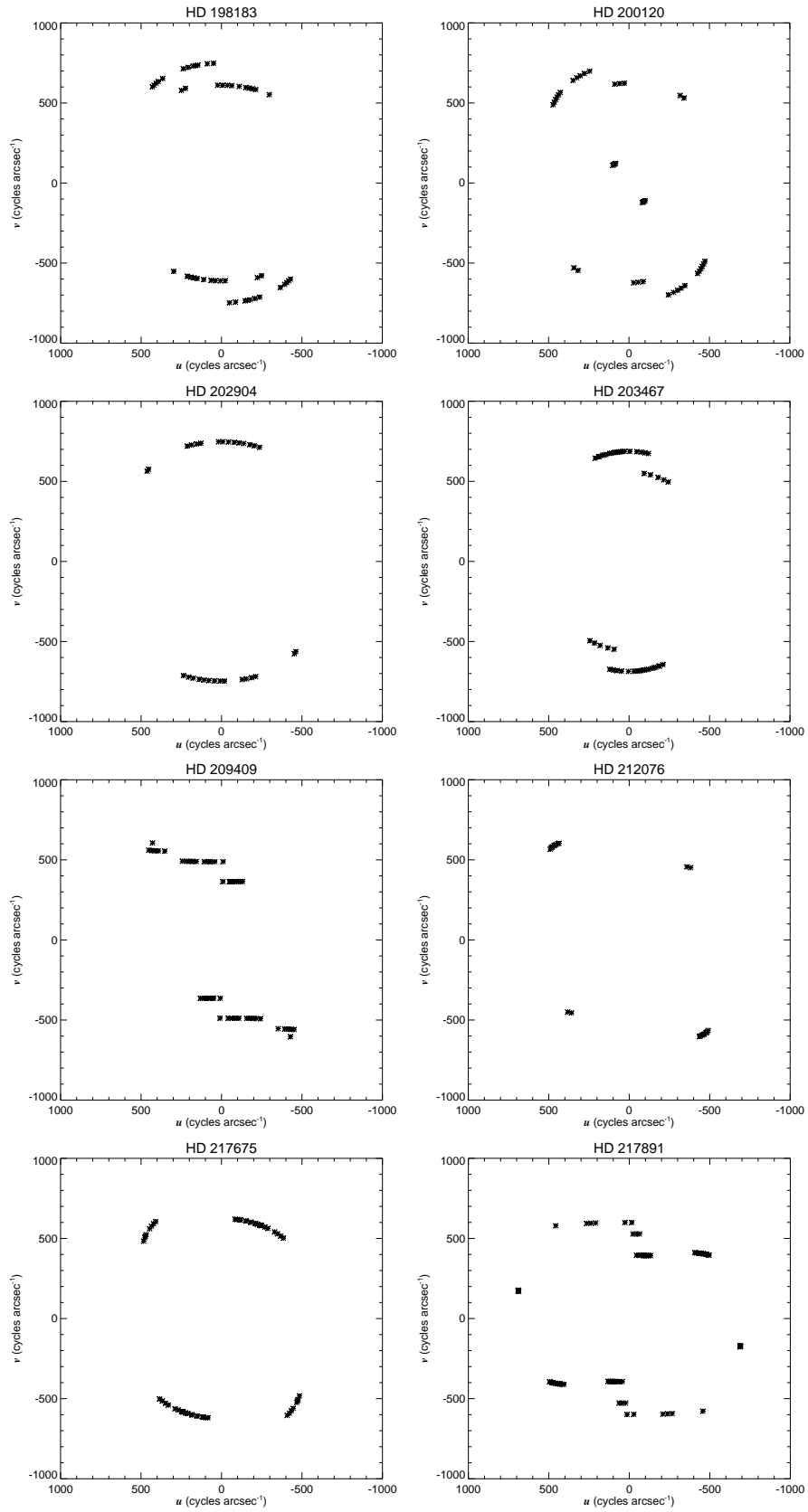
Figure 6.5: Sampling of the frequency (u, v) plane by the K-band observations for our sample stars, in the same format as Fig. 6.3.

6.3   Correction for the Flux of Nearby Companions

Many Be stars are known binaries or multiple systems with companions that are suspected to be main-sequence stars, subdwarfs, white dwarfs, or neutron stars. We checked for evidence of the presence of companions in our Be star sample through a literature search with frequent consultation of the Washington Double Star Catalog (Mason et al. 2001), the Fourth Catalog of Interferometric Measurements of Binary Stars (Hartkopf et al. 2001), and the Third Photometric Magnitude Difference Catalog[1]. We only considered those companions close enough to influence the interferometry results, i.e., those with separations less than a few arcsec. We show our adopted binary results in Table 6.6. The columns of Table 6.6 list the star name, number of components, reference code for speckle interferometric observations, and then in each row, the component designation, orbital period, angular semimajor axis, the estimated K-band magnitude difference between the components $\triangle K$, a Y or N for whether or not a correction for the flux of a companion was applied to the data, and a second reference code for investigations on the particular system.

Entries appended with a semi-colon indicate estimates with large uncertainties. Details about each system are collected in Appendix B. Remarkably, only 10 of our 24 targets are probable single stars, and the rest have one or more companions. In the latter cases, we need to estimate and correct for the changes in the interferometric visibility introduced by the flux of companion star(s) (unless the companion is too faint). In general the correction requires reliable estimates for both the separation and the position angle of the companion at the time of the observations together with the magnitude difference relative to the Be star

---

[1]http://www.usno.navy.mil/USNO/astrometry/optical-IR-prod/wds/dm3

plus disk. We discuss the assumptions and correction procedure in Appendix C, and we list the corrected values of visibility and associated error in columns 10 and 11 of Table 6.5.

Table 6.6: Binary Star Properties

Star Name	Number of Components	Speckle obs.ref.	Binary designation	P (yr)	a (mas)	ΔK (mag)	Corr.	Ref.
HD 004180	3	1	A,B	2.824	17	2.6	Y	2
			Ba,Bb	0.01:	0.4:	0:	Y	3
HD 005394	3	1	A,B	1800:	2070:	6.5:	N	4
			Aa,Ab	0.557	8.2:	$3.5-5.5$	N	5,6
HD 010516	2	1	A,B	0.347	4.9	3.1	Y	7
HD 022192	1	1	...	...	...	...	N	8
HD 023630	1	1	...	...	...	...	N	4
HD 023862	3	9	Aa,Ab	35:	145:	2.0:	Y	10
			Aa1,Aa2	0.597	8.8	$1.0-5.0$	Y	11
HD 025940	1	...	...	...	...	...	N	8
HD 037202	2	1	A,B	0.364	7.7	$2.7-4.5$	N	12
HD 058715	1	1	...	...	...	...	N	1
HD 109387	2	...	A,B	0.169	3.3	$1.4-3.1$	N	13
HD 138749	2	14	A,B	161:	500:	1.8	Y	15
HD 142926	2	1	A,B	0.126	2.7	$1.0-2.5$	N	16
HD 142983	1	...	...	...	...	...	N	17
HD 148184	2	...	A,B	0.0934	3.1	$3.8-5.9$	N	18
HD 164284	2	14	A,B	43:	132:	2.1	Y	19
HD 166014	2	14	...	...	...	2.5	Y	3
HD 198183	3	14	A,B	461	777	1.40	Y	20
			Aa,Ab	11.63	48	0:	Y	21
HD 200120	3	14	Aa,Ab	161:	208:	2.6	Y	22
			Aa1,Aa2	0.077	1.1	$2.8-4.7$	Y	23
HD 202904	1	1	...	...	...	...	N	24
HD 203467	1	...	...	...	...	...	N	25
HD 209409	1	1	...	...	...	...	N	26
HD 212076	1	1	...	...	...	...	N	27
HD 217675	4	14	A,B	117.4	295	1.77	Y	28
			Aa,Ab	5.7:	30:	1.92	Y	28
			Ba,Bb	0.090	1.9	-0.03	Y	28
HD 217891	1	1	...	...	...	...	N	29

References - 1. Mason et al. (1997); 2. Koubský et al. (2010); 3. Grundstrom (2007); 4. Roberts et al. (2007); 5. Harmanec et al. (2000); 6. Miroshnichenko et al. (2002); 7. Gies et al. (2007); 8. Delaa et al. (2011); 9. Mason et al. (1993); 10. Luthardt & Menchenkova (1994); 11. Nemravová et al. (2010); 12. Ruždjak et al. (2009); 13. Saad et al. (2005); 14. Mason et al. (2009); 15. Fabricius & Makarov (2000); 16. Koubský et al. (1997); 17. Rivinius et al. (2006); 18. Harmanec (1987); 19. Tokovinin et al. (2010); 20. Starikova (1982); 21. Balega & Balega (1988); 22. B. D. Mason, priv. communication; 23. Maintz et al. (2005); 24. Neiner et al. (2005); 25. Koubský et al. (2003); 26. Oudmaijer & Parr (2010); 27. Rivinius et al. (2003); 28. Zhuchkov et al. (2010); 29. Dachs et al. (1986).

6.4 SEDs of Be Stars

There are two important reasons to consider the spectral energy distributions (SEDs) of the Be stars in this study. First, we need to estimate the photospheric angular diameter of the Be star itself because of the dependence of the total visibility of the system star-plus-disk on the stellar angular diameter. The visibility component from the photosphere may decline slightly below unity in observations made with the longest baselines in a way that can be estimated if we know the stellar angular diameter. The most reliable means to estimate angular diameter is to compare the model and observed SED, as we did to find the angular diameters of the calibrator stars (see §6.2.2). Second, fitting the photospheric part of the SED immediately provides the IR flux excess from a comparison of the observed and extrapolated stellar IR fluxes (discussed in Chapters 3 and 4). Then, the observed IR flux excess can be directly compared with the disk flux fraction derived from fits of the visibilities from the CHARA Array observations.

The IR flux excess derived from spectrophotometric observations are usually normalized to the optical flux for the current state of the central star. But because Be stars are highly variable, this approach may introduce errors in the estimate of the IR flux excess, especially if the SED is normalized to a brighter state of the Be star when the disk contribution in the optical is important. For this reason, we advocate fitting the photospheric flux in the ultraviolet (UV) part of the spectrum as a better way to estimate the IR flux excesses of Be stars. There are several additional advantages to making fits of the photospheric flux in the ultraviolet.

First, all of the stars in our sample were observed in the UV with the NASA/ESA *International Ultraviolet Explorer* (IUE) satellite, so we have a uniform set of accurately

calibrated UV spectra for all the targets. Second, the bound-free and free-free emission from the disk sharply declines with increasing frequency, so that the disk contributions are minimal in this part of the spectrum (see Fig. 2 of Carciofi et al. 2006). And third, we can estimate the interstellar extinction to the target based upon the characteristics of the UV spectrum alone. For example, the interstellar extinction increases between 3000 and 1500 Å by 2.5 $E(B-V)$ magnitudes, where $E(B-V)$ is the standard interstellar reddening, so the shape of the stellar SED is very sensitive to the adopted reddening (Fitzpatrick 1999). Furthermore, the excess extinction found in the vicinity of the 2200 Å "bump" also varies directly with $E(B-V)$ (Beeckmans & Hubert-Delplace 1980). Note that because of the effects of gravity darkening in rapidly rotating Be stars, the intrinsic stellar UV fluxes can be lower than those for non-rotating, spherical Be stars (Collins et al. 1991). In this section, we will use fits of the UV spectrum to derive estimates of the interstellar reddening, the IR flux excess, and stellar angular diameter for our sample.

We obtained IUE spectra of all our targets from the NASA Multimission Archive at STScI[2]. We selected spectra made with the large aperture that record all of the stellar flux. In most cases, we used the available low dispersion, SWP (1150 - 1900 Å) and LWP/LWR (1800 - 3300 Å) spectra, but if there were fewer than two each of these, we also obtained high dispersion spectra for these two spectra ranges. In the case of HD 217891, all but one of the spectra were made with the small aperture, so we first formed an average spectrum based upon these, and then we rescaled the flux to that in the one large aperture spectrum and those from the TD-1 satellite (Thompson et al. 1978). In the case of HD 203467, there were no long wavelength spectra available in the IUE archive, so we used a combination of IUE

---

[2]http://archive.stsci.edu/iue/

SWP spectra (1150 - 1900 Å), SKYLAB objective-prism spectrophotometry (1900 - 2300 Å; Henize et al. 1979), and OAO-2 spectral scans (2300 - 3200 Å; Meade & Code 1980). Fluxes from each spectrum were averaged into 10 Å bins from 1155 - 3195 Å, and then the fluxes from all the available spectra for a given target were averaged at each point along this same wavelength grid.

We created model spectra to compare with the IUE observations by interpolating in the grid of model LTE spectra obtained from R. Kurucz. They were calculated for solar abundances and a microturbulent velocity of 2 km s^{-1}. The interpolation was made in effective temperature and gravity using estimates for these parameters from the Be star compilation of Frémat et al. (2005). For those sample stars in binaries, we formed a composite model spectrum by adding a model spectrum for each companion that was scaled according to our adopted K-band magnitude difference (Table C.1).

We then made a non-linear, least-squares fit of observed UV spectrum with a model spectrum transformed according to the extinction curve of Fitzpatrick (1999) and normalized by the stellar, limb-darkened angular diameter θ_{LD}. We assumed a ratio of total to selective extinction of $R = 3.1$ for the interstellar extinction curve, so our fits have only two parameters, $E(B-V)$ and θ_{LD}. Finally, we compared the extension of the fitted photospheric SED into the K-band, and we determined an IR flux excess from

$$E^{\star}(UV - K) = 2.5 \log(1 + \frac{F_{tot}}{F_1} \frac{F_{obs} - F_{tot}}{F_{tot}})$$

where the monochromatic, K-band fluxes are F_1 for the Be star, F_{tot} for the sum of the photospheric fluxes of the Be and all companions (if any), and F_{obs} is the observed flux from 2MASS (Cohen et al. 2003; Cutri et al. 2003).

Table 6.7: SED fits of Be Stars

HD Number	$E(B-V)$ (mag)	$\delta E(B-V)$ (mag)	θ_s (mas)	$\delta \theta_s$ (mas)	$E^\star(UV-K)$ (mag)	$\delta E^\star(UV-K)$ (mag)	c_p	δc_p	PA (deg)	r
4180	0.118	0.008	0.333	0.009	0.070	0.016	0.938	0.014	164	0.582
5394	0.096	0.008	0.446	0.012	1.442	0.230	0.265	0.057	20	0.764
10516	0.162	0.010	0.235	0.008	0.936	0.283	0.422	0.111	117	0.322
22192	0.099	0.008	0.307	0.008	0.533	0.264	0.612	0.150	125	0.280
23630	0.014	0.008	0.638	0.019	0.662	0.234	0.544	0.118	124	0.727
23862	0.017	0.008	0.229	0.006	0.547	0.023	0.604	0.013	159	0.438
25940	0.104	0.008	0.329	0.009	0.671	0.312	0.539	0.157	55	0.798
37202	0.044	0.009	0.445	0.015	0.785	0.280	0.485	0.127	122	0.071
58715	0.001	0.008	0.664	0.020	0.175	0.264	0.851	0.209	140	0.779
109387	0.022	0.008	0.385	0.011	0.435	0.036	0.670	0.022	102	0.660
138749	0.000	0.008	0.296	0.008	0.198	0.019	0.833	0.014	177	0.200
142926	0.012	0.008	0.183	0.005	0.202	0.015	0.830	0.011	70	0.300
142983	0.000	0.007	0.172	0.004	1.329	0.020	0.294	0.005	50	0.405
148184	0.354	0.010	0.201	0.007	2.008	0.280	0.157	0.041	20	0.947
164284	0.089	0.008	0.179	0.005	0.328	0.027	0.739	0.018	18	0.685
166014	0.000	0.007	0.521	0.013	0.066	0.354	0.941	0.312	89	0.868
198183	0.000	0.007	0.199	0.005	0.314	0.029	0.749	0.020	30	0.826
200120	0.000	0.007	0.149	0.004	1.446	0.348	0.264	0.086	95	0.310
202904	0.113	0.008	0.295	0.009	0.053	0.404	0.952	0.363	27	0.887
203467	0.156	0.010	0.197	0.007	0.948	0.031	0.418	0.012	76	0.799
209409	0.015	0.008	0.268	0.007	0.472	0.016	0.647	0.010	96	0.364
212076	0.059	0.008	0.189	0.005	0.782	0.017	0.487	0.008	148	0.955
217675	0.046	0.008	0.396	0.010	0.003	0.458	0.997	0.443	25	0.022
217891	0.001	0.008	0.259	0.008	0.330	0.020	0.738	0.014	38	0.943

Our results are listed in Table 6.7 that gives the HD catalog number of the star, the derived reddening $E(B - V)$ and its error, the stellar angular diameter θ_{LD} and its error, and infrared excess from the disk $E^{\star}(UV - K)$ and its error. Our derived interstellar reddening values are generally smaller than those derived from the optical colors because of the disk's growing flux contribution with increasing wavelength through the optical band mimics interstellar reddening (Dougherty et al. 1994). Also, our angular diameters may be smaller in some cases from previous estimates because of the neglect of the flux of the companions in earlier work. We also list the photospheric fraction of flux c_p and its error that is related to the IR flux excess by

$$E^{\star}(UV - K) = -2.5 \log c_p.$$

The final two columns list predictions for the position angle of the projected major axis of the disk that should be 90° different from the intrinsic polarization angle (Yudin 2001) and for the ratio of the minor to major axis sizes according to the estimated stellar inclination from Frémat et al. (2005) and the relation given by Grundstrom & Gies (2006; see their eq. 6). We will compare these various estimates to results from the fits of the visibilities in the following sections.

6.5 Gaussian Elliptical Fits

6.5.1 Method

In order to interpret the interferometric data, it is important to quantify the total IR flux excess received from Be stars and to separate the observed disk emission from the purely stellar photospheric contribution. In this chapter, we use a two-component geometrical

model to fit the CHARA Classic observations in order to measure the characteristic sizes of the circumstellar disks and their dependance on the properties of their central stars. We constrain the angular size and the geometry of the emitting regions by fitting the data with a simple geometrical model that consists of a small uniform disk representing the central star and an elliptical Gaussian component representing the circumstellar disk. Because the Fourier transform function is additive, the total visibility of the system is the sum of the visibility function of the central star and the disk. Thus, the total visibility of the system star plus disk, as shown in detail in §2.2.3, is given by

$$V_{tot} = c_p V_s + (1 - c_p) V_d \tag{6.1}$$

where V_{tot}, V_s, and V_d are the total, stellar, and disk visibilities, respectively, and c_p is the ratio of the photospheric flux contribution to the total flux of the system. Because the central star is mostly unresolved even at the longest baseline of the interferometer, its visibility is close to unity, $V_s \simeq 1$. The disk model visibility is given by a Gaussian distribution

$$V_d = \exp\left[-\frac{(\pi \theta s)^2}{4 \ln 2}\right] \tag{6.2}$$

where θ is the full width at half-maximum (FHWM) of the Gaussian distribution, and s is given by

$$s = \sqrt{r^2(u \cos \phi - v \sin \phi)^2 + (u \sin \phi + v \cos \phi)^2} \tag{6.3}$$

where r is the axial ratio and ϕ is the position angle of the disk major axis. As mentioned in §2.2.3, this simple elliptical Gaussian model has four free parameters which are the photospheric contribution c_p, the axial ratio r, the position angle PA, and the disk angular size θ_{maj}, and in the following section, we present the data fits using this model, and present our best-fit parameter results.

This simplistic representation of the system may suffer from a degeneracy that exists between two fundamental parameters of the Gaussian elliptical model: the Gaussian full width at half maximum (FWHM), which is represented by the angular size of the disk θ_{maj}, and the photospheric contribution c_p. In order to explain the ambiguity in the model, we consider the case of a locus of $(c_p, \theta_{\mathrm{maj}})$ that produce the same visibility measurement at a particular baseline. To illustrate this correlation, Figure 6.6 shows an example of a series of $(c_p, \theta_{\mathrm{maj}})$ Gaussian elliptical visibility curves that produce a visibility point $V = 0.8$, at a projected baseline of 200 m, and a wavelength $\lambda = 2.1329$ μm, and using a typical angular diameter of a Be star of $\theta_{\mathrm{UD}} = 0.3$ mas.

The solid curve in Figure 6.6 is for the Gaussian elliptical model $(c_p, \theta_{\mathrm{maj}}) = (0.156, 0.6$ mas), the dotted curve is for $(c_p, \theta_{\mathrm{maj}}) = (0.719, 1.2$ mas), and the dashed curve is for $(c_p, \theta_{\mathrm{maj}}) = (0.816, 2.4$ mas). All three curves in Figure 6.6 go through the same visibility point $V = 0.8$ at a projected baseline of 200 m, indicating that additional measurements at different baselines are necessary to solve this ambiguity. Figure 6.7 shows the relationship between the Gaussian elliptical full width at half maximum representing the angular size of the circumstellar disk and the stellar photospheric contribution for the family of curves that go through the observed point $V = 0.8$ at 200 m baseline. The plot shows that a larger circumstellar disk requires a larger stellar flux contribution, and vice-versa, which
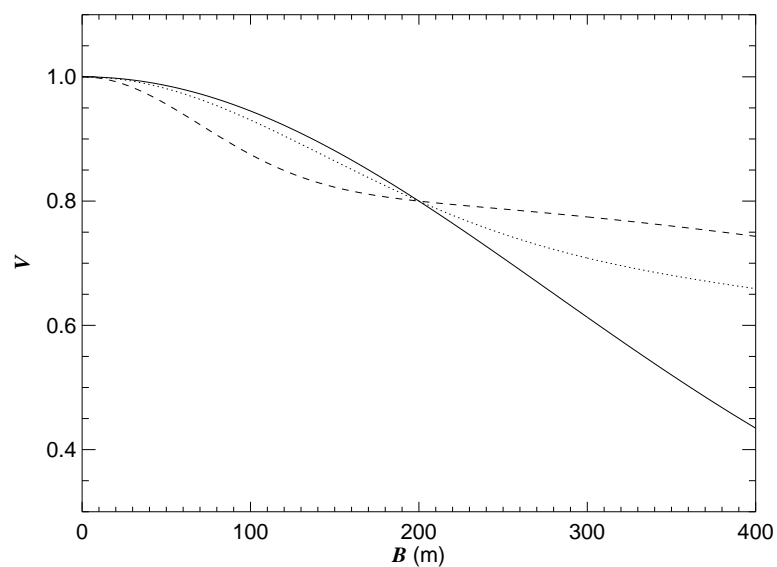
Figure 6.6: A set of three Gaussian elliptical models of different $(c_p, \theta_{\mathrm{maj}})$ that produce a visibility point $V = 0.8$ at a 200 m projected baseline. The solid curve is for $(c_p, \theta_{\mathrm{maj}}) = (0.156, 0.6 \text{ mas})$, the dotted curve is for $(c_p, \theta_{\mathrm{maj}}) = (0.719, 1.2 \text{ mas})$, and the dashed curve is for $(c_p, \theta_{\mathrm{maj}}) = (0.816, 2.4 \text{ mas})$.
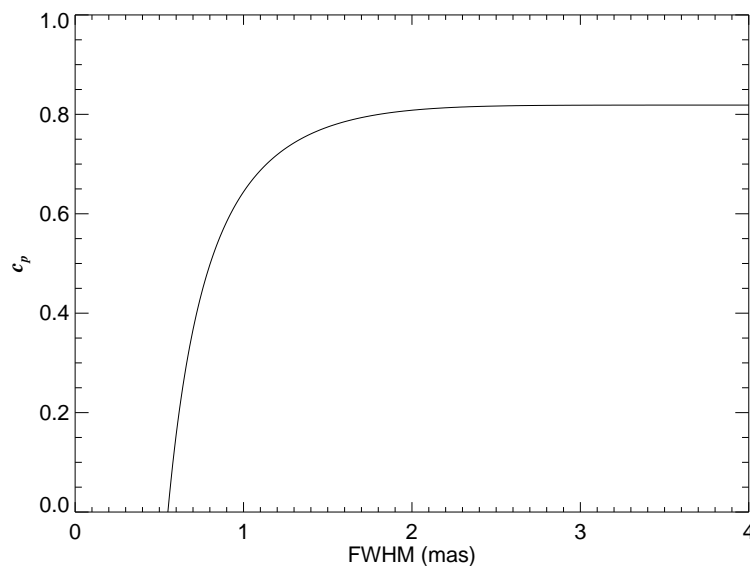
Figure 6.7: A series of $(c_p, \theta_{\mathrm{maj}})$ Gaussian elliptical visibility models that go through the same observed point of $V = 0.8$ at a 200 m baseline.

demonstrates that a single measurement does not discriminate between a bright small disk and a large faint one.

Note also that if the observations are all located in one location in the (u, v) plane, than the disk properties are defined in only one dimension. Thus, in such circumstances, it is not possible to estimate the axial ratio r or the position angle of the disk major axis PA, nor the angular size along the major axis θ_{maj}.

6.5.2 Fitting Results

The circumstellar disk is modeled with a Gaussian elliptical distribution centered on the Be star. The Gaussian elliptical disk model has four independent parameters (r, PA, c_p, θ_{maj}), and the fitting procedure consisted of solving for the model parameters using the IDL non-linear least squares curve fitting routine MPFIT (Markwardt 2009), which provides a robust way to perform least-squares curves and multiple-parameter surface fitting. Model parameters can be fixed or free depending on how well the distribution of the (u, v) coverage of each star is constrained. Also, simple boundary constraints can be imposed on parameters that are well defined from previous studies, especially for the cases of Be systems where the fitting fails because of lack of data coverage in the (u, v) plane.

In the cases where the collected (u, v) coverage was poor, such as the cases of HD 58715, HD 148184, and HD 164284, setting some model parameter to fixed values was necessary for the model to fit the data. We adopted values of the axial ratio r from the published measurements of the disk inclination angle listed by Frémat et al. (2005), and we adopted values of the disk position angle derived from the intrinsic polarization angle plus 90° listed by McDavid (1999) and Yudin (2001). We used values of the IR flux excess derived from

the SED fits of Be stars to estimate the stellar photospheric contribution c_p when needed. These values are listed in Table 6.7, and the fitting results are summarized in Table 6.8. Note that the cases with a fixed model-parameter are identified by a zero value assigned to its corresponding error. Column 1 of Table 6.7 lists the HD number of the star, columns 2 and 3 list the best-fit axial ratio r and its error, respectively, columns 4 and 5 list column the best-fit disk position angle along the major axis PA and its error, respectively, columns 6 and 7 list the best-fit values of the photospheric contribution c_p and its error, respectively, columns 8 and 9 list the best-fit angular size of the disk major axis θ_{maj} and its error, respectively, column 10 lists the reduced χ_ν^2, columns 11 and 12 list the corrected photospheric contribution $c_p(\mathrm{corr})$ (see §6.5.4) and its error, respectively, columns 13 and 14 list the disk-to-star size ratio R_d/R_s and its error, respectively, and finally, column 15 lists the cases of resolved disks (Y), marginally resolved disks (M), and unresolved disks (N).

Plots of these best-fit solutions showing the visibility curves of the system disk-plus-star as a function of the effective baseline in meters along with the data are presented in Figures 6.8 to 6.10. The panels are labeled for each Be star in our sample, and show the interferometric data along with the four-parameter Gaussian elliptical disk models. The solid lines in Figures 6.8 - 6.10 represent the best-fit visibility model of the disk along the major axis, the dotted lines represent the best-fit visibility model of the disk along the minor axis, and the star signs represent the interferometric data.

Table 6.8: Gaussian Elliptical Fits of the Interferometric Visibilities

Star Name	r	δr	PA (deg)	δPA (deg)	c_p	δc_p	θ_{maj} (mas)	$\delta\theta_{maj}$ (mas)	χ^2_ν	c_p(corr)	δc_p(corr)	R_d/R_s	$\delta R_d/R_s$	Res.
HD 004180	0.583	0.101	101.4	13.8	0.500	0.000	1.027	0.173	3.03	0.558	0.019	3.243	0.493	Y
HD 005394	0.722	0.038	38.2	5.0	0.082	0.036	1.236	0.063	15.63	0.190	0.032	2.946	0.134	Y
HD 010516	0.100	0.000	135.5	3.5	0.682	0.017	2.441	0.198	8.18	0.700	0.016	10.437	0.838	Y
HD 022192	0.251	0.562	136.8	4.5	0.518	0.000	1.030	0.264	1.50	0.612	0.090	3.502	0.898	Y
HD 023630	1.000	0.000	0.0	0.0	0.448	0.297	0.091	0.000	5.85	1.000	0.000	1.010	0.000	N
HD 023862	0.438	0.000	159.0	0.0	0.500	0.000	0.364	0.220	3.33	0.715	0.057	1.879	2.315	M
HD 025940	0.866	0.000	108.0	0.0	0.412	0.000	0.597	0.245	2.55	0.539	0.009	2.072	0.676	Y
HD 037202	0.148	0.027	125.4	1.3	0.422	0.016	1.790	0.073	4.30	0.534	0.013	4.146	0.159	Y
HD 058715	0.783	0.000	139.5	0.0	0.717	0.000	0.777	0.181	2.77	0.851	0.132	1.539	0.194	Y
HD 109387	1.000	0.000	0.0	0.0	0.803	0.025	3.214	0.749	6.36	0.805	0.025	8.407	1.932	Y
HD 138749	0.200	0.000	177.0	0.0	0.500	0.000	0.261	0.177	2.06	0.907	0.056	1.332	0.470	N
HD 142926	0.270	0.082	98.4	5.7	0.822	0.000	1.329	0.714	0.51	0.830	0.005	7.330	3.824	M
HD 142983	0.405	0.000	50.0	0.0	0.242	0.000	0.836	0.164	0.75	0.294	0.005	4.963	0.936	Y
HD 148184	0.947	0.000	20.0	0.0	0.123	0.000	0.858	0.142	1.59	0.157	0.004	4.385	0.690	Y
HD 164284	0.685	0.000	18.0	0.0	0.728	0.000	0.892	0.187	2.92	0.739	0.005	5.082	1.025	M
HD 166014	0.435	0.279	67.8	32.5	0.250	0.000	0.337	0.105	1.88	0.941	0.069	1.191	0.108	M
HD 198183	0.826	0.000	30.0	0.0	0.133	0.000	0.163	0.198	4.91	0.749	0.177	1.292	0.779	N
HD 200120	0.310	0.000	95.0	0.0	0.143	0.000	0.554	0.190	4.67	0.264	0.023	3.852	1.219	M
HD 202904	0.258	0.129	108.8	2.9	0.541	0.370	1.211	0.786	1.75	0.604	0.319	4.225	2.544	Y
HD 203467	0.799	0.000	76.0	0.0	0.343	0.000	0.528	0.087	1.62	0.418	0.006	2.861	0.415	Y
HD 209409	0.249	0.059	107.5	2.2	0.617	0.000	1.525	0.642	1.80	0.647	0.006	5.776	2.374	Y
HD 212076	0.955	0.000	148.0	0.0	0.308	0.000	0.295	0.044	1.61	0.487	0.032	1.852	0.202	M
HD 217675	0.022	0.000	25.0	0.0	0.340	0.195	0.056	0.000	2.23	1.000	0.000	1.010	0.000	N
HD 217891	0.702	0.150	30.6	17.1	0.692	0.309	0.804	0.593	1.81	0.722	0.279	3.261	2.098	Y

Errors of zero indicate those cases where the parameter was fixed in advance of the fit.

We found that the circumstellar disks of four Be stars, HD 23630, HD 138749, HD 198183, and HD 217675, were unresolved with CHARA, while the circumstellar disks of HD 23862, HD 142926, HD 164284, HD 166014, HD 200120, and HD 212076 were only marginally resolved in our data (see notes on individual target below). This was expected since these targets exhibited no or only a small flux excess in K-band as measured during the spectrophotometry campaign that we conducted simultaneously using the Mimir spectrograph at Lowell Observatory (see §3.3). Those were the targets that we had to fix r, PA, and c_p and set their corresponding errors to zero (see Table 6.8) in order produce accurate Gaussian elliptical model fits to the data. On the other hand, we successfully resolved the circumstellar disks around the other 14 Be stars. We were able to perform four-parameter Gaussian elliptical fits on most of these targets, and to determine the axial ratio r, the disk position angle PA, the stellar photospheric contribution c_p, and the disk angular size θ_{maj} with confidence.
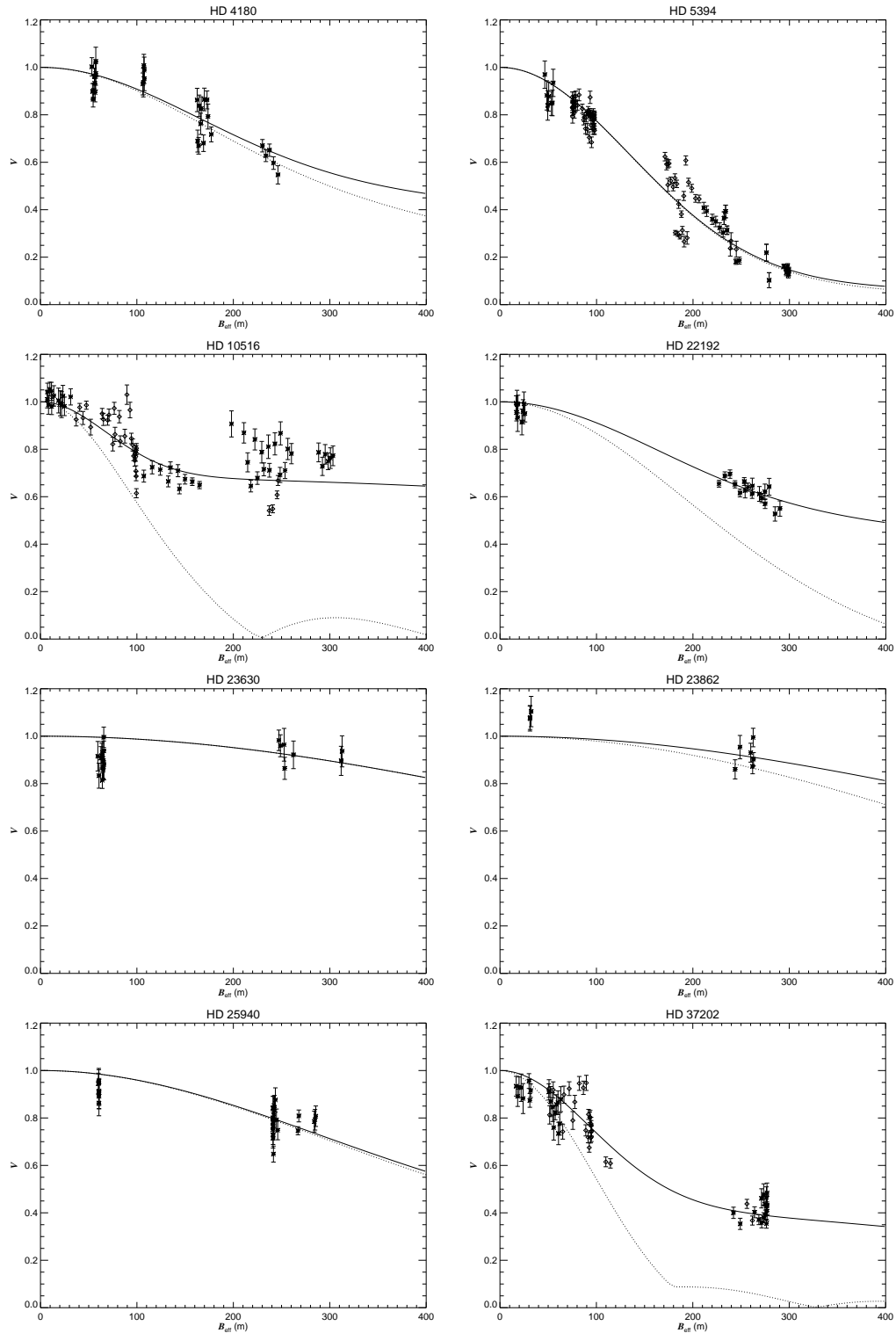
Figure 6.8: Calibrated or corrected visibilities versus the effective baseline. The solid line and the dotted lines represent the Gaussian elliptical model along the major and minor axes, respectively, and the star signs represent the interferometric data.
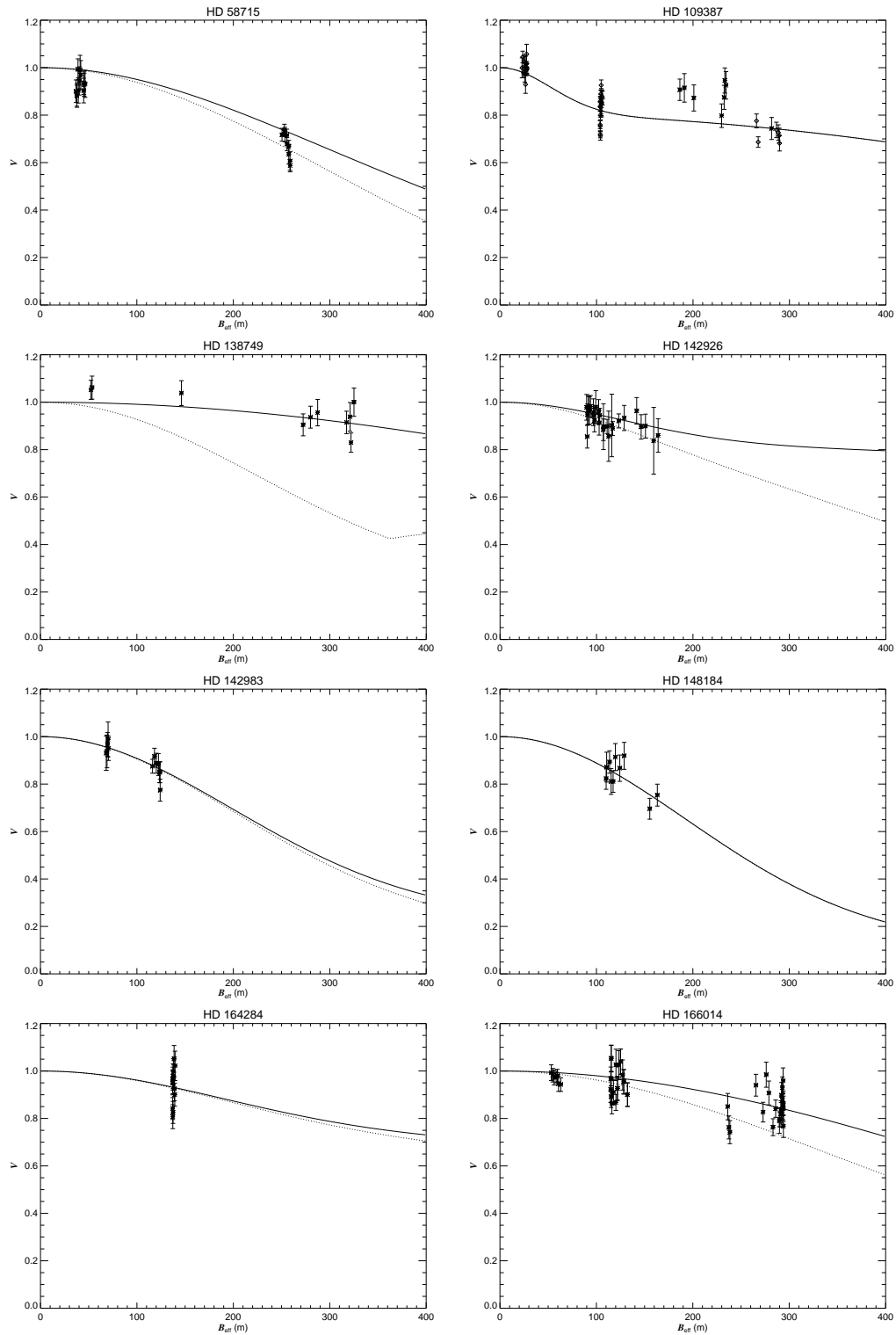
Figure 6.9: Calibrated or corrected visibilities versus the effective baseline. The solid and the dotted lines represent the Gaussian elliptical model along the major and minor axes, respectively, and the star signs represent the interferometric data, in the same format as Fig. 6.8.
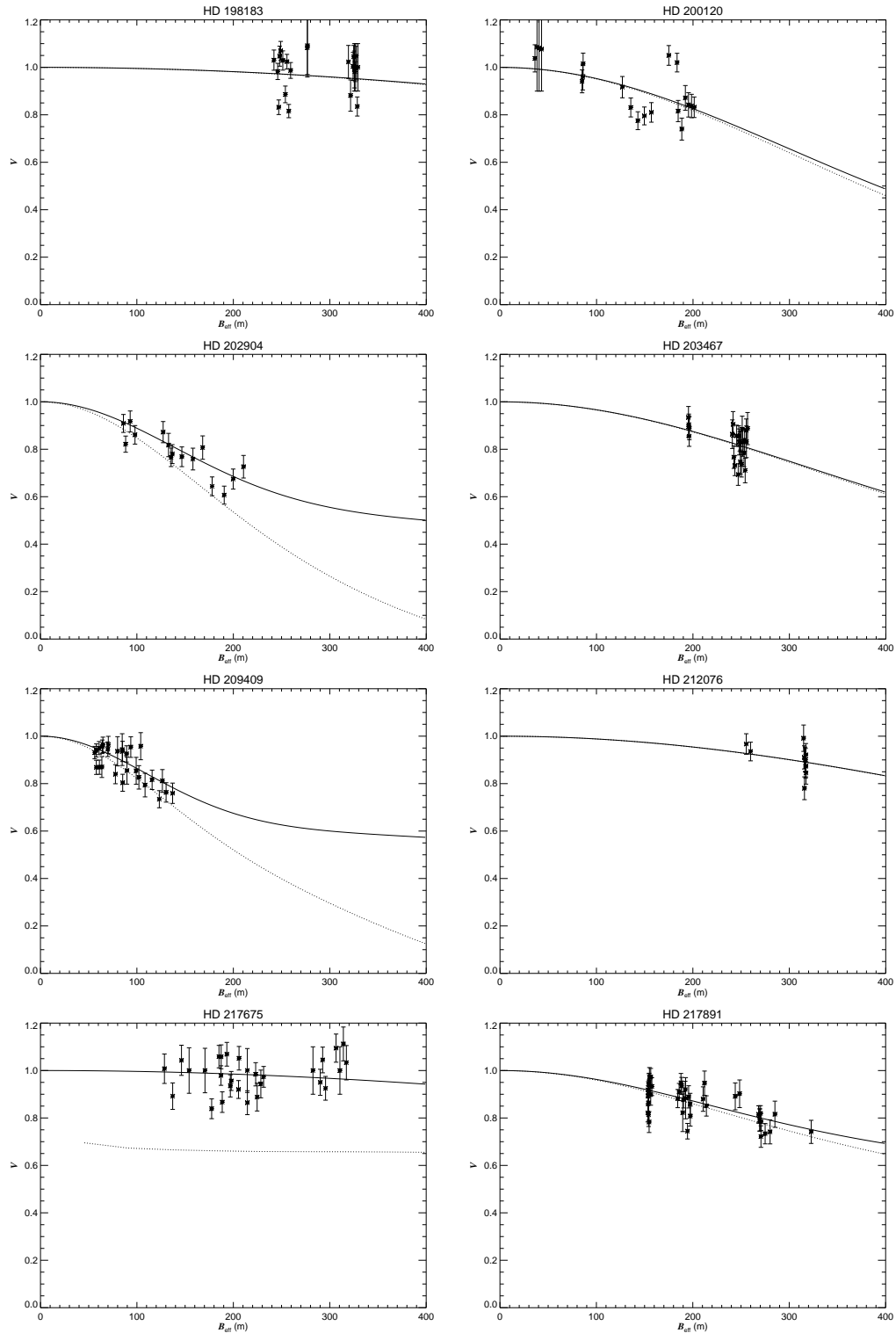
Figure 6.10: Calibrated or corrected visibilities versus the effective baseline. The solid line represents the Gaussian elliptical model and the star signs represent the interferometric data, same as in Fig. 6.8.

6.5.3 Notes on Individual Targets

• **HD 4180**

The best-fit Gaussian elliptical model is found with $c_p = 0$, which is inconsistent with rather small infrared excess estimates. However, almost equally good fits are found up to $c_p = 0.6$ (larger excluded by the lowest visibilities observed). We show a representative fit for $c_p = 0.5$. The other three parameters change by amounts comparable to the quoted errors over the range $c_p = 0.4$ to 0.6.

• **HD 5394**

As decribed in Chapter 5, there are archival Classic as well as new Classic and FLUOR data for γ Cas. We have included the entire set of measurements for the Gaussian elliptical fits.

• **HD 10516**

The Gaussian elliptical fit was made of the visibilities from both archival (Gies et al. 2007) and new observations. Corrections were made for the influence of the faint subdwarf companion. The four parameter solution has a best fit at the lower limit of r, but fits with larger r are almost equally good. We present a sample solution for $r = 0.1$. The relatively large visibilities at long baseline yield a stellar flux contribution that is somewhat higher than expected from the SED fits. We also tried separate fits for the archival and new data sets, and while the results are generally consistent, there is a possible change in PA from 143 ± 6 for the Gies et al. (2007) set to 118 ± 5 deg for the new set.

• **HD 22192**

The best-fit model ran to $c_p = 0$, inconsistent with the IR excess. Instead we solved for fixed c_p between 0.2 and 0.5, and we found acceptable solutions throughout this range. We show

a solution for c_p that is consistent with the IR excess from the SED. The orientation of the major axis agrees with the results of Delaa et al. (2010; 115 ± 20 deg) and Quirrenbach et al. (1997; 147 ± 11 deg), and is close to that from radio measurements by Dougherty & Taylor (1992; 158 ± 10 deg).

● **HD 23630**

The shorter baseline data have visibilities below unity that cannot be easily fit unless there is an unknown of incoherent source of flux in the beam (a close binary). However, the visibility decline at longer baselines is approximately that expected for the photosphere alone (the fit forces the disk size to the lower limit corresponding to $R_d/R_s = 1.01$). Thus, our observations do not resolve the disk in this case. We note that the interferometric result $c_p(\mathrm{corr}) = 1$ differs from the prediction from the SED fit, $c_p(\mathrm{corr}) = 0.54 \pm 0.12$.

● **HD 23682**

The binary correction we applied was too large for the short baseline data and resulted in visibilities greater than one. We have only one other group of observations with limited (u, v) coverage. These observations do indicate that the disk is partially resolved, but the severe limitation in baseline and position angle means that the data may be fit with a family of $(c_p,\ \theta_{\mathrm{maj}})$ curves (as described earlier). We made a representative fit by fixing r and PA according to the values in Table 6.7, and then made a series of fits with c_p fixed. We present a representative solution for $c_p = 0.5$, but equally good fits can be made over the range $c_p = 0.1$ to 0.9. The error estimates for θ_{maj} reflect the spread in these fits. Although the disk is detected, the observations are too few to characterize its parameters with any accuracy.

● **HD 25940**

This star is probably observed close to pole-on with an axial ratio of approximately $r = 0.88$ (Quirrenbach et al. 1997; Delaa et al. 2011), so it appears almost round in the sky. This combined with the limited (u, v) coverage of our observations makes it impossible for us to determine the orientation with confidence. Consequently, we simply set r and PA to those values found by Delaa et al. (2011) in fitting the visibilities. Our short baseline data are well below unity, and a two parameter fit yields $c_p = 0.82$ and $\theta_{\mathrm{maj}} = 3.0$ mas. However, this angular size is larger than found by Delaa et al. (2011) for the Hα emission, 2.1 mas, and this c_p is larger than we expect from the SED fits. Thus, we also tried fits with lower c_p, and we present a solution that is consistent with the IR excess from the SED. Although the disk is resolved in our observations, its parameters are poorly constrained.

- **HD 37202**

We combined the new and archival data for the fit, which is consistent with that presented in Gies et al. (2007) and that for H-band observations from Schaefer et al. (2010).

- **HD 58715**

Our (u, v) coverage is restricted to a small range in PA, so we need additional constraints to fit the observations. Kraus et al. (2012) obtained CHARA MIRC and VLTI/AMBER observations of β CMi that characterize accurately the disk orientation, so we adopted their values for r and PA for fits of our data. Our short baseline data fall somewhat below expectations for all reasonable fitting parameters, so the fit is defined by the clump of long baseline observations. As discussed previously, in such circumstances there is a family of $(c_p, \theta_{\mathrm{maj}})$ curves that will fit this clump, and we found that good fits could be made for $c_p = 0.1$ to 0.8, and we present a sample fit for a c_p that yields a flux excess equal to that expected from the SED. The quoted errors reflect the range in the results for the span in

possible c_p.

- **HD 109387**

We added the data from Gies et al. (2007) to the new observations. A four parameter fit converged to $r = 0$ presumably because of the importance of the mid-baseline data in the fit and their close (u, v) distribution. However, several investigations suggest that the disk is closer to a pole-on configuration, so we adopted a circular disk (Jones et al. 2008). There is significant scatter in the longer baseline data that may be related to the flux of the binary companion (no binary correction was made though, because the magnitude difference is unknown).

- **HD 138749**

After binary flux correction, all the visibilities are close to one. We set r and PA from the predictions in Table 6.7, and we found that the entire range of c_p gave acceptable solutions. We present an example fit for $c_p = 0.5$ and the errors on the angular size represent the spread over the full range of c_p. The disk is so small in this case that the corrected stellar flux is always large (§6.5.5), which is consistent with the small infrared excess. No detection of the disk can be claimed in this case.

- **HD 142926**

The (u, v) coverage is rather limited in this case, so there exists a family of $(c_p, \theta_{\mathrm{maj}})$ solutions with similar goodness of fit. We selected the solution that led to the predicted IR flux excess from the UV SED analysis. The angular size errors are set by the fitting results over the range in possible c_p. The disk in this system is partially resolved.

- **HD 142983**

The disk is resolved by our data but the (u, v) coverage is too limited to make a four param-

eter fit successfully. We set r and PA from Table 6.7 (PA set orthogonal to the polarization data of McDavid 1999), and then selected from the (c_p, θ_{maj}) family the fit that matched the IR excess from the UV SED fit. Our θ_{maj} result is similar to the pure Gaussian fit model of KI data, 0.96 ± 0.03 mas, determined by Pott et al. (2010).

- **HD 148184**

This star is seen from a nearly pole-on orientation (Tycner et al. 2008). Our (u, v) coverage is restricted to a narrow range of position angle, so we must fix the orientation parameters r and PA from the estimates in Table 6.7. We selected from the family of (c_p, θ_{maj}) solutions to find the one that matched the IR excess from the SED study. The errors on θ_{maj} show the range in the fitted value for the acceptable range in c_p.

- **HD 164284**

The (u, v) coverage is quite restricted, so we applied the values of r and PA from Table 6.7. We then selected a fit among the (c_p, θ_{maj}) set of solutions that agreed with the IR excess. The disk is only marginally resolved in our observations.

- **HD 166014**

There is a range in c_p from 0.0 to 0.5 that all give good fits. We show the solution that yields the same IR excess predicted from the SED. The disk is small in this system, and a fit of the star alone produces $\chi_\nu^2 = 2.73$, which is only slightly higher than the best fit value of $\chi_\nu^2 = 1.88$. Thus, this is only a marginal detection of the disk.

- **HD 198183**

After making corrections for the companions, the resulting visibilities are all close to unity, which suggests that the disk is unresolved. We fixed r and PA from Table 6.7, and then found solutions over the full range of c_p. We present that solution that best matches the IR

excess from the SED. No detection of the disk is claimed in this case.

- **HD 200120**

The corrections to the visibilities introduce additional scatter that only partially constrains the disk parameters. We fixed r and PA from Table 6.7, and then determined the c_p consistent with the IR excess from the SED. The errors in θ_{maj} reflect the fitted values over the range in acceptable c_p. This probably represents a marginal detection of the disk.

- **HD 202904**

The (u, v) coverage here is sufficient for a four parameter fit. The disk is resolved in this case.

- **HD 203467**

The distribution in (u, v) is somewhat limited so we had to assume r and PA from Table 6.7, and then find a c_p solution consistent with the IR excess from the SED. The disk is resolved for this star.

- **HD 209409**

We found that a four parameter fit led to $c_p = 0$, so we instead solved for a series of models of varying c_p that led to an IR excess that was within $\pm 20\%$ of c_p. The errors for the other parameters are based on the range of best fit values over the allowable c_p range. The disk is resolved.

- **HD 212076**

Our data are sparse, so we set r and PA from Table 6.7 to then find a c_p that is consistent with the IR excess from the SED. The errors in angular size reflect the fits over the span of reasonable c_p. The disk is only marginally detected here.

- **HD 217675**

After correcting for the companion fluxes, the resulting visibilities are close to unity. In order to see if there is any evidence of a disk, we set r and PA from Table 6.7 and found that the best fit was for no disk component. Thus, no disk detection is claimed here.

- **HD 217891**

The (u, v) distribution was sufficient for a four parameter fit. The resulting parameters have values close to their expected ones in Table 6.7. The disk is resolved here, although with somewhat large errors attached to the parameters.

6.5.4 Corrections to the Gaussian Fit Model

Fitting an elliptical Gaussian model to the disk intensity distribution is convenient but not completely realistic. The flux distribution in the model assumes that both light components received from the circumstellar disk and the central star are summed and that no mutual obscuration occurs. It is important to note that, in the case of small disks, most of the model disk flux is spatially coincident with the photosphere of the star, so the assignment of the flux components becomes biased.

As an example, we show in Figure 6.11 the model fit components made for a case like that of η Tau (HD 23630), where the derived disk flux contribution is very modest. The dotted line in Figure 6.11 shows the assumed form of the intensity of the uniform disk of the star (for an angular diameter of 0.68 mas), the dashed line shows the Gaussian distribution of the circumstellar disk along the projected major axis, and the solid line shows the sum of the two intensity components. In this case, where the circumstellar disk is small, the Gaussian θ_{maj} (indicated by the dash-dotted line in Fig. 6.11) is smaller than the stellar
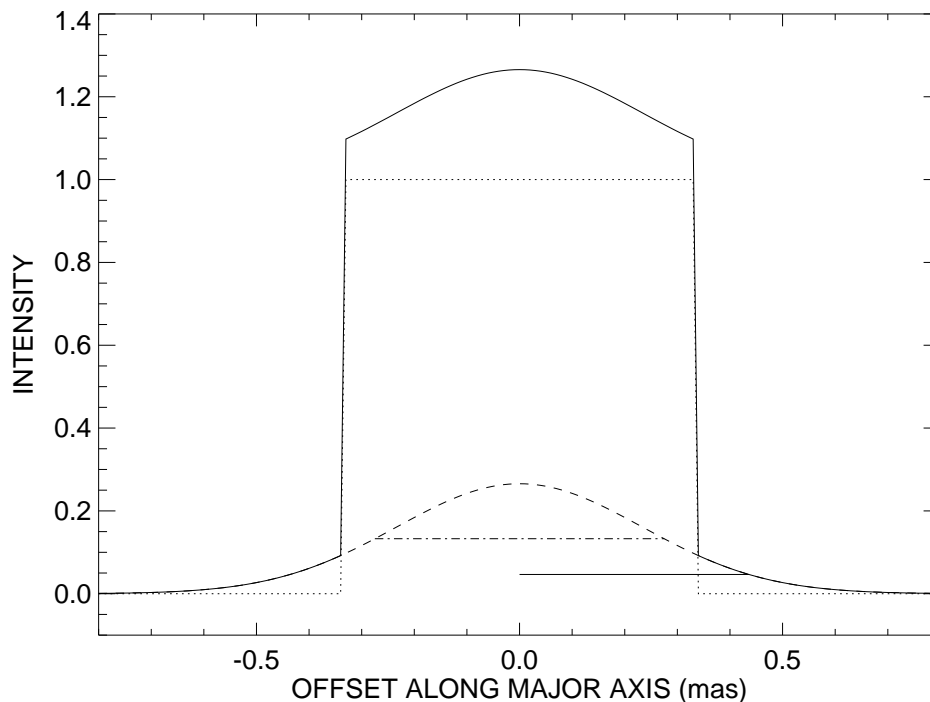
Figure 6.11: The intensity versus the offset along the major axis for η Tau (HD 23630), where the disk flux contribution is very modest and where the mutual obscuration needs to be corrected for in the Gaussian elliptical model fits.

diameter, and most of the Gaussian flux occurs over the stellar photosphere where the sum produces a distribution similar to that of a limb darkened star.

The interpretation of the results obtained from the Gaussian elliptical fits must be regarded with caution in situations like this where the the derived disk radius is smaller than the star's radius and a significant fraction of the disk flux is spatially coincident with that of the star. We have thus corrected the Gaussian elliptical fitting results in two ways. First, we suggest that the disk radius should be set based upon the relative intensity decline from the stellar radius, and we adopt the disk radius to be that distance where the Gaussian light distribution along the major axis has declined to half its value at the stellar equator. The resulting ratio of disk radius to star radius is then given by

$$\frac{R_d}{R_s} = (1 + (\theta_{\text{maj}}/\theta_s)^2)^{1/2} \tag{6.4}$$

where θ_{maj} is the Gaussian full-width at half maximum along the major axis derived from the fits and shown in Table 6.8, and θ_s is the angular diameter of the central star. Secondly, we suggest that the model intensity over the photosphere of the star from both the stellar and disk components should actually be assigned to flux from the star in an optically thin approximation. The fraction of the model disk flux that falls on top of the star is $f(1 - c_p)$, where f is found by integrating over the stellar disk the Gaussian spatial distribution given by

$$I_{\text{env}}(x, y) = \frac{4 \ln 2}{\pi r \theta_{\text{maj}}^2} \exp \left[-\frac{(x^2/r^2 + y^2)}{\theta_{\text{maj}}^2/4 \ln 2} \right] \tag{6.5}$$

where r is the axial ratio, and (x, y) are the sky coordinates in the direction of the minor and major axes. Consequently, this fraction of the model disk flux should be reassigned to the star and removed from the disk contribution. Then the revised ratio of total disk to stellar flux is:

$$\frac{F_d}{F_\star} = \frac{(1 - c_p)(1 - f)}{c_p + (1 - c_p)f}$$

which will be lower than the simple estimate of $(1 - c_p)/c_p$. We list in the last four columns of Table 6.8 the revised values of the stellar flux contribution c_p and the Be disk radius R_d/R_s and obtained from applying this correction along with their corresponding errors.

Another useful test that we can consider relates to the physical validity of the Gaussian elliptical models. We expect that the surface brightness of the disk close to the star will be no

brighter than the star's average intensity because the disk is probably cooler than the star. Consequently, we can use this limit on disk surface intensity to check for consistency with the model flux allocations to the star and disk. The average stellar intensity in normalized units is

$$I_s = \frac{c_p}{\pi(\theta_s/2)^2}$$

where θ_s is the uniform disk angular diameter of the star. The model disk intensity at the position of the stellar radius $\theta_s/2$ is

$$I_d = (1 - c_p)\frac{4\ln 2}{\pi r \theta_{\mathrm{maj}}^2} 2^{-(\theta_s/\theta_{\mathrm{maj}})^2}$$

where θ_{maj} is the angular FWHM of the Gaussian distribution for the disk. The limit $I_d(\theta_s/2) < I_s$ then leads to the inequality

$$c_p > c_p(\mathrm{min}) = \frac{1}{1 + x}$$

where x is given by

$$x = \frac{r}{\ln 2}(\theta_{\mathrm{maj}}/\theta_s)^2 \; 2^{(\theta_s/\theta_{\mathrm{maj}})^2}.$$

This constraint is only significant in cases where x is small, i.e., where r is small and/or $\theta_{\mathrm{maj}}/\theta_s \approx (\ln 2)^{1/2} = 0.83$. We checked our model fits and found that $c_p(\mathrm{fit}) > c_p(\mathrm{min})$ in all but four cases. Three of these are situations where the disk was not detected (HD 138749, HD 198183) or marginally detected (HD 166014), so they pose no special significance. However, the last case is HD 5394 $= \gamma$ Cas where the disk is clearly detected. Here

$c_p(\text{fit}) = 0.08 \pm 0.04$ and $c_p(\text{min}) = 0.10$, so the model fit suggests that the inner disk has a surface brightness comparable to the stellar intensity. This may not be surprising because γ Cas represents one of the strongest disk emission cases in our sample, so its inner disk is probably very dense and bright (§5).

As we mentioned above, there were several cases where we had to fix one or more parameters in order to perform a Gaussian elliptical fit to the data. Those were cases where we mainly lacked (u, v) coverage and/or observations at long baselines. We set the photospheric contribution c_p to equal c_p values that we derived from the SED fits for these cases, and for comparison, we plot in Figure 6.12 these estimates versus the values derived from the full four-parameter Gaussian elliptical fits. We find that, generally, there is good agreement between the two quantities. Similarly, we compare the values for the disk axial ratio using inclinations from Frémat et al. (2005) and R_d/R_s from the Gaussian elliptical fits ($r \approx \cos i + 0.022\sqrt{\frac{R_d}{R_s}} \sin i$; Grundstrom & Gies 2006), with the ones derived from interferometry, and we show our results in Figure 6.13. A comparison between the values of the disk position angle PA that were set equal to position angles derived from polarimetric studies (Yudin 2001) were also compared to ones we derived from elliptical fits of the data, and we show our results in Figure 6.14.
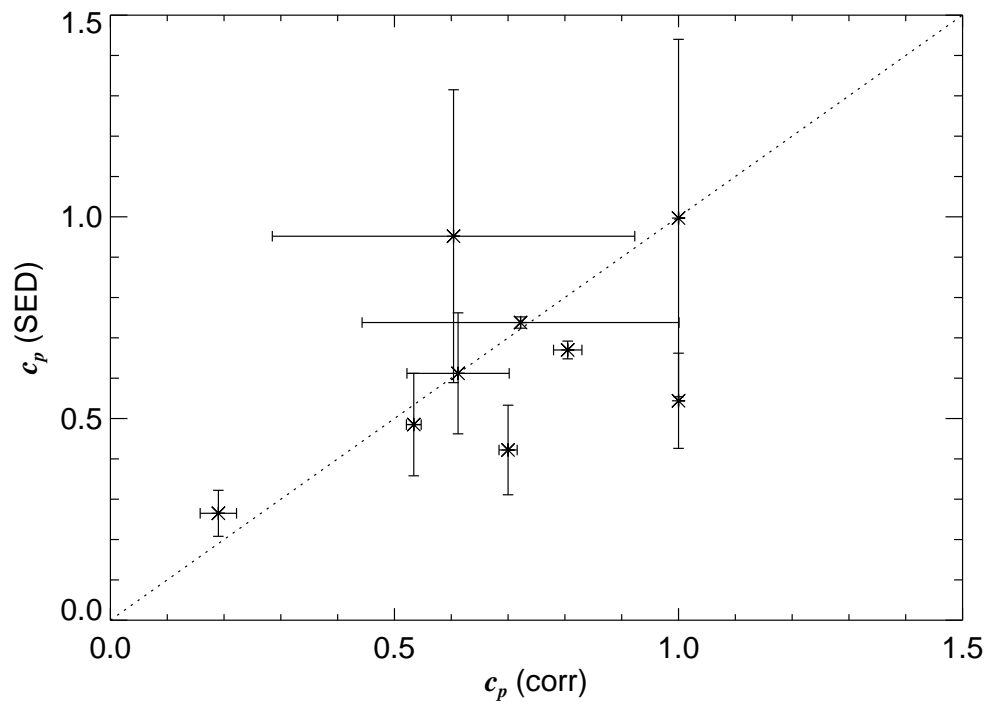
Figure 6.12: A comparison between the values of the photospheric contribution c_p derived from the SED fits, and the ones derived from the Gaussian elliptical fits.
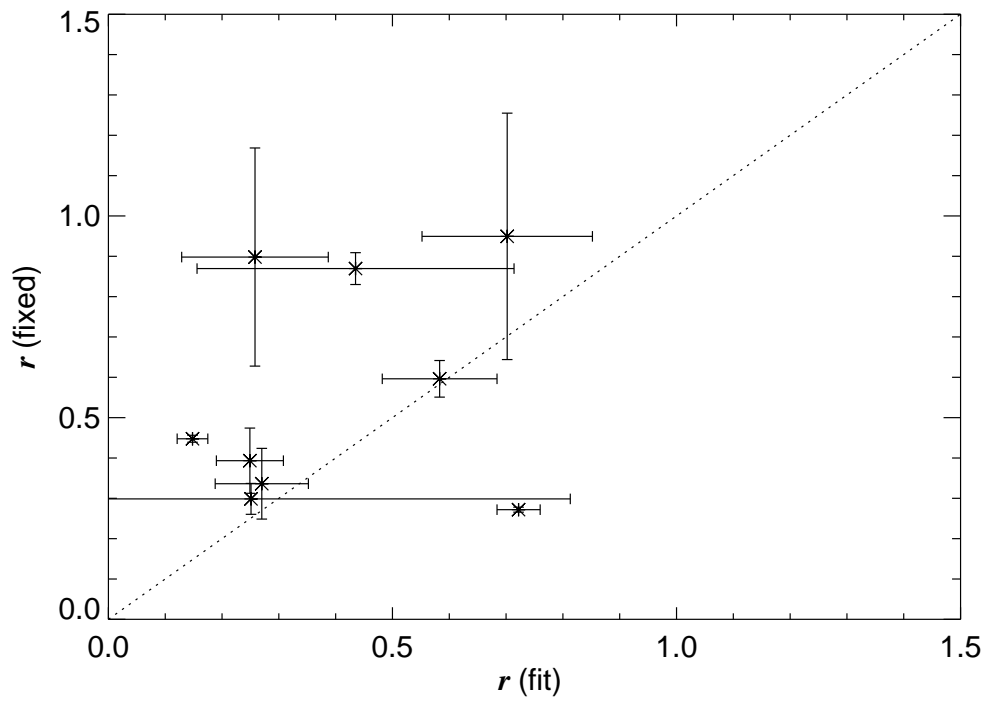
Figure 6.13: A comparison between the values of the disk axial ratio r adopted from Frémat et al. (2005), and the ones derived from the Gaussian elliptical fits.
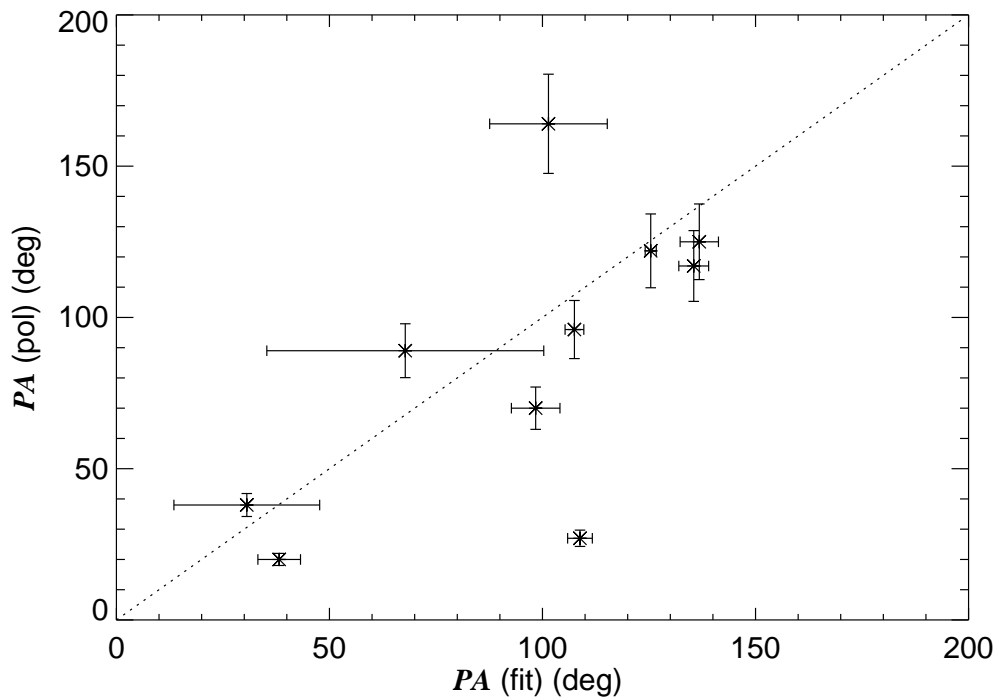
Figure 6.14: A comparison between the values of the disk position angle PA adopted from the intrinsic polarization angle plus 90° (McDavid 1999; Yudin et al. 2001), and the ones derived from the Gaussian elliptical fits.

6.6 Discussion

6.6.1 Detection Limits

We found that the criterion for a confidant detection of the disk was usually a decline in visibility below $V = 0.8$ at the longest baselines available. We can use this to estimate the limitations on disk sizes that we can detect for Be stars at different distances. The visibility measured along baselines aligned with the projected major axis of the disk is a function of the photospheric flux fraction c_p, the ratio of disk to stellar radius R_d/R_s, and the stellar angular diameter θ_s. We argued above that the latter two parameters are related to the Gaussian elliptical θ_{maj} by

$$R_d/R_s = (1 + (\theta_{\mathrm{maj}}/\theta_s)^2)^{1/2} \tag{6.6}$$

so given R_d/R_s and θ_s we can find θ_{maj}. The remaining parameter to estimate is c_p, the photospheric flux component. In practice this could be estimated from an analysis of the SED, but for the purpose at hand, we prefer to estimate this parameter from the disk angular size. If we suppose that there is a relationship between the disk and stellar surface brightness for large disks (which might be the case for optically thick disks with a temperature equal to some fraction of the stellar effective temperature), then the ratio of disk flux to stellar flux would be given by the ratio of their respective projected areas (with r equal to the disk axial ratio),

$$\frac{F_d}{F_s} = \frac{1 - c_p}{c_p} \propto r(\frac{\theta_{\mathrm{maj}}}{\theta_s})^2 - 1$$

where we subtract one in the last term to remove that part of the disk area that overlaps the star. We show in Figure 6.15 this relation for the 14 stars in our sample with a confirmed
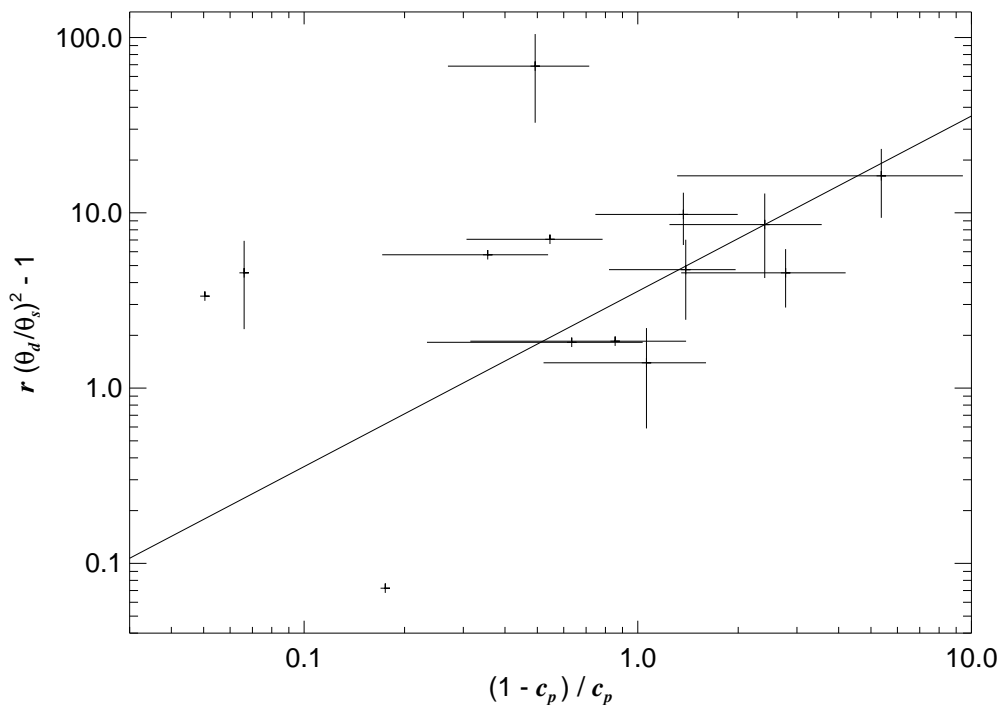
Figure 6.15: A plot of the ratio of projected disk to stellar area on the sky as a function of the flux ratio $F_d/F_s = (1 - c_p)/c_p$. A linear relationship is expected for large optically thick disks. The scatter is largest among faint disk systems (the point at the top represents HD 109387 = κ Dra, while the lower point represents HD 58715 = β CMi).

detection of their disk. The x-axis gives the flux ratio F_d/F_s from the SED analysis while the

y-axis gives the ratio of projected areas from our Gaussian elliptical fits of the interferometric

visibilities. The errors are too large to draw a firm conclusion, but it appears that the flux

ratio does increase with increasing ratio of projected areas (the solid line shows the mean

slope for a constant of proportionality of 3.57). However, this relationship is poor for fainter

disks ($(1-c_p)/c_p < 1$), where the disks become optically thin and the ratio of areas argument

no longer applies.

We adopt this relationship to make an approximate estimate of c_p from the given values

of R_d/R_s and θ_s (with an assumed value of $r = 0.5$ for the purpose of illustration). The

stellar angular diameter is found from the assumed stellar radius and distance, and we made estimates for two cases, B0 V and B8 V types for the Be star, and three distances corresponding to visual magnitudes 3, 5, and 7.

We used the stellar radii and magnitudes for these classifications from the compilation of Gray (2005), and we neglected any extinction in the calculation of distance from the magnitude difference. Figures 6.16 and 6.17 show the resulting predicted visibilities for a K-band measurement with a projected baseline of 300 m as a function of R_d/R_s for these different cases. Each plot shows how the visibility at this baseline declines as the disk size increases, and we can use these to estimate the smallest disk detectable. For example, we see in Figure 6.16 for a B0 V star of apparent magnitude 5 that the curve dips below $V = 0.8$ at $R_d/R_s = 3.6$ from which we would infer that only disks larger than this would be detected with the CHARA Array. As expected, we can detect smaller disks in nearer (brighter) Be stars. Figure 6.17 shows the case for a later B8 V type that is somewhat more favorable because such stars are closer for a given apparent magnitude, and the ratio of disk-to-star radius appears somewhat larger. Note that at small disk radii we simply assume that all the flux is stellar, so the limiting visibility near $R_d/R_s = 1$ corresponds to the stellar visibility (less than one because of the finite size of the star).
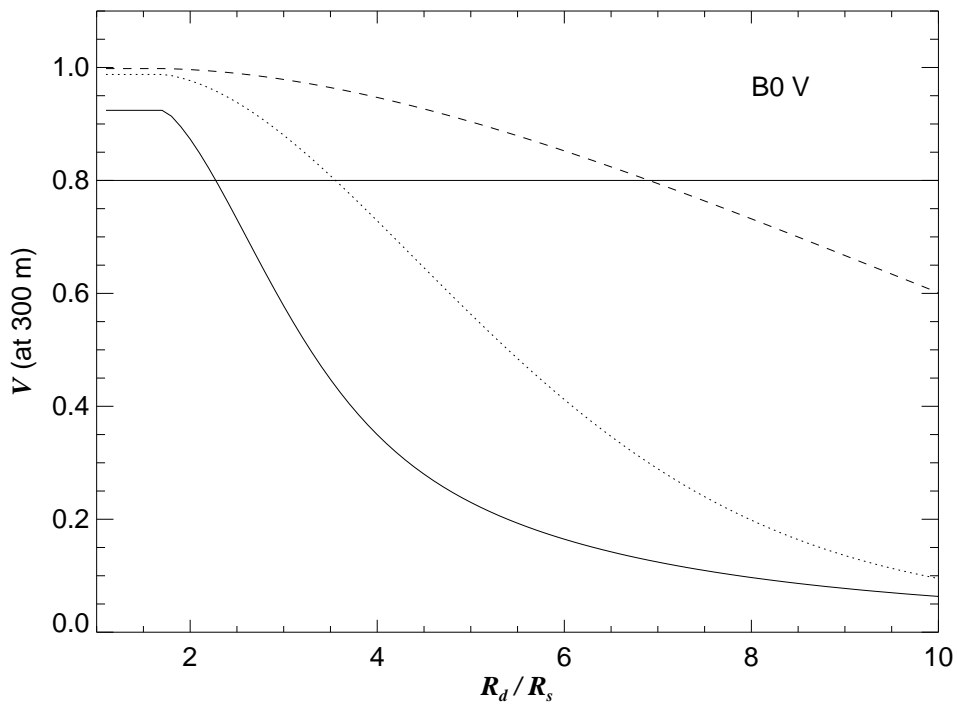
Figure 6.16: A plot of the expected calibrated visibility measured at a baseline of 300 m for a Be star of type B0 V as a function of disk to stellar radius along the major axis. The thick solid, dotted, and dashed lines correspond to predictions for a star of visual magnitude 3, 5, and 7, respectively. The thin horizontal line marks the $V = 0.8$ criterion, and if the visibility drops below this line then the disk is detected with some confidence.
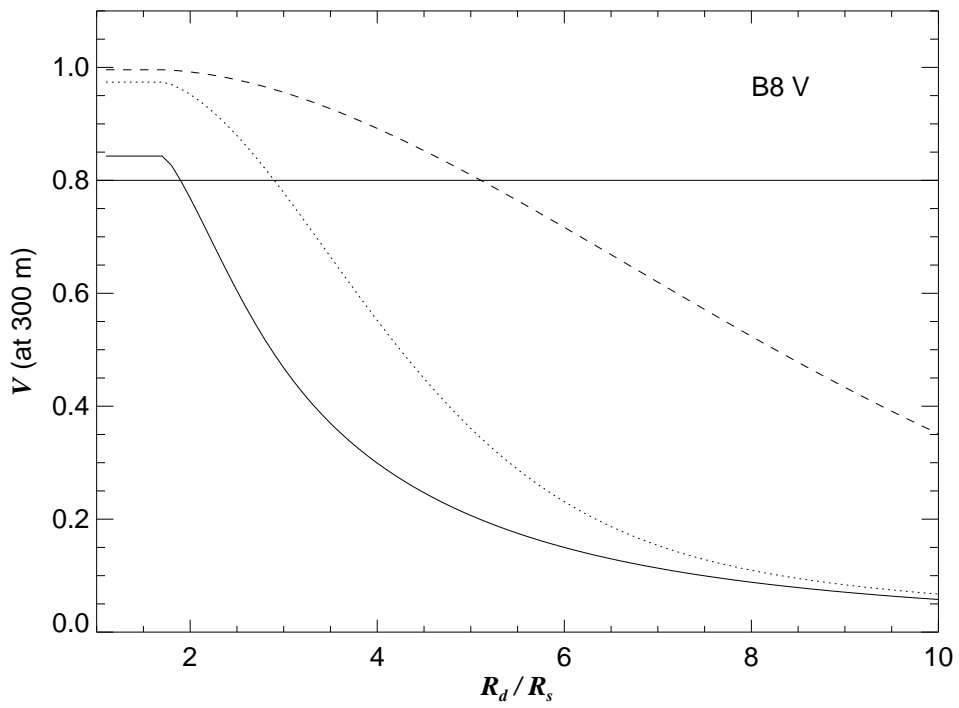
Figure 6.17: A second plot of predicted visibility as a function of disk to stellar radius but this time for a star of type B8 V (same format as Fig. 6.16)

6.6.2 K-band and Hα Disk Sizes

The physical processes responsible for the continuum disk emission in the near-IR are different from the processes responsible for the emission lines. Since the source of the emission detected in the near-IR continuum originates within only a few stellar radii from the star while the Hα flux originates within a larger extent from the stellar photosphere, we expect these two properties to be correlated with the physical size of both emitting regions of the circumstellar disk. Therefore, we aimed to look for a correlation between the K-band disk sizes derived from our interferometric measurements and Hα disk sizes that we gathered for a dozen Be stars from Hα interferometric observations. We list the values of the Hα disk sizes from interferometry in Table 6.9. We also derived the Hα disk sizes for all stars using Hα equivalent widths (Grundstrom & Gies 2006), and we list our results in Table 6.10. We used inclinations that we derived from the Gaussian elliptical fits ($i \approx \arccos(r)$) and adopted the effective temperatures listed in Table 6.1.

Table 6.9: Hα Disk Sizes of Be stars from Interferometry

Star Name	$\theta_{H\alpha}$ (mas)	$\delta\theta_{H\alpha}$ (mas)	Ref.
HD 004180	1.90	0.10	Koubský et al. (2010)
HD 005394	3.47	0.02	Quirrenbach et al. (1997)
	3.59	0.04	Tycner et al. (2006)
HD 010516	2.67	0.20	Quirrenbach et al. (1997)
	2.89	0.09	Tycner et al. (2006)
HD 022192	3.26	0.23	Quirrenbach et al. (1997)
	4.00	0.20	Delaa et al. (2011)
HD 023630	2.65	0.14	Quirrenbach et al. (1997)
	2.08	0.18	Tycner et al. (2005)
HD 025940	2.77	0.56	Quirrenbach et al. (1997)
	2.10	0.20	Delaa et al. (2011)
HD 037202	4.53	0.52	Quirrenbach et al. (1997)
	3.14	0.21	Tycner et al. (2004)
HD 058715	2.65	0.10	Quirrenbach et al. (1997)
	2.13	0.50	Tycner et al. (2005)
HD 109387	2.00	0.30	C. Tycner, priv. comm
HD 148184	3.46	0.07	Tycner et al. (2008)
HD 202904	1.00	0.20	C. Tycner, priv. comm
HD 217891	2.40	0.20	C. Tycner, priv. comm

Table 6.10: Hα Disk Sizes Derived from Hα Equivalent

Widths

Star Name	$W_\lambda(\mathrm{H}\alpha)$ (Å)	R_d (R_s)
HD 004180	-33.5 ± 0.3^a	12.53 ± 0.05
HD 005394	-31.2 ± 0.3^a	8.89 ± 0.04
HD 010516	-30.1 ± 0.3^a	8.69 ± 0.04
HD 022192	-37.7 ± 0.3^a	13.09 ± 0.05
HD 023630	-04.2 ± 0.3^a	4.37 ± 0.15
HD 023862	-17.1 ± 0.3^a	10.25 ± 0.08
HD 025940	-28.1 ± 0.3^a	9.78 ± 0.05
HD 037202	-18.1 ± 0.3^a	8.61 ± 0.06
HD 058715	-17.7 ± 0.3^b	9.73 ± 0.08
HD 109387	-20.9 ± 0.3^c	8.65 ± 0.06
HD 138749	$\dots$	$\dots$
HD 142926	-01.1 ± 0.3^c	3.06 ± 0.33
HD 142983	-21.0 ± 0.3^c	9.90 ± 0.07
HD 148184	-55.2 ± 0.3^c	12.14 ± 0.03
HD 164284	-08.3 ± 0.3^b	5.23 ± 0.09
HD 166014	$+06.7\pm0.3^b$	1.00 ± 1.25
HD 198183	$+04.7\pm0.2^b$	1.00 ± 0.97
HD 200120	-13.5 ± 0.3^a	7.07 ± 0.07
HD 202904	-25.8 ± 0.3^a	10.25 ± 0.05
HD 203467	-25.3 ± 0.3^b	9.35 ± 0.05
HD 209409	-20.8 ± 0.3^c	10.88 ± 0.07
HD 212076	-24.3 ± 0.3^a	8.46 ± 0.05
HD 217675	$+04.7\pm0.4^a$	1.00 ± 0.82
HD 217891	-11.1 ± 0.3^a	7.34 ± 0.09

References - [a] Touhami et al. (2010); [b] Grundstrom (2007); [c] Silaj et al. (2010); [d] Hernández et al. (2005)
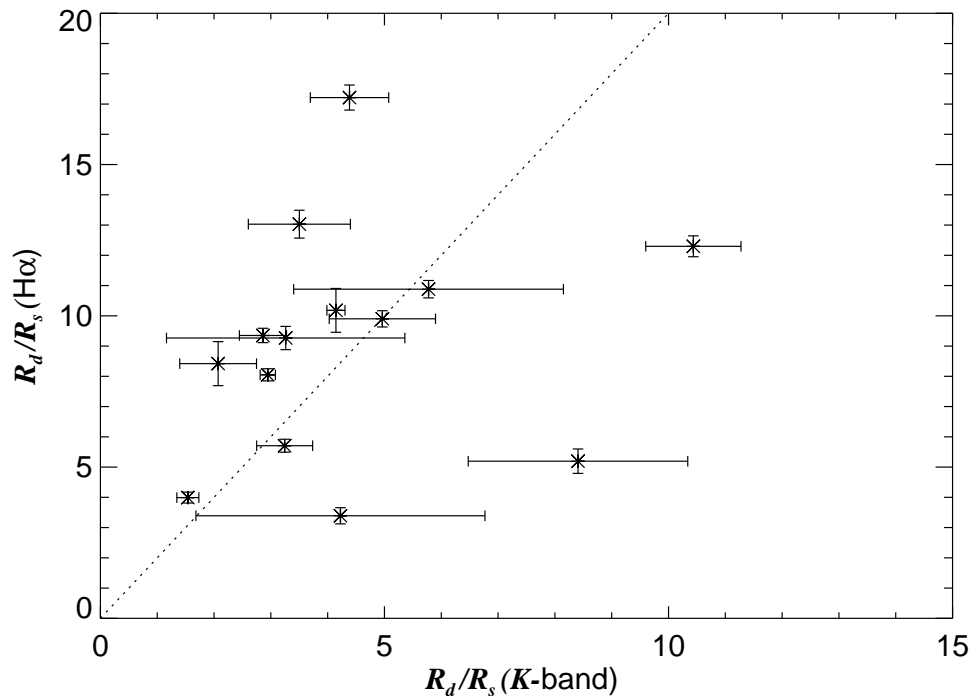
Figure 6.18: A comparison of the K-band disk angular diameters with the Hα angular diameters. The dotted line represents a straight line of a constant slope of 0.5.

We plot in Figure 6.18 our K-band measurements of the disk-to-star size ratio R_d/R_s that we derived from the Gaussian elliptical fits versus the Hα disk sizes (either observed or derived from Hα equivalent widths; see Table 6.10) for the sub-sample of Be stars with resolved disks. The Hα angular sizes derived from Hα interferometry and listed in Table 6.9 were transformed to R_d/R_s by using estimates of the stellar angular diameters that we derived from fitting the SEDs of Be stars. The dashed line in Figure 6.18 represents a possible relationship between the two quantities, a straight line with a slope of 0.5.

The correlation between the Hα and the K-band continuum disk sizes was mentioned by Gies et al. (2007), where the authors found that disk measurements of four Be stars γ Cas, ζ Tau, ϕ Per, and κ Dra in the K-band were about half the disk angular diameter measured

in the Hα. They attributed this to the difference in the opacity of Hα and the free-free and bound-free opacities that dominate the disk emission process in the infrared. Such a correlation is extremely helpful in predicting the size of the circumstellar disk in the K-band from Hα observations and vice-versa, especially since Be star disks are highly variable and that simultaneous, multiwavelength observations of these targets is usually difficult to achieve.

6.6.3 Emission Lines and Disk Sizes

One characteristic of Be star disks is the correlation that exists between the strength of the different hydrogen emission lines detected in Be star spectra and the spatial extension of their circumstellar disks. Quirrenbach et al. (1997) and Tycner et al. (2006) showed that Be stars with stronger Hα emission have larger disks, but because both their samples were not large and the scatter in their results was considerable, the issue bears further consideration. Previous results reported in §3.4 indicate that the strength of the different hydrogen emission lines are correlated with the IR flux excess derived from the SED of Be stars. In fact, we showed that the disk IR flux excess is better correlated with the equivalent-widths of high excitation transitions like Brγ or Hu14. On the other hand, we showed in §4.2 that the IR flux excess is also correlated with the circumstellar disk size. Consequently, we expect to find a correlation between the strength of the infrared emission lines Brγ and Hu14, and the K-band size of the disk.

Grundstrom & Gies (2006) demonstrated that such a relationship exists between the Hα equivalent width and the Hα disk size by presenting numerical models of Be disks that compute the flux distribution of the disk in Hα as well as synthetic Hα emission lines.

Grundstrom & Gies (2006) adopted a power-law disk density distribution, similar to what we have used for our physical thick disk model (see eq. 2.6 in §2.3.1), and calculated synthetic line profiles over a range from -2000 to +2000 km s^{-1} at 10 km s^{-1} intervals by summing the product of the projected area and the specific intensity over a wide disk grid. The model equivalent-widths of Hα are then computed by integrating the synthetic line profile relative to the continuum. The model shows a relationship between the the Hα equivalent-widths and the Hα projected disk major axis to the radius of the star according to the relation

$$\frac{R_d}{R_s} = \sqrt{\frac{I_s}{I_d} \frac{W_\lambda(1 + \epsilon)}{< \Delta\lambda > \cos i}} \tag{6.7}$$

where I_s and I_d are the stellar and disk emission intensities, respectively, W_λ is the line equivalent-width, ϵ is the ratio of disk continuum flux to stellar flux, and i is the disk inclination angle. The authors show that this relationship depends mainly upon the disk temperature, the disk inclination angle, and the adopted disk outer boundary.

In order to investigate this correlation and the correlation between the K-band disk sizes and Hα equivalent widths, we use the 14 Be stars with resolved disks, and we plot in Figure 6.19 the values of the disk sizes derived from Hα interferometry versus Hα equivalent widths (diamond signs), and the K-band disk sizes versus Hα equivalent widths (star signs). For targets with no Hα interferometric angular sizes, we adopted estimates that we derived from contemporaneous Hα equivalent widths according to the procedure given Grundstrom & Gies (2006).

We then made use of the spectrophotometric measurements of a sub-sample of Be stars (HD 4180, HD 5394, HD 10516, HD 22192, HD 23862, HD 25940, HD37202, HD 200120, HD 202904, HD 212076, and HD 217891) in order to investigate similar patterns that may
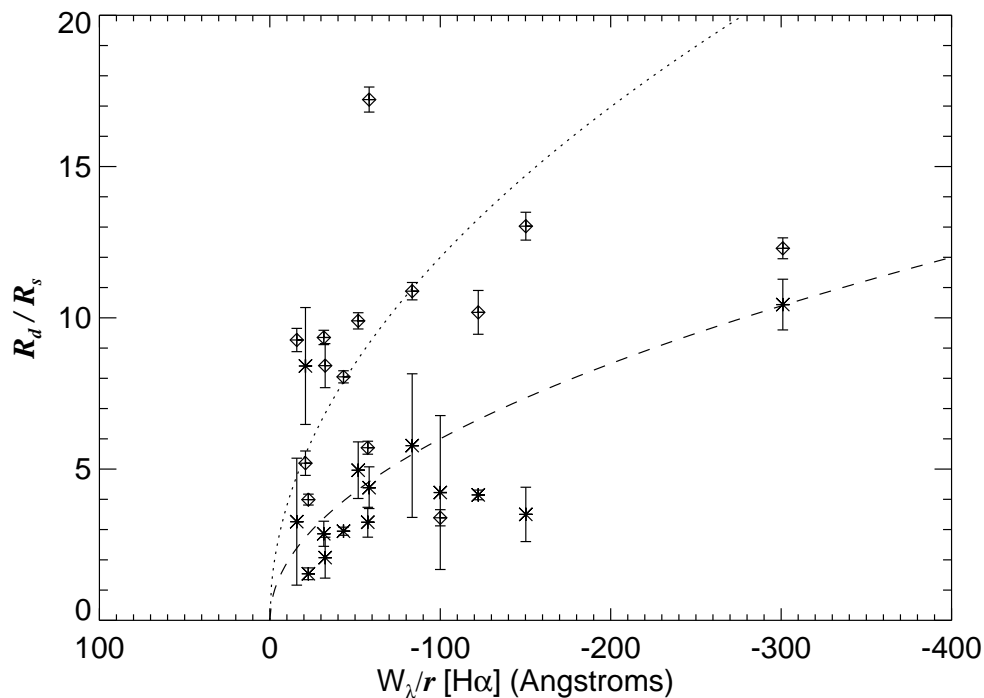
Figure 6.19: Disk-to-star size ratios versus Hα line equivalent-widths divided by the disk axial ratio. The dotted line represents a simple square-root function fit of the Hα disk sizes (diamonds) using a multiplication factor of 1.2. The dashed line represents a square-root function fit of the K-band disk sizes (stars) using multiplication factor of 0.6.

exist between the different equivalent-widths of the hydrogen infrared emission lines and the

K-band disk size. Because our spectrophotometric data cover only a subset of the sample,

we included Be stars with disks that were marginally resolved. As previously discussed

in §3.4, our spectrophotometry campaign conducted at Lowell Observatory allowed us to

obtain estimates of equivalent-widths of the hydrogen emission lines Brγ and Hu14 that are

contemporaneous with the interferometric data. The values of Brγ and Hu14 equivalent-

widths (listed in Table 3.5) were corrected for the disk flux excess at the corresponding

wavelength in order to estimate the emission flux relative to the stellar continuum using

$$W_\lambda^\star = W_\lambda \; 10^{0.4E^\star(V-\lambda)}. \tag{6.8}$$
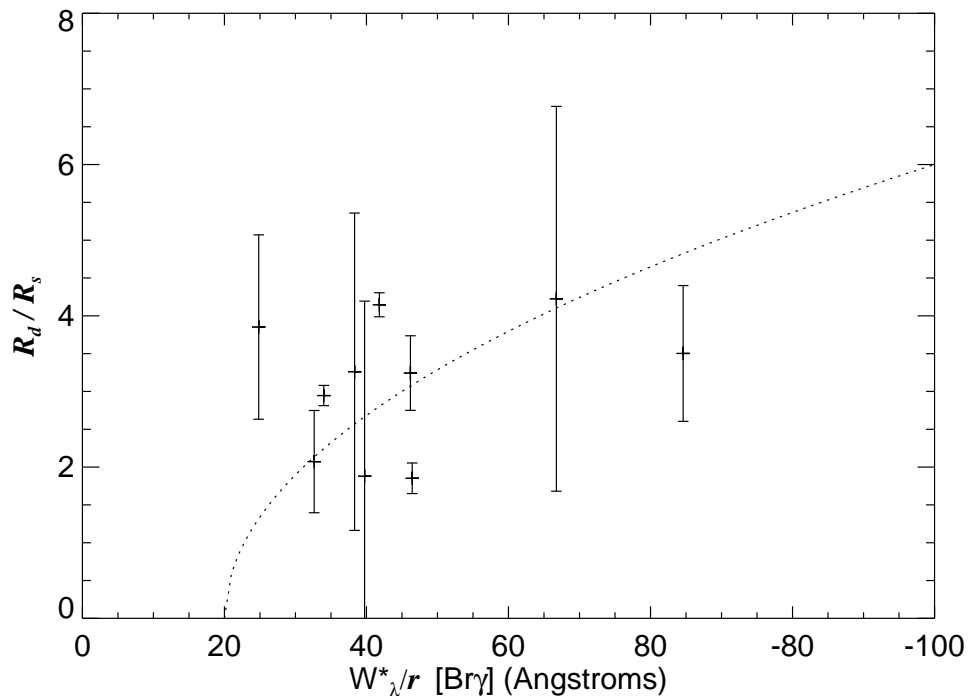
Figure 6.20: A comparison between the disk-to-star size ratios derived from interferometry with the equivalent-widths of the Brγ emission lines divided by the axial ratio. The dotted line represents a simple square-root function fit of the data using a multiplication factor of 0.6.

Since the K-band disk size is related to the IR flux excess, and this latter is related to the equivalent-width of the hydrogen high excitation emission lines, we suspect that similar correlations could exist between the K-band disk size and the equivalent-width of Brγ and Hu14, which might also have the functional form $\frac{R_d}{R_s} \propto \sqrt{\frac{W_\lambda^\star}{r}}$. In order to investigate such a correlation, we plotted Brγ and Hu14 emission line equivalent-widths derived from spectrophotometry, divided by the cosine of the inclination angle, as a function of the K-band disk-to-star size ratios, and we present our results in Figures 6.20 and 6.21, respectively. The plots shows that the K-band sizes are indeed correlated with the equivalent widths of the infrared emission lines. The data in both figures are shown with plus signs, and the
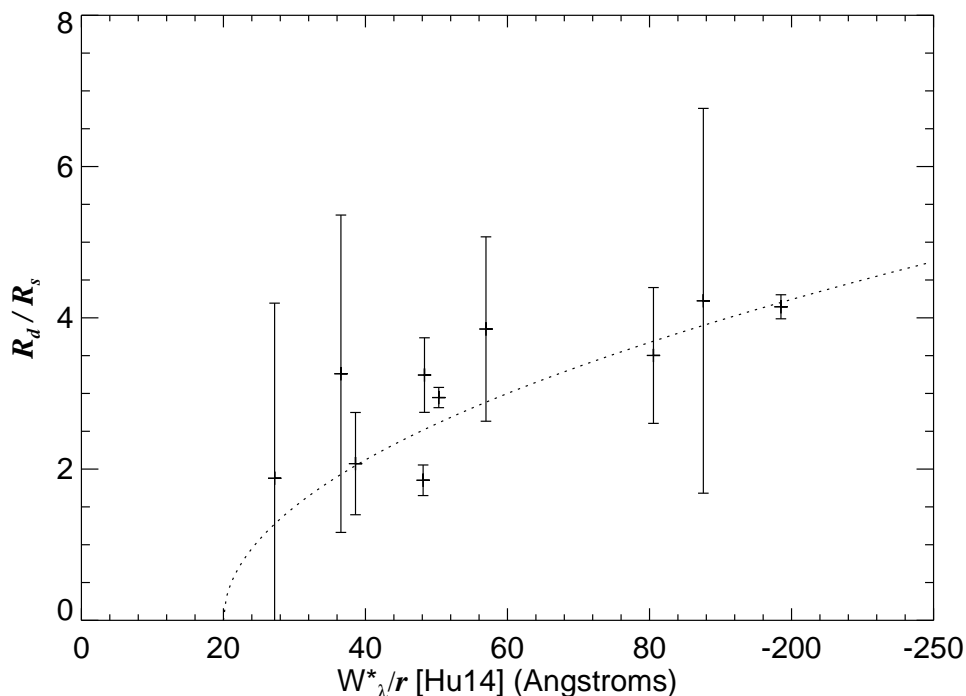
Figure 6.21: A comparison between the disk-to-star size ratios derived from interferometry with the equivalent-widths of the Hu14 emission lines divided by the axial ratio. The dotted line represents a simple square-root function fit of the data using a multiplication factor of 0.3.

dotted lines represent a simple square-root function fit to the data. These correlations could

be considered as diagnostic tools useful to probe the state of the circumstellar disks of Be

stars in the near infrared and in Hα.

6.6.4 Distributions of Be Disk Sizes and Inclinations

The sample of 14 Be stars with resolved disks allows us to conduct a study of the distributions

of the circumstellar disk sizes and inclination angles determined in the K-band for the first

time. For this purpose, we constructed histograms of the disk-to-star size ratios as a function

of the number of systems, shown in Figure 6.22, and for the disk inclination angles as a

function of the number of systems, shown in Figure 6.23. The distribution of the disk-to-
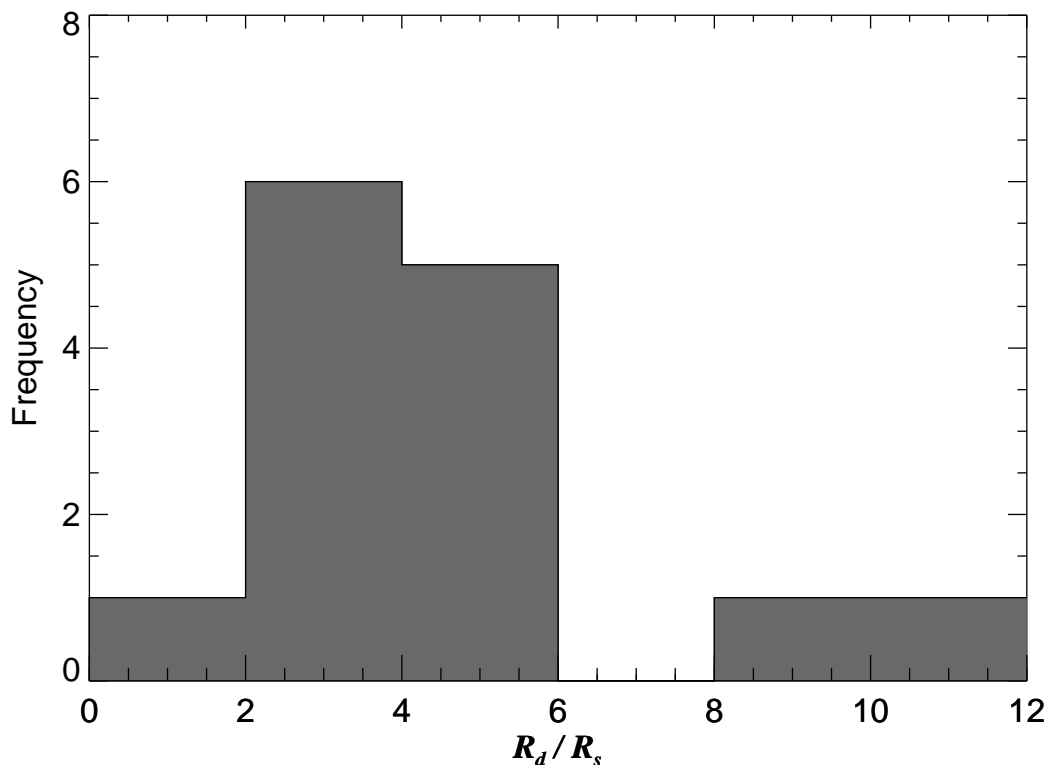
Figure 6.22: A histogram of the distribution of our sample stars as a function of the disk-to-star size ratio.

star size ratios shows a large scatter in the values of the disk sizes, with a peak at occurs at about $R_d/R_s \sim 4.5$.

The histogram of the distribution of the disk inclination presented in Figure 6.23 shows that a tendency toward high values of inclination exists among our sample stars. In fact, we find that more than half of our sample stars have inclination angles of $55°$ and higher, which is similar to statistical analysis derived from the rotational characteristic study of Be stars performed by Moujtahid et al. (1999), where the mean values for disk inclinations were found to be $\approx 59°$ for B3 - B5.5 spectral type Be stars and $\approx 55°$ inclination angles for Be stars with spectral type B6 to B9.5.
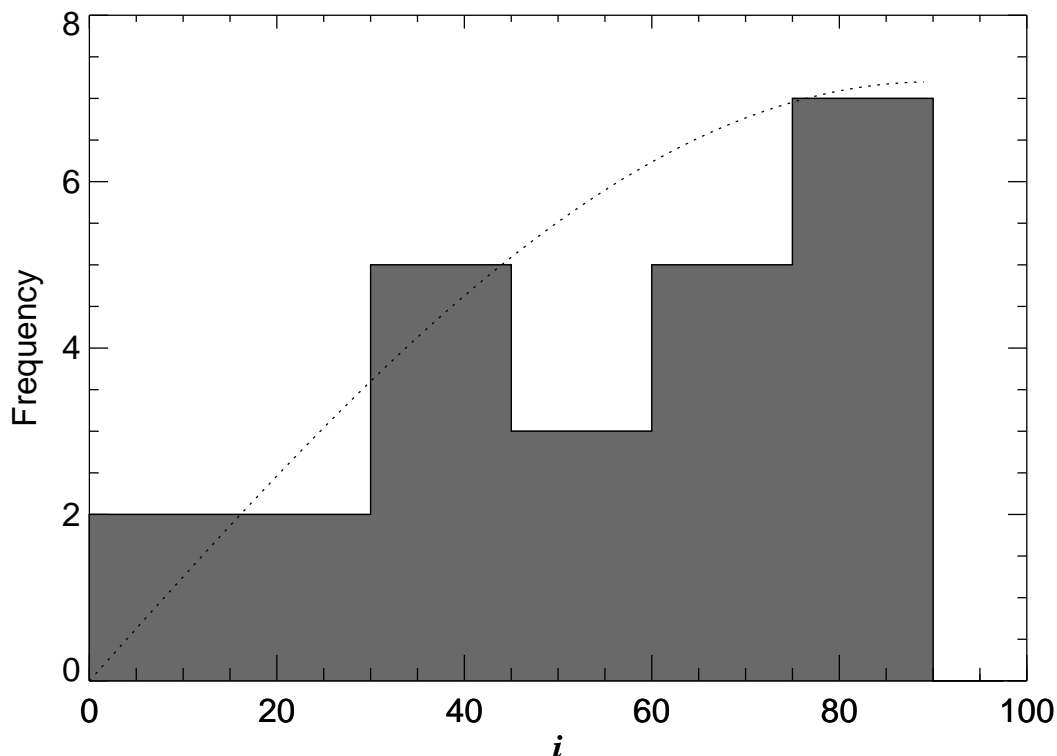
Figure 6.23: A histogram of the distribution of our sample stars as a function of the disk inclination angle. The dotted line shows the expected probability for the disk inclinations, which is proportional to a sinus function ($P_{inc} \propto \sin i$) for random orientations.

6.6.5 Be Star Linear Rotational Velocities

One crucial characteristic of Be stars is that they rotate more rapidly than any other class of non-degenerate stars. The absorption lines in Be star spectra are usually broader than those normal B-type stars, which led Struve (1931) to suggest that Be stars are rapidly rotating B-type stars. Struve (1931) assumed that the rotational velocity of the Be star has reached its critical value so that matter could escape the stellar photosphere by rotational instability, and form an equatorial disk around the star. However, many studies showed that the actual rotational velocity of Be stars is subcritical, with $V_{\rm rot}/V_{\rm crit} \simeq 0.7$ - 0.8 (e.g.

Porter 1996; Frémat et al. 2005), and that a rotational velocity very close to critical (i.e. $V_{\rm rot}/V_{\rm crit} \simeq 0.95$) is required to efficiently reduce the stellar gravity and to contribute to the mass loss of material at the stellar photosphere (Townsend et al. 2004).

In order to investigate the rotational aspect of Be stars, we adopt the values of the projected rotational velocities $v \sin i$ listed in Table 6.1, and estimates of the disk inclination angle i derived from the values of the disk axial ratio ($r \simeq \cos i$) for a total of 14 Be stars with resolved disks (see §6.5.2). We also adopt the stellar parameters listed in Table 6.1 to compute the critical rotational velocity $V_{\rm crit}$ for the sub-sample by using

$$V_{crit} = \sqrt{GM_s/R_s}, \qquad (6.9)$$

where M_s and R_s are the mass and the radius of the Be star, respectively. Note that because of the rapid rotation of the star, the stellar photosphere is oblate, and thus the stellar radius at the equator could be up to ≈ 1.5 times the stellar radius at the poles.

Using the projected rotational velocity $v \sin i$ and the inclination i derived from our interferometric data, we were able to estimate the actual rotational velocity $V_{\rm rot}$ for the 14 Be stars, and we list our results in Table 6.11. Column 1 lists the star name, column 2 lists the adopted values of the projected rotational velocity $v \sin i$, column 3 lists the actual linear rotational velocity ($V_{\rm rot} = v \sin i / \sin i$), and column 4 lists our estimates of the critical velocity. We list the rotational rate $q_1 = \frac{V_{\rm rot}}{V_{\rm crit}}$ derived by using our estimates of the critical velocities in column 5, and for comparison, we list values of q_2, which are derived by using values of the critical velocity $V_{\rm crit}$ from Frémat et al. (2005), in column 6.

Table 6.11: Linear Rotational and Critical Velocities of

Be Stars

Star Name	$v \sin i$ (km s^{-1})	$V_{\rm rot}$ (km s^{-1})	$V_{\rm crit}$ (km s^{-1})	q_1	q_2^a
HD 004180	195	240.01± 21.41	486.29	0.49	0.72
HD 005394	432	624.37± 35.78	543.69	1.15	1.08
HD 010516	440	442.22± 00.00	521.96	0.85	0.75
HD 022192	275	284.10± 42.77	433.92	0.64	0.71
HD 025940	197	393.96± 00.00	469.09	0.84	1.02
HD 037202	310	313.45± 01.28	591.78	0.53	0.67
HD 058715	230	369.77± 00.00	509.27	0.73	0.97
HD 109387	209	⋯	378.19	⋯	⋯
HD 142983	407	445.14± 00.00	608.16	0.73	0.89
HD 148184	151	470.06± 00.00	521.98	0.90	0.81
HD 202904	167	171.85± 06.16	563.78	0.31	0.37
HD 203467	153	254.44± 00.00	704.16	0.36	0.71
HD 209409	282	291.17± 04.56	410.53	0.71	0.74
HD 217891	95	133.39± 27.69	484.04	0.28	0.36

[a] Critical Velocities $V_{\rm crit}$ from Frémat et al. (2005).
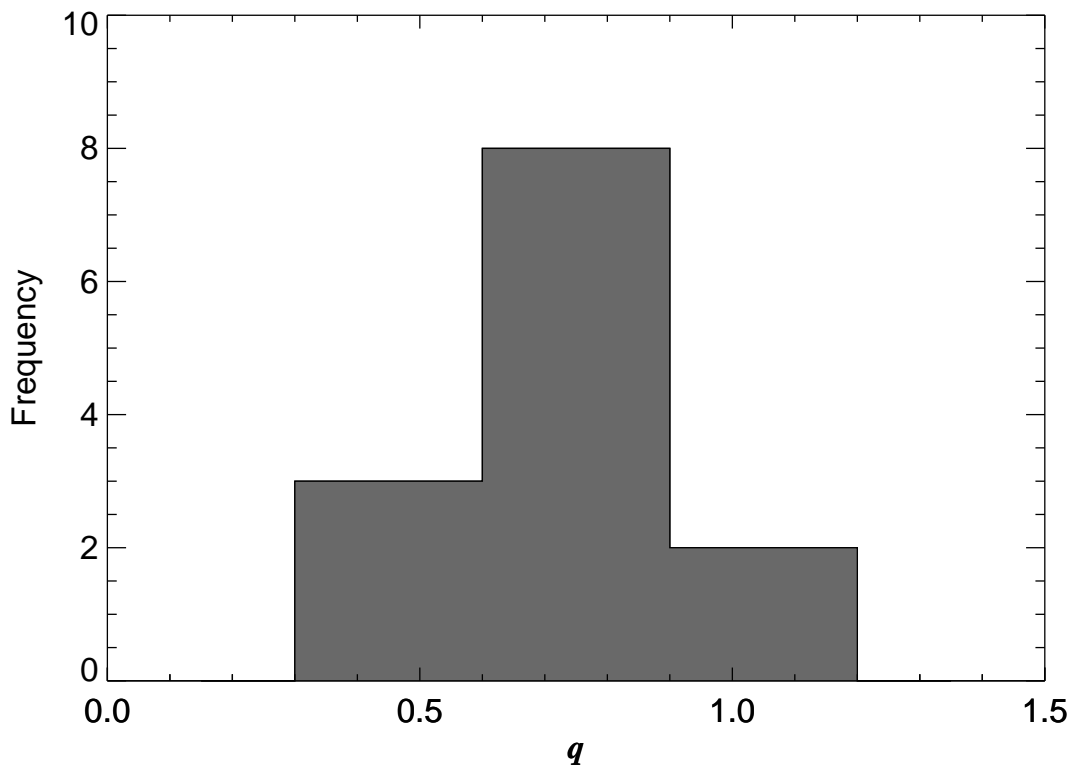
Figure 6.24: A histogram of the distribution of our sample stars as a function of their linear rotational rates.

We find that the rotational rates of our sub-sample obtained by averaging the values of q_1 and q_2 range between 0.6 and 0.9 with a larger number of stars rotating very close to their critical velocities ($q \approx 0.8$), and that γ Cas is the only Be star that rotates at its critical velocity. Figure 6.24 shows the histogram of the distribution of the rotational rates as a function of the number of systems in our sub-sample. Note that these values are subject to large systematic errors that arise mainly from the uncertainties in the adopted mass and linear radius of the Be stars. In addition, most values of $v \sin i$ are usually derived without correcting for the gravity darkening effect, which also leads to systematic underestimates of the true projected equatorial velocities (Townsend et al. 2004). The uncertainties in the

inclination angles of Be disks range between $4°$ and $11°$, and thus only induce small effects on the values of the actual rotational velocities derived here. Frémat et al. (2005) measured a mean intrinsic equatorial velocity of $< V_{\mathrm{rot}}/V_{\mathrm{crit}} > = 0.83$, which indicate that Be stars rotate very rapidly, but with velocities that are subcritical. Our results suggest the same conclusion, with the exception of γ Cas only. These results suggest that rapid rotation plays an important role, but not the only role, in the Be phenomenon.

6.7 Conclusions

In this chapter, we have presented results from our interferometric survey conducted with the CHARA Array interferometer at multiple baselines. We have interpreted the visibility measurements with a simple geometrical model assuming a Gaussian elliptical brightness distribution of the disk. We then present the best-fit disk size, axial ratio, position angle, and photospheric contribution for our sample stars. We find that the best-fit values for the K-band disk angular diameters of some of our targets are consistent with values reported by Gies et al. (2007) and Kraus et al. (2012). Furthermore, we show that the K-band continuum disk size is correlated with the strength of the hydrogen infrared emission lines Brγ and Hu14. By combining the projected rotational velocity of a sample of 14 Be star with disk inclinations derived from interferometry, we provide estimates of the equatorial rotational velocities and we show that these stars rotate very close to their critical velocities.

It is said an Eastern monarch once charged his wise men to

invent him a sentence to be ever in view, and which should

be true and appropriate in all times and situations. They

presented him the words: "And this, too, shall pass away."

—— Abraham Lincoln

Determining the Fundamental Stellar Properties of the Yellow Hypergiant ρ Cassiopeia

ABSTRACT

The yellow hypergiant ρ Cassiopeia is approaching the end of its stellar evolution, and due to its extreme mass and evolutionary stage, it is very unstable and undergoing many violent outbursts. Here we report the observations of ρ Cas in the K-band, obtained with the CHARA Array interferometer using the CHARA Classic and FLUOR beam combiners. The high quality of the data, especially the FLUOR data, allowed us to derive a precise angular diameter of the star, which combined with an estimate of the bolometric flux yield the effective temperature of the yellow hypergiant ρ Cas at the time of our observations. We find that the limb-darkened angular diameter is 1.72± 0.02 mas, which correspond to a linear diameter of $R_{\mathrm{LD}} = 570 \pm 97 R_\odot$. We also find that our interferometric data are compatible with a circularly symmetric brightness distribution on the sky with evidence for a diffuse emission around the star during our observational time frame. Using the best-fit angular diameter of the star, we derived estimates of its fundamental stellar properties such as its linear radius and its effective temperature.

7.1 Introduction

ρ Cassiopeia (HD224014, V=4.5 mag, K=2.1 mag) belongs to the group of yellow hypergiants, which are massive stars in the supergiant phase characterized by very high luminosities and extreme mass loss rates ($L \sim 10^6 L_\odot$, $\dot{M} \sim 10^{-2} M_\odot$ yr^{-1}; Gorlova et al. 2006). According to theoretical studies, yellow hypergiants start their zero-age main sequence phase

with a large mass, and because of the different mass loss processes they undergo, they evolve to a mass range of 15 - 20 $M_\odot$ as Wolf-Rayet stars or pre-supernovae (Lobel et al. 2003). The yellow hypergiant ρ Cas has a spectral type range that ranges from F8 to G2, which corresponds to an effective temperature that varies between $T_{\text{eff}} = 6500 - 7200$ K. The star has a luminosity class of IaO, which implies a luminosity of $\log L_*/L_\odot \sim 5.7$ and an estimated radius range of ~ 400 - 500 $R_\odot$. Evolutionary tracks puts ρ Cas in the range of ~ 40 $M_\odot$ star with a possible age range of 4 - 6 Myr (Lejeune & Schaerer 2001). ρ Cas might soon end its life in a giant supernova explosion, and it provides one of the best examples of the complicated physical processes that lead to the extreme mass loss rates in this late stage of the life of a massive star.

Percy et al. (2000) reported over 5700 days of VRI photometry of the yellow hypergiant star ρ Cas, and confirmed that it varies by up to a magnitude in V-band through several cycles on timescales of 200 to 500 days. They find that ρ Cas also varies in $V - I$ color on a timescale of 4000 days. Their results along with spectroscopic results suggest that the star is pulsating in a complex mixture of radial and nonradial modes, on which are superimposed the effects of occasional shell ejections. Lobel et al. (2003) presented an overview of ρ Cas spectral variability obtained from an 8.5-year monitoring campaign. They recorded the 2000 - 2001 outburst event. They show that during the outburst a central emission appears above the local continuum level in the Na D lines at 589 nm and that a prominent optical emission line spectrum appears in variability phases of fast wind expansion. The outburst spectra indicated the formation of a low-temperature, optically thick circumstellar gas shell of about 3×10^{-2} $M_\odot$ during 200 days, caused by the dynamical instability of the upper atmosphere near the Eddington luminosity limit. Lobel et al. (2003) found that the mass-loss rate during

the outburst is of the same order of magnitude as has been proposed for the outbursts of η Carinae. The mass loss rate of ρ Cas was found to be about $\sim 10^{-4} M_\odot$ y^{-1} in quiescent phases, and it increased by two orders of magnitude during this outburst episode (Lobel et al. 2003).

Gorlova et al. (2006) presented a high-resolution spectroscopic study of ρ Cas. Their observations cover one pulsation cycle in $2003 - 2004$ over the wavelength range from the optical to 4μm. The authors identified several prominent emission lines in the L-band spectrum observed near maximum brightness, and they presented K-band spectra obtained during the last outburst in $2000 - 2001$. They argued that the split absorption-line profiles detected in ρ Cas are not caused by two separately ejected shells during rare outbursts of the hypergiant, but rather are a commonly observed combination of a static narrow central emission line superimposed on the core of a broad absorption line. They further discussed a number of alternative explanations for the origin of the ubiquitous emission lines that could be due to a quasi-chromosphere or a steady shock wave at the interface of a fast expanding wind and the interstellar medium. Yamamuro et al. (2007) presented spectroscopic observations of three yellow hypergiants including ρ Cas in the 0.9 - 2.4 μm wavelength range. Their spectra have a resolving power of 2600 and they cover a fifteen month time-period. The spectra of ρ Cas show a series of variations in 2.3μm CO features that range from non-detection to absorption through emission during $2002 - 2004$. Yamamuro et al. (2007) interpreted these variations as the result of an expanding gas shell whose excitation temperature cooled down to about 800 K. The authors estimated a shell mass of 2×10^{-3} $M_\odot$ assuming a spherical symmetry for the expanding shell with a constant expansion velocity of 35 km s^{-1}, an effective temperature of 7000 K, and a radius of 400 $R_\odot$.

In this chapter, we present our results from interferometric and spectrophotometric observations of ρ Cas made with the CHARA Array interferometer and the Mimir spectrograph. An overview of the observations and the data analysis process is described in §7.2. The analysis of the continuum data and a model of the circumstellar structure around ρ Cas (its geometrical extension and physical properties) are presented in §7.3. In §7.4, we summarize our results and draw our conclusions.

7.2 Observations and Data Processing

We observed ρ Cas with the CHARA Array interferometer between 2006 and 2009. We used the CHARA Classic (ten Brummelaar et al. 2005) and the FLUOR (Fiber Linked Unit for Optical Interferometry; Coudé du Foresto et al. 1998; Mérand et al. 2005) beam combiners both operating in the K-band of the near infrared, at $\lambda = 2.1329\mu$m for CHARA Classic (Aufdenberg et al. 2006), and $1.94 \leq \lambda \leq 2.34\mu$m. Several baselines of CHARA were used in order to sample ρ Cas's brightness distribution at multiple spatial frequencies. The data reduction of the Classic interferometric observations was performed using REDU-CEIR (ten Brummelaar et al. 2005), and the reduction of FLUOR data was performed using the reduction software package described in Coudé du Foresto et al. (2003). The visibility measurements were corrected for atmospheric and instrumental effects by using several unresolved stars as calibrators for our observations. We list in Table 7.1 the stellar properties of the chosen calibrator stars, along with estimates of their angular diameters and the corresponding errors.

Estimates of the angular diameter of the calibrator stars are computed by direct comparison of the observed and model flux distributions. The model SEDs are based on the
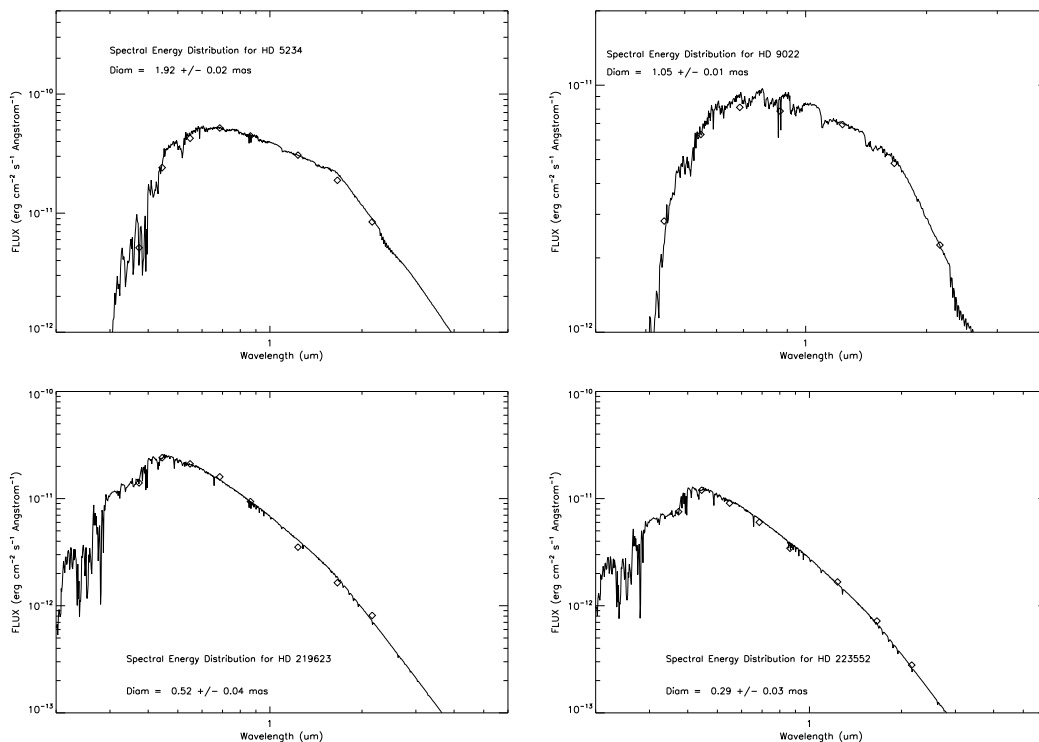
Figure 7.1: SED fits of the calibrator stars used for ρ Cas observations along with estimates of their angular diameters.

stars adopted effective temperature T_{eff} and surface gravity $\log g$, and on the limb-darkening coefficients given by Claret (2000). We then transformed the limb-darkened diameter to an equivalent uniform disk angular diameter of the stars assuming a baseline of 300 m. Plots of the models SEDs along with the data are shown in Figure 7.1.

Table 7.1: Calibrator Star Angular Diameters

Calibrator Name	$T_{\rm eff}$ (K)	$\log g$ (cm s^{-2})	Spectral Classification	$E(B-V)$ (mag)	θ_{LD} (mas)	θ_{UD} (mas)	Ref.
HD 5234	4380	2.63	K2 III	0.08 ± 0.06	1.97 ± 0.02	1.92 ± 0.02	1
HD 9022	5000	2.0	K2-3 III	0.28 ± 0.06	1.08 ± 0.01	1.05 ± 0.01	2
HD 219623	6087	4.14	F7 V	0.002 ± 0.001	0.48 ± 0.05	0.52 ± 0.04	3
HD 223552	6723	4.29	F3V	0.004 ± 0.001	0.29 ± 0.04	0.29 ± 0.03	4

References - 1. Takeda et al. (2007); 2. Mérand et al. (2005) and the spectral classification calibration of Gray (2005). 3. Soubiran et al. (2008); 4. Ammons et al. (2006).

The estimated errors on the visibility measurements are generally due to the internal uncertainty that result from calculating the raw instrumental visibilities. Fitting the fringe power spectrum to extract the raw visibilities introduces errors that are usually about $\sim 5\%$. Uncertainties are also introduced by the adopted stellar parameters of the calibrator stars used to estimate their angular diameters, but these uncertainties are generally less than a percent ($\leq 1\%$). A detailed summary of the CHARA Classic observations is listed in Table 7.2. The first column of Table 7.2 lists the heliocentric Julian date of the observations, column 2 lists the telescope pair used for each observation, columns 3 and 4 list the u and v coordinates in cycles arcsec^{-1}, column 5 lists the interferometric projected baseline in meters, column 6 lists the calibrated visibility measurements, and finally, column 7 lists the errors on the visibility.

FLUOR observations of ρ Cas were conducted in 2006 November, in the K'-band, using the intermediate baselines of the telescope pair $W1/W2$. The FLUOR data reduction pipeline (Coudé du Foresto et al. 2003) produces squared visibilities and their corresponding errors. Thus, for comparison with CHARA Classic data, we transformed the squared visibility to visibility as the square root of the squared visibilities $V = \sqrt{V^2}$, and computed the corresponding errors as $\delta V = \frac{\delta V^2}{2V}$. A summary of the FLUOR observations is presented in Table 7.3. The resulting (u, v) distribution on the sky showing both Classic and FLUOR sets of data is plotted in Figure 7.2. The star signs in Figure 7.2 represent the CHARA Classic data while the square signs represent the FLUOR data.
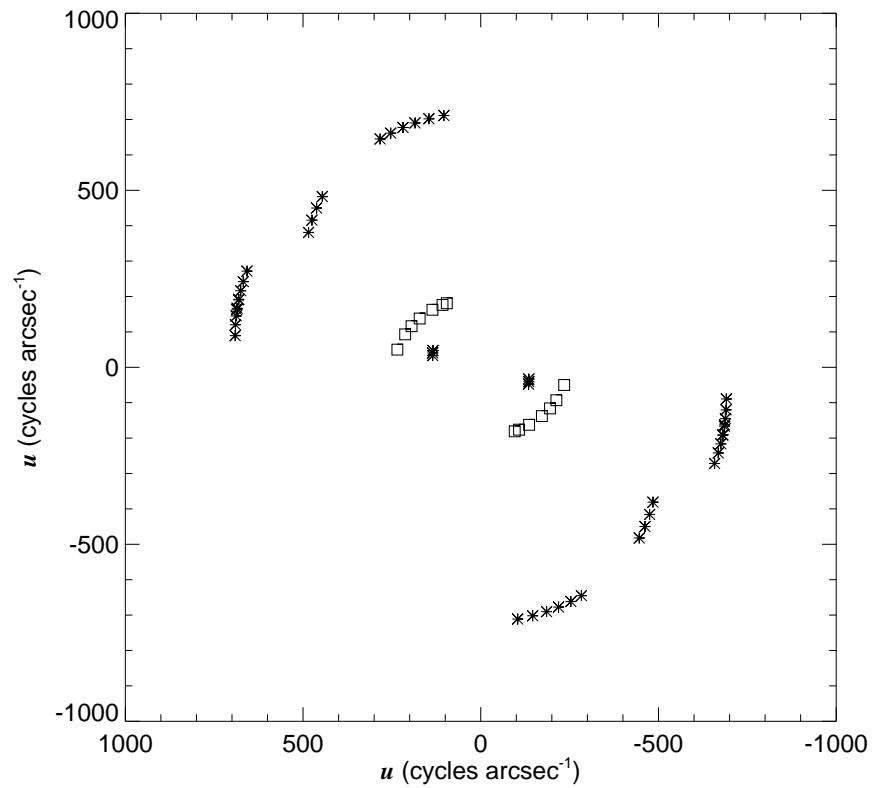
Figure 7.2: (u, v) plane coverage of our interferometric observations. Star signs are for CHARA Classic data, and the square signs are for FLUOR data. The scales are in units of $\frac{B}{\lambda}$ expressed in cycles arcsec^{-1}.

Table 7.2: CHARA Classic Calibrated Visibilities

Date (HJD-2,400,000)	Telescope Pair	u (cycles arcsec^{-1})	v (cycles arcsec^{-1})	Baseline (m)	V	δV
54786.675	S1/E1	−283.278	−645.033	309.952	0.064	0.004
54786.687	S1/E1	−253.361	−661.422	311.621	0.054	0.005
54786.699	S1/E1	−218.759	−677.361	313.170	0.048	0.005
54786.710	S1/E1	−185.105	−690.119	314.359	0.055	0.005
54786.722	S1/E1	−145.890	−701.920	315.419	0.047	0.004
54786.738	S1/E1	−103.944	−711.198	316.225	0.043	0.005
55116.648	S1/E1	−484.563	−380.938	271.181	0.144	0.011
55116.664	S1/E1	−475.043	−415.697	277.724	0.122	0.010
55116.675	S1/E1	−461.939	−449.835	283.679	0.099	0.010
55116.687	S1/E1	−445.826	−482.121	288.906	0.117	0.011
55128.672	E1/E2	135.327	33.163	61.301	0.971	0.034
55128.683	E1/E2	135.142	40.540	62.075	0.896	0.021
55128.691	E1/E2	134.456	47.419	62.727	0.919	0.018
55152.644	E1/W1	690.852	89.387	306.483	0.043	0.002
55152.656	E1/W1	690.160	120.269	308.221	0.040	0.002
55152.660	E1/W1	688.212	144.912	309.427	0.044	0.012
55152.667	E1/W1	685.478	166.494	310.354	0.037	0.001
55152.675	E1/W1	681.275	190.611	311.246	0.042	0.010
55153.663	E1/W1	686.054	162.521	310.192	0.041	0.002
55153.671	E1/W1	681.004	191.959	311.292	0.035	0.002
55153.679	E1/W1	675.438	216.302	312.034	0.038	0.002
55153.687	E1/W1	668.170	241.970	312.653	0.039	0.002
55153.695	E1/W1	657.884	271.726	313.162	0.038	0.002

Table 7.3: FLUOR Calibrated Visibilities

Date (HJD-2,400,000)	Telescope Pair	u (cycles arcsec^{-1})	v (cycles arcsec^{-1})	Baseline (m)	V^2	δV^2	V	δV
54054.387	W1/W2	95.484	180.896	89.867	0.716	0.011	0.845	0.018
54055.246	W1/W2	234.696	49.980	105.425	0.585	0.010	0.764	0.015
54055.281	W1/W2	212.783	93.060	102.035	0.623	0.011	0.789	0.018
54055.301	W1/W2	194.692	116.059	99.582	0.672	0.012	0.819	0.019
54055.324	W1/W2	171.934	137.819	96.810	0.689	0.011	0.829	0.019
54055.355	W1/W2	135.976	162.493	93.088	0.683	0.013	0.826	0.020
54055.375	W1/W2	107.599	176.241	90.721	0.663	0.012	0.814	0.019

7.3 Angular Diameter Fits

7.3.1 Uniform Disk Model

In order to interpret the visibility measurements, we have used simple uniform and limb-darkened disk models to fit the interferometric data. In the case of a uniform disk case, we model the stellar photosphere with a circularly symmetric brightness distribution. The visibility function V_{UD} in this case is given by

$$V_{UD}(u, v) = 2\frac{J_1(\pi\theta_{UD}\sqrt{u^2 + v^2})}{\pi\theta_{UD}\sqrt{u^2 + v^2}}, \tag{7.1}$$

where J_1 is the first-order Bessel function and u and v are the spatial frequencies, which are given by the east-west and south-north components of the projected baseline on the plane of the sky divided by the wavelength of the observation, and θ_{UD} is the angular diameter of the uniform disk. We have included the bandwidth smearing effect by computing the bandwidth-smeared average visibility as:

$$V(B, \lambda_0) = \frac{\int V(B, \lambda_i)S(\lambda_i)d\lambda_i}{\int S(\lambda_i)d\lambda_i} \tag{7.2}$$

where $S(\lambda)$ is the K-band filter transmission distribution used for the CHARA Classic (McAlister et al. 2005) and for FLUOR (Mérand et al. 2005; Aufdenberg et al. 2006). We first used the uniform disk model to fit each set of FLUOR and Classic data separately, and then we combined both data sets to determine one best-fit solution. We find that the best-fit angular diameter of ρ Cas using only FLUOR data set is $\theta_{UD} = 1.83 \pm 0.02$ mas with a $\chi^2_\nu = 0.66$. The best fit angular diameter using the CHARA Classic data set is $\theta_{UD} = 1.64 \pm 0.03$ mas

with a $\chi_\nu^2 = 9.24$. Combining both data sets yields a best-fit uniform disk angular diameter of $\theta_{UD} = 1.65 \pm 0.03$ mas with a $\chi_\nu^2 = 9.49$.

7.3.2 Limb-Darkened Disk Model

Although we have no interferometric data that sample the second lobe of the visibility curve of ρ Cas, the fact that our measurements are so close to the first null of the visibility curve is sufficient motivation to fit a limb-darkened disk model to the data. In this model, the intensity distribution of the star is dependent on the cosine of the angle between the line of sight and the stellar surface normal μ, and in the linear approximation, the limb-darkening law is given by

$$I(\mu, \lambda) \, / I(1, \lambda) = 1 - a_1(1 - \mu^{1/2}) - a_2(1 - \mu) - a_3(1 - \mu^{3/2}) - a_4(1 - \mu^2) \qquad (7.3)$$

where in this simplistic approximation, $I(1)$ is the specific intensity at the center of the star, and where a_k are the limb-darkening coefficients that depends on the stellar effective temperature T_{eff}, the surface gravity $\log g$, and the wavelength of the observations λ (Claret 2000). We have determined the limb-darkening coefficient by extrapolating coefficients given by Claret (2000) to the effective temperature of $T_{\text{eff}} = 6000$ K and surface gravity $\log g = 0.7$ cm s^{-2} of ρ Cas listed in Table 3.2.

In this model, we also accounted for the bandwidth smearing introduced by the transmission function of the CHARA Classic detector. We the used the model to fit each set of FLUOR and Classic data separately. We find that the best-fit angular diameter of ρ Cas using only FLUOR data is $\theta_{LD} = 1.86 \pm 0.01$ mas, with a $\chi_\nu^2 = 0.66$, while the best-
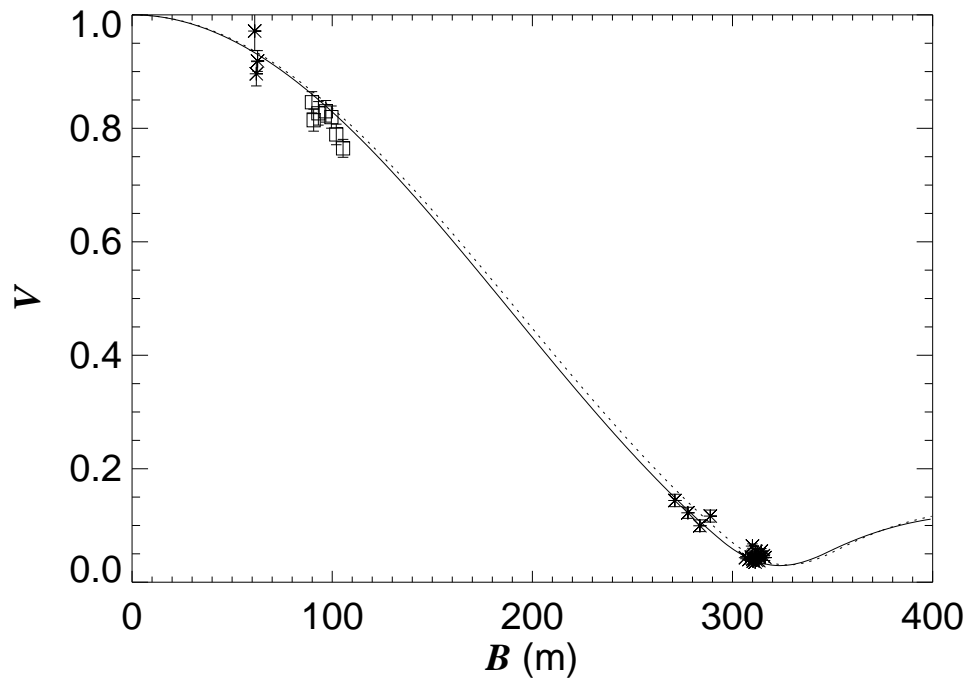
Figure 7.3: Calibrated visibilites versus the effective baseline for ρ Cas. The solid line represents the limb-darkened model fit and the dotted line is the uniform disk model fit. The star signs represent CHARA Classic data and the square signs represent FLUOR data.

fit angular diameter using only CHARA Classic data is $\theta_{LD} = 1.71 \pm 0.02$ mas, with a $\chi_\nu^2 = 5.37$. Combining both sets of data yields an angular diameter of a limb-darkened disk of $\theta_{LD} = 1.72 \pm 0.02$ mas with a $\chi_\nu^2 = 4.77$.

Figure 7.3 shows the interferometric visibilities along with the best-fit disk models. The star signs in Figure 7.3 represent the CHARA Classic data and the square signs represent the FLUOR data. The solid line in Figure 7.3 shows the best-fit limb-darkened disk model and the dotted line shows the best-fit uniform disk model. We find that the limb-darkened disk model fits the data the best and we adopt the value of θ_{LD} as the best estimate of the angular diameter of the star.

Interestingly, our estimates of the K-band angular diameter of ρ Cas are much smaller than the star's angular diameter measured in the 0.65 - 0.85 μm, where it was found to equal $\theta_{UD} = 2.36 \pm 0.05$ mas using a uniform disk model and equal to $\theta_{LD} = 2.47 \pm 0.05$ mas using a limb-darkened disk model (Nordgren et al. 1999). Percy et al. (2000) reported short-term variations of the star on timescales of 200 to 500 days from VRI photometry, and long-term variation on timescales of about 4000 days. These results suggest that ρ Cas is pulsating, and we suspect that the wide difference in the angular size of the star between our K-band result and results reported by Nordgren et al. (1999) is mainly due to variability.

7.4 Discussion

7.4.1 The Effective Temperature of ρ Cas

The effective temperature of ρ Cas, assuming that the star radiates as a blackbody, is usually derived using the best-fit limb-darkened angular diameter of the star through

$$T_{\text{eff}} = 7400 \ \left[\frac{F_{Bol}}{10^{-13} \ W \ cm^{-2}} \right]^{1/4} \ \left[\frac{1 \ \text{mas}}{\theta} \right]^{1/2} \text{K}, \qquad (7.4)$$

where F_{Bol} is the stellar bolometric flux. Several measurements of the star bolometric flux are given in the literature, but since ρ Cas is a variable star, we expect that estimates of the bolometric fluxes vary as well. We had then to rely only on our spectrophotometric measurements of ρ Cas obtained in 2008 (see §2.3 and §2.4) to fit the spectral energy distribution of the star and determine its effective temperature. We used fluxes are at 0.44, 0.68, 1.65, and 2.179 μm listed in Table 3.3 (see plot of the SED derived in Figure 3.3).

In order to estimate the effective temperature, we ran a series of atmospheric models with a grid of effective temperatures that range between 4000 K and 7000 K, and assuming

a constant surface gravity of $\log g = 0.7$ (Gorlova et al. 2006). These models of the flux distribution of ρ Cas are calculated using grids of models of R. L. Kurucz[1], which are based on solar abundances, plane-parallel, local thermodynamic equilibrium (LTE) approximations, and a turbulence velocity of 4 km s^{-1}. The generated SEDs were then compared to the spectrophotometric data, and for each model, we determine the limb-darkened angular diameter $\theta_{\text{LD, SED}}$ and the interstellar reddening $E(B - V)$ using

$$\frac{f_{\lambda, \text{ obs}}}{f_{\lambda, \text{ model}}} = \frac{10^{-0.4 \; R_\lambda \times E(B-V)}}{4} \theta^2_{\text{LD, SED}} \tag{7.5}$$

where $R_\lambda = A_V/E(B-V)$ is set at a value of 3.1. We list the resulting interstellar reddening $E(B - V)$ and the limb-darkened angular diameter of the star θ_{LD} for the temperature grid in Table 7.4.

Table 7.4: SED models for different effective temperature

T_{eff} (K)	$E(B - V)$ (mag)	θ_{LD} (mas)	χ^2_ν
4000	0.000 ± 0.007	2.274 ± 0.386	439.01
4400	0.000 ± 0.007	1.965 ± 0.125	53.46
4600	0.000 ± 0.007	1.848 ± 0.054	3.74
4800	0.059 ± 0.012	1.798 ± 0.047	0.52
5000	0.146 ± 0.014	1.782 ± 0.047	0.47
5200	0.237 ± 0.018	1.771 ± 0.050	1.64
5400	0.321 ± 0.024	1.762 ± 0.054	2.86
5600	0.398 ± 0.028	1.753 ± 0.058	4.28
5800	0.468 ± 0.033	1.746 ± 0.061	5.71
6000	0.531 ± 0.036	1.739 ± 0.064	7.04
6200	0.593 ± 0.040	1.735 ± 0.068	8.81
6400	0.649 ± 0.044	1.731 ± 0.072	10.65
6800	0.744 ± 0.049	1.718 ± 0.077	13.43
7000	0.783 ± 0.051	1.709 ± 0.078	14.11

[1]http://kurucz.cfa.harvard.edu/

The spectrophotometric measurements of ρ Cas taken in 2008 seem to prefer solutions that range between atmospheric models with effective temperature of $4800 \leq T_{\mathrm{eff}} \leq 5200$ K and an interstellar reddening that ranges between $0.06 \leq E(B-V) \leq 0.24$ mag. Note that by using our best-fit limb darkened angular diameter that we obtained from fitting the entire set of data, we interpolated the model grid values at that angular size, and we find that the effective temperature that corresponds to the interferometric size is $T\mathrm{eff} = 6738$ K, which is much higher than the adopted effective temperature of the star of 6000 K. The corresponding interstellar reddening is $E(B-V) = 0.729 \pm 0.018$ mag, which is also higher than the value of 0.42 mag given by Zsoldos & Percy (1991). We used these values to reproduce the SED of the star, and we show our results in Figure 7.4. These discrepancies are probably due to the rapid variations of the star. Simultaneous spectrophotometric and interferometric monitoring is thus are necessary in order to determine the effective temperature of the star.
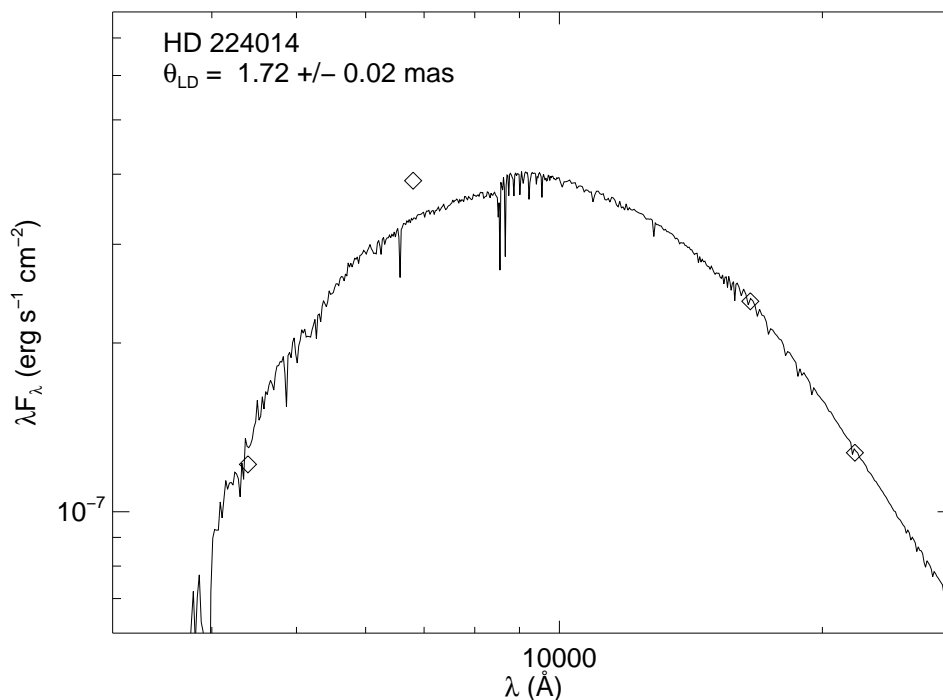
Figure 7.4: A fit of the spectral energy distribution of ρ Cas using an the best-fit limb-darkened angular diameter derived from interferometry.

7.4.2 Time Variability

In order to investigate the time variation of the star during the time period of our observations (2006 - 2009), we divided the data set to four epochs, and fitted each set separately. Table 7.5 lists the best-fit limb-darkened angular diameter of ρ Cas, the corresponding χ^2_ν, and contemporaneous estimates of the V magnitude of the star[2]. Figure 7.5 shows plots of these best-fit models at each epoch of observation. From the upper left panel to the lower right panels of Figure 7.5, we show visibility curves for data taken in 2006 Nov, 2008 Nov, 2009 Oct, and 2009 Nov, respectively. We suspect that these variations in the limb-darkened angular diameter of the yellow hypergiant are related to the pulsation of the star.

---

[2]http://www.aavso.org/
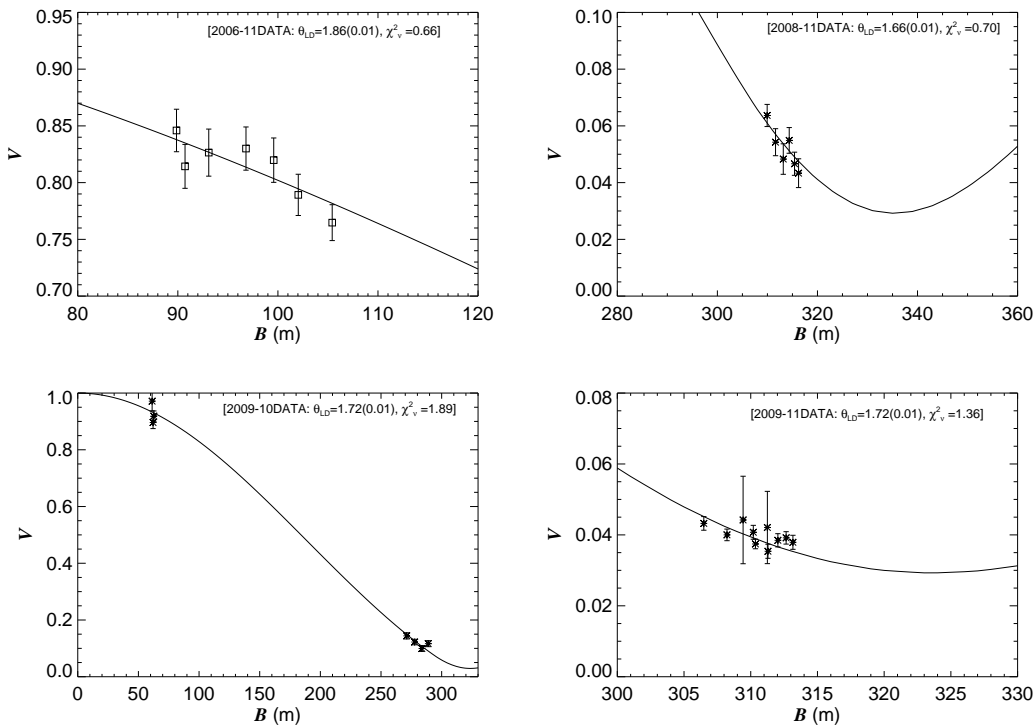
Figure 7.5: Fits of the interferometric data of ρ Cas at each epoch of observation.

Table 7.5: Best-fit Limb-darkened Angular Diameters By

Year

Obs. Epoch	θ_{LD} (mas)	χ^2_ν	V (mag)
2006-11	1.86 ± 0.01	0.66	4.57
2008-11	1.66 ± 0.01	0.76	4.62
2009-10	1.72 ± 0.01	1.89	4.47
2009-11	1.72 ± 0.01	1.36	4.48

7.4.3 Linear Radii

We provide the list of the adopted stellar properties along with recent photometric measurements of the yellow hypergiant ρ Cas in Table 7.6. We used $d = 3.1 \pm 0.5$ kpc as a distance

to the star with $A_\nu = 1.3$ mag (Zsoldos & Percy 1991), which is similar to the distance derived from the parallax estimate of $\pi = 0.28 \pm 0.21$ mas based on the new reduction of the HIPPARCOS parallaxes provided by van Leeuwen (2007). Using the best-fit limb-darkened disk angular diameter of the star, we find a linear radius of $R_{LD} = 570 \pm 97$ $R_\odot$, respectively. These linear radii values are consistent with the linear radius of 400 ± 100 $R_\odot$ predicted by Lobel et al. (2003).

Table 7.6: ρ Cas Basic Stellar Properties and Photometry

Parameter	Value	Ref.
RA (2000)	$23^{\mathrm{h}}54^{\mathrm{m}}23.11^{\mathrm{s}}$	1
Dec (2000)	$57°29'57.6"$	1
Spect. Classification	F8 Ia0	1
M $(M_\odot)$	40	1
R $(R_\odot)$	400 ± 100	1
L $(L_\odot)$	10^6	1
T_{eff} (K)	6000	2
$\log g$ (cm s^{-2})	0.70	3
$v \sin i$ (km s^{-1})......	17.1	4
U (mag)	6.864	2
B (mag)	5.714	2
V (mag)	4.517	2
R (mag)	3.780	5
I (mag)	3.220	6
J (mag)	2.269	2
H (mag)	1.915	5
K (mag)	1.670	2

References - 1: Lobel et al. (2003); 2: Soubiran et al. (2010); 3: Gorlova et al. (2006); 4: Glebocki & Gnacinski (2005); 5: Zacharias et al. (2004); 6: Monet et al. (2003).

7.4.4 Diffuse Emission

Several spectroscopic studies of ρ Cas have shown short-term and long-term variations in its spectrum, and attributed these variations to the star's pulsation and outbursts. The spectrum of ρ Cas exhibits features that range from no-line to absorption lines to emission lines, and which are interpreted as a result of an expanding shell of gas generated after outburst episodes. The most recent outburst of ρ Cas occurred between 2000 and 2001 (Lobel et al. 2003), and assuming a spherically symmetric gas shell expending at an average velocity of 35 km s^{-1}, the radius of the expanded shell reached a size of about 6 R_s only two years after its ejection in late 2002 October. The mass-loss rate of ρ Cas during this episode reached an exceptionally high estimate of $\approx 5 \times 10^{-2} M_\odot$ y^{-1}.

In interferometry, the presence of a shell is revealed by a quick drop in the visibility values from a typical first-order Bessel-function profile. To demonstrate this case, we show a synthetic image of a resolved circumstellar shell around a typical star in the left panel of Figure 7.6, and its interferometric signature in the right panel of Figure 7.6. We modeled the flux of the circumstellar shell with a Gaussian intensity distribution of 0.6 times the stellar intensity, and for this demonstrative case, we computed the interferometric visibility for several angular sizes of this shell. We show plots of the visibility curves versus baseline for the central star (solid line), for shell size of a $2R_s$ (dotted line), for a shell size of $3R_s$ (dashed line), and for a shell size $4R_s$ (dot-dashed line) in the right panel of Figure 7.6. These simple models show that the presence of circumstellar material distributed in a shell geometry at a radius of $2R_s$ induces a drop of about 25% in the visibility measurements at
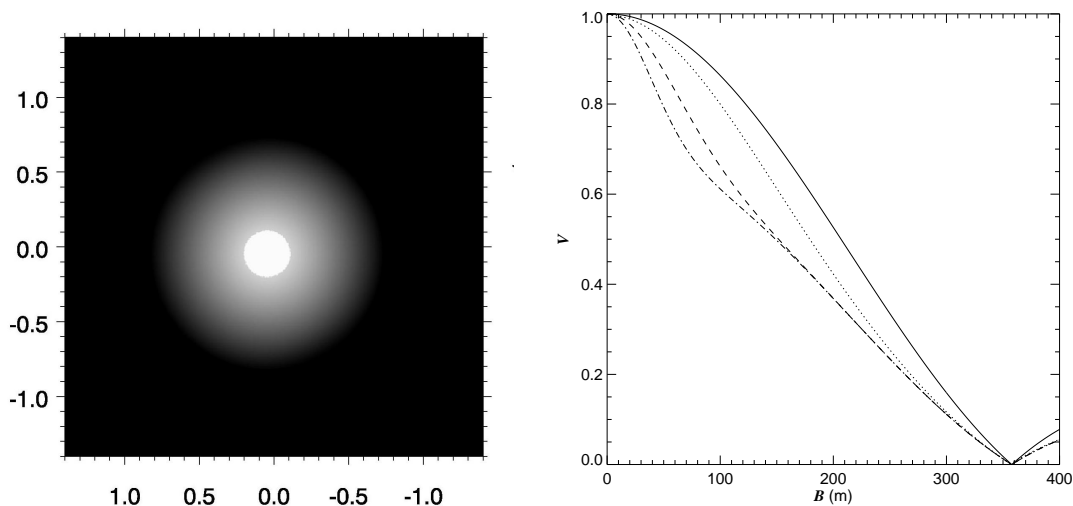
Figure 7.6: Left panel: synthetic image of a star surrounded by a circumstellar shell. Right panel: visibility curve versus baseline for a typical star (solid line) surrounded by a circumstellar shell of a radius of $2R_s$ (dotted line), $3R_s$ (dashed line), and $4R_s$ (dot-dashed line).

a 100 m baseline, while a presence of a shell at 3 R_s induces a drop of about 35% in the visibility measurements at a 100 m baseline.

In order to look for a detectable signature of expelled shell in the K-band continuum, we considered a sub-sample of our interferometric observations taken at short baselines (~ 60 m and 120 m) where the visibility measurements are more sensitive the presence of an ejected shell surrounding the photosphere of ρ Cas. The short-baseline data, especially the FLUOR data show an apparent decrement of visibility from the limb-darkened disk model suggesting that an additional source of light is present within the field of view of the interferometer. In order to explain the visibility deficit, we added a uniformly-distributed diffuse emission to our simple limb-darkened disk model. Fitting this model to the short-baseline data provides an estimate of the K-band flux ratio for the incoherent-light component of $2.3 \pm 0.2\%$, with

a reduced χ^2 of 1.2. Figure 7.7 shows the model visibility of the limb-darkened model with (solid line) and without (dotted line) an incoherent light source.
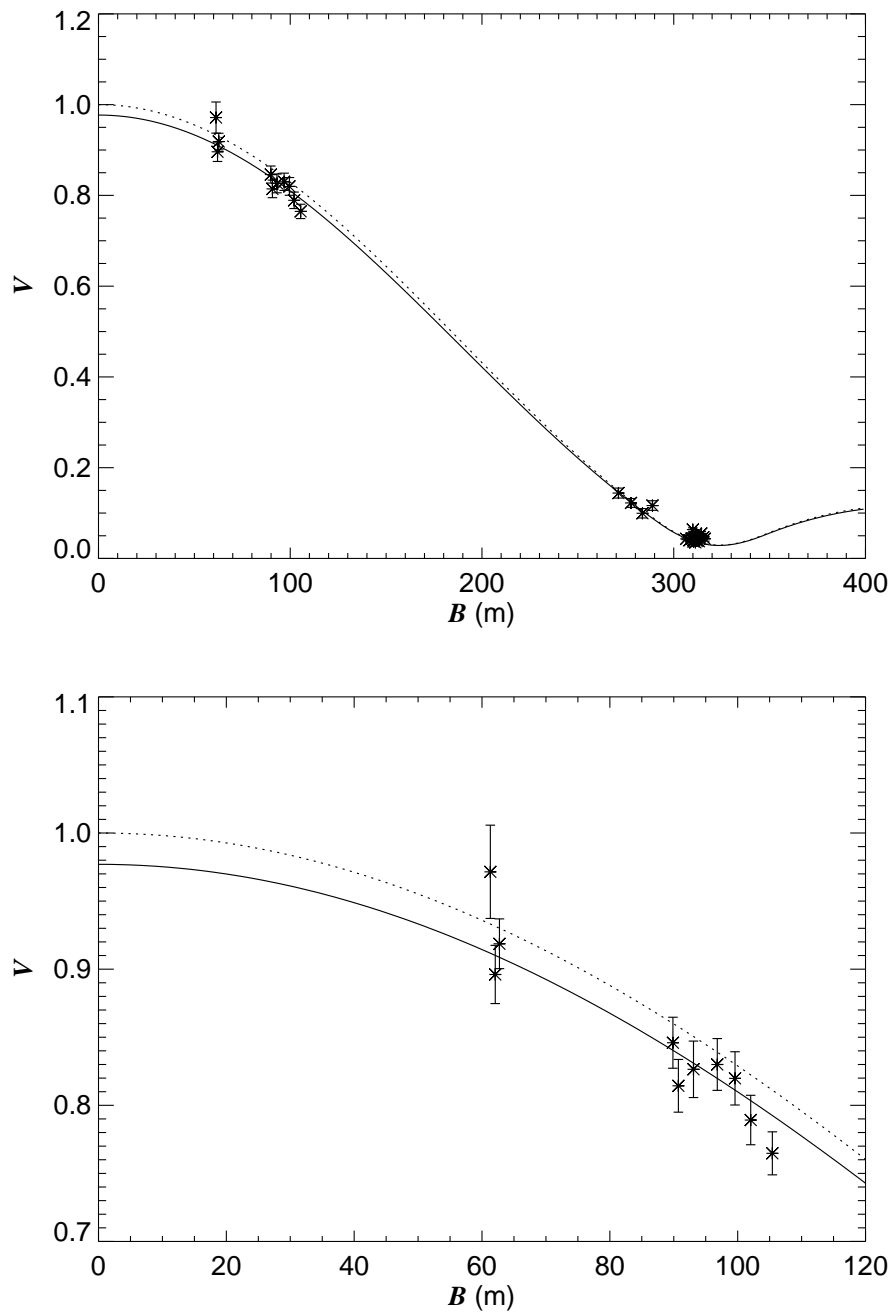
Figure 7.7: Model visibility curves of the yellow hypergiant ρ Cas. The solid and the dotted lines represent the limb-darkened disk model with and without a diffuse light component, respectively. The top panel displays the data over all baselines, while the bottom panel displays the short-baseline data.

7.5 Conclusion

We have obtained interferometric measurements of the yellow hypergiant ρ Cas that enabled us to determine the limb-darkened angular diameter of the star in the K-band continuum. Using this angular diameter of ρ Cas, we derive an estimate of the star's effective temperature. Our measurements show evidence for a 2.3 % diffuse emission in the field of view of the interferometer that could be due to the presence of a fully resolved circumstellar shell around the stellar photosphere at the time of our observations. The emission could be the result from the most recent outburst detected in the circumstellar environment of ρ Cas.

By three methods we may learn wisdom: First, by reflection, which is noblest; Second, by imitation, which is easiest; and third by experience, which is the bitterest.

—— Confucius

<center>– 8 –</center>

<center>**Summary of Results**</center>

8.1 The Circumstellar Disks of Be Stars

In this dissertation, we have conducted the largest survey of Be stars in the near-IR at the high spatial resolution provided by the CHARA Array long baseline interferometer. For a complete study, our interferometric survey was accompanied by a simultaneous spectrophotometric survey conducted using the Mimir high-resolution spectrograph at Lowell Observatory.

Our study resulted in measurements of the characteristic spatial extensions of circumstellar disks of Be stars that are responsible for the near-IR emission detected in these systems. We have demonstrated that most Be disks are easily resolvable in the K-band at CHARA's longest baselines. We found that, although our interferometric data are limited in the spatial frequency coverage to image these systems, the data provide good constraints on the brightness distribution of the disk in most cases. We fitted the interferometric data with a geometrical model that assumes a Gaussian elliptical brightness distribution of the disk, and we presented the best-fit K-band sizes along with the best-fit inclination and position angle of the disks. We then fitted the data with a radiative-transfer disk model where the opacity sources are due to the free-free-and bound-free processes in the disk.

By comparing the physical model to the data, we were able to constrain the density structure of the emitting regions in the disk for those Be stars with a good (u, v) coverage. Our results are consistent with a disk-like geometry of the circumstellar matter around the central star, which is in agreement with previous studies of Be star circumstellar environments. We show in Figure 8.1 the location of the stars in the H-R diagram, based on the
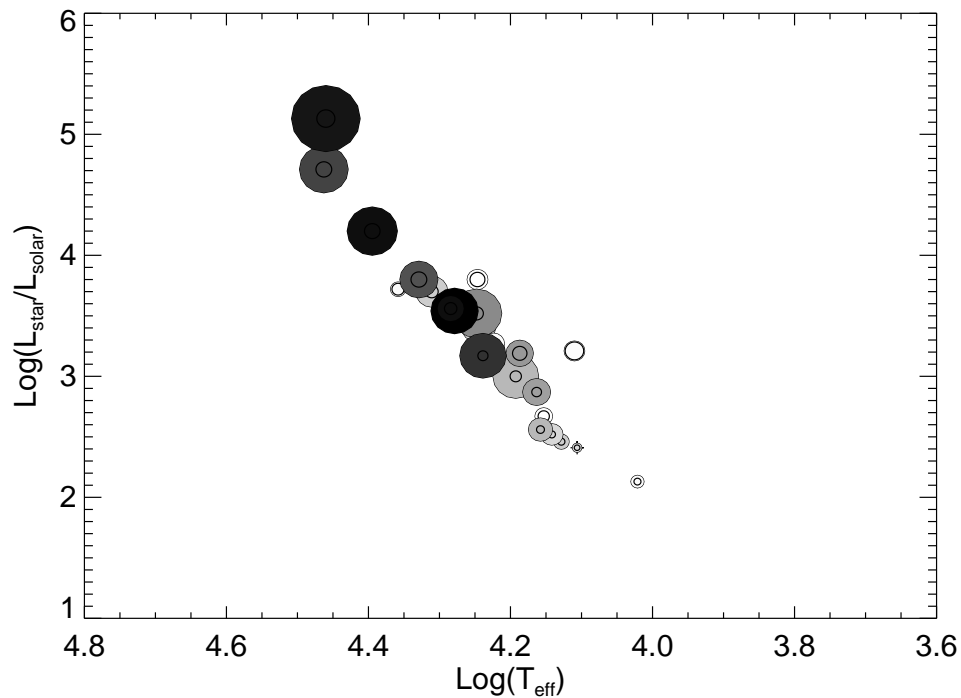
Figure 8.1: Our sample in the HR diagram. The size of each symbol is proportional to the measured linear size of the Be disk in the K-band, and the color of each symbol is proportional to the IR flux excess. The solid circles are proportional to the linear stellar sizes, and the inner dashed circle are proportional to the size of the Be star.

adopted effective temperature and luminosities listed in Table 6.1. In the diagram, the solid line circles represent the stellar linear diameters, the size of the superimposed gray circles represent the disk linear diameter, and the color is proportional to the IR flux excess of these objects (the darker the circle, the redder the object). The sources which we found to be resolved are the ones which show a higher IR flux excess. It can be seen that although there is a tendency for the excess sources with the largest disk sizes and highest brightness to be located in the upper left part of the H-R diagram, the dependence of these two quantities with the stellar luminosities and the effective temperature is rather weak as we have shown in §4.3.

By combining the inclination angles derived from interferometry with contemporaneous measurements of the projected stellar rotational velocity $v \sin i$, we were able to estimate the actual rotation rate for our sample stars, and we find that a large fraction of Be stars are rapidly rotating with rates that ranges between 0.8 - 0.9 of their critical rotational velocities.

We also explored the relationship between the disk IR flux excess and the Hα and other high level transitions of hydrogen emission lines. In particular, we found a clear correlation between the IR flux excess and the equivalent-width of the Hα emission line, and a tighter correlation between the IR flux excess and equivalent-widths of high excitation hydrogen lines such as Hu14. The latter result clearly suggests that the near-IR continuum and upper level line emission both form in the inner dense parts of the circumstellar disk, close to the stellar photosphere.

In addition, we have conducted a multiwavelength analysis of the Be disks by modeling the emitting regions of these disks at 1.7, 2.1, 4.8, 9, and 18 μm. For this purpose, we have expanded the thick disk model to a more compact radiative-transfer code that computes in detail the disk density structure, the disk color excess relative to the stellar V-band flux, and the disk spatial extension at each wavelength. We have tested our model with a sample of 130 Be stars using photometry from 2MASS and the AKARI infrared camera all-sky survey, and we have demonstrated that the resulting color excesses are in good agreement with the observed color excesses of Be stars. We have also shown that our results of the projected disk sizes on the Be stars γ Cas and ζ Tau as a function of wavelength and the model predictions are consistent with interferometric observations in the H, K, and some 12 μm VLTI observations.

8.2 Future Prospects

This work has demonstrated that circumstellar disks around Be stars are easily resolved with the CHARA Array. Follow up observations in the K- and H-band, as well as in the optical, with as extensive (u, v) coverage as possible are necessary for discriminating between competing models, as well as for the study of the mass loss process in Be stars since these object are variable.

One of the most important achievements at CHARA is the combination of light from six telescopes by the Michigan beam combiner (MIRC-6T). This new capability provides excellent Fourier coverage of the targets and more visibility and closure phase information, which in turn yields better imaging fidelity. Other instrumental upgrades are currently underway at CHARA, such as the introduction of a new fringe tracking system, an adaptive optics system, and sensitivity improvements to the VEGA and PAVO beam combiners that operate in the optical part of the spectrum.

It is clear that research on Be star disks will tremendously benefit from these upgrades. In fact, we have recently started a new follow-up observational campaign using the 3-telescope CLIMB beam combiner and the 4-telescope MIRC beam combiner in order to obtain a more complete characterization of the brightest Be stars in our sample, and we are in the process of reducing the first data sets. The use of multiple telescopes and different beam-combiners operating at different wavelengths will greatly improve the constraints that can be placed on the physical and geometrical properties of the circumstellar disks around Be stars.

REFERENCES

Ammons, S. M., Robinson, S. E., Strader, J., Laughlin, G., Fischer, D., & Wolf, A. 2006, ApJ, 638, 1004

Aufdenberg, J. P. et al. 2006, ApJ, 645, 664

Baize, P. 1983, A&AS, 51, 479

——. 1993, A&AS, 99, 205

Baldwin, R. B. 1939, ApJ, 90, 204

Balega, I. I., & Balega, Y. Y. 1988, Soviet Astronomy Letters, 14, 393

Balega, I. I., Balega, Y. Y., Vasyuk, V. A., & McManus, J. J. 1992, in Astronomical Society of the Pacific Conference Series, Vol. 32, IAU Colloq. 135: Complementary Approaches to Double and Multiple Star Research, ed. H. A. McAlister & W. I. Hartkopf, 469

Beardsley, W. R. 1969, Publications of the Allegheny Observatory of the University of Pittsburgh, 8, 91

Bidelman, W. P. 1957, PASP, 69, 573

Bjorkman, J. E., & Bjorkman, K. S. 1994, ApJ, 436, 818

Bonanos, A. Z. et al. 2010, AJ, 140, 416

Bouret, J., Donati, J., Martins, F., Escolano, C., Marcolino, W., Lanz, T., & Howarth, I. D. 2008, MNRAS, 389, 75

Carciofi, A. C., & Bjorkman, J. E. 2006, ApJ, 639, 1081

——. 2008, ApJ, 684, 1374

Carciofi, A. C., Magalhães, A. M., Leister, N. V., Bjorkman, J. E., & Levenhagen, R. S. 2007, ApJ, 671, L49

Carciofi, A. C. et al. 2006, ApJ, 652, 1617

Carciofi, A. C., Okazaki, A. T., Le Bouquin, J., Štefl, S., Rivinius, T., Baade, D., Bjorkman, J. E., & Hummel, C. A. 2009, A&A, 504, 915

Chesneau, O. et al. 2005, A&A, 435, 275

Claret, A. 2000, A&A, 363, 1081

Clarke, A. J., Oudmaijer, R. D., & Lumsden, S. L. 2005, MNRAS, 363, 1111

Clemens, D. P., Sarcia, D., Grabau, A., Tollestrup, E. V., Buie, M. W., Dunham, E., & Taylor, B. 2007, PASP, 119, 1385

Code, A. D., Bless, R. C., Davis, J., & Brown, R. H. 1976, ApJ, 203, 417

Cohen, M., Wheaton, W. A., & Megeath, S. T. 2003, AJ, 126, 1090

Collins, II, G. W. 1987, in IAU Colloq. 92: Physics of Be Stars, ed. A. Slettebak & T. P. Snow (Cambridge: Cambridge Univ. Press), 3

Collins, II, G. W., Truax, R. J., & Cranmer, S. R. 1991, ApJS, 77, 541

Cote, J., & van Kerkwijk, M. H. 1993, A&A, 274, 870

Cote, J., & Waters, L. B. F. M. 1987, A&A, 176, 93

Coudé du Foresto, V. et al. 2003, in Society of Photo-Optical Instrumentation Engineers (SPIE) Conference Series, Vol. 4838, Society of Photo-Optical Instrumentation Engineers (SPIE) Conference Series, ed. W. A. Traub, 280

Coudé du Foresto, V., Perrin, G., Ruilier, C., Mennesson, B. P., Traub, W. A., & Lacasse, M. G. 1998, in Society of Photo-Optical Instrumentation Engineers (SPIE) Conference Series, ed. R. D. Reasenberg, Vol. 3350, 856

Cushing, M. C., Vacca, W. D., & Rayner, J. T. 2004, PASP, 116, 362

Cutri, R. M. et al. 2003, 2MASS All Sky Catalog of Point Sources (Pasadena: Univ. Massachusetts/IPAC)

Dachs, J., Hanuschik, R., Kaiser, D., Ballereau, D., & Bouchet, P. 1986, A&AS, 63, 87

Delaa, O. et al. 2011, A&A, 529, A87

Dougherty, S. M., Waters, L. B. F. M., Burki, G., Cote, J., Cramer, N., van Kerkwijk, M. H., & Taylor, A. R. 1994, A&A, 290, 609

Dudley, R. E., & Jeffery, C. S. 1993, MNRAS, 262, 945

Ekström, S., Meynet, G., Maeder, A., & Barblan, F. 2008, A&A, 478, 467

Elias, II, N. M., Wilson, R. E., Olson, E. C., Aufdenberg, J. P., Guinan, E. F., Guedel, M., van Hamme, W. V., & Stevens, H. L. 1997, ApJ, 484, 394

Fabricius, C., & Makarov, V. V. 2000, A&A, 356, 141

Fitzpatrick, E. L. 1999, PASP, 111, 63

Floquet, M., Hubert, A. M., Chauville, J., Chatzichristou, H., & Maillard, J. P. 1989, A&A, 214, 295

Floquet, M. et al. 2002, A&A, 394, 137

Frémat, Y., Zorec, J., Hubert, A.-M., & Floquet, M. 2005, A&A, 440, 305

Frontera, F., dal Fiume, D., Robba, N. R., Manzo, G., Re, S., & Costa, E. 1987, ApJ, 320, L127

Gehrz, R. D., Hackwell, J. A., & Jones, T. W. 1974, ApJ, 191, 675

Gerbaldi, M., Faraggiana, R., & Caffau, E. 2007, A&A, 472, 241

Gies, D. R. et al. 2007, ApJ, 654, 527

Gies, D. R., Bagnuolo, Jr., W. G., Ferrara, E. C., Kaye, A. B., Thaller, M. L., Penny, L. R., & Peters, G. J. 1998, ApJ, 493, 440

Ginestet, N., & Carquillat, J. M. 2002, ApJS, 143, 513

Glebocki, R., & Gnacinski, P. 2005, VizieR Online Data Catalog, 3244, 0G

Gorlova, N., Lobel, A., Burgasser, A. J., Rieke, G. H., Ilyin, I., & Stauffer, J. R. 2006, ApJ, 651, 1130

Gray, D. F. 2005, The Observation and Analysis of Stellar Photospheres (Cambridge: Cambridge Univ. Press)

Gray, R. O. 1998, AJ, 116, 482

Grundstrom, E. D. 2007, Ph.D. dissertation, Georgia State Univ.

Grundstrom, E. D. et al. 2007, ApJ, 660, 1398

Grundstrom, E. D., & Gies, D. R. 2006, ApJ, 651, L53

Halonen, R. J. et al. 2008, PASP, 120, 498

Hanuschik, R. W. 1996, A&A, 308, 170

Harmanec, P. 1987, in IAU Colloq. 92: Physics of Be Stars, ed. A. Slettebak & T. P. Snow (Cambridge: Cambridge Univ. Press), 339

Harmanec, P. et al. 2000, A&A, 364, L85

Hartkopf, W. I., Mason, B. D., & Worley, C. E. 2001, AJ, 122, 3472

Henize, K. G., Wray, J. D., Parsons, S. B., & Benedict, G. F. 1979, Catalog of far-ultraviolet objective-prism spectrophotometry: SKYLAB experiment S-019, ultraviolet steller astronomy, ed. Henize, K. G., Wray, J. D., Parsons, S. B., & Benedict, G. F.

Hernández, J., Calvet, N., Hartmann, L., Briceño, C., Sicilia-Aguilar, A., & Berlind, P. 2005, AJ, 129, 856

Hoffleit, D., & Jaschek, C. 1982, The Bright Star Catalogue, Fourth revised edition (Containing data compiled through 1979), ed. Hoffleit, D. & Jaschek, C.

Hohle, M. M., Neuhäuser, R., & Schutz, B. F. 2010, Astronomische Nachrichten, 331, 349

Hony, S. et al. 2000, A&A, 355, 187

Howarth, I. D. 1979, Journal of the British Astronomical Association, 89, 378

Howells, L., Steele, I. A., Porter, J. M., & Etherton, J. 2001, A&A, 369, 99

Hubert, A. M., & Floquet, M. 1998, A&A, 335, 565

Hummel, W., & Vrancken, M. 2000, A&A, 359, 1075

Ishihara, D. et al. 2010, A&A, 514, A1

Ita, Y. et al. 2010, A&A, 514, A2

Janson, M. 2010, MNRAS, 408, 514

Jarad, M. M., Hilditch, R. W., & Skillen, I. 1989, MNRAS, 238, 1085

Jones, C. E., Molak, A., Sigut, T. A. A., de Koter, A., Lenorzer, A., & Popa, S. C. 2009, MNRAS, 392, 383

Jones, C. E., Sigut, T. A. A., & Porter, J. M. 2008, MNRAS, 386, 1922

Kanaan, S., Meilland, A., Stee, P., Zorec, J., Domiciano de Souza, A., Frémat, Y., & Briot, D. 2008, A&A, 486, 785

Karataş, Y., & Schuster, W. J. 2006, MNRAS, 371, 1793

Kastner, J. H., & Mazzali, P. A. 1989, A&A, 210, 295

Kervella, P., Bersier, D., Mourard, D., Nardetto, N., & Coudé du Foresto, V. 2004, A&A, 423, 327

Kervella, P., & Domiciano de Souza, A. 2006, A&A, 453, 1059

Kervella, P., Domiciano de Souza, A., Kanaan, S., Meilland, A., Spang, A., & Stee, P. 2009, A&A, 493, L53

Koubský, P. et al. 1997, A&A, 328, 551

——. 2010, A&A, 517, A24

Koubský, P., Yang, S., Floquet, M., Hubert, A.-M., Škoda, P., Šarounová, L., & Netolický, M. 2003, in Astronomical Society of the Pacific Conference Series, ed. L. A. Balona, H. F. Henrichs, & R. Medupe, (San Francisco: ASP), Vol. 305, 295

Kraus, S. et al. 2012, ApJ, 744, 19

Lambert, D. L., & Reddy, B. E. 2004, MNRAS, 349, 757

Lamers, H. J. G. L. M., de Groot, M., & Cassatella, A. 1983, A&A, 128, 299

Lamers, H. J. G. L. M., & Waters, L. B. F. M. 1984, A&A, 136, 37

Landolt, A. U., & Uomoto, A. K. 2007, AJ, 133, 2429

Lanz, T., & Hubeny, I. 2003, ApJS, 146, 417

Lee, U., Osaki, Y., & Saio, H. 1991, MNRAS, 250, 432

Lejeune, T., & Schaerer, D. 2001, A&A, 366, 538

Lenorzer, A., de Koter, A., & Waters, L. B. F. M. 2002a, A&A, 386, L5

Lenorzer, A., Vandenbussche, B., Morris, P., de Koter, A., Geballe, T. R., Waters, L. B. F. M., Hony, S., & Kaper, L. 2002b, A&A, 384, 473

Leushin, V. V. 2001, Astronomy Letters, 27, 634

Lobel, A. et al. 2003, ApJ, 583, 923

Luthardt, R., & Menchenkova, E. V. 1994, A&A, 284, 118

Maintz, M., Rivinius, T., Stahl, O., Stefl, S., & Appenzeller, I. 2005, Publications of the Astronomical Institute of the Czechoslovak Academy of Sciences, 93, 21

Markwardt, C. B. 2009, in Astronomical Society of the Pacific Conference Series, Vol. 411, Astronomical Data Analysis Software and Systems XVIII, ed. D. A. Bohlender, D. Durand, & P. Dowler, 251

Mason, B. D., Hartkopf, W. I., Gies, D. R., Henry, T. J., & Helsel, J. W. 2009, AJ, 137, 3358

Mason, B. D., Hartkopf, W. I., McAlister, H. A., & Sowell, J. R. 1993, AJ, 106, 637

Mason, B. D., ten Brummelaar, T., Gies, D. R., Hartkopf, W. I., & Thaller, M. L. 1997, AJ, 114, 2112

Mason, B. D., Wycoff, G. L., Hartkopf, W. I., Douglass, G. G., & Worley, C. E. 2001, AJ, 122, 3466

McAlister, H. A. et al. 2005, ApJ, 628, 439

McDavid, D. 1999, PASP, 111, 494

McSwain, M. V., Huang, W., Gies, D. R., Grundstrom, E. D., & Townsend, R. H. D. 2008, ApJ, 672, 590

Meade, M. R., & Code, A. D. 1980, ApJS, 42, 283

Meilland, A. et al. 2011, A&A, 532, A80

Meilland, A., Millour, F., Stee, P., Spang, A., Petrov, R., Bonneau, D., Perraut, K., & Massi, F. 2008, A&A, 488, L67

Meilland, A., Stee, P., Chesneau, O., & Jones, C. 2009, A&A, 505, 687

Meilland, A. et al. 2007, A&A, 464, 59

Meilland, A., Stee, P., Zorec, J., & Kanaan, S. 2006, A&A, 455, 953

Mennickent, R. E., Sabogal, B., Granada, A., & Cidale, L. 2009, PASP, 121, 125

Mérand, A., Bordé, P., & Coudé du Foresto, V. 2005, A&A, 433, 1155

Mérand, A., Coudé du Foresto, V., Kellerer, A., ten Brummelaar, T., Reess, J.-M., & Ziegler, D. 2006, in 62681F, Vol. 6268, Society of Photo-Optical Instrumentation Engineers (SPIE) Conference Series

Millar, C. E., & Marlborough, J. M. 1998, ApJ, 494, 715

Miroshnichenko, A. S., Bjorkman, K. S., & Krugov, V. D. 2002, PASP, 114, 1226

Monet, D. G. et al. 2003, AJ, 125, 984

Monnier, J. D. 2003, Reports on Progress in Physics, 66, 789

Moujtahid, A., Zorec, J., & Hubert, A. M. 1999, A&A, 349, 151

Mourard, D., Bosc, I., Labeyrie, A., Koechlin, L., & Saha, S. 1989, Nature, 342, 520

Murakami, T., Koyama, K., Inoue, H., & Agrawal, P. C. 1986, ApJ, 310, L31

Najarro, F., Hillier, D. J., & Stahl, O. 1997, A&A, 326, 1117

Neiner, C. et al. 2005, A&A, 437, 257

Nemravová, J. et al. 2012, A&A, 537, A59

——. 2010, A&A, 516, A80

Nordgren, T. E. et al. 1999, AJ, 118, 3032

Okazaki, A. T., Bate, M. R., Ogilvie, G. I., & Pringle, J. E. 2002, MNRAS, 337, 967

Okazaki, A. T., & Negueruela, I. 2001, A&A, 377, 161

Oudmaijer, R. D., & Parr, A. M. 2010, MNRAS, 405, 2439

Percy, J. R., Kolin, D. L., & Henry, G. W. 2000, PASP, 112, 363

Philip, A. D., & Egret, D. 1980, A&AS, 40, 199

Pols, O. R., Cote, J., Waters, L. B. F. M., & Heise, J. 1991, A&A, 241, 419

Porter, J. M. 1996, MNRAS, 280, L31

——. 1999, A&A, 348, 512

Porter, J. M., & Rivinius, T. 2003, PASP, 115, 1153

Quirrenbach, A. 2001, Europhysics News, 32, 237

Quirrenbach, A. et al. 1997, ApJ, 479, 477

Quirrenbach, A., Hummel, C. A., Buscher, D. F., Armstrong, J. T., Mozurkewich, D., & Elias, II, N. M. 1993, ApJ, 416, L25

Rayner, J. T., Toomey, D. W., Onaka, P. M., Denault, A. J., Stahlberger, W. E., Vacca, W. D., Cushing, M. C., & Wang, S. 2003, PASP, 115, 362

Renson, P., & Manfroid, J. 2009, A&A, 498, 961

Richardson, N. D., Morrison, N. D., Gies, D. R., Markova, N., Hesselbach, E. N., & Percy, J. R. 2011, AJ, 141, 120

Rieke, G. H. et al. 2008, AJ, 135, 2245

Rinehart, S. A., Houck, J. R., & Smith, J. D. 1999, AJ, 118, 2974

Rivinius, T. 2007, in Astronomical Society of the Pacific Conference Series, Vol. 361, Active OB-Stars: Laboratories for Stellar and Circumstellar Physics, ed. A. T. Okazaki, S. P. Owocki, & S. Stefl, 219

Rivinius, T., Baade, D., & Štefl, S. 2003, A&A, 411, 229

Rivinius, T., Štefl, S., & Baade, D. 2006, A&A, 459, 137

Roberts, Jr., L. C., Turner, N. H., & ten Brummelaar, T. A. 2007, AJ, 133, 545

Ruždjak, D. et al. 2009, A&A, 506, 1319

Saad, S. M. et al. 2005, Ap&SS, 296, 173

Schaefer, G. H. et al. 2010, AJ, 140, 1838

Searle, S. C., Prinja, R. K., Massa, D., & Ryans, R. 2008, A&A, 481, 777

Shull, J. M., & van Steenberg, M. E. 1985, ApJ, 294, 599

Sigut, T. A. A., & Jones, C. E. 2007, ApJ, 668, 481

Sigut, T. A. A., McGill, M. A., & Jones, C. E. 2009, ApJ, 699, 1973

Silaj, J., Jones, C. E., Tycner, C., Sigut, T. A. A., & Smith, A. D. 2010, ApJS, 187, 228

Skrutskie, M. F. et al. 2006, AJ, 131, 1163

Slettebak, A. 1988, PASP, 100, 770

Soubiran, C., Bienaymé, O., Mishenina, T. V., & Kovtyukh, V. V. 2008, A&A, 480, 91

Soubiran, C., Le Campion, J.-F., Cayrel de Strobel, G., & Caillo, A. 2010, A&A, 515, A111

Starikova, G. A. 1982, Soviet Astronomy Letters, 8, 166

Stee, P. 2003, A&A, 403, 1023

Stee, P., & Bittar, J. 2001, A&A, 367, 532

Stee, P., & Meilland, A. 2006, in Astronomical Society of the Pacific Conference Series, Vol.
    355, Stars with the B[e] Phenomenon, ed. M. Kraus & A. S. Miroshnichenko, 233

Steele, I. A., & Clark, J. S. 2001, A&A, 371, 643

Sterken, C., Vogt, N., & Mennickent, R. 1994, A&A, 291, 473

Struve, O. 1931, ApJ, 73, 94

Takeda, Y., Taguchi, H., Yoshioka, K., Hashimoto, O., Aikawa, T., & Kawanomoto, S. 2007,
    PASJ, 59, 1127

Tanabé, T. et al. 2008, PASJ, 60, 375

Tannirkulam, A. et al. 2008, ApJ, 677, L51

ten Brummelaar, T. A. et al. 2005, ApJ, 628, 453

Tetzlaff, N., Neuhäuser, R., & Hohle, M. M. 2011, MNRAS, 410, 190

Thom, C., Granes, P., & Vakili, F. 1986, A&A, 165, L13

Thompson, G. I., Nandy, K., Jamar, C., Monfils, A., Houziaux, L., Carnochan, D. J., &
    Wilson, R. 1978, Catalogue of stellar ultraviolet fluxes. A compilation of absolute stellar
    fluxes measured by the Sky Survey Telescope (S2/68) aboard the ESRO satellite TD-1,
    ed. Thompson, G. I., Nandy, K., Jamar, C., Monfils, A., Houziaux, L., Carnochan, D. J.,

& Wilson, R.

Tokovinin, A., Mason, B. D., & Hartkopf, W. I. 2010, AJ, 139, 743

Tokovinin, A. A. 1985, A&AS, 61, 483

Touhami, Y., Gies, D. R., & Schaefer, G. H. 2011, ApJ, 729, 17

Touhami, Y. et al. 2010, PASP, 122, 379

Townsend, R. H. D., Owocki, S. P., & Howarth, I. D. 2004, MNRAS, 350, 189

Tycner, C. et al. 2006, AJ, 131, 2710

——. 2004, AJ, 127, 1194

Tycner, C., Jones, C. E., Sigut, T. A. A., Schmitt, H. R., Benson, J. A., Hutter, D. J., &
Zavala, R. T. 2008, ApJ, 689, 461

Tycner, C. et al. 2005, ApJ, 624, 359

Underhill, A., & Doazan, V. 1982, B Stars with and without emission lines, parts 1 and 2,
ed. Underhill, A. & Doazan, V.

Štefl, S. et al. 2009, A&A, 504, 929

Vacca, W. D., Cushing, M. C., & Rayner, J. T. 2003, PASP, 115, 389

van Kerkwijk, M. H., van Paradijs, J., & Zuiderwijk, E. J. 1995, A&A, 303, 497

van Leeuwen, F. 2007, A&A, 474, 653

Walborn, N. R. 1976, ApJ, 205, 419

Waters, L. B. F. M. 1986, A&A, 162, 121

Waters, L. B. F. M., Cote, J., & Lamers, H. J. G. L. M. 1987, A&A, 185, 206

Waters, L. B. F. M., & Lamers, H. J. G. L. M. 1984, A&AS, 57, 327

Waters, L. B. F. M. et al. 2000, in Astronomical Society of the Pacific Conference Series,
Vol. 214, IAU Colloq. 175: The Be Phenomenon in Early-Type Stars, ed. M. A. Smith,

H. F. Henrichs, & J. Fabregat, 145

Wegner, W. 1994, MNRAS, 270, 229

Woolf, N. J., Stein, W. A., & Strittmatter, P. A. 1970, A&A, 9, 252

Yamamuro, T., Nishimaki, Y., Motohara, K., Miyata, T., & Tanaka, M. 2007, PASJ, 59, 973

Yudin, R. V. 2001, A&A, 368, 912

Zacharias, N., Monet, D. G., Levine, S. E., Urban, S. E., Gaume, R., & Wycoff, G. L. 2004, in Bulletin of the American Astronomical Society, Vol. 36, American Astronomical Society Meeting Abstracts, 1418

Zhang, P., Chen, P. S., & Yang, H. T. 2005, New A, 10, 325

Zhuchkov, R. Y., Malogolovets, E. V., Kiyaeva, O. V., Orlov, V. V., Bikmaev, I. F., Balega, Y. Y., & Safina, D. I. 2010, Astronomy Reports, 54, 1134

Zorec, J., & Royer, F. 2012, A&A, 537, A120

Zsoldos, E., & Percy, J. R. 1991, A&A, 246, 441

Appendices

<center>

– A –

IDL Routine of The Multiwavelength Disk Model

</center>

In this appendix, we present the IDL routine used to create synthetic images of Be disks at several wavelengths of the infrared. The input parameters of the routine are the wavelength of the observation, the stellar radius, the Be disk outer boundary, the disk inclination, the stellar mass, the stellar effective temperature, the disk gas base density, the disk density exponent, the position angle of the spin axis, and the half size of the image. The output parameters of the model are a synthetic image of the Be star system, the grid values of the image, and the total flux.

```
 PRO hvthickdisk,wavelength,rs,rd,inc,mass,teff,n0,m,sppa,di,image,xg,yg,hdmax,flux


; Input:
; rs   = stellar radius
; rd   = disk outer radius
; inc  = inclination of spin axis
; mass = stellar mass
; teff = stellar effective temperature
; n0   = base number density  (g cm^-3)
; m    = radial density exponent (approximately 2 in HV)
; sppa = spin axis position angle
; di   = half size of image (stellar radii)
        ; wavelength = wavelength of the observations


; Output:
; image = model image
; xg, yg = grid values for model

; get disk outer radius = Roche radius
incrad=inc/180.D*!pi
sininc=sin(incrad)
cosinc=abs(cos(incrad))

; create image grid
ni=512
pixel=2.*di/(ni-1.)
xg=-di+pixel*findgen(ni)
yg=xg
image=fltarr(ni,ni)

; disk temperature
td=0.6*teff  ; Carciofi & Bjorkman astro-ph/0511228


case wavelength of
      'V*':  lambda =   5531.
      'H':   lambda =  16600.
      'K':   lambda =  21329.
```

```
      '4.8': lambda =  48000.
      '9':   lambda =  90000.
      '14':  lambda= 140000.
      '18':  lambda = 180000.
       endcase
;;;;;;;;;;;;;;;;;;;;;;;;;;;;;;;;;;;;;;;;;;;;;;;;;;;;;;;;;;;;;;;;

; set approximate ionization parameters for B-stars for each
; see Lamers & Waters 1984, A&A, 136, 37; Appendix A

      if (lambda eq 5500.)  then begin
         z2mean=1.008
   gamma=1.003
   muion=1.300
   mumol=0.6487
      getkh, lambda, td, gbfff
      gbfff=gbfff(0)
      endif

       if (lambda eq 5501.)  then begin
if (td gt 15000.) then begin
         ; hot set: H+, He+, CNO++
   z2mean=1.008;
   gamma=1.003
   muion=1.300;
   mumol=0.6487;
   ; Gaunt factors from Water & Lamers 1984 Table IVd (approximate)
   tg=[20000.,22500.,25000.,27500.,30000.,35000.,40000.,45000.,50000.]
   gb=[2.157,2.047,1.967,1.909,1.861,1.805,1.770,1.750,1.740]; 1 um
   gr=[2.167,2.058,1.980,1.922,1.877,1.821,1.787,1.769,1.759] ; 1.1 microns
         ; Corrected Angstrom-micron mismatch
   gf=gb+(gr-gb)*(lambda(0)-16600.)/(20000.-16600.)
   gbfff=interpol(gb,tg,[td])
   gbfff=gbfff(0)
       print,'gbfff = ' , gbfff
   endif else begin
      ; warm set: H+, He, CNO+
      z2mean=0.912
      gamma=1.000
      muion=1.425
      mumol=0.6794
      ; Gaunt factors from Water & Lamers 1984 Table IVb
      tg=[8000., 9000.,10000.,12500.,15000.,17500.,20000.,22500.,25000.]
      gb=[4.901,4.173,3.674,2.935,2.540,2.301,2.144,2.035,1.956]; 1. um from
            ; Walters & Lamers, 1984.
            gr=[4.907,4.179,3.681,2.951,2.559,2.322,2.166,2.059,1.983] ; 1.1 microns
            gf=gb+(gr-gb)*(lambda(0)-16600.)/(20000.-16600.)
            gbfff=interpol(gb,tg,[td])
      gbfff=gbfff(0)
         endelse
        endif


      if (lambda eq 16600.)  then begin
if (td gt 15000.) then begin
   ; hot set: H+, He+, CNO++
   z2mean=1.008
   gamma=1.003
   muion=1.300
   mumol=0.6487
   ; Gaunt factors from Water & Lamers 1984 Table IVd (approximate)
   tg=[20000.,22500.,25000.,27500.,30000.,35000.,40000.,45000.,50000.]
   gb=[1.810,1.768,1.743,1.726,1.715,1.707,1.710,1.719,1.739]; 1.66 um
   gr=[1.832,1.796,1.772,1.757,1.749,1.744,1.750,1.774,1.840] ; 2.0 microns
   ; Corrected Angstrom-micron mismatch
   gf=gb+(gr-gb)*(lambda(0)-16600.)/(20000.-16600.)
   gbfff=interpol(gb,tg,[td])
   gbfff=gbfff(0)
```

```
    endif else begin
       ; warm set: H+, He, CNO+
       z2mean=0.912
       gamma=1.000
       muion=1.425
       mumol=0.6794
       ; Gaunt factors from Water & Lamers 1984 Table IVb
       tg=[8000., 9000.,10000.,12500.,15000.,17500.,20000.,22500.,25000.]
       gb=[2.815,2.566, 2.387, 2.109,1.954,1.861,1.800,1.759,1.734]; 1.66 um from
               ; Walters & Lamers, 1984.
               gr=[2.827,2.579,2.402,2.126,1.975,1.883,1.824,1.788,1.764] ; 2.0 microns
               gf=gb+(gr-gb)*(lambda(0)-16600.)/(20000.-16600.)
       gbfff=interpol(gb,tg,[td])
       gbfff=gbfff(0)
           endelse
         endif


      if (lambda eq 21329.) then begin
if (td gt 15000.) then begin
   ; hot set: H+, He+, CNO++
   z2mean=1.008
   gamma=1.003
   muion=1.300
   mumol=0.6487
   ; Gaunt factors from Water & Lamers 1984 Table IVd (approximate)
   tg=[ 8000., 9000.,10000.,12500.,15000.,17500.,20000.,22500.,25000.]
   gb=[ 2.827, 2.579, 2.402, 2.126, 1.975, 1.883, 1.824, 1.788, 1.764]+0.008 ; 2.00 microns
   gr=[ 2.834, 2.587, 2.410, 2.137, 1.987, 1.894, 1.840, 1.805, 1.782]+0.008 ; 2.22 microns
   ; Corrected Angstrom-micron mismatch
   gf=gb+(gr-gb)*(lambda(0)-20000.)/(22200.-20000.)
   gbfff=interpol(gf,tg,[td])
   gbfff=gbfff(0)
   endif else begin
      ; warm set: H+, He, CNO+
      z2mean=0.912
      gamma=1.000
      muion=1.425
      mumol=0.6794
      ; Gaunt factors from Water & Lamers 1984 Table IVb
      tg=[ 8000., 9000.,10000.,12500.,15000.,17500.,20000.,22500.,25000.]
      gb=[ 2.827, 2.579, 2.402, 2.126, 1.975, 1.883, 1.824, 1.788, 1.764] ; 2.00 microns
      gr=[ 2.834, 2.587, 2.410, 2.137, 1.987, 1.894, 1.840, 1.805, 1.782] ; 2.22 microns
      gf=gb+(gr-gb)*(lambda(0)-20000.)/(22200.-20000.)
      gbfff=interpol(gf,tg,[td])
      gbfff=gbfff(0)
      endelse
           endif


       if (lambda eq 48000.)  then begin
if (td gt 15000.) then begin
   ; hot set: H+, He+, CNO++
   z2mean=1.008
   gamma=1.003
   muion=1.300
   mumol=0.6487
   ; Gaunt factors from Water & Lamers 1984 Table IVd (approximate)
   tg=[20000.,22500.,25000.,27500.,30000.,35000.,40000.,45000.,50000.]
   gb=[1.656,1.674,1.695,1.749,1.811,1.924,2.023,2.112,2.193]; 4.65 um
   gr=[1.670,1.690,1.722,1.789,1.851,1.963,2.063,2.154,2.233] ; 5.0 microns
   ; Corrected Angstrom-micron mismatch
   gf=gb+(gr-gb)*(lambda(0)-46500.)/(50000.-46500.)
   gbfff=interpol(gb,tg,[td])
   gbfff=gbfff(0)
   endif else begin
      ; warm set: H+, He, CNO+
      z2mean=0.912
      gamma=1.000
      muion=1.425
```

```
        mumol=0.6794
        ; Gaunt factors from Water & Lamers 1984 Table IVb
        tg=[8000., 9000.,10000.,12500.,15000.,17500.,20000.,22500.,25000.]
        gb=[1.712,1.678,1.655,1.628,1.625,1.634,1.649,1.667,1.688]; 4.65 um from
                ; Walters & Lamers, 1984.
                gr=[1.719,1.686,1.661,1.639,1.637,1.647,1.663,1.683,1.714] ; 5.0 microns
                gf=gb+(gr-gb)*(lambda(0)-46500.)/(50000.-46500.)
        gbfff=interpol(gb,tg,[td])
        gbfff=gbfff(0)
            endelse
          endif

          if (lambda eq 90000.) then begin
if (td gt 15000.) then begin
   ; hot set: H+, He+, CNO++
   z2mean=1.008
   gamma=1.003
   muion=1.300
   mumol=0.6487
   ; Gaunt factors from Water & Lamers 1984 Table IVd (approximate)
   tg=[20000.,22500.,25000.,27500.,30000.,35000.,40000.,45000.,50000.]
   gb=[ 1.813,1.899,1.978,2.050,2.116,2.236,2.340,2.432,2.516] ; 8.7 micron
   gr=[ 1.872,1.960,2.041,2.114,2.182,2.303,2.408,2.502,2.586] ; 10 microns
   ; Corrected Angstrom-micron mismatch
   gf=gb+(gr-gb)*(lambda(0)-87000.)/(100000.-87000.)
   gbfff=interpol(gf,tg,[td])
   gbfff=gbfff(0)
   endif else begin
       ; warm set: H+, He, CNO+
       z2mean=0.912
       gamma=1.000
       muion=1.425
       mumol=0.6794
       ; Gaunt factors from Water & Lamers 1984 Table IVb
       tg=[ 8000., 9000.,10000.,12500.,15000.,17500.,20000.,22500.,25000.]
       gb=[ 1.607,1.605,1.608,1.628,1.659,1.710,1.806,1.893,1.972] ; 8.7 microns
       gr=[1.578,1.583,1.593,1.626,1.665,1.766,1.865,1.954,2.034] ; 10 microns
       gf=gb+(gr-gb)*(lambda(0)-87000.)/(100000.-87000.)
       gbfff=interpol(gf,tg,[td])
       gbfff=gbfff(0)
            endelse
          endif

          if (lambda eq 140000.)  then begin
if (td gt 15000.) then begin
   ; hot set: H+, He+, CNO++
   z2mean=1.008
   gamma=1.003
   muion=1.300
   mumol=0.6487
   ; Gaunt factors from Water & Lamers 1984 Table IVd (approximate)
   tg=[20000.,22500.,25000.,27500.,30000.,35000.,40000.,45000.,50000.]
   gb=[1.985,2.076,2.158,2.232,2.301,2.423,2.529,2.623,2.708]; 12 um
   gr=[2.072,2.163,2.246,2.321,2.390,2.513,2.620,2.715,2.800]; 15 microns
   ; Corrected Angstrom-micron mismatch
   gf=gb+(gr-gb)*(lambda(0)-120000.)/(150000.-120000.)
   gbfff=interpol(gb,tg,[td])
   gbfff=gbfff(0)
   endif else begin
       ; warm set: H+, He, CNO+
       z2mean=0.912
       gamma=1.000
       muion=1.425
       mumol=0.6794
       ; Gaunt factors from Water & Lamers 1984 Table IVb
       tg=[8000., 9000.,10000.,12500.,15000.,17500.,20000.,22500.,25000.]
       gb=[1.576,1.590,1.606,1.651,1.763,1.878,1.979,2.069,2.151]; 12 um
            gr=[1.578,1.597,1.618,1.709,1.845,1.962,2.065,2.156,2.238] ; 15 microns
```

```
               gf=gb+(gr-gb)*(lambda(0)-120000.)/(150000.-120000.)
        gbfff=interpol(gb,tg,[td])
        gbfff=gbfff(0)
            endelse
          endif


        if (lambda eq 180000.) then begin
if (td gt 15000.) then begin
   ; hot set: H+, He+, CNO++
   z2mean=1.008
   gamma=1.003
   muion=1.300
   mumol=0.6487
   ; Gaunt factors from Water & Lamers 1984 Table IVd (approximate)
   tg=[20000.,22500.,25000.,27500.,30000.,35000.,40000.,45000.,50000.]
   gb=[ 2.072,2.163,2.246,2.321,2.390,2.513,2.620,2.715,2.800] ; 15 micron
   gr=[ 2.216,2.310,2.394,2.470,2.540,2.664,2.772,2.867,2.953] ; 20 microns
   ; Corrected Angstrom-micron mismatch
   gf=gb+(gr-gb)*(lambda(0)-150000.)/(200000.-150000.)
   gbfff=interpol(gf,tg,[td])
   gbfff=gbfff(0)
   endif else begin
      ; warm set: H+, He, CNO+
      z2mean=0.912
      gamma=1.000
      muion=1.425
      mumol=0.6794
      ; Gaunt factors from Water & Lamers 1984 Table IVb
      tg=[ 8000., 9000.,10000.,12500.,15000.,17500.,20000.,22500.,25000.]
      gb=[1.578,1.597,1.618,1.709,1.845,1.962,2.065,2.156,2.238] ; 15 microns
      gr=[1.593,1.621,1.676,1.845,1.984,2.104,2.209,2.302,2.385] ; 20 microns
      gf=gb+(gr-gb)*(lambda(0)-150000.)/(200000.-150000.)
      gbfff=interpol(gf,tg,[td])
      gbfff=gbfff(0)
            endelse
          endif


        ;disk scale height
vtherm=12.85*sqrt(td/10000.)
cs=vtherm/sqrt(2.*mumol)
hdmax=cs*(rd/rs)^1.5/(436.6*sqrt(mass/rs))
print,' Max. scale height = ', hdmax, ' at disk radius ',rd/rs

; calculate base electron density
mh=1.672622d-24 ; hydrogen proton mass (g)
nionbase=n0/(muion*mh)
nelectron=gamma*nionbase
print,' Base electron number density = ',nelectron

; ratio of source functions
sl=planck(lambda,td)/planck(lambda,teff)
sl=sl(0)

; optical depth Dougherty et al. 1994 eqtn. 5
nu=2.997925d18 / lambda(0)
hnudivk=4.799216d-11 * nu
c=3.692e8*(1.-exp(-hnudivk/td))*z2mean/(muion*mh)^2/sqrt(td)/nu^3*gamma*gbfff
rscm=rs*6.96265e10 ; radius in centimeters
c=c*rscm
print,' Optical depth coefficient = ',c

; set up intensity matrix
zeta=1.0 ; for sl normalization
flux=0.0
hrd=3.0*hdmax      ; full z extent of disk at rd in stellar radii
hrdproj=hrd*sininc ; projected value
```

```
rdrs=rd/rs          ; disk radius in stellar radii

for ix=ni/2,ni-1 do begin ; right half
   for iy=0,ni-1 do begin ; bottom to top

      if (xg(ix)^2+yg(iy)^2 gt 1.) then begin

         ; against sky

         if (xg(ix) gt rdrs) then dflux=0. else begin ; too far right
            yedge=hrdproj+rdrs*cosinc*sqrt(1.-(xg(ix)/rdrs)^2)
            if ((yg(iy) gt yedge) or (yg(iy) lt -yedge)) then dflux=0. else begin ; too high/low
               ; visible disk contribution
               gettau,xg(ix),yg(iy),rdrs,cosinc,sininc,n0,m,hdmax,c,tau
               dflux=sl*(1.-exp(-tau))
               endelse
            endelse

         endif else begin

         ; against stellar disk

         yedgeu=hrdproj-rdrs*cosinc*sqrt(1.-(xg(ix)/rdrs)^2)>(-cosinc*sqrt(1.-xg(ix)^2))
         yedgel=-hrdproj-rdrs*cosinc*sqrt(1.-(xg(ix)/rdrs)^2)
         if ((yg(iy) gt yedgeu) or (yg(iy) lt yedgel)) then dflux=zeta else begin ; clear view to star
            ; disk seen against star
            gettau,xg(ix),yg(iy),rdrs,cosinc,sininc,n0,m,hdmax,c,tau
            dflux=sl*(1.-exp(-tau))+zeta*exp(-tau)
            endelse

         endelse

      image(ix,iy)=(dflux>0)
      flux=flux+(dflux>0)
      endfor
   endfor

; copy to left half
for iy=0,ni-1 do image(0,iy)=reverse(image(256:511,iy))
flux=2.*flux*pixel^2/!pi

; get emission spatial FWHM along axis
ixtop=fix((1.+1./di)*511./2.+1.)
ftop=max(image(ixtop,*))
itop=!c
g=where(image(*,itop) gt 0.5*ftop,cnt)
if (cnt gt 0) then begin
   gix=max(g)
   if (gix eq 511) then print,' Disk half width larger than di.' else begin
      fw=xg(gix)+pixel*(image(gix,itop)-0.5*ftop)/(image(gix,itop)-image(gix+1,itop))
      print,' Emission FWHM / stellar diameter = ',fw
      endelse
   endif

; rotate image
newim=rot(image,-sppa,1.0,255.5,255.5,cubic=-0.5,missing=0.0,/pivot)
image=newim>0

print,' Total flux = ',flux
stelflux=1.  ; primary alone

diskflux=flux-stelflux
evmk=2.5*alog10(1.+diskflux/stelflux)
print,' Model E(V-wavelength) = ',evmk

return
end
```

```
;;;;;;;;;;;;;;;;;;;;;;;;;;;;;;;;;;;;;;;;;;;;;;;;;;;;;;;;;;;;;;;;;;;;;;;;;;;;;;;;;;;;;;;;;

pro penray,xo,yo,cosinc,sininc,s,x,y,z,r
; determine the orthogonal and cylindrical coordinates
; for projected position (xo,yo) and ray position s
x=xo
y=yo*cosinc - s*sininc
z=yo*sininc + s*cosinc
r=sqrt(x^2+y^2)*1.D
return
end


;;;;;;;;;;;;;;;;;;;;;;;;;;;;;;;;;;;;;;;;;;;;;;;;;;;;;;;;;;;;;;;;;;;;;;;;;;;;;;;;;;;;;;;;;
        pro getkh, lambda, td, gbfff

        cc = 2.99792458d+10;
        h = 6.62618d-27;
        kh = 1.38054d-16;
        Rh = 1.097e5;cm-1
        nu=cc/(lambda*1.e-8)
        x=1./(lambda*1.e-4)
        stim = 1.0 - exp(-h*cc/(kh*td)/(lambda*1.e-8))


        m=findgen(10)+1.
        ybf=[[0.9916,0.09068,-0.2524],[1.105,-0.7922,0.4536],[1.101,-0.329,0.1152],
        [0.9736,0.,0.],[1.03,0.,0.],[1.097,0.,0.],[1.098,0.,0.],[1.,0.,0.],[1.,0.,0.],[1.,0.,0.]]

        gbf=dblarr(10)
        for i=0,9 do gbf(i)= ybf(0,i)+ybf(1,i)/x+ (ybf(2,i)/x/x) ;b-f for each atomic level m

        um=dblarr(10)
        for i= 0,9 do  um(i)=(h*Rh)/(kh*td*(m(i))^2.)
        mstar=sqrt(13.6*1.6e-12*lambda*1.e-8/h/cc);level that matters at nu
        ; e.g. Paschen continuum m=3 dominate in visible

        sum =0.
        kkk=dblarr(10)
        for i=0, 9 do begin
        kkk(i) = gbf(i)*exp(um(i))/m(i)^3.
        sum = sum + kkk(i)
        endfor
        ; print,'gbf==', sum

  theta=5040./td
        gff=1.084+(0.188/theta)+((0.00161+0.02661/theta)/x)+(0.0192-0.03889/theta
        + 0.02833/theta^2.-0.007828/ theta^3.+ 0.0007304/theta^4.)/x^2.
        ; print,'gff===', gff

        gbfff=sum(0)+gff(0)
        ; print,'gbfff==', gbfff

        return
        end


;;;;;;;;;;;;;;;;;;;;;;;;;;;;;;;;;;;;;;;;;;;;;;;;;;;;;;;;;;;;;;;;;;;;;;;;;;;;;;;;;;;;;;;;;

pro gettau,xo,yo,rdrs,cosinc,sininc,n0,m,hdmax,c,tau
; get optical depth along ray through xo,yo

; get integration step size
; use outer height for rays that miss disk
test=(xo/rdrs)^2+(yo/(rdrs*cosinc))^2
if (test gt 1.) then step=0.25*hdmax else begin
   ; for inner rays use local scale height
   rc=sqrt(xo^2+(yo/cosinc)^2)
   step=0.25*hdmax*(rc/rdrs)^1.5
```

```
    endelse

; get integration limits
if (sininc ne 0.) then smaxr=yo*cosinc/sininc+sqrt(rdrs^2-xo^2)/sininc else smaxr=1.e6
if (sininc ne 0.) then sminr=yo*cosinc/sininc-sqrt(rdrs^2-xo^2)/sininc else sminr=-1.e6
if (cosinc ne 0.) then smaxz=(3.*hdmax-yo*sininc)/cosinc else smaxz=1.e6
if (cosinc ne 0.) then sminz=(-3.*hdmax-yo*sininc)/cosinc else sminz=-1.e6
smax=min([smaxr,smaxz])
smin=max([sminr,sminz])
nomstep=(smax-smin)/10.
step=step<nomstep

; for stellar obscuration by disk, lower limit is R=1
r2test=1.-xo^2-yo^2
if (r2test ge 0.) then smin=sqrt(r2test)
; if (a eq 1.) then smin=smin>((yo*cosinc+sqrt(1.-xo^2))/sininc) ; old version

; set up ray
ns=long((smax-smin)/step)+1
s=step*findgen(ns)+smin
; get coordinates along ray
penray,xo,yo,cosinc,sininc,s,x,y,z,r

; get densities for these positions
hr=hdmax*(r/rdrs)^1.5
densqr=dblarr(ns)
g=where(abs(z/hr) lt 7.)
densqr=r^(-2.*m)*exp(-1.D*(z/hr)^2.)
tau=(n0^2*c*step*total(densqr))<50.
;print,xo,yo,ns,smin,smax,tau

return
end
```

– B –

Notes on Individual Be Stars

B.1 HD 4180

Koubský et al. (2010) present a single-lined spectroscopic orbit for HD 4180. Interferometric observations from NPOI of the resolved system (A, B) give good estimates of the orbital parameters (Koubský et al. 2010). The components of this binary system are too close for speckle resolution, and the object appeared in single in observations by Mason et al. (1997). Grundstrom (2007) observed spectral features corresponding to two similar late-B or early-A stars that showed Doppler shifts on a timescale of approximately 4 days, and these probably form in the close (Ba, Bb) system that was suspected by Koubský et al. (2010). We have estimated the K-band magnitude difference using the magnitude difference from NPOI $\triangle R = 2.9$ mag (Koubský et al. 2010), the estimated spectral types from Koubský et al. (2010), the near-IR color calibration from Wegner (1994), and the flux excess $E^\star(V^\star - K) = 0.13$ mag from Touhami et al. (2011).

B.2 HD 5394

γ Cas is a single-lined spectroscopic binary with a faint (undetected) companion (Harmanec et al. 2000; Miroshnichenko et al. 2002). Although this binary could be resolved in our CHARA visibility observations, the expected large magnitude difference made the detection very difficult. The distant and faint B companion (Roberts et al. 2007) has no influence on our measurements.The interferometric visibilities for γ Cas show a disk inclined by 55°, at a position angle of 32°.

B.3 HD 10516

ϕ Per is a double-lined spectroscopic system with a hot subdwarf companion (Gies et al. 1998). We have used the FUV flux ratio, temperatures, and gravities from Gies et al. (1998) and have derived magnitude differences by scaling model spectral energy distributions from Lanz & Hubeny (2003).

B.4 HD 22192

No evidence for a companion detection in speckle data (Mason et al. 1997) nor in the CHARA VEGA interferometric observations (Delaa et al. 2011). An almost edge-on disk clearly fits the data for ψ Per.

B.5 HD 23630

Alcyone is a bright Pleiades member with seven visual components listed in the WDS, but all these components have separations greater than 79 arcsec. The star appears single in speckle (Mason et al. 1997) and AO observations (Roberts et al. 2007). This source is almost unresolved, which indicates that this Be star is in a quite state.

B.6 HD 23862

Pleione is a single-lined spectroscopic binary with a low mass companion, possibly a hot subdwarf or a M-dwarf (Nemravová et al. 2010). The next companion is CHARA 125 that has a separation of $\rho \approx 0\rlap{.}''23$ (Mason et al. 1993; Roberts et al. 2007), but it is not always detected in speckle measurements, indicating a large magnitude difference of $\triangle V \approx 3.5$ mag. Luthardt & Menchenkova (1994) present a radial velocity study that suggests that the orbital period is ≈ 35 year, and the eccentricity is found to be large. There are five other,

fainter but wider ($\rho > 4\rlap{.}''6$), visual companions in the WDS, which should not affect our measurments.

B.7 HD 25940

No companion is evident in the CHARA VEGA observations of Delaa et al. (2011). No speckle observations of this star are published. The interferometric visibilities for 48 Per show a disk inclined by 51°, at a position angle of 34°.

B.8 HD 37202

Ruždjak et al. (2009) present an analysis of the single-lined spectroscopic orbit for ζ Tau. No other components are found in speckle (Mason et al. 1993) or interferometric observations (Štefl et al. 2009; Schaefer et al. 2010). ζ Tau has a quite long history of interferometric observations.

B.9 HD 58715

Jarad et al. (1989) suggest that β CMi is a single-lined, spectroscopic binary with a period of 218 d, but this result has not yet been confirmed by other investigators. Interferometric studies by Meilland et al. (2009) and Kraus et al. (2012) show no evidence of a close companion. Furthermore, no companion is found in speckle data (Mason et al. 1993) and AO imaging (Janson 2010). Eight faint and distant companions are listed in the WDS.

B.10 HD 109387

Saad et al. (2005) show that κ Dra is a single-lined, spectroscopic binary with a faint companion. Gies et al. (2007) found that the addition of a hot companion improved the fit of the K-band interferometry, but Jones et al. (2008) point out that density exponent found by

Gies et al. (2007) is significantly lower than that determined from Hα interferometry. There are no published speckle measurements.

B.11 HD 138749

θ CrB has a companion whose separation has increased from $0\rlap{.}''642$ in 1976 to $0\rlap{.}''813$ in 2010 according to the WDS, but the position angle varied by only $4°$ over the same interval, and this suggests a large orbital eccentricity and/or an inclination $\approx 90°$. The B, V-band magnitudes were measured by Fabricius & Makarov (2000), and these suggest that the system consists of a B6 Vnne primary and a A2 V secondary. Assigning masses for these classifications and assuming that the semimajor axis is close to the smallest observed ($a = 0\rlap{.}''5$), we have calculated a preliminary period that is given in Table 6.9. There are no obvious radial velocity variations indicative of a spectroscopic binary (Rivinius et al. 2006).

B.12 HD 142926

Koubský et al. (1997) present a single-lined spectroscopic orbit for 4 Her. They argue that the companion star must be a small object since they see no evidence of its spectral features. No other companions are observed with speckle (Mason et al. 1997) nor found in the WDS.

B.13 HD 142983

The spectrum of 48 Lib is dominated by shell features that vary on a timescale of a decade, and it is very difficult to study the photospheric spectrum of the star (B3: IV:e shell) to search for radial velocity variations (see Rivinius et al. 2006). Unfortunately, there are no published speckle observations, and there are no companions indicated in the WDS. We assume it is a single object.

B.14 HD 148184

Harmanec (1987) presents a preliminary single-lined orbit χ Oph with a period of 34.121 d. There are no available speckle observations, and no companion is indicated in the WDS. Tycner et al. (2008) obtained interferometric observations at Hα to measure the disk, and they make no mention of evidence of a companion. The interferometric visibilities for χ Oph are consistent with a disk inclined by 63°.

B.15 HD 164284

The visual companion of 66 Oph was first discovered by Mason et al. (2009) and confirmed by Tokovinin et al. (2010). We assumed that the current separation corresponds to the angular semiamplitude, and we estimated the orbital period by assigning masses assuming main sequence stars, the temperature from Frémat et al. (2005), and the measured $\triangle V = 2.7$ mag (Tokovinin et al. 2010). Floquet et al. (2002) discuss spectroscopy of the star and pulsational behavior, but no mention is made of a spectroscopic binary companion.

B.16 HD 166014

Tokovinin (1985) reported a marginal detection of a close companion to o Her at a separation of 60 mas, but this was not confirmed in later speckle observations by Mason et al. (2009). There is no known spectroscopic companion, and Grundstrom (2007) found no evidence of radial velocity variability (see also Beardsley 1969). The interferometric measurements for this particular target showed lower visibilities at short baselines, which could not be fitted by the standard Gaussian elliptical model. We have thus assumed a companion that is 2.5 mag fainter than the Be star in the K-band, and applied the binary correction to fit the data.

B.17 HD 198183

The λ Cyg system consists of at least four stars. Component C is distant and faint. The AB system has a long period ($\approx$ 461 y), and the magnitude difference was determined by Fabricius & Makarov (2000). We used the classifications of B5 V and B7 V for A and B (Hoffleit & Jaschek 1982), the $V - K$ color calibration from Wegner (1994), and $\triangle V$ from Fabricius & Makarov (2000) to find $\triangle K$. Balega & Balega (1988) and Balega et al. (1992) determined an astrometric orbit for the close pair McA 63 Aa,Ab that apparently consists of almost equal magnitude stars. However, this close pair was not detected in recent speckle observations by Mason et al. (2009). Grundstrom (2007) notes the presence of some short term line profile variability that might be explained as the result of a Be star plus a single-lined spectroscopic binary.

B.18 HD 200120

59 Cyg has a nearby B companion (Mason et al. 2009) plus three other very distant and faint components. B. Mason kindly provided us with a preliminary orbit for A,B that we used to estimate the position and separation at the times of our CHARA Array observations. The Be star is also a spectroscopic binary with a hot subdwarf companion (Maintz et al. 2005), and consequently we assume that the smaller $\triangle K$ (brighter) estimate is more reliable in Table 6.9.

B.19 HD 202904

υ Cyg has four faint and distant companions listed in the WDS, but there is no close companion detected in speckle interferometric observations (Mason et al. 1997). Neiner et

al. (2005) discuss spectroscopic radial velocities that may be consistent with binary motion for a period of 11.4 year,but further measurements are required to verify their suggestion.

B.20 HD 203467

There are no companions of 6 Cep listed in the WDS, and, unfortunately, there are no published speckle observations of this star. Spectroscopic observations are discussed by Koubský et al. (2003) who show that the profiles vary with a 1.621 d cycle, a period is that is probably related to pulsation or rotation.

B.21 HD 209409

There are no companions of o Aqr listed in the WDS, and no companions werefound by Oudmaijer & Parr (2010) using adaptive optics observations with VLT/NACO. Rivinius et al. (2006) discuss spectroscopy of this Be-shell star and note no evidence of a binary companion.

B.22 HD 212076

No companions of 31 Peg are listed in the WDS. Rivinius et al. (2003) describe the short term spectroscopic variations related to pulsations, but there is no evidence of a spectroscopic companion.

B.23 HD 217675

Zhuchkov et al. (2010) present a re-analysis of all the existing plus new astrometric and radial velocity measurements for o And. They show that the system has a $2 + 2$ hierarchy and the pairs share a wide orbit with a period of 117 year. The A component is probably a

spectroscopic binary consisting of the Be star and late-B star companion in a 5.7 year orbit, while the B component consists of a pair of similar late-B stars in a 33 d spectroscopic orbit.

B.24 HD 217891

No companions of β Psc are listed in the WDS and none were found in adaptive optics observations by Roberts et al. (2007). Dachs et al. (1986) discuss radial velocity measurements that appear to be relatively constant.

<div align="center">

– **C** –

Correction for the Flux of Nearby Companions

</div>

C.1 Magnitude Difference and Orbital Elements for Binary Visibility Corrections

The visibility measured for a binary or a multiple star system will be altered by the flux of the companion(s). We can correct for this by considering the co-addition of fringe patterns for each star. This requires a knowledge of the projected separation between the stars and their flux ratio. Unfortunately, in most cases the magnitude differences between the Be star primary and the companion are only available in the V-band. Here we need the magnitude differences in the K-band in order to determine the affect of the companion's flux on our visibility measurements. For this purpose, we want to find the color difference between the components and how much brighter the Be star plus disk appears in the K-band compared to the V-band. The predicted magnitude difference is

$$\triangle K_{\mathrm{obs}} = -2.5 \log_{10} \frac{F_{\mathrm{comp}}}{F_{\mathrm{Be}} + F_{\mathrm{disk}}} = -2.5 \log_{10} \frac{F_{\mathrm{comp}}}{F_{\mathrm{Be}}} + 2.5 \log_{10}(1 + \frac{F_{\mathrm{disk}}}{F_{\mathrm{Be}}}) \qquad (\mathrm{C}.1)$$

where $F_{\mathrm{comp}}, F_{\mathrm{Be}}, F_{\mathrm{disk}}$ are the monochromatic K-band fluxes for the companion, Be star, and Be disk, respectively. We can estimate the first term from the color differences of the Be star and companion,

$$\triangle K_{\mathrm{bin}} = -2.5 \log_{10} \frac{F_{\mathrm{comp}}}{F_{\mathrm{Be}}} = \triangle V_{\mathrm{bin}} + (V - K)_{\mathrm{Be}} - (V - K)_{\mathrm{comp}} \qquad (\mathrm{C}.2)$$

where we will assume that the disk contribution is negligible in the V-band so that $\triangle V_{\mathrm{bin}} = \triangle V_{\mathrm{obs}}$. In the absence of other information, we estimated the color differences $(V - K)$ by assuming that both the Be star and companion are main sequence objects, and we used the relationship between $(V - K)$ and magnitude difference from a primary star of effective

temperature $T_{\text{eff}}(\text{Be})$ (Frémat et al. 2005) for main sequence stars from Lejeune & Schaerer (2001) to find $(V - K)$ for both stars.

We can determine the infrared flux excess term $(1+F_{\text{disk}}/F_{\text{Be}})$ from our observed estimate of $E^{\star}(V^{\star} - K)$ (Touhami et al. 2011), which is related by

$$E^{\star}(V^{\star} - K) = 2.5 \log \frac{F_{\text{tot}}^{K}}{F_{\text{tot}}^{V}(F_{\text{Be}}^{K}/F_{\text{Be}}^{V})} = 2.5 \log_{10} \frac{[1 + F_{\text{disk}}/F_{\text{Be}} + F_{\text{comp}}/F_{\text{Be}}]^{K}}{[1 + F_{\text{disk}}/F_{\text{Be}} + F_{\text{comp}}/F_{\text{Be}}]^{V}} \qquad \text{(C.3)}$$

where the superscripts indicate the filter band. Again, if we suppose that disk contributes no flux in the V-band, then we can rearrange this equation to find the K-band flux excess relative to that of the Be star alone. Then we can combine the results from the two equations above to predict (after some algebra) the K-band magnitude difference that would be observed,

$$\triangle K_{\text{obs}} = \triangle K_{\text{bin}} + E^{\star}(V^{\star} - K) + 2.5 \log_{10}(1 + 10^{-0.4\triangle V_{\text{bin}}} - 10^{-0.4(\triangle K_{\text{bin}} + E^{\star}(V^{\star} - K))}). \quad \text{(C.4)}$$

There are several instances where the Be star is a single-lined spectroscopic binary with a companion of an unknown type and $\triangle V_{\text{obs}}$. We consider two hypothetical cases. First, we assume that the companion is a main sequence star of one solar mass, and we use the Lejeune & Schaerer (2001) main sequence relation to obtain the magnitude and color differences of the companion. The second case is to assume that the companion is a hot subdwarf (similar to the case of ϕ Per; see Gies et al. 1998) with a typical effective temperature of 30 kK and a stellar radius of $1R_{\odot}$. We then estimate $\triangle K_{\text{obs}}$ by adopting the main sequence radius for the Be star according to its effective temperature and by using the Planck function to estimate the monochromatic K-band flux ratio. Table 6.6 (§6.3) lists the magnitude difference range between a hot subdwarf (smaller) and a solar-type companion (larger). However, we made no visibility corrections in most of these cases because the nature of the companion is so

uncertain (with the exception of ϕ Per where the companion's spectrum was detected and characterized by Gies et al. 1998).

Table C.1: Binary Orbital Elements

HD Number	P (d)	e	T (HJD)	ω (deg)	a (mas)	i (deg)	Ω (deg)	$\triangle K_{obs}$ (mag)	Ref.
4180	1031.550	0.00	2452792.200	180.0	17.00	115.0	267	2.6	Koubský et al. 2010
10516	126.673	0.00	2450091.770	180.0	4.90	72.5	117	3.1	Gies et al. 1998
23862	12615.000	0.90	2453629.000	115.0	150.47	138.0	357	2.1	This work
138749	73048.440	0.50	2433000.000	30.0	581.61	98.0	21	1.8	This work
164284	9861.539	0.40	2451150.000	165.0	103.23	52.0	180	2.1	This work
166014	...	...	...	...	...	...	...	2.5	This work
198183	4272.603	0.52	2444797.000	253.5	48.70	135.1	119	0.7	Baize (1993) and this work
198183	168559.275	0.35	2378057.800	322.0	770.00	146.3	144	1.2	Baize (1983)
200120	58973.320	0.26	2460416.414	265.5	207.60	145.8	205	2.6	B. Mason, priv. comm.
217675	2059.966	0.22	2452859.405	55.0	61.00	152.0	318	2.1	Zhuchkov et al. 2010
217675	42879.434	0.37	2455050.859	144.2	295.00	109.6	7	2.2	Zhuchkov et al. 2010

In order to correct our visibility measurements for the flux of a nearby companion, we also need to determine the companion's separation and position angle at the time of our observations in order to find how the companion's fringes interfere with those of the Be star. In principle, the visibility data might be analyzed directly for evidence of the binary signal, but in practice it takes many interferometric observations distributed around the orbit to make a reliable solution of the astrometric orbital elements. Our survey data are too fragmentary and limited in time to make such an analysis, so we must rely on other studies in general to estimate the orbital parameters of the binaries. We show in Table C.1 our adopted orbital parameters for those binaries where visibility corrections were possible. In several of these cases, we made preliminary orbital solutions ourselves based upon literature measurements and we give details of these fits in Appendix B.

C.2 Seeing and Effective Flux Ratio

Our CHARA Classic observations were recorded on a single pixel on the CHARA Near Infrared Observer (NIRO) camera, and the physical size of the pixel corresponds to a square of dimensions 0.8×0.8 arcsec on the sky. Companions with separations small compared to 0.8 arcsec will be more or less completely recorded in the observations, but companions at larger separations may be only partially recorded according to the separation and seeing conditions at the time of observation. Thus, we need to calculate the effective flux ratio of companion to target based upon the relative amounts of flux recorded by this one pixel.

We did this following the example given by Boyajian et al. (2008) by calculating the effective flux recorded of the seeing disks of both stars. Seeing information is recorded in real time according to tip-tilt measurements based on the V-band flux of the targets. We

assume that the K-band seeing differs according to wavelength by $\lambda^{-1/5}$ (Young 1974), so that the K-band seeing disk is 0.76 times that in V.

The corrected flux ratio is given by

$$F_{\text{comp}}/F_{\text{target}} = I_2/I_1 \tag{C.5}$$

where I_1 and I_2 are the net intensity contributions of the primary and secondary component, respectively, recorded by the pixel. We first assume a Gaussian distribution for the seeing pattern as projected on the detector,

$$I(x, x_0, y, y_0) = \frac{1}{2\pi\sigma^2} \exp\left[-\frac{1}{2\sigma^2}[(x - x_0)^2 + (y - y_0)^2]\right], \tag{C.6}$$

where (x_0, y_0) are the coordinates of the central position of the star on the detector chip, and σ is related to the seeing estimate at the time of the observation, $\sigma = 2.355^{-1} \theta_{seeing}$. The intensity distributions of the primary and the secondary components integrated over one pixel on the detector are thus given by

$$I_1 = Q \int \int I(x, 0, y, 0) \, dx \, dy \tag{C.7}$$

$$I_2 = \int \int I(x, 0, y, \rho_{12}) \, dx \, dy \tag{C.8}$$

where ρ_{12} is the separation of the binary, and Q is the actual intensity ratio of the secondary to the primary. This last quantity is derived from the magnitude difference of the binary in the K-band

$$Q = 10^{-0.4 \, \triangle K_{\text{obs}}}. \tag{C.9}$$

C.3 Fringe Visibility for Be Stars in Binaries

It is helpful to consider how the fringe patterns of binaries overlap in order to assess the changes in visibility caused by a binary companion. Let us first examine the case of the patterns for two unresolved stars in a binary, and then extend the analysis to the situation where one star (Be plus disk) is partially resolved. The fringe packet for star i observed in an interferometric scan of changing path length has the form

$$F_i = \frac{\sin x}{x} \cos(2\pi \frac{a}{\lambda} + \phi) \tag{C.10}$$

where $x = \pi a / \wedge_{coh}$, a is the scan position relative to the center of the fringe, $\wedge_{coh}$ is the coherence length given by $\lambda^2 / \delta\lambda$ (equal to 13 μm for the CHARA Classic K' filter), and ϕ is the phase of the fringe packet. If two stars are present in the pixel field of view and separated along the scan vector by x_2, then their fringe patterns may overlap and change the composite appearance,

$$F_{tot} = \frac{1}{1 + f_2/f_1} F_1 + \frac{f_2/f_1}{1 + f_2/f_1} F_2. \tag{C.11}$$

We show a series of such combined fringe patterns in the panels of Figure C.1 for an assumed flux ratio of $f_2/f_1 = 0.5$. In the top panel, projected separation is zero, and the two patterns add to make the fringe pattern of a single unresolved star. The associated visibility that we would measure

$$V = (\max(F_{tot}) - \min(F_{tot}))/(2 + \max(F_{tot}) + \min(F_{tot})) \tag{C.12}$$

equals one in this case. However, in the second panel from the top, we show how a projected separation of 1 μm results in a much lower visibility because the peaks associated with star 1 are largely eliminated by the troughs associated with star 2. In the third panel from the
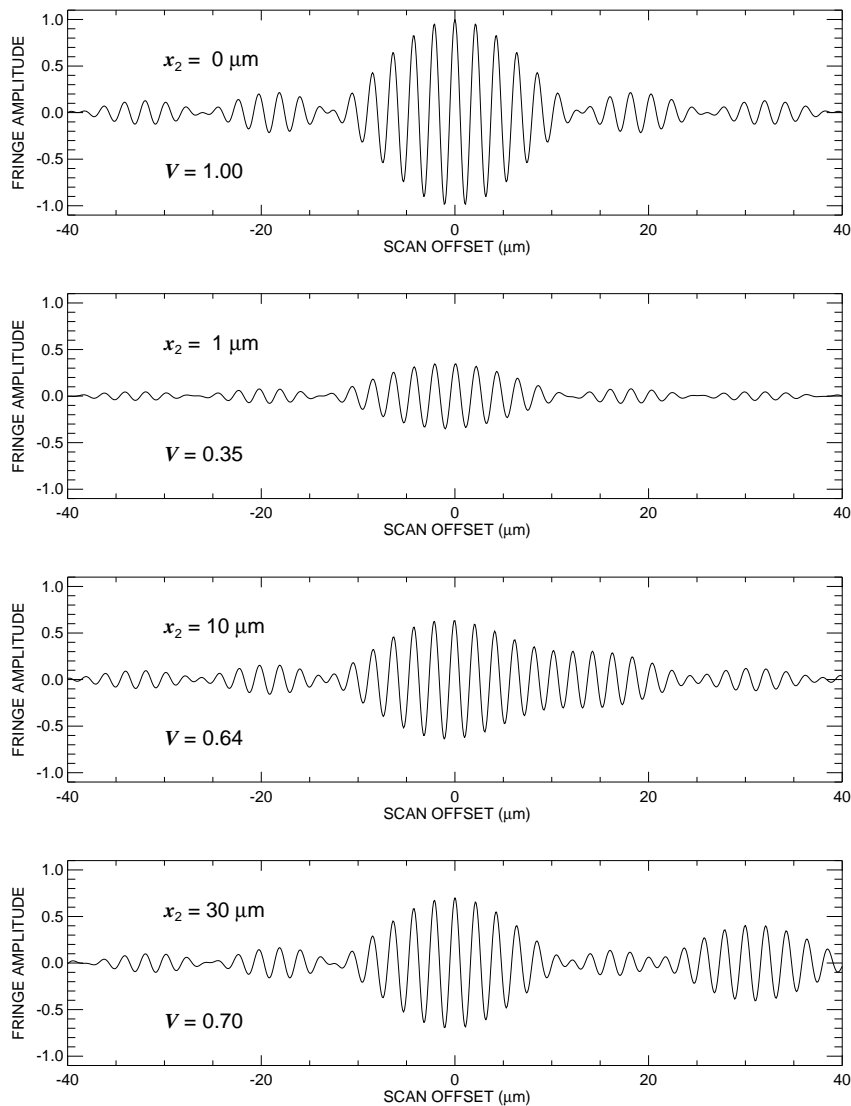
Figure C.1: A series of combined fringe patterns for an assumed flux ratio of $f_2/f_1 = 0.5$ and a projected separation of zero (upper panel), 1 μm (second panel from the top), 10 μm (third panel from the top), and 30 μm (bottom panel).

top, the separation is just large enough (comparable to the coherence length) that the fringe pattern of the companion emerges from the blend, and the lower panel shows a separated fringe packet in which both fringe patterns are clearly visible.

We show in Figure C.2 the net visibility that would be measured as a function of projected separation x_2. This shows that in general the observed visibility will be less than that of a
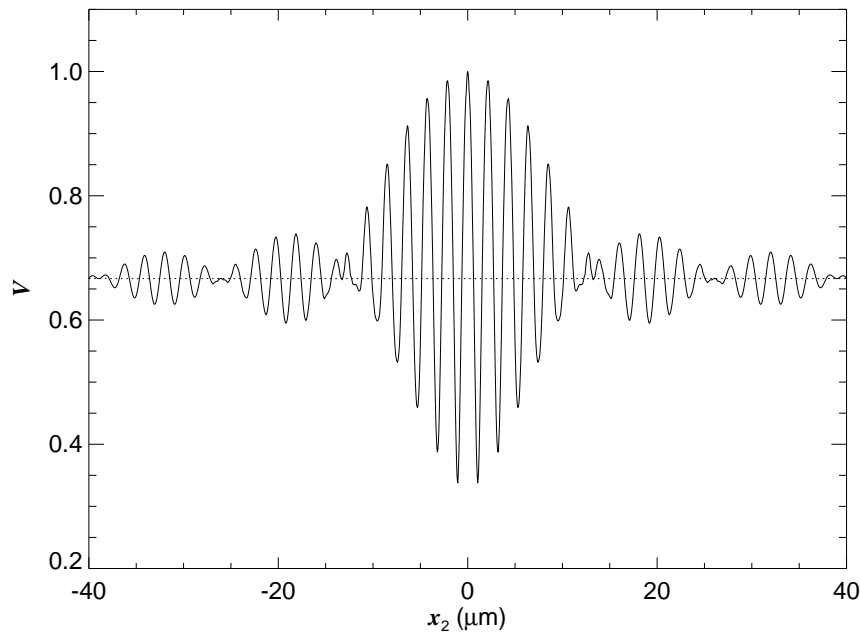
Figure C.2: The net visibility as a function of the binary projected separation x_2

single star. For very close separations the visibility varies sinusoidally with separation, while

at large separations, the visibility approaches the value $\frac{1}{1+f_2/f_1}$ equal to the amplitude of the

flux diluted fringe pattern of the target.

Now suppose that star 1 is a Be star with a disk that is partially resolved, so that if it were

observed alone, it would show a visibility $V = V_c < 1$. Consequently, its fringe pattern would

have an amplitude given by $\frac{V_c}{1+f_2/f_1}$. We show a selection of model binary fringe patterns in

Figure C.3 again for $f_2/f_1 = 0.5$ and a specific separation of $x_2 = 10$ μm. The panels show

from top to bottom the progressive appearance of the combined fringe patterns as V_c drops

from 1 to 0.25. Now the visibility drops in tandem until $V_c = 0.50$ where the maximum

and minimum are set by the fringe pattern of the companion. We show the relationship

between the Be star visibility V_c and the net observed visibility V_o in Figure C.4 (solid line

for $x_2 = 10$ μm). At this separation, there is some slight destructive interference between the

fringe patterns that decreases the maximum amplitude for star 2, and as V_c declines to zero, the net visibility attains the amplitude of star 2 alone $\frac{f_2/f_1}{1+f_2/f_1}$. Figure C.4 shows the (V_c, V_o) relationship for two other separations. The dotted line shows the case of zero separation for maximum constructive interference, and here the visibility declines linearly to $\frac{f_2/f_1}{1+f_2/f_1}$ as V_c tends to zero. Finally, the dashed line shows the case for a very large separation in which the fringe pattern of star 2 falls beyond the recorded portion of the scan. Here the visibility starts at its diluted value of $\frac{1}{1+f_2/f_1}$ at $V_c = 1$ and declines to near zero at $V_c = 0$.

Thus, to correct the observed visibilities for the presence of a companion, we need a diagram like Figure C.4 for each observation of a target. We calculated the projected separation of the stars at the time of the observation, and then created an associated (V_c, V_o) diagram based upon the separation and effective flux ratio. The corrected visibility V_c was then found by interpolating in the relationship at the observed V_o value. In some rare circumstances, we encountered a double-valued (V_o, V_c) relation, so no correction was attempted because of this ambiguity. The corrected visibilities and their corresponding errors are listed in the last two columns of Table 6.5.
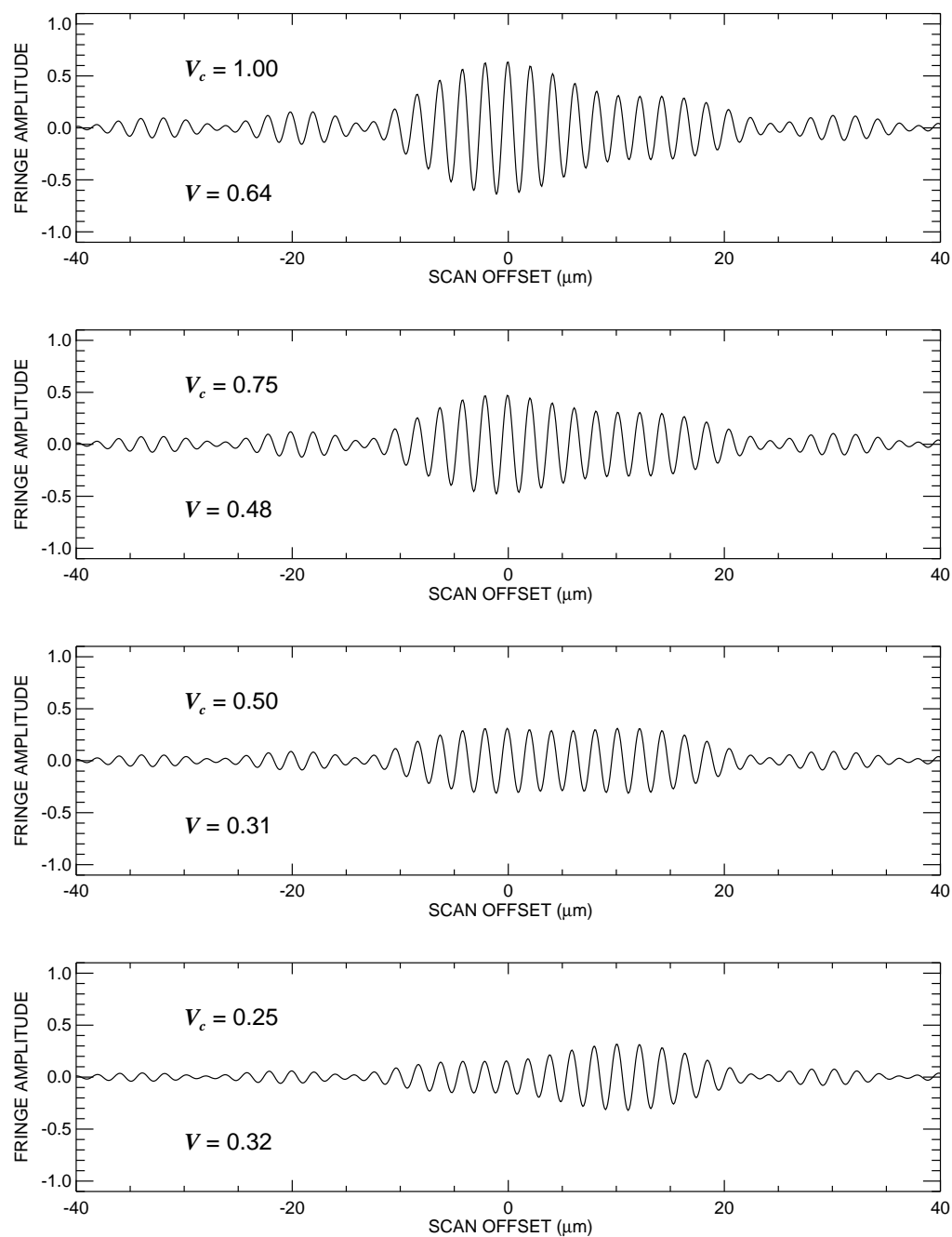
Figure C.3: Model binary fringe patterns for $f_2/f_1 = 0.5$ and a separation of 10 μm. From top to bottom, the panels show the progressive appearance of the combined fringe patterns as the visibility of a star-plus-disk V_c drops from 1 to 0.25.
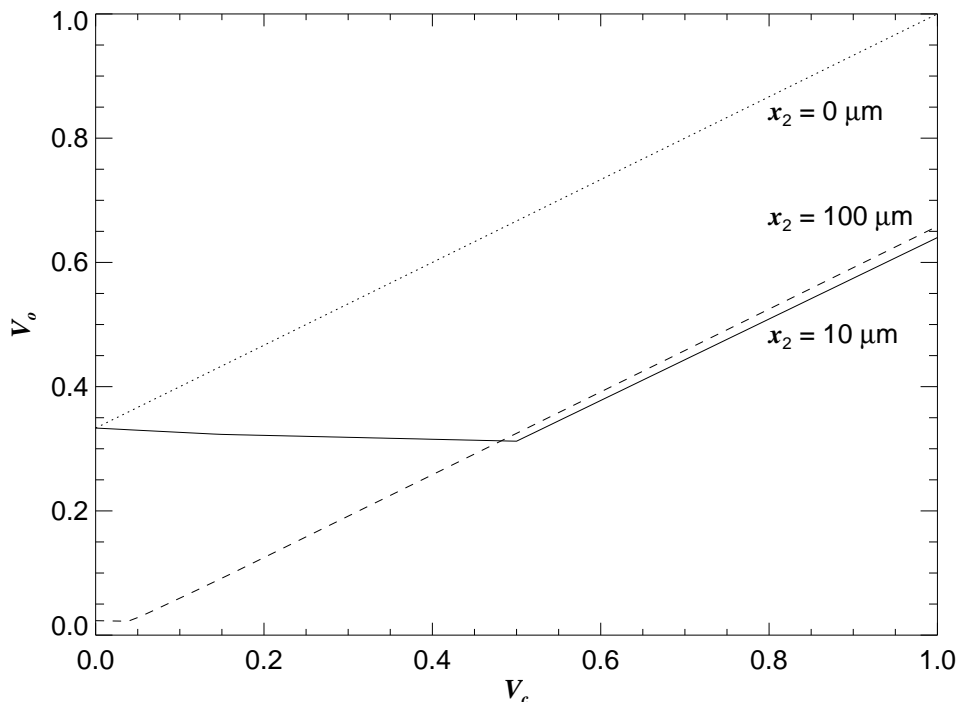
Figure C.4: The relationship between the Be star visibility V_c and the net observed visibility V_o.

C.4 Fringe Visibility for Be Stars in Multiple Systems

There are six systems in our sample with two or more companions. In the cases of HD 5394 (γ Cas), HD 23862 (Pleione), and HD 200120 (59 Cyg), the inner companion remains largely undetected, so corrections were made for only the outer companion (if sufficiently bright). The spectroscopic pair that comprises the B component of HD 4180 (o Cas) was treated as a single object, so this system was corrected as a binary star. This left two systems, HD 198183 (λ Cyg) and HD 217675 (the quadruple o And), that required corrections for additional flux components. Details about these systems are given in Appendix B.

We made visibility corrections for these two systems in much the same way as for the binaries, except in this case the fringe normalizations were assigned by

$$F_{tot} = \frac{1}{1 + f_2/f_1 + f_3/f_1} F_1 + \frac{f_2/f_1}{1 + f_2/f_1 + f_3/f_1} F_2 + \frac{f_3/f_1}{1 + f_2/f_1 + f_3/f_1} F_3. \qquad \text{(C.13)}$$

Again, we formed model visibilities from the coaddition of the fringe patterns, determined the (V_c, V_o) relationships for the time and baseline configuration of each observation, and then used the inverted relation (V_o, V_c) to determine the corrected visibility.

Unfortunately, there are significant uncertainties surrounding both the magnitude differences and orbital elements for the companions of HD 198183 and HD 217675, and these introduce corresponding uncertainties in the amounts of visibility correction. Our results on these two systems must therefore be regarded as representative visibility solutions rather than definitive ones. However, the corrected visibilities are all close to one for these two Be stars, and this suggests that their disks are only marginally resolved if at all. On the other hand, the much lower uncorrected visibilities of these two show that the signal of the companions is present, and both targets will be important subjects for future, multiple baseline observations with the CHARA Array.